Freie Universität Berlin

Fachbereich Geowissenschaften der Freien
Universität Berlin

Dissertation

zum Erwerb des Akademischen Grades

Doctor rerum naturalium (Dr. rer. nat.)

„Geochemical proxy records identifying
climatic and environmental changes across
the Permian-Triassic boundary of key sections in NW Iran“

vorgelegt von

Martin Amandus Nicola Schobben

Berlin, September 2014

Leibniz Association

museum für
naturkunde
berlin

Gutachter der Dissertation

Erster Gutachter:	Prof. Dr. Frank Riedel (Freie Universität Berlin)
Zweiter Gutachter:	PD Dr. Christoph Korte (Freie Universität Berlin)
Dritter Gutachter:	Prof. Dr. Harald Strauß (Westfälische Wilhelms-Universität Münster)
mündlichen Prüfung:	27 Januar 2015

Hiermit versichere ich, dass ich die vorliegende Arbeit selbstständig verfasst und keine anderen als die angegebenen Hilfsmittel benutzt habe. Die Stellen der Arbeit, die anderen Werken wörtlich oder inhaltlich entnommen sind, wurden durch entsprechende Angaben der Quellen kenntlich gemacht.

Diese Arbeit hat in gleicher oder ähnlicher Form noch keiner Prüfungsbehörde vorgelegen.

Martin Amandus Nicola Schobben, Berlin, den 26 September 2014

Abstract

This thesis presents quantitative evidence for climatic and environmental changes, which characterize the transition from the Palaeozoic into the Mesozoic. The study concentrates on better resolving the causes and causal relationships, which are responsible for the end-Permian mass extinction, the largest mass extinction of the Phanerozoic. This is achieved by investigating the geochemical signatures locked in the sedimentary rocks and their fossil content of sections in northwestern Iran.

The geochemistry of sedimentary rocks as well as fossil organisms and their shells is known to archive information about the physical and chemical parameters of the ambient environment in which the studied minerals were precipitated. Excursions in geochemical records visualized by isotopic analysis of conodont apatite, carbonate-associated sulphate and bulk-sedimentary rock, straddling the Permian-Triassic interval, are indicative of profound climatic and environmental changes.

The oxygen isotope record from conodonts strongly supports an abrupt warming event paralleling the end-Permian mass extinction. This climate change is associated with synergistic effects acting on global warming and corroborates with a scenario of a more active hydrological cycle and subsequent increase of weathering fluxes from the continent, possibly documented as a contemporaneous lithological change in the studied sections to more clay-rich deposits.

Simultaneous sulphur and oxygen isotope fluctuations measured in sulphate, which is structurally substituted in carbonate, provides an insight into the sulphur biogeochemical cycle within the extinction interval. A change towards increased organic matter production and consequential remineralization by sulphate-reducing bacteria is a scenario that can explain the patterns observed in the isotope proxies from sulphate associated with carbonate. This is likely linked to eutrophication of marine shelf settings by large fluxes of terrestrial material entering the ocean, a potential effect of climatic warming.

These observations underline the interactions between Earth surface processes and imply proximal causes, such as thermal stress and widespread marine anoxia as well as euxinia, as drivers behind the mass extinction. The findings presented in this study cannot unequivocally be assigned to an ultimate cause for the environmental and biotic catastrophe in the latest Permian. However, large-scale volcanism related to time-equivalent emplacement of Siberian trap basalts is a likely culprit that could have initiated this CO_2 induced climate catastrophe.

A volcanic injection of isotopically depleted carbon into the ocean/atmosphere could explain the long-term negative carbon isotope excursion of the studied marine bulk-carbonate rock. This carbon isotope pattern is similar to that observed at other localities worldwide. However, the observation of second-order variability among bulk-rock $\delta^{13}C$ curves at different localities and spatial heterogeneity in diagenetic processes urges a critical view of the fidelity of these records. This observation raises questions about the time-resolution at which palaeodata can be reliably read from carbon isotope records based on measurements from marine bulk-carbonate rock. This later example demonstrates that all the physical and chemical processes that acted upon these ancient rocks, before and after deposition, must be considered when interpreting their geochemical signals. It is shown that obtaining a reliable palaeodata record requires sufficient screening of the geochemical dataset for effects of post-depositional alteration. A good approach used on the studied material was a comparison of different chemical species as well as different mineralogical phases, such as conodont apatite and calcite brachiopod shells. In addition, it is shown that palaeoenvironmental interpretations are strengthened by comparison with results from numerical models.

Kurzfassung

Die vorliegende Arbeit befasst sich mit paläoklimatischen und paläoökologischen Veränderungen am Paläozoikum–Mesozoikum-Übergang. Die Studie konzentriert sich auf Ursachen und Wechselwirkungen, die für das größte Massenaussterben des Phanerozoikums am Ende des Perms verantwortlich gewesen sein könnten. Dafür wurden Isotopenanalysen an Sedimentgesteinen und Fossilien von nordwest-iranischen Sektionen durchgeführt. Die geochemischen Signaturen stellen, bei guter Erhaltung des Probenmaterials, ein Archiv für die physikalischen und chemischen Eigenschaften des Paläomerwassers zur Zeit der Ausfällung dar. Die Charakteristik der Schwankungen im Isotopensignal zeigt, dass tiefgreifende klimatische und ökologische Veränderungen an der Perm/Trias-Grenze existierten.

Die Sauerstoffisotopen von Conodonten-Apatit zeigen eine abrupte Erwärmung unmittelbar während des Massenaussterbens. Dieser deutliche globale Klimawandel erzeugte Synergieeffekte, die in einem verstärkten Wasserkreislauf und eine dadurch verursachte erhöhte kontinentale Verwitterung resultierten. Der daraus folgende erhöhte Eintrag von Siliziklastika ins Meerwasser verursachte wahrscheinlich den vorübergehenden lithologischen Wechsel zu tonreicheren Sedimenten in den untersuchten Karbonatabfolgen.

Schwankungen im Schwefel- und Sauerstoffisotopensignal im karbonatsubstituiertem Sulfat beweisen am und nach dem Aussterbeereignis eine erhöhte Produktion von organischem Material im Meerwasser. Die daraus resultierende Remineralisierung durch sulfatreduzierende Bakterien war wahrscheinlich gekoppelt mit einer Eutrophierung des Meeresbodens ausgelöst durch den verstärkten fluviatilen Eintrag von nährstoffreichem, terrestrischen Material. Dieses Szenario wurde wahrscheinich durch die Klimaerwärmung verursacht.

Die Ergebnisse und Interpretationen der vorliegenden Studie unterstreichen, wie das Zusammenspiel von Erdoberflächenprozessen mit globaler Erwärmung und daraus resultierender weit verbreiteter mariner Anoxia/Euxinia das P/Tr-Massenaussterben verursacht haben könnte. Die neu generierten Daten können noch nicht eindeutig die ultimative Ursache für die biotische Krise erklären. Es kann jedoch eine kausale Verbindung zwischen der zeitgleichen und umfangreichen CO_2-Injektion aus dem sibirischen Trap-Vulkanismus und der der Erderwärmung erkannt werden. Die vulkanisch induzierte Injektion von isotopisch leichtem Kohlenstoff in das Atmosphäre/Ozean System kann die langfristige negative Kohlenstoffisotopenexkursion von Karbonatsedimenten erklären. Ähnliche Kohlenstoffisotopenmuster wurden an verschiedenen Sektionen unterschiedlicher Regionen für dasselbe Zeitintervall nachgewiesen. Fluktuationen höherer Ordnungen erfordern jedoch eine kritische Bewertung dieser Muster hinsichtlich diagenetischer Alteration. Hieraus resultieren Fragen nach der zeitlichen Auflösung, für welche Paläo-Daten verlässlich aus Isotopendaten interpretiert werden können, die aus Messungen an marinem Karbonatgestein gewonnen wurden. Dieses Beispiel zeigt deutlich, dass bei der Interpretation geochemischer Signale sämtliche physikalischen und chemischen Prozesse berüksichtigt werden müssen, die auf das Gestein gewirkt haben. Einen verlässlichen Ansatz bietet dabei ein Vergleich der chemischen Proxies von unterschiedlichen, organisch produzierten Mineralen, wie Conodontenapatit und Brachiopodenschalencalcit. Darüberhinaus werden die Paläoumweltinterpretationen durch Ergebnisse numerischer Modelle unterstützt.

Preface and author's contributions

This thesis consist of an introductory part, which includes a background of the end-Permian mass extinction, some aspects about methodology, geology of the research area and a section that recapitulates the most important findings from the papers and relates them to the original working hypothesis. These sections are the sole responsibility of the author. Moreover the thesis contains two scientific papers, which have already been published as well as 2 papers, which are about to be submitted. From three out of the four papers, the PhD candidate (M.S.) is the first-author. In the 4th paper M.S is a co-author.

The papers are tackling the following themes:

Paper 1 Ghaderi, A. Leda, L., Schobben, M., Korn, D., Ashouri, A.R. (2014) High-resolution stratigraphy of the Changhsingian (Late Permian) successions of NW Iran and the Transcaucasus based on lithological features, conodonts and ammonoids Ghaderi, Fossil Record, 17, pp: 41-57. *This paper was conceived and written by Abbas Ghaderi and contributions from the other co-authors. The author (M.S.) contributed to the lithostratigaphic correlation of the studied sections.*

Paper 2 Schobben, M., Joachimski, M.M., Korn, D., Leda, L., Korte, C. (2014) Palaeotethys seawater temperature rise and an intensified hydrological cycle following the end-Permian mass extinction, Gondwana Research 26, pp: 675–683 *The first-author (M.S.) designed the paper and has taken the lead for the discussion and contributed the most of the analytical data with contributions from Michael M. Joachimski and Christoph Korte.*

Paper 3 Schobben, M., Ullmann, C.V., Leda, L., Korn, D., Struck, U., Reimold, W.U., Algeo, T.J, Korte, C. (manuscript) Uncovering palaeoenvironmental information from bulk-carbonate δ^{13}C of Permian-Triassic 'Boundary Clay' sections *This paper was designed and written by the first-author (M.S.) with contributions from the co-authors. The first-author performed research and analysed data with contributions from Clemens V. Ullmann, Lucyna Leda and Ulrich Struck.*

Paper 4 Schobben, M., Stebbins, A., Ghaderi, A., Strauss, H., Korn, D., Hannigan, R., Korte, C. (manuscript) A flourishing ocean caused the marine Late Permian mass extinction. *This paper was designed and written by the first-author (M.S.) with contributions from the co-authors. The first-author performed research and analysed data with contributions from Harald Strauss and Alan Stebbins. Abbas Ghaderi provided a biostratigraphic framework for the basal Triassic of the studied sites.*

Acknowledgements

I would like to express my appreciation and thanks to my supervisors Christoph Korte and Dieter Korn for their support an advice. Their effort and guidance helped me grow as a scientist. Much appreciation and thanks goes out to the academic staff and students from the Museum für Naturkunde (MfN), in particular the support for this project by Uwe Reimold, Ulrich Struck and Hedi Oberhänsli as well as my close colleagues Lucyna Leda and Abbas Ghaderi who helped me in many phases of my research. The project relied much on geochemical measurements in external laboratories at the universities of Copenhagen, Münster and Erlangen-Nürnberg. Clemens V. Ullmann, Harald Strauss and Michael M. Joachimksi are acknowledged for the essential analytical work as well as guidance in analysing the data and constructing the respective manuscripts. In addition, I would like to thank my co-authors Alan Stebbins, Robyn Hannigan and Thomas J. Algeo for there contributions to the respective manuscripts and Sony A. Walton and Brandon Kilbourne for English spelling and grammar checks of the manuscripts as well as the thesis.

Another important aspect in making this geochemically oriented project successful is the technical support at the MfN by Kathrin Krahn, Robert Schreiber, Ralf-Thomas Schmidt, Jörg Fritz, Melanie Rühl, Kirsten Born, Carina Klein, Sebastian Sladeczek and Jonas Jahn. I thank them for helping with performing analytical measurements as well as sample processing and preparation.

Many thanks are due to Vachik Hairapetian and many more for their assistance in the field. Their effort is an important aspect in the success of this study and it would have been impossible without hem. The Aras Free Zone office and Adel Najafzadeh is thanked for permission to sample the locations in the Julfa region. I acknowledge the funding agency for enabling this project, the Deutsche Forschungsgemeinschaft (project KO2011/8-1 and KO1829/12-2).

Last but not least. Many thanks go out to my family and friends. Especially my mother and father for their tremendous support and guidance. There never-ending support kept me going even through the hard times. My brother is, in addition, thanked for helping me with the graphical design of the thesis. Finally, I want to show my gratitude to my beloved girl-friend, Melanie. She was not only a mental support during the course of my PhD but helped me at many stages of writing this thesis, including; assistance with statistical analyses, introduced me to the software R and Latex, reviewed text and helped improve layout and design of my thesis.

Contents

1 Introduction

1.1 Background

The end-Permian mass extinction (EPME) is unique when compared with any other biodiversity crisis of the Phanerozoic in terms of severity and impact on animal life. The mass extinction erased many lineages of marine organisms typical for the Palaeozoic era, which in the aftermath were replaced by a fauna composed of taxonomic groups that would dominate the oceans from the Mesozoic onward (Sepkoski Jr., 1984; Erwin, 1994). On land the extinction event was marked by a loss of many vertebrate species and major vegetation changes (Ward et al., 2005; Looy et al., 1999).

The causes of this catastrophe had an immediate and abrupt effect on life (Jin et al., 1994) and is confined to an interval of ∼61kyr based on radiometric dates (Burgess et al., 2014). However, their effects reached possibly into the Triassic, as a full recovery of biodiversity only commenced after 5 Myr (Erwin, 2001). In contrast to a generally depaupered Early Triassic fauna, some taxa, e.g., ammonites and bivalves, were strongly affected but diversified relatively soon after the catastrophe (Hautmann et al., 2011; Brayard et al., 2009). Trophic structures and ecosystem functioning in the marine realm were affected with a dominance of only a few genera (Chen and Benton, 2012). The extent of ecosystem impairment, however, varied among regions and biomes with, for instance, metazoan reefs in tropical latitudes being unequally hard hit (Foster and Twitchett, 2014).

The search for the trigger and kill mechanisms related to the EPME has been ongoing since its recognition (e.g., Schindewolf, 1954). This led to many proposed killing agents and identification of possible synergistic effects, with at its centre massive magma outpouring linked to the synchronous emplacement of the Siberian Trap basalts (Renne and Basu, 1991; Campbell et al., 1992; Erwin, 1993). Some examples of scenarios brought forward link massive volcanism to the mass extinction are, e.g., release of toxic gasses (Black et al., 2012), short-term global cooling caused by aerosols (Campbell et al., 1992) and CO_2 induced global warming (Erwin, 1994; Sobolev et al., 2011).

Evidence for extraterrestrial perpetrators, such as those generally accepted for the K-Pg boundary mass extinction, are existing for the EPME as well (Becker, 2001; Kaiho et al., 2001). Supporting evidence for a time-equivalent bolide impact, however, are not convincing: (1) supposed shocked quartz minerals found at sites in Australia appear to be falsely identified (Renne et al., 2004). (2) No unequivocal impact structure has been found that matches temporally with the end-Permian biotic crisis (Renne et al., 2004). (3) Globally recorded geochemical features allegedly diagnostic for an impact, platinum group elements and a sulphur isotope excursion, can as well be related to Earth-bound causes, such as volcanism an marine anoxia (Koeberl et al., 2002, 2004).

Other workers, have looked for causes of the EPME in oceanic changes, such as sealevel changes (e.g., Holser and Magaritz, 1987), but such a long-term process is hard to reconcile with the presumed rapid mass extinction (Jin et al., 1994; Shen et al., 2012; Burgess et al., 2014). Many arguments exist for widespread anoxia within deep and shallow marine settings, the latter possibly in conjunction with a marine transgression (Wignall and Hallam, 1992; Wignall and Twitchett, 1996; Isozaki, 1997). Lowered marine O_2 levels would lead to asphyxia, possibly exaggerated by higher O_2 demands of organisms under warmer temperatures (Wignall and Twitchett, 1996). Hypotheses that included the different proposed mechanisms, such as marine anoxia and volcanism, in a tangled web of interacting causes and effects are favoured (Erwin, 1994; Wignall and Twitchett, 1996; Wignall, 2007; Kidder and Worsley, 2004).

Recent advances in quantitative palaeontological and geochemical research, as well as modelling exercises, strengthened especially the notion of climate change in a close association with an atmospheric carbon injection by, volcanism, as first postulated by Erwin (1994). This is supported by better age constrains on the deposition of the Siberian trap basalts (Reichow et al., 2009), knowledge of basalt interaction with country rock, such as evaporite and organic rich shale (Svensen et al., 2009) and coal beds (Retallack and Krull, 2006; Retallack and Jahren, 2008), and proxy records suggestive of climate warming (Joachimski et al., 2012; Sun et al., 2012) all in close temporal association with the EPME.

Such a CO_2 induced catastrophe by a volcanic injection of isotopically depleted carbon could account for a contemporaneous negative carbon isotope excursion recorded in marine carbonate rock and terrestrial organic matter (Korte et al., 2010; Schneebeli-Hermann et al., 2013). However, other mechanisms could account as well for at least a part of the carbon isotopic excursions, such as sudden oceanic overturn of ^{13}C depleted water, an influx of terrestrial organic matter or dissociation of methane clathrates (Kajiwara et al., 1994; Berner, 2002). Clues suggestive for enhanced ocean uptake of CO_2 can be found in the fossil record as thick-shelled marine organisms (e.g., brachiopods as well as rugose and tabulate corals) experienced selective extinction when compared with other marine organisms (e.g., conodonts) (Knoll et al., 2007). Together with climate driven enhanced vertical water column stratification and subsequent seawater deoxygenation, these synergistic effects of global warming are referred to as the 'deadly trio' (Bijma et al., 2013).

Recently, the role of organisms interacting with their physical and chemical environment has been put forward as a means to work out Earth system feedback mechanisms. Increased planktonic organic matter production and subsequent O_2 consumption by carbon re-mineralization is seen as the main agent responsible for marine anoxia (Algeo et al., 2013). This would have been a consequence of increased weathering fluxes into ocean shelf settings, thereby fertilizing these marine environments (Algeo and Twitchett, 2010; Sephton et al., 2005). Even novel evolutionary events, such as a rapid expansion of a clade of methanogens[1] and consequential massive methane release, have now been related to a major disruption of the carbon biogeochemical cycle (Rothman et al., 2014).

The former summary explains that the time interval of the EPME is still a rapidly evolving area of scientific research, with many new ideas and insight generated in a great pass. In addition, it also shows that fundamental questions remain about cause and causal relationships among the mass extinction, the large perturbations in the biogeochemical cycles and climate change.

1.2 Working hypothesis

This study considers the possible role of climate change caused by atmospheric greenhouse gasses upon the EPME (Joachimski et al., 2012; Kidder and Worsley, 2004). In addition, the close temporal link between this biotic crisis and magmatic outpouring as the Siberian Trap basalt has been attested (Reichow et al., 2009). Siberian Trap volcanism is related to increased input of CO_2 to the atmosphere by direct magma-outgassing (Sobolev et al., 2011) and indirect processes, such as interaction of magmas with the surrounding sedimentary deposits (Svensen et al., 2009). I, therefore, hypothesize that the EPME is caused by greenhouse induced climate change, which is an effect of contemporaneous massive volcanism.

This hypothesis, however, raises a number of research questions. I will discuss whether climate warming is associated with the mass extinction from an oceanic perspective. To evaluate this hypothesis it is also necessary to ascertain if time-equivalent atmospheric greenhouse levels changed, or if a volcanic injection of CO_2 occurred. Thermal stress by high ambient seawater can induce physiological changes within an organism, e.g., protein denaturation and a reduced capacity of oxygen uptake by tissues (Bijma et al., 2013). Besides this lethal effect of raised temperatures on the organism, it is likely that a CO_2 climate catastrophe would be accompanied by synergistic effects such as ocean acidification and marine anoxia. These climate change side-effects may be equally important for the EPME and are considered in this working hypothesis as well.

---

[1] A clade of microbes that produce methane as a by-product of their metabolism

In order to answer these questions, I draw conclusions about the environment and climate of this turbulent time interval, based upon newly collected palaeodata. This palaeodata consist of geochemical signatures of fossils and bulk carbonate rock, collected in outcrops of Late Permian to Early Triassic marine successions located in the Julfa region (NW Iran).

In a first step, I generated stratigraphic profiles of the marine sedimentary successions. Emphasis was placed on the construction of a litho- and biostratigraphic framework for the studied localities. This allows for a regional and possibly even global correlation with other P-Tr boundary sections. This is advantageous, as it enables a comparison of the geochemical data among different parts of the region and potentially the rest of the world. Such a global correlation is especially important as it provides a relative chronology for (1) the observed biotic crisis and (2) the changes in environment and climate. Comparison of evidence for biotic, climatic and environmental changes in a stratigraphic framework can also show whether these observations are globally synchronous.

In a second step, I assessed the reliability of applying this geochemical data as a tool to reconstruct the climate and environment of the study interval. This is important as the fossils and carbonate rocks are mainly the product of biological process. Species-specific metabolic effects, as well as habitat preferences, all assert a control on the chemical composition of the biominerals that make up these samples. These biological and ecological signals may obscure the investigated environmental signal. Highly relevant is also the potential chemical and structural alteration of the studied fossil and sedimentary rock by post-depositional processes during lithification and subsequent burial.

In a third step, as the ultimate purpose of this study, I aimed to shed some light on the possible cause and causal relationships among CO_2 induced climate change on the end-Permian biodiversity crisis. I compared proxy records designed to investigate different aspects of the Earth system whereby I also took into consideration that many of the Earth surface processes may act in concert as positive feedback loops or synergistic effects.

1.3 Relevance of the study

Anthropogenic carbon release has an eminent effect on Earth's climate and its inhabitants. This carbon release inflicted by humans, has measurably risen atmospheric CO_2 since pre-industrial time and can be directly related to increased global surface temperatures as stated in the fifth report of the Inter-governmental Panel on Climate Change (IPCC 2013). However, global warming is not the sole problem of increasing atmospheric CO_2 as absorption by oceans of this anthropogenic carbon leads to ocean acidification (Caldeira and Wickett, 2003). This uptake is a phenomenon that has been measured as a lowering of surface waters pH in today's oceans (Doney et al., 2009). Other directly observable effects related to CO_2 induced global warming are the expansion of anoxic "dead" zones (Diaz and Rosenberg, 2008), thinning of sea-ice sheets (Polyakov et al., 2010) and rising sea levels (Cazenave et al., 2008). These CO_2 induced (side)effects will grow under the predicted greenhouse gas emissions within the next decades (Stocker et al., 2013). Even after cessation of carbon emissions these negative consequences will not be reversed due to a large inertia of the climate and ocean system (Caldeira and Wickett, 2003; Doney et al., 2012)

The adverse effect from rising CO_2 on biota has already been observed in the changing marine populations and declining number of sensitive species (Hoegh-Guldberg and Bruno, 2010; Doney et al., 2012; Bijma et al., 2013). The most evident and well-documented effect of climate change upon biota is coral bleaching observed in modern tropical oceans (Hughes et al., 2003). Future projections are suggestive of increased extinction risk in the coming decades to centuries (Harnik et al., 2012; Barnosky et al., 2012). Biodiversity loss in the marine realm would be fuelled by ocean acidification, hypoxia, thermal stress and a long list of potential other effects (Doney et al., 2012; Bijma et al., 2013). Similarly, rising greenhouse gas concentrations and related climate change will also drive changes in terrestrial communities, such as shifting vegetation biomes (Brook et al., 2013).

Proximal causes acting in past extinction scenarios are likely to contribute to future extinctions, such as the leading role of greenhouse conditions in the end-Permian biodiversity crisis (Harnik et al., 2012; Payne and Clapham, 2012). The former notion makes the study of the Permian-Triassic (P-Tr) time interval important in the understanding of current effects of anthropogenic induced climate warming by burning fossil fuel. The event does not allow quantitative inferences upon physical aspects of climate and current climate change, mainly by the lack of resolution, time constrains and fundamentally different continental configuration, and, as such is no perfect future analogue (e.g., Lunt et al., 2013). However, from the perspective of the biotic response to an atmospheric carbon injection, lessons can be drawn form the rock and fossil record encompassing this great mass extinction (also Payne and Clapham, 2012) and gives weight to the working hypothesis (section 1.2).

2 Study area

2.1 Previous studies of Iranian and Azerbaijanian P-Tr sections

Pioneering studies of the outcrops near the towns of Dzhulfa, Azerbaijan and Julfa, Iran, began in the late 19^{th} Century and the beginning of the 20^{th} century, are the first reports of the P-Tr sections in this region. The studies include descriptions of invertebrate fossils, e.g., ammonites, and propose a first lithological subdivisions (Abich, 1878; Frech and Arthaber, 1900; Stoyanow, 1910).

More detailed descriptions of the rock succession and its fossil content led to the assignments of the outcrops near Dorasham in the Araxes gorge, as type locality of the latest Permian Dorashamian Stage (Rostovtsev and Azaryan, 1973). This follows the Dzhulfian Stage, named after its respective type locality in the Dzhulfa region (Schenck et al., 1941). Both stages, however, were later abandoned for the respective Wuchiapingian and Changhsingian stages, defined in their type localities in China (Furnish, 1973)

The first detailed description of the succession of conodont zones of P-Tr sections in the Julfa region, among which the Dorasham sections played an important role (Kozur et al., 1980), which led to the proposal of this section to be the stratotype section for the P-Tr boundary (Kotlyar et al., 1983). However, the GSSP[2] was eventually assigned to the Meishan section in South China (Yin et al., 2001). Zakharov (1992) placed the P-Tr boundary of the section within a first limestone bed containing bivalves of the genus *Claraia* occurring 2 m above the latest Permian argillites. The interval he proposed resemblances the P-Tr transition facies observed at the studied sites with the occurrence of the diagnostic marker for the base of the Triassic system, the conodont species *Hindeodus parvus* (Kozur, 2007).

There discussed sections, Kuh-e-Ali Bashi and Zal, both discovered more recently Stepanov et al. (1969) show a close resemblance with the Dorasham section. However, possibly erroneous documentations of Teichert et al. (1973), both in the lithological descriptions of the members as well as in the conodont descriptions mainly at the Kuh-e-Ali Bashi section 4, fuelled an intense debate about their cross-correlation (Sweet and Mei, 1999; Kozur, 2004; Henderson et al., 2008). Based on our high resolution sampling of these localities we proposed, based on lithostratigraphic observations and conodont biozones, a new correlation, which might be useful to solve open problems.

In the last decade the biostratigraphy of these sections was described in great detail (Kozur, 2004, 2005, 2007; Richoz et al., 2010; Shen and Mei, 2010). In addition, several geochemical studies have been performed on samples from these localities (Baud et al., 1989; Korte et al.,

---

[2] The abbreviation GSSP stand for Global Stratotype Section and Point and defines the lower boundary of a stage on the geological timescale. In its physical form it is a reference point in a section which has been chosen by an international committee

2004a; Korte and Kozur, 2005; Kakuwa and Matsumoto, 2006; Horacek et al., 2007; Richoz et al., 2010)

2.2 General lithostratigraphy

The descriptions of Stepanov et al. (1969) divided the lithology of the studied P-Tr sections located in NW Iran, in 8 units (A to H). Of interest for this study were, in stratigraphic order, units C and D, also known as the Julfa Beds (after Ruzhencev et al., 1965) of probable Wuchiapingian age, consisting of limestone, marls and shales rich in fossils, such as brachiopods and ammonites. Unit E, a dominantly shaly unit with some intercalations of marl and limestone, belonging to Ali Bashi formation. Unit F, is a conspicuous cliff forming red nodular limestone unit, also known as the *Paratirolites* Limestone, after the ammonite genus *Paratirolites.* Both unit E and F belong to the Changhsingian. Unit G, is part of the Elikah formation Stepanov et al. (1969) consisting of thin bedded limestones and some thin shale beds. A further subdivision considers the lower part of the latter unit, separate, as the 'Boundary Clay' (e.g., Kozur, 2004; Korte and Kozur, 2005). Based on conodont biostratigraphy this unit still belongs to the Changhsingian, whereas the transition to the more dominant carbonate unit, referred to as the *Claraia* Beds, after the dominant fauna of bivalves belonging to *Claraia*, contains at the base the first occurrence of the Triassic marker, *H. parvus* (Kozur et al., 1980; Kozur, 2004, 2007).

2.3 Geological setting

The Iranian block consists of several crustal remains belonging to the Cimmerian microcontinents (Sengör, 1979; Besse et al., 1998). They detached from the eastern margin of Gondwana during the Early Permian after opening of the Neotethys ocean, (Sengör, 1979; Muttoni et al., 2009a). During the Permian until the Late Triassic the Cimmerian terranes drifted northwards, and amalgamation of the Iranian block started when they reached the southern margin of the Eurasian continent (Besse et al., 1998; Stampfli and Borel, 2002; Torsvik and Cocks, 2004; Muttoni et al., 2009a). At the P-Tr boundary, the Iranian plates were, based on palaeomagnetic data probably located close to or at an equatorial latitude (Besse et al., 1998; Muttoni et al., 2009b). This reconstruction is similar to the simulated position by the plate tectonic model of Stampfli and Borel (2002), as depicted in Figure 1.

2.4 Palaeogeographical setting

Geographic distributions of oceans and land is not only important for macro-evolutionary processes (e.g., Murienne et al., 2014), but it is also relevant for palaeoceanographic dynamics and distribution of climatic belts. The palaeogeographical reconstruction shown in Figure 1, displays the size of oceanic basins and position of continents at Permo-Triassic boundary. Such maps may help to infer on marine or terrestrial sedimentation conditions and general oceanic circulation patterns in time and space. It has for instance been postulated that the Pangaea supercontinent formed at this time an almost closed meridional barrier preventing the formation of a circumpolar circulation which established only some 220 Ma later in the Palaeogene ocean (Winguth et al., 2002). A restricted circulation has also been suggested for the Tethyian Ocean and thereby could have hampered exchange with the large superocean, the Panthalassa. As a result the former should have acted as a nutrient trap (Meyer et al., 2008; Meyer and Kump, 2008).

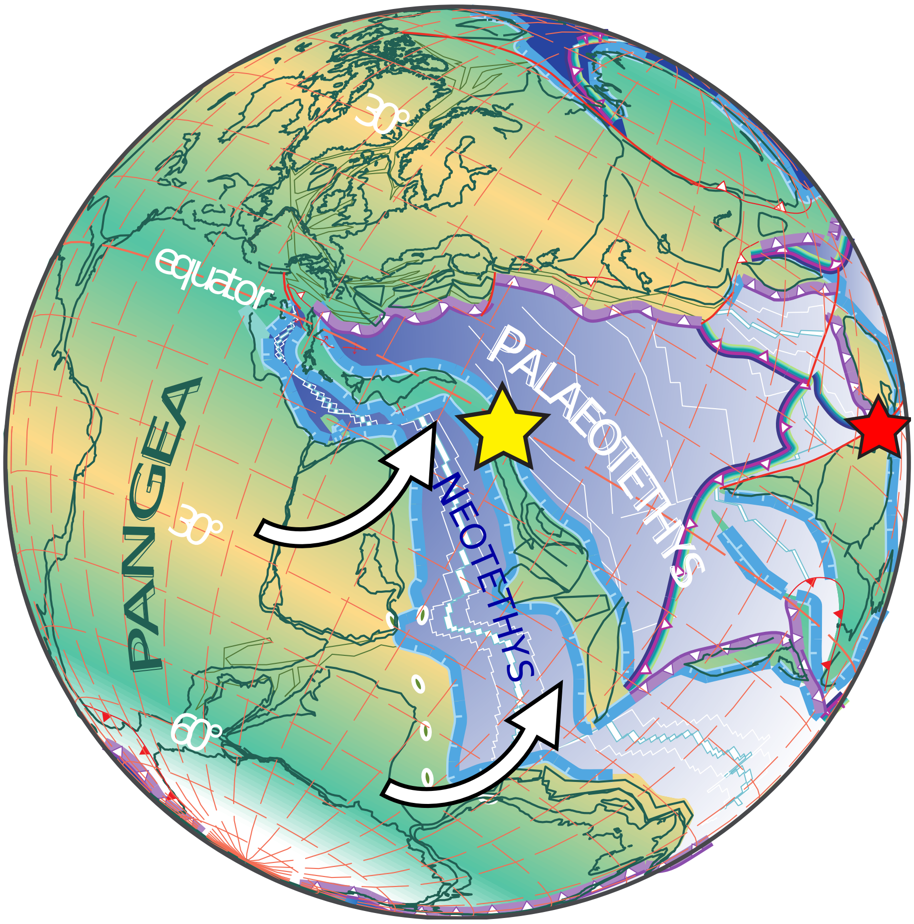

Figure 1 Palaeogeography during the P-Tr boundary interval adapted from Stampfli and Borel (2002, and Stampfli pers. com.). Drawn is the palaeoposition of the studied sections (yellow star), the Meishan P-Tr GSSP section (red star) and the general movement path which the Cimmerian microcontinents followed through the Permian (white arrows), thereby creating the Neotethys ocean.

3 General methodology and materials

3.1 Localities

In the attempt to gain more knowledge on the causes and causal relationships between environmental and climate change, perturbations of the major biogeochemical cycles and the EPME, the fossiliferous marine carbonate successions located in NW Iran are investigated. During several field expeditions, we studied six profiles of Late Permian to Early Triassic marine rock.

(1)Aras Valley (39.015°N, 45.434°E): This section has been described previously by Leda et al. (2014); it is located about 19 km WNW of the towns of Dzhulfa (Azerbaijan) and Julfa (Iran). The outcrop is exposed on the south side of a small hill immediately west of the Aras (Araxes) River, which coincides with the political boundary between Iran and the province of Nakhichevan; Azerbaijan. The Aras Valley section is approximately 2 km north- west of the classical Dorasham II section described by Ruzhencev et al. (1965).

(2–5) Kuh-e-Ali Bashi (9 km west of Julfa): P-Tr boundary beds crop out in parallel sections over a range of about 1.5 km. Four of the numerous parallel sections were sampled: Kuh-e-Ali Bashi 1 section (38.940°N, 45.520°E) and Kuh-e-Ali Bashi 4 section (38.942°N, 45.516°E) of Teichert et al. (1973) as well as the Kuh-e-Ali Bashi N section (38.941°N, 45.516°E) of Leda et al. (2014) and Kuh-e-Ali Bashi M section (38.935°N, 45.524 °E) sensu section I, from I-IV, of Kozur (2005).

(6) Zal, located about 22 km SSW of Julfa and approximately 2.2 km NNW of the village of Zal (38.733°N, 45.580°E). This section is considered as one of the best outcrops of P-Tr transitional beds and is characterised by an extended Early Triassic succession (e.g., Horacek et al., 2007; Richoz et al., 2010).

Figure 2 Geographic setting of the P-Tr sections in the Julfa region (NW Iran). The white dots represent the locations of the sections studied and exception to this is the Dorasham 2 section on Azerbaijan territory.

Careful documentation and high-resolution sampling of these sites provided an overview of the changing lithologies and its respective fossil content and resulted in a high-resolution sample sets. In the field the top of *Paratirolites* Limestone unit, equivalent to the 'extinction horizon' (Kozur, 2007) was easily recognizable and served as a reference bed. All sample labels record the relative distance to this horizon in m distance.

3.2 Sample preparation

In the lab, a 1-2 kg portion of the sampled rock was reserved to extract the microfossil content. The remainder of the sample was trimmed for obvious diagenetic phases and subsequently ground with a mechanic agate mill (Retsch RS 100) at the MfN, Berlin (Germany). To acquire a homogeneous grain size, the ground samples were sieved with a 160 μm mesh.

3.3 Conodont extraction

One kilogram of bulk limestone or marl sample were dissolved in 8% formic acid to obtain the conodont elements at MfN, Berlin (Germany). Clay rich samples were additionally treated with hydrogen peroxide. The samples were subsequently dried at room temperature. These last two steps were repeated until the sample disintegrated sufficiently to obtain conodont specimens. The resulting residue, were then processed through an magnetic separator (Frants lb-1). This procedure increased the concentration of conodont elements in the sample by separating out the predominant ferromagnetic clay particles. The extraction of conodonts was performed with the help of Dieter Korn and Carina Klein.

3.4 Conodont micro-structure and mineralogy

I analysed a part of the conodont material for there micro-structure using the JEOL JSM-6610LV Scanning Electron Microscopy (SEM) at the MfN, Berlin (Germany), with assistance from Kirsten Born. The conodont samples were prepared by mounting them on a SEM stub. This stub was subsequently placed into sample holder of the SEM upon which the whole sample chamber is evacuated with a pump. When the required pressure was reached, an electron beam of 60 nA is emitted from a tungsten filament operating under a 15 kV acceleration voltage. The SEM can operate under low-vacuum, therefore the SEM stub was not sputter coated and enabled successive Raman sceptroscopy measurements on these conodont specimens. The produced images enable an evaluation of the preservation state of the conodont elements. For instance, microreticulation is thought to represent the original surface structure (Fig. 4 A-F) whereas, rough surface structures could be indicative of post-depositional recrystallization. In addition, Raman spectroscopy (Dilor Labram), carried out at the MfN (Germany) under supervision of Jörg Fritz, is used to analyse the mineralogy of the conodont elements. Precision is acquired by calibrating the machine with pure silicon, which ensures an external reproducibility of better than 1 cm^{-1}. According to the method of Thomas et al. (2011) the peak position of the $v1$-PO_4 (phosphate symmetric stretching bound) and the FWHM (full width at half maximum) have been measured (Fig. 3), to asses the degree of post-depositional re-crystallization. Internal reproducibility was monitored by replicate analysis of the sample and was better than 0.6 cm^{-1} and 1.1 cm^{-1} for the $v1$-PO_4 and FWHM. Magmatic apatite from the mineralogical collection and a modern fish tooth sample from the ichthyology collection of the MfN, Berlin (Germany) have been used to represent most and least diagenetically altered apatite.

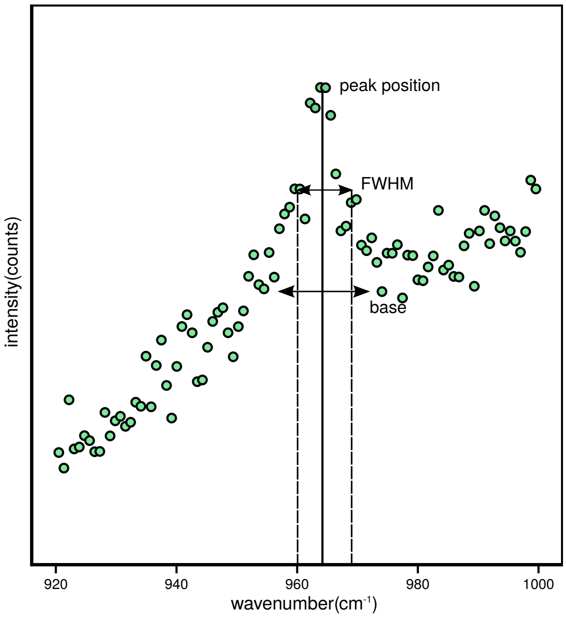

Figure 3 The $v1$-PO_4 (phosphate symmetric stretching bound) of conodont apatite obtained by Raman spectroscopy. Calculation of the FWHM (full width at half maximum) and peak position of $v1$-PO_4 are performed by the software provided with the machine.

3.5 Conodont oxygen isotopes

I handpicked conodont elements under a binocular microscope and the collected specimens were weighted in a polyethyelene (PE) beaker on a micro-balance, at the MfN, Berlin (Germany). A weight of 1 mg was strived for each sample and elements were divided in platform (or P1) elements of *Hindeodus* sp. and *Clarkina* sp. In post-extinction strata, the strived sample weight

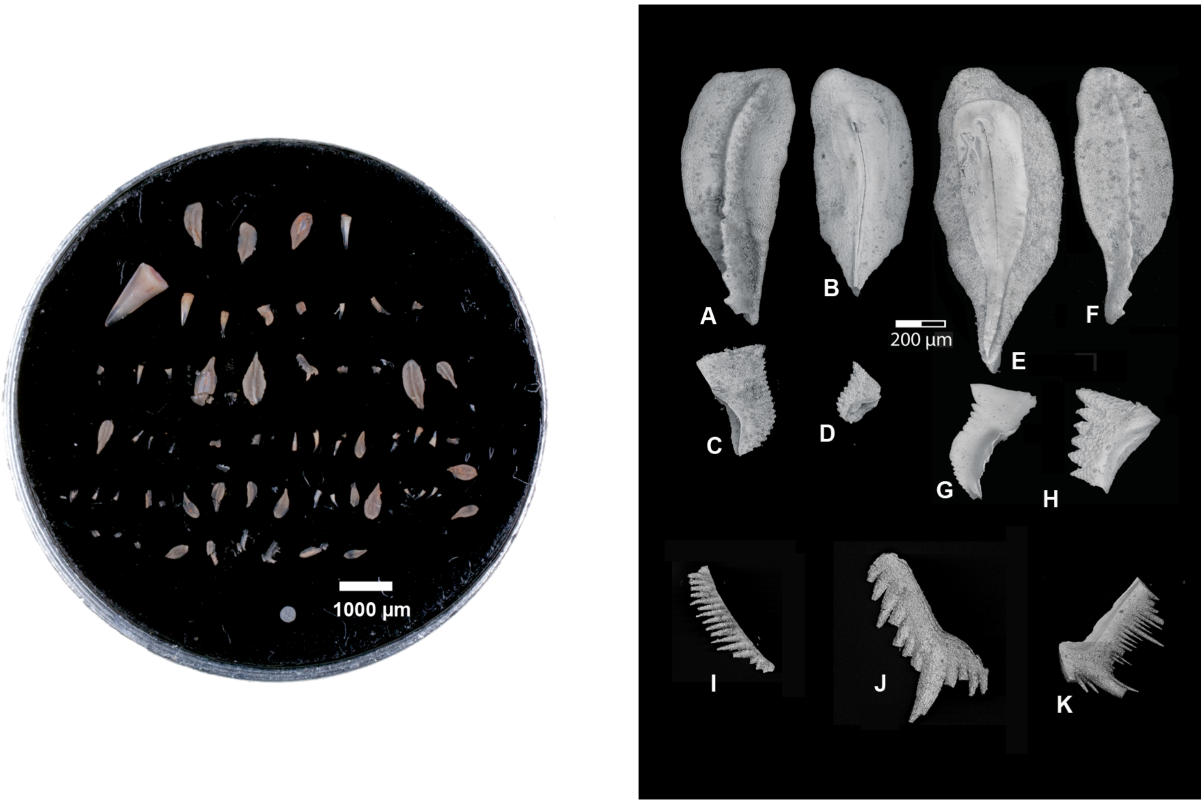

Figure 4 (Left) SEM stub with adhered conodont samples. (Right) SEM images of P1 elements of *Clarkina* sp. (A) Kuh-e-Ali Bashi -0.10 m, (B) Kuh-e-Ali Bashi -0.30 m, (E) Zal -1.25 m, (F) Zal -1.25 m). P1 elements of *Hindeodus* sp. (C) Kuh-e-Ali Bashi -0.56 m, (D) Kuh-e-Ali Bashi -1.05 m, (G) Zal -13.70 m, (H) Zal +14.50 m. ramiform elements (I) Kuh-e-Ali Bashi -0.80 m, (J) Kuh-e-Ali Bashi -1.40 m, (k) Kuh-e-Ali Bashi 0.00 m. Note, that the P1 elements of *Clarkina* sp. are marked by a pitted surface or microreticulation, a sign of good preservation.

was difficult to attain due to low overall conodont element concentrations (Fig. 5) and ramiform conodont elements were added to the sample when needed.

Conodonts consist of the biomineral carbonate–apatite (francolite). Francolite can be chemically visualised by a non-stoichiometric formula approximating $Ca_5Na_{0.14}(CO_3)_{0.16}(PO_4)_{3.01}(H_2O)_{0.85}F_{0.73}$ (Pietzner et al., 1968). A large part of the oxygen (90%) resides in the diagenetically stable phosphate. Following the protocol, outlined in Joachimski et al. (2009), the PO_4 is isolated from conodont francolite. As a first step, I added 33μl 2 M HNO_3 to the collected conodont material contained in the PE beaker. This was left overnight to dissolve the carbonate-apatite of the conodont specimens. Upon which, the resulting solution was neutralized by addition of 33μl 2 M KOH and Ca was removed from the supernatant by adding 33μl 4% HF. Successive centrifugation (Heraeus Megafuse 1.0) helped separate the residue from the liquid, which was subsequently removed with a glass pipette. The solution containing the solubilized PO_4 was then transferred to a clean PE beaker. As a final step, a silver amine-solution was added to the PO_4 containing supernatant. Upon successive heating this resulted in an ionic reaction, producing tri-silver-phosphate crystals (Ag_3PO_4). The produced Ag_3PO_4 crystals were thoroughly rinsed with ultra-pure water and subsequently put in a ultra-sonic bath (Fisher FB15051). This step was repeated until the crystal surfaces were clean, in order to obtain a primary O isotope signal of the PO_4. Approximately 0.2 to 0.3 mg of the precipitated Ag_3PO_4 was weighted of in silver foil cups.

Oxygen isotope measurements of Ag_3PO_4 precipitates was done at the University of Erlangen-Nürnberg (Germany) by Michael M. Joachimski. The Ag_3PO_4 precipitates were converted to CO by a High Temperature Conversion Elemental Analyzer (TC-EA) and mediated by reduction

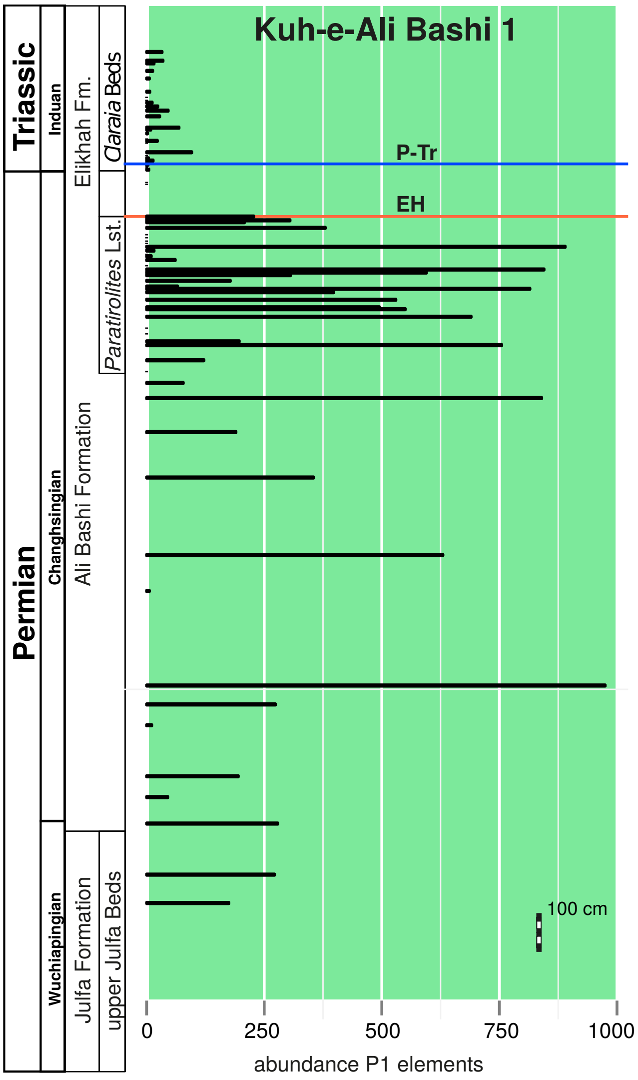

Figure 5 The abundance of P1 elements throughout the Kuh-e-Ali Bashi 1 section. Counts for large quantities (>250) are estimates upon visual inspection.

with graphite. Carbon monoxide was subsequently measured for oxygen isotopic composition using a coupled online to ThermoFinnigan Delta Plus mass spectrometer. Oxygen isotope ratios are reported as ‰ in standard δ notation relative to Vienna Standard Mean Ocean Water (VSMOW). To ensure best accuracy of the measurements, internal reproducibility was monitored by triplicate measurements of samples and standards and was better than 0.18‰. In addition, external reproducibility of internationally distributed standard NBS 120c was ±0.25‰ (2σ). Measurement of this certified standard also documented a good precision, with a measured value of 21.7‰ (cf. Lécuyer et al., 1993).

3.6 Carbonate-associated sulphate (CAS) sulphur and oxygen isotopes

I prepared bulk-rock carbonate samples for isotopic analysis of CAS, at the MfN, Berlin (Germany). In order to do so, 2 l beaker glasses containing up to 0.7 kg pulverized rock samples were leached in a 10% NaCl solution, according to the method described in Wotte et al. (2012a). The resulting sediment slush was constantly stirred for approximately 24 h. This leaching step is designed to eliminate the influence of sulphate phases other then CAS on the final isotope measurements. These soluble sulphate phases are lumped under the name ”leachable non-CAS”. The sediment slush was subsequently filtrated by a fluted filter (Fig. 8) and a cellulose nitrate

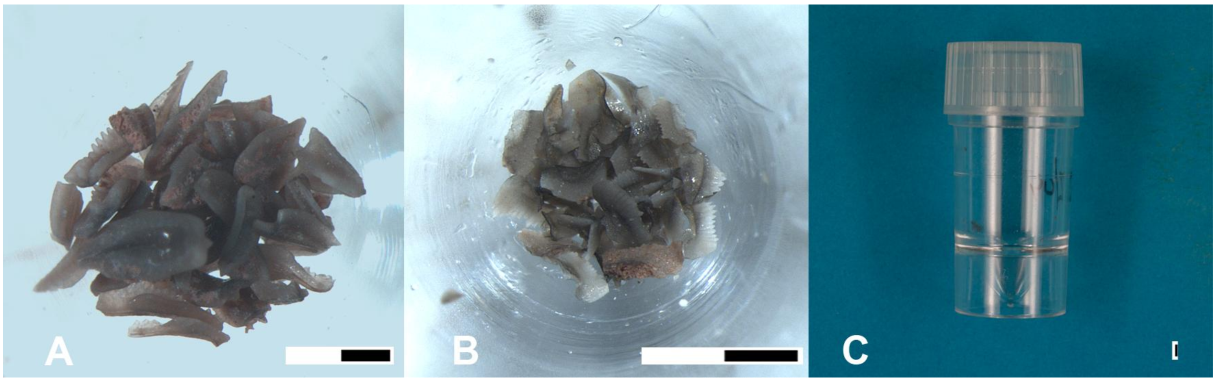

Figure 6 Preparation of selected conodont samples for PO_4 extraction procedure. (A) P1 elements of *Clarkina* sp. within PE beaker. (B) P1 elements of *Hindeodus* sp. within PE beaker. (C) PE beaker. Scale bars are 500 μm.

membrane filter (mesh 0.45 μm; Fig. 9). The latter method involved the use of a vacuum created by an electric pump (Fig. 9). In a next step, 100 ml of a 8.5% BaCl solution was added to the filtered solution to invoke an ionic precipitation of $BaSO_4$. The $BaSO_4$ precipitate was extracted from solution by filtration with a cellulose nitrate membrane filter (mesh 0.45 μm). The concentration of non-CAS were determined relative to the final weight of precipitated $BaSO_4$. The before outlined steps were repeated until close to none non-CAS was detected, some samples required up to four repetitions of this leaching step (Fig. 7).

Upon elimination of non-CAS the sample were acid digested in 25% HCl, which was added slowly by a dropping funnel (Fig. 9). Exchange with the atmosphere was restricted by covering the beaker glas with a plastic foil (Fig. 9). This step is to prevent the potential oxidation of reduced sulphur species, such as pyrite or greigite. Insoluble residue was removed by the same filtering as for the NaCl leaching procedure with the subsequent use of a fluted filter and cellulose nitrate filter. The resulting solution contains the liberated CAS which is precipitated as $BaSO_4$ by addition of a 12% BaCl solution. The weight of CAS was determined gravimetrically, relative to the precipitated $BaSO_4$ in this final step.

Oxygen and sulphur isotope measurements were performed at the University of Münster (Germany) by Harald Strauss. Sulphur isotopic composition of the $BaSO_4$ precipitates was analysed by an Elemental Analyzer connected to ThermoFinnigan Delta Plus mass spectrometer. The sulphur isotope measurements are reported as standard δ notation in ‰ relative to Vienna Cañon Diablo Troilite (VCDT). The repeated measurements of international reference materials for $\delta^{34}S_{CAS}$ (IAEA-S-1, IAEA-S-2, IAEA-S-3, NBS127) and in-house standards (CdS, Ag2S) yielded an accuracy on average better than 0.09‰ and a reproducibility of on average better than 0.40‰ (2σ), also Table 1.

Oxygen isotope composition of the $BaSO_4$ precipitates was determined by a TC/EA interfaced to a ThermoFinnigan Delta Plus XL mass spectrometer. The oxygen isotope composition is denoted in standard δ notation ‰ relative to VSMOW. The accuracy for $\delta^{18}O_{CAS}$ was monitored by repeated measurements on international reference material (IAEA-SO-5, IAEA-SO-6, NBS127) and in-house reference material ($BaSO_4$) and was better than 0.40‰. The reproducibility of the repeated measurements on the standards for $\delta^{18}O_{CAS}$ is ±0.80‰ (2σ), also Table 1. Extraction and isotopic measurements of sulphide minerals, used in paper 4, are performed by Alan Stebbins at the University of Massachusetts at Boston (US).

3.7 Bulk-carbonate carbon and oxygen isotopes

Samples for the carbon and oxygen isotope measurements were taken on fresh surfaces of carbonate bearing rocks using a microdrill at the MfN, Berlin (Germany), with the help of Lucyna Leda. Cracks, veins, and stylolites were avoided. Small portions of the powdered bulk-rock

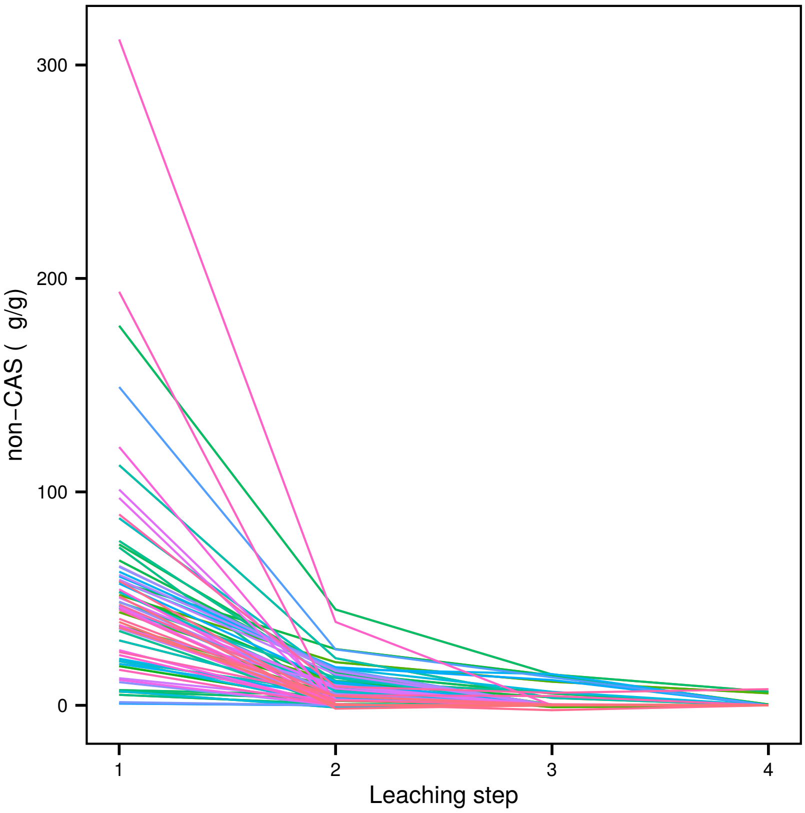

Figure 7 Consecutive leaching steps to remove non-CAS compounds within all sample material. Some samples required up to 4 repetitions of the leaching procedure. The non-CAS is markedly reduced after the first leaching step.

Table 1 Results of S and O isotope measurements on reference material, compared with published values (Brand et al., 2014).

	δ^{34}S (‰)	2σ
IAEA -S-1		
measured	-0.35	0.20
published	-0.30	
IAEA -S-2		
measured	21.52	0.16
published	21.55	
IAEA -S-3		
measured	-31.31	0.44
published	-31.40	
NBS 127		
measured	20.38	0.17
published	20.30	
Ag2S (Lab.)		
measured	2.47	0.39
CdS (Lab.)		
measured	10.76	0.32

	δ^{18}O (‰)	2σ
NBS 127		
measured	8.94	0.85
published	9.30	
IAEA-SO-5		
measured	11.97	0.70
published	12.00	
IAEA-SO-6		
measured	-11.36	0.50
published	-11.34	
$BaSO_4$ (Lab.)		
measured	12.59	1.05

samples (100-400 μg) were placed in 10 ml vials that were sealed with rubber septum lids. After flushing for 6 min with helium and adding H_3PO_4, generated CO_2 was measured for carbon and

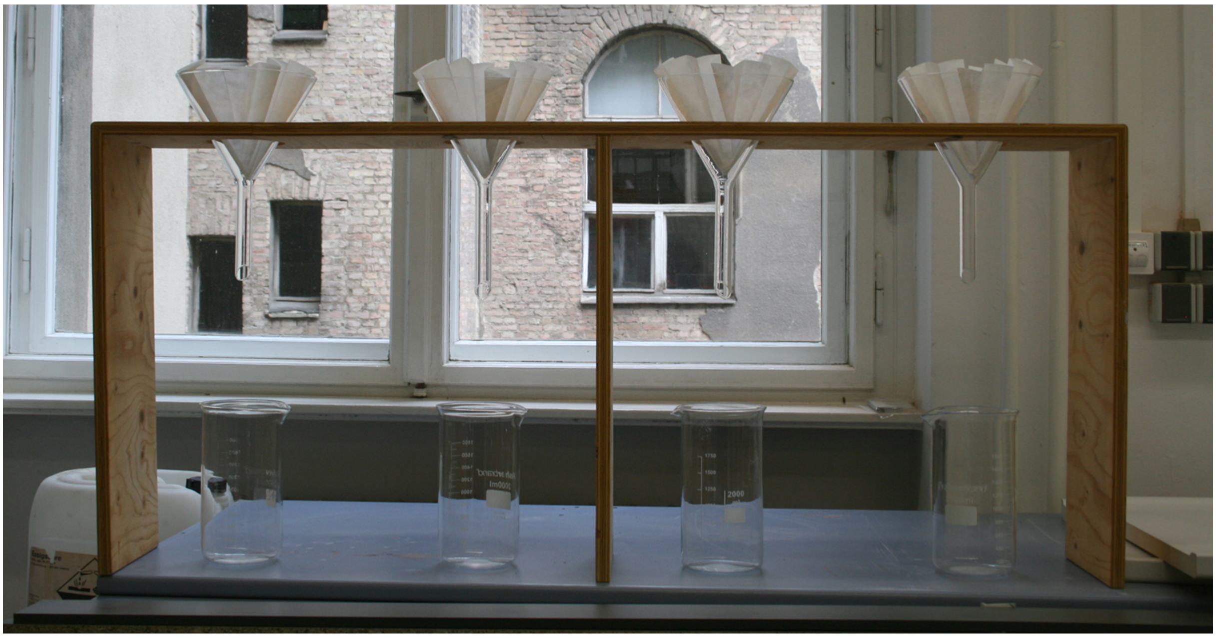

Figure 8 Fluted filters for extracting the coarse sample fraction from the sediment NaCl or HCl slush. The set-up was designed to process four samples at once.

oxygen isotope composition on a Thermo Finnigan GASBENCH II linked online to a Thermo Finnigan DELTA V mass spectrometer at the MfN, Berlin (Germany) by Ulrich Struck. The isotope values were calibrated against Vienna Pee Dee Belemnite (VPDB) and are reported in conventional δ notation. The reproducibility (1σ) of replicated standards (Pfeil STD; Solenhofen Limestone) was better than 0.10‰ for both $\delta^{13}C$ and $\delta^{18}O$. Brachiopod shell preparation for carbon and oxygen isotopes analysis and the isotope measurements used in paper 2, have been performed by Christoph Korte at the University of Copenhagen (Denmark).

3.8 Bulk-carbonate element/Ca ratios

The protocol for the elemental analysis on the calcite fraction of bulk-rock material is inspired on sequential extraction procedures, such as Kryc et al. (2003) and Brand and Veizer (1980) and an adaptation of the procedure outlined in Wotte et al. (2012b). These extraction methods are designed to dissolve the $CaCO_3$ part of sediment or sedimentary rock with a minimal contribution of other mineral phases and elements to the final measured material. This preparation procedure for element analysis was conducted at the MfN, Berlin (Germany). I weighted one gram of powdered rock material in 50 ml Greiner tubes. Twenty ml of 2% acetic acid was added to the sample material for approximately 48 h while constantly being agitated on a shaker (Edmund Bühler ks 15). Subsequently, the suspension was filtered with a cellulose nitrate membrane filter (mesh 0.45 μm). The solution was dried down and both the insoluble and soluble residues were weighted. Gravimetric quantification of the weight loss, due to the acid digestion procedure, enabled an approximate calculation of the $CaCO_3$ fraction dissolved. To prepare the acid-soluble residue for ICP-OES measurement, the aliquots were transferred to 15 ml greiner tubes and dissolved in a 0.2 M nitric acid solution. This last step creates a matrix-matched solution for subsequent Element/Ca measurements.

Element/Ca measurements were performed at the University of Copenhagen (Denmark) with the help of Clemens V. Ullmann. The previous quantification of $CaCO_3$ and thus Ca content of the acid-soluble residue enabled creating a best possible matrix match for the used blank solution and multi-element reference solutions. The reference solutions are used to create a three-point calibration in the subsequent elemental/Ca measurements by Perkin Elmer Optima 7000 DV Inductively Coupled Plasma Optical Emission Spectrometer (ICP-OES). Precision was

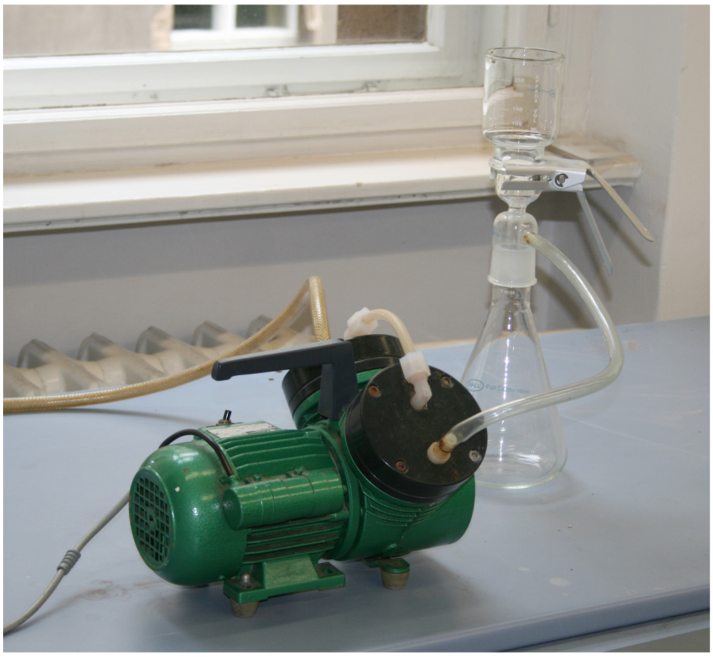


Figure 9 (Left) The filtration device to separate the fine sample-fraction or $BaSO_4$ precipitates from the solution. This is mediated by a vacuum created in the glass filtration flask by an electric pump. (Right) A glass dropping funnel designed to titrate the 25% HCl on the sample to slowly dissolve the carbonate fraction, thereby liberating CAS. The magnetic stirrer ensures that the sediment slush and acid are well mixed during the procedure. The beaker glass is sealed with a plastic foil to restrict exchange with the atmosphere thereby reducing the risk of oxidation of reduced sulphur species.

checked by the international standards JDo-1 and JLs-1. This yielded an accuracy for Sr/Ca, Mn/Ca and Mg/Ca on average better than 5 % upon comparison with published values and a reproducibility of on average better than 10% (2σ) (Imai et al., 1996, Table 2).

Table 2 Replicate element/Ca analysis by ICP-OES on certified reference material and comparison to published values by Imai et al. (1996). Values are given in mmol/mol.

	Sr/Ca	2σ	Mn/Ca	2σ	Mg/Ca	2σ
JDo-1 (n=3)						
measured	0.21	0.04	0.14	0.02	750.11	21.04
published	0.22		0.15		761.21	
JLs-1 (n=23)						
measured	0.34	0.01	0.03	0.00	14.09	0.24
published	0.34		0.03		15.02	

4 Synthesis

4.1 Stratigraphy

In paper 1, a detailed report is given about the litho- and biostratigraphy of the latest Permian in the sections of the Julfa region. In this section, this is extended to include the complete studied stratigraphic range, covering the upper part of the Permian system into the basal Triassic system. Furthermore, some remarks are placed on the possible correlations with other P-Tr sections located in Iran and in South China, in particular, the P-Tr GSSP defined at Meishan, which is an important aspect of papers 2, 3 and 4.

Leda et al. (2014) have shown that it is possible to correlate the P-Tr sections of the Julfa region based on lithology, for the carbonate rock bracketing the boundary. In accordance with Stepanov et al. (1969), lithological correlation is also possible for the rock approximately 20 m below the P-Tr boundary. This rock unit, known as the Julfa Beds (Stepanov et al., 1969) found throughout the Julfa region, contains conodont assemblages assigned to the *Clarkina orientalis* biozone (Fig. 12).

The base of the Ali Bashi Formation consists of a shaly interval with minor intercalations of marl and limestone bed, which has been named the Zal Member, measuring 13.50, 18.00, 12.50 and 16.00 m in the Aras Valley, Kuh-e-Ali Bashi 4, Kuh-e-Ali Bashi 1 and Zal section, respectively. The Changhsingian stage is defined in this study by the *C. orientalis* – *C. subcarinata* interval zone, which is taken as equivalent for the absent Changhsingian conodont marker species *C. wangi* (Jin et al., 2006, Fig. 10). The stage boundary is located close to the base of the Zal Member (Figs. 11 and 12). This biozone is followed by the *C. subcarinata* and *C. chanxingensis* zone, which can be found as well in the South Chinese sections, although the latter biozone is about 3 times more expanded in the Meishan section (Yuan et al., 2014, Fig. 12). The *C. chanxingensis* zone has not been reported from P-Tr localities in Iran by Kozur (2005, 2007, Fig. 10) but was included in the scheme of Shen and Mei (2010).

This unit is followed by the *Paratirolites* Limestone unit, which is a characteristic unit for the whole Julfa region (e.g., Leda et al., 2014). This cliff-forming carbonate unit of the Changhsingian Stage has a thickness of roughly 5 m (Aras Valley: 4.60 m, Kuh-e-Ali Bashi 4: 4.15 m, Kuh-e-Ali Bashi 1: 4.15 m, Zal: 5.10 m). Similar lithological units can also be found in central Iran (Leda et al., 2014; Kozur, 2007), although with a less developed nodular structure. This unit is seemingly lithologically homogeneous. Leda et al. (2014) provided, however, a more detailed subdivision based on microfacies analysis and showed that the upper 30 cm displays signs of stratigraphic condensation in the form of hardgrounds. They relate these features to submarine dissolution under carbonate under-saturated seawater. The lithological unit captures 4 conodont zones, in ascending order , *C. bachmanni*, *C. nodosa*, *C. yini* and *C. hauschkei* (Fig. 11). This zonation scheme deviates from interpretations of Kozur (2007) and Shen and Mei (2010) as the former author did not describe the *C. yini* zone (Fig. 10), and the latter scheme does not contain the *C. hauschkei* zone.

The top of this unit is marked by the cessation of limestone beds, and is conformably overlain by a unit consisting dominantly of clay, here called the Aras Member (formerly 'Boundary Clay', e.g., Kozur, 2004; Korte and Kozur, 2005). The boundary between the *Paratirolites* Limestone and Aras Member is referred to as the 'extinction horizon' (e.g., Kozur, 2004; Korte and Kozur, 2005; Leda et al., 2014, Fig. 12). At this interval, all corals and brachiopods disappear as well as substantial decreases in ammonite and conodont abundances (Fig. 5). However, ostracods, foraminifera and sponge spiculae remain abundant (Kozur, 2007; Leda et al., 2014). This unit, which varies markedly in thickness between sections (Zal: 0.50 m, Kuh-e-Ali Bashi 1: 1.18 m, Aras valley: 3.00 m; Fig. 12), harbours two conodont zones *H. praeparvus-H. changxingensis* and *M. ultima-S. ?mostleri*. The former conodont zone is somewhat similar to the *C. meishanensis-H. praeparvus* of Kozur (2005, 2007) reported in both central and NW Iran, whereas in this study no representatives of *C. meishanensis* have been found in the Aras Member. The latter biozone is also established in most P-Tr sections located in Iran Kozur (2005, 2007) but, at least for the here studied sites, this zone is marked by a rather heterogeneous stratigraphic distribution and is likely less useful as a correlation tool (Fig. 12).

The last lithological unit, is part of the Elikah formation, consisting of grey platy limestone with abundant *Claraia* specimens, and is therefore also known as the *Claraia* Beds (Fig. 12). Calcite of this unit has a tentative microbial origin (Leda et al., 2014; Richoz et al., 2010) and the complete unit reaches up to 280 m in thickness (Stepanov et al., 1969). At the Kuh-e-Ali Bashi sections, however, the lower 0.87 m of this unit is constituted by nodular limestone, bearing similarity to the pre-extinction *Paratirolites* Limestone unit (Fig. 12). The basal part of this lithology is marked by the FAD of *H. parvus*, making it largely of Triassic age in agreement with

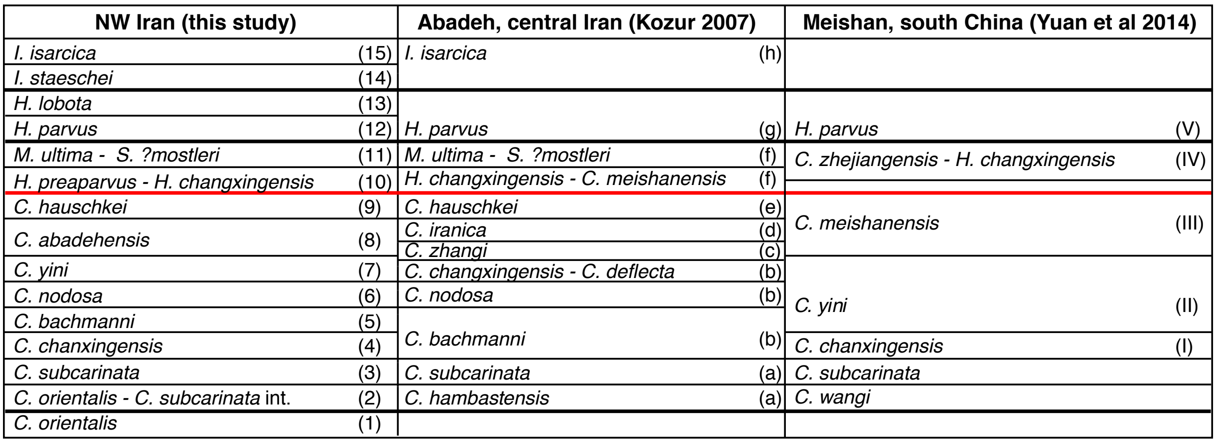

NW Iran (this study)	Abadeh, central Iran (Kozur 2007)	Meishan, south China (Yuan et al 2014)
I. isarcica (15)	*I. isarcica* (h)	
I. staeschei (14)		
H. lobota (13)		
H. parvus (12)	*H. parvus* (g)	*H. parvus* (V)
M. ultima - S. ?mostleri (11)	*M. ultima - S. ?mostleri* (f)	*C. zhejiangensis - H. changxingensis* (IV)
H. preaparvus - H. changxingensis (10)	*H. changxingensis - C. meishanensis* (f)	
C. hauschkei (9)	*C. hauschkei* (e)	*C. meishanensis* (III)
C. abadehensis (8)	*C. iranica* (d) *C. zhangi* (c)	
C. yini (7)	*C. changxingensis - C. deflecta* (b)	*C. yini* (II)
C. nodosa (6)	*C. nodosa* (b)	
C. bachmanni (5)	*C. bachmanni* (b)	
C. chanxingensis (4)		*C. chanxingensis* (I)
C. subcarinata (3)	*C. subcarinata* (a)	*C. subcarinata*
C. orientalis - C. subcarinata int. (2)	*C. hambastensis* (a)	*C. wangi*
C. orientalis (1)		

Figure 10 A scheme for the conodont zones of NW Iran, central Iran (Abadeh section) and South China (Meishan section). A correlation based on conodont zones between NW Iran and central Iran follows paper 1. A correlation between South China and the P-Tr interval in Iran can only be achieved, with great confidence, for the thick lined conodont zones and the 'extinction horizon' (red line).

Kozur (2007). The latter two lithological unit (Aras member and *Claraia* Beds can be found in central Iran as well, as part of Unit 8 (and references therein, Korte et al., 2004b, Fig. 12) or Unit a (Taraz et al., 1981). A regional correlation is further possible for the FAD of *H. parvus* with the P-Tr sections in central Iran (Kozur, 2005, 2007, Fig. 12).

The Meishan section was located on the South Chinese microcontinent (Fig. 1), during Late Permian and Early Triassic time, and differs substantially in lithology, as well as the latest Permian conodont assemblages (for a discussion, see Kozur, 2007, Fig. 12). However, a correlation of the Meishan section with the localities in Iran is possible for the 'extinction horizon' and the FAD of *H. parvus* and *I. staeschei* (Kozur, 2007, Fig. 10 and 12). In addition, the Wuchiapingian-Changhsingian (Wu-Ch) boundary can be followed across the studied sections (Figs. 10 and 12, paper 1).

The time constraint Wu-Ch boundary, 'extinction horizon' and the FAD of *H. parvus* and *I. isarcica* (*I. staeschei* for NW Iran) at the Meishan section (Burgess et al., 2014; Shen et al., 2012) and the correlation of these markers with sections in Iran, allow the construction of a timeframe (Fig. 12). The Zal Member and the *Paratirolites* Limestone, have been related to a deepening of the marine basin, accompanied by lower sediment accumulation rates for the later unit (Mohtat Aghai et al., 2009; Richoz et al., 2010). To adjust for this change in accumulation rate of the Julfa sections, a separate sedimentation rate for the nodular limestone unit of the Abadeh section is calculated. This calculation can be achieved, as this locality has a near to homogeneous nodular limestone lithology for the complete Changhsingian stage. Based on the datums for the 'extinction horizon' and Wu-Ch, this calculation equates to a 0.3 cm/kyr sedimentation rate (Fig. 12), which is typical for these types of nodular limestone beds that undergo relative little post-depositional compression (Flügel, 2004). The near to identical Changhsingian lithologies in NW Iran (e.g., Leda et al., 2014) allow an extrapolation of this obtained sedimentation rate to these sites (Fig. 12), which also agrees with sedimentation rate estimates of Richoz et al. (2010). This way the geochemical investigations can be put in an absolute chronology, which gives insight about rate of change and time resolution of the geochemical studies.

To exemplify, this time frame results in a time-resolution for whole-rock δ^{13}C of the most intensively studied interval of the Kuh-e-Ali Bashi 1 section (5.00 m below and above the 'extinction horizon' and a sampling density of about 10 cm) of 46 kyr, 2 kyr and 1 kyr, for the *Paratirolites* Limestone, Aras Member and the *Claraia* Beds, respectively. In addition, conodont zones found at sites in Iran are between 50 to 300 kyr for the Permian, but markedly decrease to 10 -20 kyr duration after the extinction (Fig. 11).

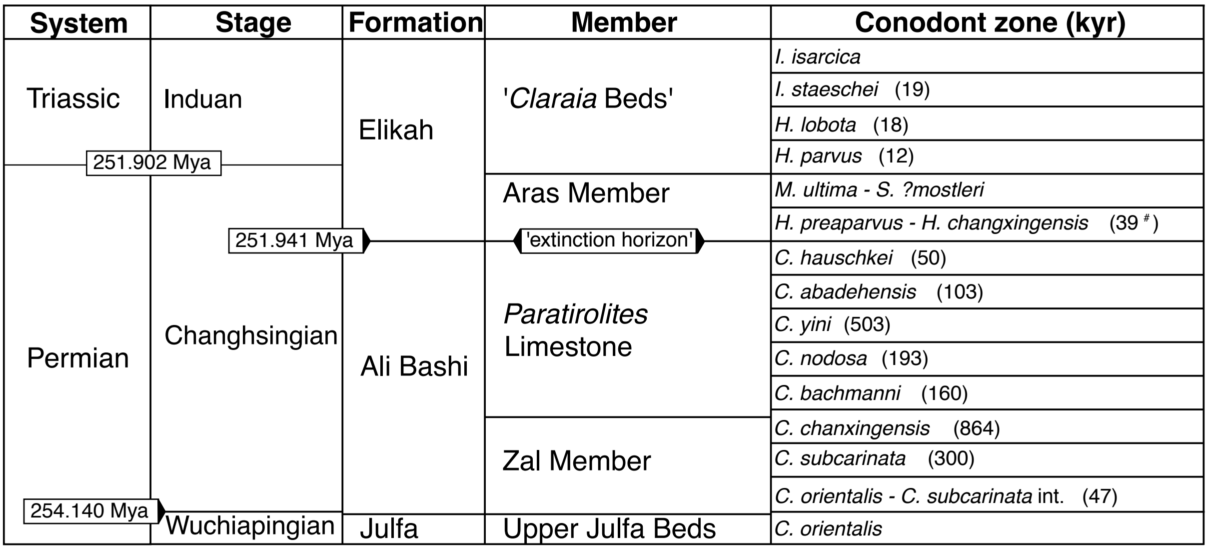

System	Stage	Formation	Member	Conodont zone (kyr)
Triassic	Induan	Elikah	'*Claraia* Beds'	*I. isarcica*
				I. staeschei (19)
				H. lobota (18)
				H. parvus (12)
251.902 Mya				
Permian	Changhsingian		Aras Member	*M. ultima - S. ?mostleri*
				H. preaparvus - H. changxingensis (39 $^{\#}$)
	251.941 Mya		'extinction horizon'	
		Ali Bashi	*Paratirolites* Limestone	*C. hauschkei* (50)
				C. abadehensis (103)
				C. yini (503)
				C. nodosa (193)
				C. bachmanni (160)
			Zal Member	*C. chanxingensis* (864)
				C. subcarinata (300)
				C. orientalis - C. subcarinata int. (47)
254.140 Mya				
	Wuchiapingian	Julfa	Upper Julfa Beds	*C. orientalis*

Figure 11 A scheme for the combined litho- and biostratigraphy of the P-Tr sections of the Julfa region. Conodont zonation as in papers 1 and 4. Age durations for conodont bio-zones following an updated scheme of interpolated datums similar as given in supplementary material from paper 4. Radiometric and calculated datums for the Meishan P-Tr GSSP section for the Wu-Ch of Shen et al. (2011) as well as the P-Tr boundary and the 'extinction horizon' (South China) of Burgess et al. (2014). $^{\#}$ duration is for the combined *H. praeparvus-H. changxingensis* as well as the *M. ultima-S. ?mostleri* conodont zones.

4.2 Uncovering palaeoclimatic and environmental information

Palaeontological and geological data have been used as qualitative and quantitative tools in attempts to reconstruct the physical and chemical conditions of the geological past. Sediments assumed to be diagnostic for certain climate regimes were used in the first qualitative palaeoclimate reconstructions (e.g., Blackett, 1961, and references therein). The chemical composition of fossils help to constrain climatic fluctuations in a more quantitative way ,e.g., landmark studies of Emiliani (1966) and Shackleton and Opdyke (1973), which helped constrain the cyclic nature of the glacial-interglacial intervals of the Pleistocene. However, the quantitative application of for instance oxygen isotope ratios in reconstructing ambient seawater temperatures is not straight forward as offsets due to local seawater chemistry ($\delta^{18}O_{sw}$)[3], vital effects and habitat preferences can obscure this approach (e.g., Zachos et al., 1994)

Especially in the geologically deep time, such as the P-Tr boundary interval, climate and environmental reconstructions become more uncertain, because fossil species have no close living relatives. In addition, a large obstacle is the effect of diagenesis on the sedimentary pile (bulk-carbonate rock and CAS) and fossil record (conodont elements), which can post-depositionally affect their respective chemical composition (e.g., Al-Aasm and Veizer, 1986; Gill et al., 2008; Barham et al., 2012). A careful examination of the signs of diagenetic alteration, which possibly impart on geochemical composition of the sedimentary record, is one way to increase the confidence of relating these signatures to genuine environmental changes.

The application of multiple proxies in palaeoenvironmental studies can, as well, strengthen interpretations if signals are consistent between the distinct geochemical records. This is shown in paper 2 were oxygen isotope records of conodont apatite and brachiopod calcite reveal a consistent signal, thereby increasing confidence in drawn climate reconstructions. Examination of bulk-rock and conodont $\delta^{18}O$, on the other hand, is suggestive of a diagenetic imprint on the absolute oxygen isotope composition of bulk-rock, while retaining a partial climate signal as a stratigraphic trend (paper 3). To further constrain the likelihood of palaeo-data contain-

---

[3] Oxygen isotope composition of seawater

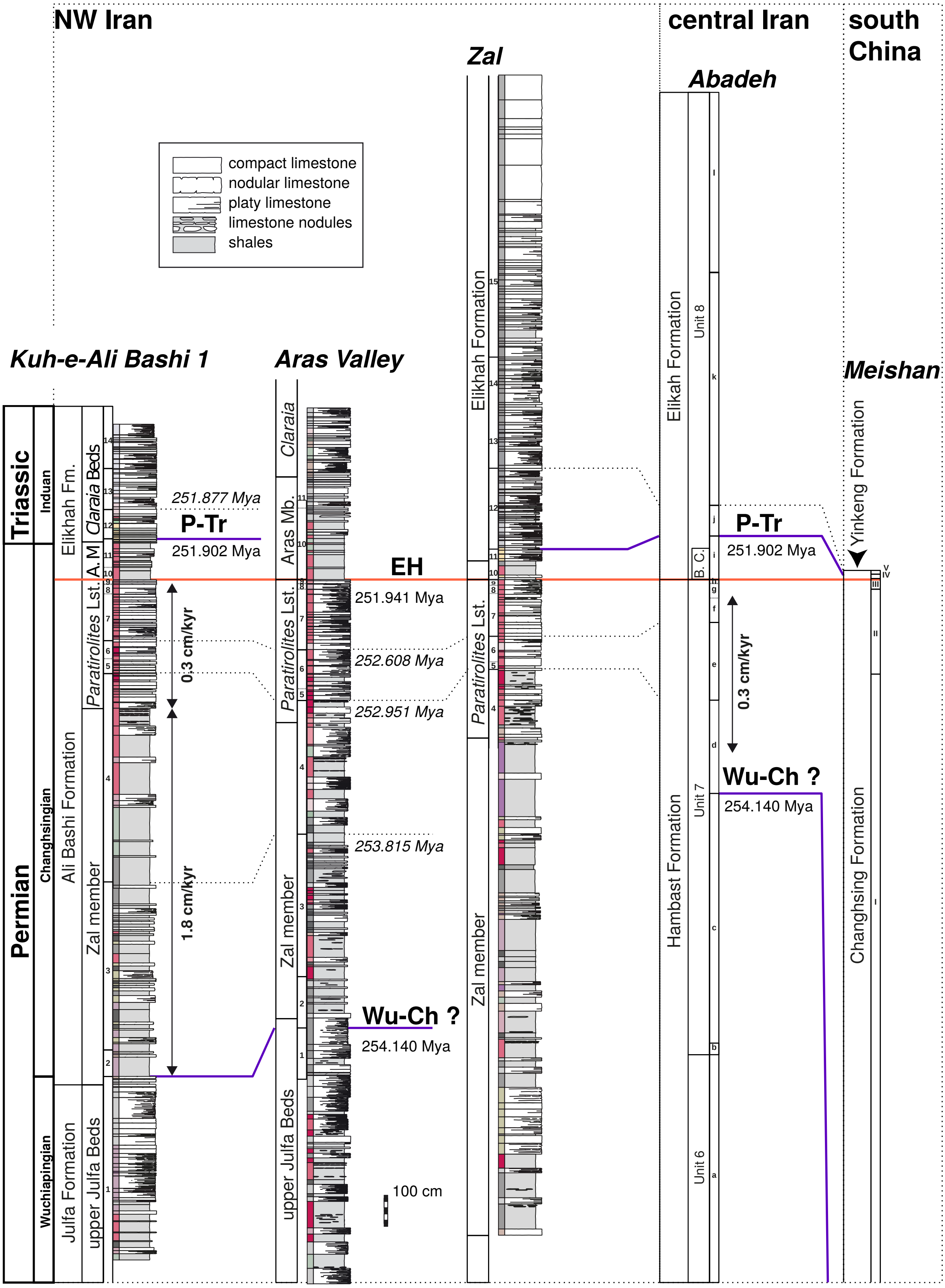

Figure 12 Combined litho- and biostratigraphy of the P-Tr sections of the Julfa region, Abadeh section (central Iran) and Meishan section (South China). Lithology and conodont zones are according to reports of Korte et al. (2004b) for the Abadeh section and Yuan et al. (2014, and pers. com. Shen 2014) for the Meishan section. The datums written in italic for conodont bio-zones are calculated dates (Supplementary material: Paper 4). The other dates are radiometric and calculated datums for the Meishan section from Shen et al. (2011); Burgess et al. (2014). Conodont zones NW Iran, Abadeh and Meishan are numbered according to Fig. 10

ing environmental information, proxy records have been constructed at multiple sites, e.g., the Kuh-e-Ali Bashi and Zal section. The independent correlation scheme based on bio- and lithostratigraphy, shown in paper 1 enables a comparison of the proxy data. This yielded reproducible trends for whole-rock δ^{13}C, CAS- sulphur and oxygen isotopes, as well as conodont δ^{18}O records (papers 2–4), and ensures a higher degree of confidence in relating these observations to carbon and sulphur biogeochemical cycle dynamics as well as climatic change, respectively.

A great hurdle in constructing calcite-based proxy records for the P-Tr sections in NW Iran is a reduction of overall carbonate content and calcite biogens in the sedimentary rocks, across the extinction interval, such as the complete absence of calcite brachiopod shells. The cause of this absence of calcite fossils might be inherent to the mass extinction event, which was possibly linked to a biocalcification crisis (Knoll et al., 2007). In paper 2, this particular problem is circumvented by construction of palaeotemperatures based on oxygen isotope ratios of conodont apatite, which remains available across this interval. In contrast, the development of bulk-rock δ^{13}C records, remains the most straightforward method for producing high-resolution δ^{13}C curves (paper 3). The alternative could be bulk-organic matter but the use of this proxy is complicated by other mechanisms mainly related to the large kinetic isotope fractionation upon C incorporation (Hayes et al., 1999) and mixing of organic carbon from different sources (Hermann et al., 2010). The carbonate of the 'Boundary Clay' has been suggested to be more prone to diagenesis than the bracketing limestone beds; this is due to a higher clastic content (paper 3 and Korte and Kozur, 2010). Stratigraphic bulk-carbonate trace element distribution, presented in paper 3, is suggestive of a late-stage dolimitization in this unit. This observation underlines the possibility of post-depositional alteration of its constituent geochemistry. These findings imply that fluctuations in δ^{13}C, as recorded in clay-rich intervals in particular, might represent a higher degree of post-depositional alteration of this geochemical signal. In this respect, care must be taken when using these small-scale carbon isotope fluctuations as stratigraphic markers and interpreting them in terms of carbon cycle perturbations.

Another approach utilized to strengthen palaeoclimatic and environmental interpretations is the qualitative comparison of proxy data and predictions made by numerical models (e.g., Lunt et al., 2013). A good agreement between oxygen isotope palaeothermometry and a modelling study by Kiehl and Shields (2005) in paper 2 exemplifies this assumption and puts confidence in both approaches to reconstruct climate around the P-Tr interval. Besides this comparative use of palaeodata and model solutions, paper 2 shows that a complementary use of these data sources is also insightful. Reconstructed palaeosalinity by Kiehl and Shields (2005, and Shields pers. com. 2013) are used to reconstruct seawater oxygen isotope values. This approach tries to resolve an uncertainty in oxygen isotope palaeothermometry which is the oxygen isotopic composition of the ambient water. This parameter is hard to constrain but possibly important due to regional influence of precipitation/evaporation ratios on the oxygen isotopic composition of surface waters and therefore constitutes a possible source of error in oxygen isotope palaeothermometry (for a discussion, see Zachos et al., 1994).

In another approach, outlined in paper 4, a simple mass-balance box model is employed in an attempt to reconcile the driving forces behind observed sulphur isotope excursions observed in CAS. The use of such simple one-box model is tenable as spatial differences in seawater sulphate are assumed to be limited (Strauss, 1999). This approach shows that changes in the amount of microbial sulphate reduction is likely to explain the observed sulphur cycle perturbations, rather than changes in other fluxes, such as mantle input of sulphur, that also regulate the isotope composition of marine sulphate.

To summarize, the presented examples are just a few possibilities in a wide range of methods to strengthen the reliability of palaeoclimatic and environmental reconstructions. The general tenet is that the use of independent lines of evidence is profitable when trying to reconstruct climates and environments in deep time. This can be achieved by construction of high-resolution multi-proxy records of several localities bound in a rigid stratigraphic framework which can, in addition, be compared with or complement model simulations.

4.3 The Earth system and the EPME

The notion that Earth surface processes, such as climate changes, are driven by both forcing and feedback mechanisms is important when invoking causal relationships for explaining the EPME. An important forcing mechanism is thermal insulation by atmospheric CO_2 (Lunt et al., 2013). This is mainly controlled by the amount of volcanic outgassing and volume of spreading ridges as well as long-term feedback mechanisms, such as weathering and organic carbon burial. These mechanism are the drivers of the large cycles, which maintain long periods (Myr-scale) of climate stasis (Berner et al., 1983; Lasaga et al., 1983), although the relative importance of the different players is debated (e.g., Raymo et al., 1988; Berner, 1999)

The long-term δ^{13}C trend straddling the P-Tr boundary, a reliable palaeorecord (paper 3), can be considered a long-term perturbation of the carbon cycle. The produced δ^{13}C curve, if interpreted as by Korte et al. (2010), would imply a $\sim$1 Myr period of volcanic outpouring by the Siberian Trap basalts and associated outgassing of isotopic depleted carbon, mainly as CO_2. Burning of organic-rich shales, petroleum bearing evaporites and coal beds by sill and dyke intrusions, related to Siberian Trap volcanism, have been interpreted to provide substantial additional isotopic depleted carbon to the ocean/atmosphere system (Svensen et al., 2009; Retallack and Krull, 2006; Retallack and Jahren, 2008). This could be an important driver for environmental and climatic changes around this time interval, but the interpretation of this long-term δ^{13}C trend is not unequivocal and can be related to other mechanisms, such as erosion of organic matter from the continents (Holser and Magaritz, 1987) or reduced primary productivity (Rampino and Caldeira, 2005).

The extinction event is possibly confined to less than 100 kyr (Burgess et al., 2014). Furthermore, the biotic crisis appears to be linked with abrupt climatic warming, based on δ^{18}O palaeothermometry at sites in Iran (paper 2) and South China (Joachimski et al., 2012) that record an >5°C warming of seawater in $\sim$ 20 kyr (paper 2 and section 4.1). These rapid perturbations of climate and biosphere may suggest that the above mentioned normal long-term feedback mechanisms could not cope, with the system being forced out of its equilibrium, and might imply fast acting positive feedback mechanisms (paper 3). The runaway greenhouse scenario, in which CH_4 emissions in the atmosphere by methane clathrate dissociation due to the crossing of a thermal gradient, elegantly explains the rapidity of the extinction (Erwin, 1993; Benton and Twitchett, 2003) and has also been invoked for climate change at the PETM[4] (Dickens et al., 1995) and the end-Triassic mass extinction (Ruhl et al., 2011).

This scenario would also explain large negative fluctuation in δ^{13}C, as recorded in the Meishan section (Cao et al., 2009), which is hard to explain by a volcanic injection of isotopic light carbon (for an alternative opinion, see Sobolev et al., 2011). As outlined in paper 3, the studied sections in NW Iran, although stratigraphically complete, do not display these short-term large δ^{13}C fluctuations. At this stage, it remains an unanswered question if these short-term negative carbon isotope excursions recorded at Meishan are really a global phenomenon and if whole-rock δ^{13}C can directly be related to the isotopic composition of Late Permian marine DIC.

The importance for extinction scenarios of such rapid or fast feedback mechanisms acting to cause perturbation to the Earth system and biosphere is reinforced by numerical models (e.g., Kiehl and Shields, 2005). These models cannot produce the low meridional thermal gradient as invoked by palaeodata, that suggest high latitude warmth (e.g., Retallack, 1995). Creating this reduced latitudinal gradient by numerical models often entails the incorporating large, possibly unrealistic, atmospheric CO_2 levels (Winguth and Winguth, 2013). Alternative mechanisms that do not directly impart on the carbon cycle are changes in cloud optical depth, enhanced ocean heat transport and polar stratospheric clouds (Kiehl and Shields, 2013) A more vigorous hydrological cycle as invoked in paper 2 with larger portions of water vapour in the atmosphere,

---

[4] The Paleocene-Eocene thermal maximum (PETM) is a period signified by an abrupt global temperature rise superimposed on already warm background conditions and is often associated with massive dissociation of methane clathrates (Dickens et al., 1995)

a potent greenhouse gas, might act as well as a positive feedback on global warming (Held and Soden, 2000).

Besides these positive climate feedbacks, other feedback mechanisms could act as synergistic killing agents in the EPME. In paper 4, a scenario of increased global water column anoxia and euxinia, based on stratigraphic patterns in CAS-oxygen and sulphur isotopes, is related to global warming, similar as hypothesized by Kump et al. (2005). The changes in ocean chemistry, O_2 draw down and H_2S build-up, relate to increased marine organic matter production and consequential (an)aerobic organic carbon re-mineralization. In turn, the increased marine organic carbon pool is related to sharply increased continental weathering and associated fluxes of terrestrial material, concomitant with the event horizon (e.g., Algeo and Twitchett, 2010) and might be directly related to global warming (paper 2). This scenario of ocean eutrophication received increasing attention in the last years and may be important in explaining the vast sum of evidence of marine anoxia as well as euxinia in shelf settings during this time interval (e.g., Algeo et al., 2013).

The rapidness of changes in climate, ocean chemistry and biosphere is in stark contrast to the aftermath of the EPME. This period, the Early Triassic, is characterised by a depaupered fauna, repeated carbon and sulphur cycle perturbation, extreme warmth, widespread marine anoxia, enhanced continental weathering and an absence of coal deposits as well as canopy forming vegetation on land (Looy et al., 1999; Payne et al., 2004; Chen and Benton, 2012; Sun et al., 2012; Algeo et al., 2013; Song et al., 2014). Besides the severity of the initial extinction, this clearly distinguishes this event form other events associated with global warming and extended stretches of ocean with anoxic conditions, such as the PETM and Mesozoic OAE's[5] which show a return to pre-disturbance conditions within a much shorter time-interval (paper 4). Another feature is that, e.g., the carbon cycle perturbation and possibly first outporings of the Siberian Trap basalt preceded the extinction (paper 3 and Shen et al., 2012). These observations might suggest that some parts of the system were already deteriorating before the majority of environmental changes and the mass extinction took place.

Combining these features, an abrupt mass extinction, pre-extinction environmental disturbances, a long recovery period for biota and a central role for climate change might point to a phenomena known as planetary regime or state shift. Planetary state shift is an concept that is related to causal chains, forced by initial drivers and feedback loops and describes how a boundary condition or tipping point in the Earth system can be crossed, causing a shift from one equilibrium state to another (Scheffer et al., 2009; Barnosky et al., 2012; Hughes et al., 2013, Fig. 13). Analogues scenarios have been suggested for the K-Pg boundary marked by the remarkable transition/state shift between non-avian dinosaurs and mammals (Renne et al., 2013). However, the exact mechanism behind this planetary state shift is illusive but elevated atmospheric CO_2 by a volcanic injection or other sources, such as methane clathrates remains a tempting explanation. More certain is that global warmth, anoxia and euxinia have played a pivotal role in the EPME (papers 2 and 4; also, see Wignall and Hallam, 1992; Wignall and Twitchett, 1996; Kump et al., 2005; Joachimski et al., 2012). In contrast to the idea of a Strangelove Ocean, the latter killing agents, are likely the effect of an increased marine biomass (mainly prokaryotes) which might have directly imparted on Early Triassic biogeochemical cycles (paper 4). Therefore, the EPME could have marked the transition towards a new equilibrium state which entails a world inhabited by different biota and associated with long-term warmth (Sun et al., 2012; Price et al., 2013).

In prospect of a pending planetary state shift in the near future, associated by a biotic crisis mediated by climate change driven by the burning of fossil fuels (Scheffer et al., 2009; Barnosky et al., 2012; Hughes et al., 2013) among other factors, stipulates the importance of studying such mass extinction events.

---

[5] OAE stands for ocean anoxic event and is a returning feature of the Middle to Late Mesozoic, which is signified by the deposition of organic rich strata in marine settings (Schlanger and Jenkyns, 1976)

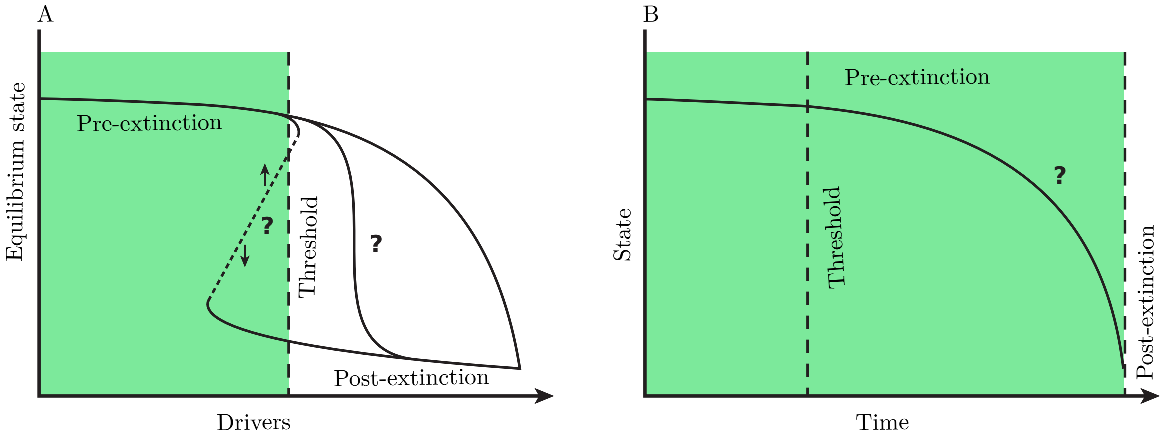

Figure 13 The idea of planetary state shift is somewhat analogues, but on a different scale, to regime shifts observed in modern ecosystems, which are caused by the crossing of a tipping point by destabilising disturbances (e.g., feedback mechanisms or drivers)(Barnosky et al., 2012; Hughes et al., 2013). This scheme modified from Hughes et al. (2013) illustrates a hypothetical scenario describing the transition from the Permian to the Triassic, through the EPME. In (A) this change can be considered to unfold in three ways: smooth, stepwise or hysteretic. The two latter scenarios include a threshold mechanism or tipping point. The sulphidic poisoning scenario, as outlined in paper 4 could be perceived as a threshold scenario. Disturbance on terrestrial communities induced by CO_2 and associated feedback loops, disturb an initial global-scale equilibrium driven by outgassing of the Siberian Trap Basalts. The initial driver would be acidification of terrestrial landscapes, which eventually triggered a surge of weathered terrestrial material into the ocean, with continental weathering rates possibly enhanced by global warming directly at the marine 'extinction horizon' (paper 2). A positive feedback mechanism of ocean fertilization spawns large masses of marine prokaryotic biomass and successively enhances (an)aerobic re-mineralization. This feedback results in a cataclysmic event of greatly increased global extend of anoxia and euxina in marine settings. Fundamental changes in biogeochemical cycles, possibly by a loss of biodiversity could usher a new equilibrium state in the extinction aftermath. In (B), the response, leading into mass extinction event, to the crossing of a certain threshold might as well post-date the initial trigger. For instance, in the above described scenario, commencing Siberian Trap volcanism would have started to disrupt terrestrial communities already before the EPME.

5 Conclusions and outlook

The findings from the P-Tr localities in NW Iran provide new insights about the strata at the sites in NW Iran as well as into the nature of the environmental and climatic changes of this time interval. The new correlation scheme for the Julfa region presented in paper 1 is the basis for this thesis as it allows the comparison of observed geochemical trends. In addition, a temporal framework could be constructed for these sites by a correlation with the radiometrically dated Meishan section (South China). However, a highly detailed correlation for the latest Permian with the well-studied localities in South China is still hampered by inconsistencies in the conodont stratigraphy and requires more investigation. The construct of an absolute temporal framework for other P-Tr with a rigid biostratigraphy would be beneficial in this respect.

Evidence for climatic warming across the P-Tr boundary interval as presented in paper 2 is an encouraging results from this thesis as it acknowledges previous evidence of dramatic climate change found at sites in South China. The downside is that all studied sections were located in tropic or sub-tropic latitudes during the Late Permian and Early Triassic. This urges for similar investigations at P-Tr localities outside of the tropics. It can be expected that a temperature increase at higher latitudes would have been more severe then at the lower latitudes.

Exploring the functioning of the carbon cycle around the P-Tr interval, in high detail, and identifying its relation to the mass extinction is of importance. This requires additional investigations and can possibly not solely rely on carbon isotope measurements from bulk-marine carbonate rock. The most straight forward solution to the before mentioned problem is possibly simultaneous measurements of specific compounds of organic matter.

The combined geochemical signatures, bulk-carbonate carbon, conodont oxygen and CAS-oxygen and sulphur isotopes sketch a scenario of a period associated with climate change and global changes in ocean chemistry, such as more widespread marine anoxia and euxinia. The operating of the 'Earth system' and its associated feedback mechanism are likely mechanisms that connect these disparate observations. The proximate causes of the mass extinction, at least in the marine realm, lies likely in the combined effect of thermal stress, deficient oxygen and sulphidic toxicity. The synchronous emplacement of the Siberian Trap basalt and the marine mass extinction make volcanism a likely ultimate trigger of the EPME.

The way forward encompasses the correlation of many sites, spread globally, bound in a rigid stratigraphic and temporal framework. Together with the use of quantitative palaeontological as well as geochemical observations, incorporating many independent lines of evidence to produce high quality palaeodata records which can be compared with or complement outcomes of numerical modelling studies.

6 Bibliography

Abich, H. 1878. Geologische Forschungen in den Kaukasischen Laendern, I: Eine Bergkalkfauna aus der Araxesenge bei Djoulfa in Armenien. *Hoelder Wien.*

Al-Aasm, I. S. and Veizer, J. 1986. Diagenetic stabilization of aragonite and low-Mg calcite, II. Stable isotopes in rudists. *Journal of Sedimentary Research*, 56(6): 763–770.

Algeo, T. J. and Twitchett, R. J. 2010. Anomalous Early Triassic sediment fluxes due to elevated weathering rates and their biological consequences. *Geology*, 38(11): 1023–1026.

Algeo, T. J., Henderson, C. M., Tong, J., Feng, Q., Yin, H., and Tyson, R. V. 2013. Plankton and productivity during the Permian–Triassic boundary crisis: An analysis of organic carbon fluxes. *Global and Planetary Change*, 105: 52–67.

Barham, M., Joachimski, M., Murray, J., and Williams, D. 2012. Diagenetic alteration of the structure and $\delta 18$O signature of Palaeozoic fish and conodont apatite: Potential use for corrected isotope signatures in palaeoenvironmental interpretation. *Chemical Geology*, 298-299: 11–19.

Barnosky, A. D., Hadly, E. A., Bascompte, J., Berlow, E. L., Brown, J. H., Fortelius, M., Getz, W. M., Harte, J., Hastings, A., Marquet, P. A., Martinez, N. D., Mooers, A., Roopnarine, P., Vermeij, G., Williams, J. W., Gillespie, R., Kitzes, J., Marshall, C., Matzke, N., Mindell, D. P., Revilla, E., and Smith, A. B. 2012. Approaching a state shift in Earth's biosphere. *Nature*, 486(7401): 52–8.

Baud, A., Magaritz, M., and Holser, W. T. 1989. Permian-Triassic of the Tethys: Carbon isotope studies. *Geologische Rundschau*, 78(2): 649–677.

Becker, L. 2001. Impact Event at the Permian-Triassic Boundary: Evidence from Extraterrestrial Noble Gases in Fullerenes. *Science*, 291(5508): 1530–1533.

Benton, M. J. and Twitchett, R. J. 2003. How to kill (almost) all life: the end-Permian extinction event. *Trends in Ecology & Evolution*, 18(7): 358–365.

Berner, R. A. 1999. A new look at the Long-Term Carbon Cycle. *GSA Today*, 9(11): 1–6.

Berner, R. A. 2002. Examination of hypotheses for the Permo-Triassic boundary extinction by carbon cycle modeling. *Proceedings of the National Academy of Sciences of the United States of America*, 99(7): 4172–4177.

Berner, R. A., Lasaga, A. C., and Garrels, R. M. 1983. The carbon-silicate geochemical cycle and its effect on atmospheric carbon dioxide over the past 100 million years. *American Journal of Science*, 283: 641–683.

Besse, J., Torcq, F., Gallet, Y., Ricou, L. E., Krystyn, L., and Saidi, a. 1998. Late Permian to Late Triassic palaeomagnetic data from Iran: constraints on the migration of the Iranian block through the Tethyan Ocean and initial destruction of Pangaea. *Geophysical Journal International*, 135(1): 77–92.

Bijma, J., Pörtner, H.-o., Yesson, C., and Rogers, A. D. 2013. Climate change and the oceans - What does the future hold? *Marine Pollution Bulletin*, 74(495-505): 436.

Black, B. A., Elkins-Tanton, L. T., Rowe, M. C., and Peate, I. U. 2012. Magnitude and consequences of volatile release from the Siberian Traps. *Earth and Planetary Science Letters*, 317-318: 363–373.

Blackett, P. M. S. 1961. Comparison of Ancient Climates with the Ancient Latitudes Deduced from Rock Magnetic Measurements. *Proceedings of the Royal Society A: Mathematical, Physical and Engineering Sciences*, 263(1312): 1–30.

Brand, U. and Veizer, J. 1980. Chemical diagenesis of a multicomponent carbonate system-1: Trace elements. *Journal of Sedimentary Research*, 50(4): 1219 –1236.

Brand, W. a., Coplen, T. B., Vogl, J., Rosner, M., and Prohaska, T. 2014. Assessment of international reference materials for isotope-ratio analysis (IUPAC Technical Report). *Pure and Applied Chemistry*, 86(3): 425–467.

Brayard, A., Escarguel, G., Bucher, H., Monnet, C., Brühwiler, T., Goudemand, N., Galfetti, T., and Guex, J. 2009. Good Genes and Good Luck: Ammonoid Diversity and the End-Permian Mass Extinction. *Science*, 325(5944): 1118–1121.

Brook, B. W., Ellis, E. C., Perring, M. P., Mackay, A. W., and Blomqvist, L. 2013. Does the terrestrial biosphere have planetary tipping points? *Trends in ecology & evolution*, 28(7): 396–401.

Burgess, S. D., Bowring, S., and Shen, S.-z. 2014. High-precision timeline for Earth's most severe extinction. *Proceedings of the National Academy of Sciences*, 111(9): 3316–3321.

Caldeira, K. and Wickett, M. E. 2003. Anthropogenic carbon and ocean pH. *Nature*, 425(6956): 365.

Campbell, I. H., Czamanske, G. K., Fedorenko, V. A., Hill, R. I., and Stepanov, V. 1992. Synchronism of the Siberian Traps and the Permian-Triassic Boundary. *Science*, 258(5089): 1760–1763.

Cao, C., Love, G. D., Hays, L. E., Wang, W., Shen, S., and Summons, R. E. 2009. Biogeochemical evidence for euxinic oceans and ecological disturbance presaging the end-Permian mass extinction event. *Earth and Planetary Science Letters*, 281(3-4): 188–201.

Cazenave, A., Lombard, A., and Llovel, W. 2008. Present-day sea level rise: A synthesis. *Comptes Rendus Geoscience*, 340(11): 761–770.

Chen, Z.-Q. and Benton, M. J. 2012. The timing and pattern of biotic recovery following the end-Permian mass extinction. *Nature Geoscience*, 5(6): 375–383.

Diaz, R. J. and Rosenberg, R. 2008. Spreading dead zones and consequences for marine ecosystems. *Science*, 321(5891): 926–9.

Dickens, G. R., O'Neil, J. R., Rea, D. K., and Owen, R. M. 1995. Dissociation of oceanic methane hydrate as a cause of the carbon isotope excursion at the end Paleocene. *Paleoceanography*, 10(6): 965–971.

Doney, S. C., Fabry, V. J., Feely, R. a., and Kleypas, J. a. 2009. Ocean Acidification: The Other CO2 Problem. *Annual Review of Marine Science*, 1(1): 169–192.

Doney, S. C., Ruckelshaus, M., Duffy, J. E., Barry, J. P., Chan, F., English, C. A., Galindo, H. M., Grebmeier, J. M., Hollowed, A. B., Knowlton, N., Polovina, J., Rabalais, N. N., Sydeman, W. J., and Talley, L. D. 2012. Climate Change Impacts on Marine Ecosystems. *Annual Review of Marine Science*, 4: 11–37.

Emiliani, C. 1966. Paleotemperature Analysis of Caribbean Cores P6304-8 and P6304-9 and a Generalized Temperature Curve for the past 425,000 Years. *The Journal of Geology*, 74(2): 109–124.

Erwin, D. H. *The great Paleozoic crisis. Life and Death in the Permian.* Columbia University Press, New York, 1993.

Erwin, D. H. 1994. The Permo-Triassic extinction. *Nature*, 367(6460): 231–236.

Erwin, D. H. 2001. Lessons from the past: Biotic recoveries from mass extinctions. *Proceedings of the National Academy of Sciences*, 98(10): 5399–5403.

Flügel, E. *Microfacies of carbonate rock.* Springer, Berlin, Germany, 2004.

Foster, W. J. and Twitchett, R. J. 2014. Functional diversity of marine ecosystems after the Late Permian mass extinction event. *Nature Geoscience*, 7(3): 233–238.

Frech, F. V. and Arthaber, G. 1900. Ueber das Palaeozoicum in Hocharmenien und Persien. Mit einem Anhang ueber die Kreide von Sirab in Persien. *Beitraege zur Palaeontologie und Geologie Oesterreich-Ungarns und des Orients*, 12: 161–308.

Furnish, W. M. Permian Stage Names. In in Logan A. and Hills L. V., E., editor, *The Permian and Triassic systems and their mutual boundary*, pages 522–548. Canadian Society of Petroleum Geologists, Calgary, memoir 2 edition, 1973.

Gill, B. C., Lyons, T. W., and Frank, T. D. 2008. Behavior of carbonate-associated sulfate during meteoric diagenesis and implications for the sulfur isotope paleoproxy. *Geochimica et Cosmochimica Acta*, 72(19): 4699–4711.

Harnik, P. G., Lotze, H. K., Anderson, S. C., Finkel, Z. V., Finnegan, S., Lindberg, D. R., Liow, L. H., Lockwood, R., McClain, C. R., McGuire, J. L., O'Dea, A., Pandolfi, J. M., Simpson, C., and Tittensor, D. P. 2012. Extinctions in ancient and modern seas. *Trends in ecology & evolution*, 27(11): 608–17.

Hautmann, M., Bucher, H., Brühwiler, T., Goudemand, N., Kaim, A., and Nützel, A. 2011. An unusually diverse mollusc fauna from the earliest Triassic of South China and its implications for benthic recovery after the end-Permian biotic crisis. *Geobios*, 44(1): 71–85.

Hayes, J. M., Strauss, H., and Kaufman, A. J. 1999. The abundance of 13C in marine organic matter and isotopic fractionation in the global biogeochemical cycle of carbon during the past 800 Ma. *Chemical Geology*, 161(1-3): 103–125.

Held, I. M. and Soden, B. J. 2000. Water Vapor Feedback and Global Warming. *Annual Review of Environment and Resources*, 25: 441–475.

Henderson, C. M., Mei, S., and Shen, S. 2008. Resolution of the reported Upper Permian conodont occurrences from northwestern Iran. *Permophiles, Newsletter of the Subcommission on Permian Stratigraphy*, 51: 2–9.

Hermann, E., Hochuli, P. a., Bucher, H., Vigran, J. O., Weissert, H., and Bernasconi, S. M. 2010. A close-up view of the Permian–Triassic boundary based on expanded organic carbon isotope records from Norway (Trøndelag and Finnmark Platform). *Global and Planetary Change*, 74 (3-4): 156–167.

Hoegh-Guldberg, O. and Bruno, J. F. 2010. The impact of climate change on the world's marine ecosystems. *Science*, 328(5985): 1523–8.

Holser, W. T. and Magaritz, M. 1987. Events near the Permian-Triassic boundary. *Modern Geology*, 11: 155–180.

Horacek, M., Richoz, S., Brandner, R., Krystyn, L., and Spötl, C. 2007. Evidence for recurrent changes in Lower Triassic oceanic circulation of the Tethys: The δ13C record from marine sections in Iran. *Palaeogeography, Palaeoclimatology, Palaeoecology*, 252(1-2): 355–369.

Hughes, T. P., Baird, a. H., Bellwood, D. R., Card, M., Connolly, S. R., Folke, C., Grosberg, R., Hoegh-Guldberg, O., Jackson, J. B. C., Kleypas, J., Lough, J. M., Marshall, P., Nyström, M., Palumbi, S. R., Pandolfi, J. M., Rosen, B., and Roughgarden, J. 2003. Climate change, human impacts, and the resilience of coral reefs. *Science*, 301(5635): 929–33.

Hughes, T. P., Carpenter, S., Rockström, J., Scheffer, M., and Walker, B. 2013. Multiscale regime shifts and planetary boundaries. *Trends in ecology & evolution*, 28(7): 389–95.

Imai, N., Terashima, S., Itoh, S., and Ando, A. 1996. 1996 Compilation of Analytical Data on Nine GSJ Geochemical Reference Samples, "Sedimentary Rock Series". *Geostandards and Geoanalytical Research*, 20(2): 165–216.

Isozaki, Y. 1997. Permo-Triassic Boundary Superanoxia and Stratified Superocean: Records from Lost Deep Sea. *Science*, 276(5310): 235–238.

Jin, Y. G., Zhang, J., and Shang, Q. H. Two phases of the end-Permian mass extinction. In Embry, A., Beauchamp, B., and Glass, D. J., editors, *Pangea: Global Environments and Resources*, volume 17, pages 813–822. Canadian Society of Petroleum Geologists, Calgary, Canada, 1994.

Jin, Y., Wang, Y., Henderson, C., Wardlaw, B. R., Shen, S., and Cao, C. 2006. The Global Boundary Stratotype Section and Point (GSSP) for the base of Changhsingian Stage (Upper Permian). *Episodes*, 29(3): 175–182.

Joachimski, M. M., Lai, X., Shen, S.-z., Jiang, H., Luo, G., Chen, B., Chen, J., and Sun, Y. 2012. Climate warming in the latest Permian and the Permian-Triassic mass extinction. *Geology*, 40(3): 195–198.

Joachimski, M., Breisig, S., Buggisch, W., Talent, J., Mawson, R., Gereke, M., Morrow, J., Day, J., and Weddige, K. 2009. Devonian climate and reef evolution: Insights from oxygen isotopes in apatite. *Earth and Planetary Science Letters*, 284(3-4): 599–609.

Kaiho, K., Kajiwara, Y., Nakano, T., Miura, Y., Kawahata, H., Tazaki, K., Ueshima, M., Chen, Z., and Shi, G. R. 2001. End-Permian catastrophe by a bolide impact: Evidence of a gigantic release of sulfur from the mantle. *Geology*, 29(9): 815–818.

Kajiwara, Y., Imai, A., Ishida, K., Ishiga, H., and Yamakita, S. 1994. Development of a largely anoxic stratified ocean and its temporary massive mixing at the Permian/Triassic boundary supported by the sulfur isotopic record. *Palaeogeography, Palaeoclimatology, Palaeoecology*, 111(3-4): 367–379.

Kakuwa, Y. and Matsumoto, R. 2006. Cerium negative anomaly just before the Permian and Triassic boundary event — The upward expansion of anoxia in the water column. *Palaeogeography, Palaeoclimatology, Palaeoecology*, 229(4): 335–344.

Kidder, D. L. and Worsley, T. R. 2004. Causes and consequences of extreme Permo-Triassic warming to globally equable climate and relation to the Permo-Triassic extinction and recovery. *Palaeogeography, Palaeoclimatology, Palaeoecology*, 203(3-4): 207–237.

Kiehl, J. T. and Shields, C. A. 2005. Climate simulation of the latest Permian: Implications for mass extinction. *Geology*, 33(9): 757–760.

Kiehl, J. T. and Shields, C. A. 2013. Sensitivity of the Palaeocene–Eocene Thermal Maximum climate to cloud properties. *Philosophical Transactions of the Royal Society A: Mathematical, Physical and Engineering Sciences*, 371(2001): 20130093.

Knoll, A. H., Bambach, R. K., Payne, J. L., Pruss, S., and Fischer, W. W. 2007. Paleophysiology and end-Permian mass extinction. *Earth and Planetary Science Letters*, 256(3-4): 295–313.

Koeberl, C., Gilmour, I., Reimold, W. U., Claeys, P., and Ivanov, B. 2002. End-Permian catastrophe by bolide impact: Evidence of a gigantic release of sulfur from the mantle: Comment and Reply:. *Geology*, 30(9): 855–856.

Koeberl, C., Farley, K. A., Peucker-Ehrenbrink, B., and Sephton, M. A. 2004. Geochemistry of the end-Permian extinction event in Austria and Italy: No evidence for an extraterrestrial component. *Geology*, 32(12): 1053–1056.

Korte, C., Kozur, H. W., and Partoazar, H. 2004a. Negative carbon isotope excursion at the Permian/Triassic boundary section at Zal, NW-Iran. *Hallesches Jahrbuech Geowissenschaften, Reihe B*, Beiheft 18: 69–71.

Korte, C. and Kozur, H. W. 2005. Carbon isotope stratigraphy across the Permian/Triassic at Jolfa (NW-Iran, Peitlerkofel (Sas de Pütia, Sass de Putia, Pufels (Bula, Bulla), Tesero (all three Southern Alps Italy) and Gerennavár (Bükk Mts., Hungary). *Journal of Alpine Geology*, 47: 119–135.

Korte, C. and Kozur, H. W. 2010. Carbon-isotope stratigraphy across the Permian–Triassic boundary: A review. *Journal of Asian Earth Sciences*, 39(4): 215–235.

Korte, C., Kozur, H. W., Joachimski, M. M., Strauss, H., Veizer, J., and Schwark, L. 2004b. Carbon, sulfur, oxygen and strontium isotope records, organic geochemistry and biostratigraphy across the Permian/Triassic boundary in Abadeh, Iran. *International Journal of Earth Sciences*, 93: 565–581.

Korte, C., Kozur, H. W., Joachimski, M. M., Pande, P., and Oberhänsli, H. 2010. Massive volcanism at the Permian–Triassic boundary and its impact on the isotopic composition of the ocean and atmosphere. *Journal of Asian Earth Sciences*, 37(4): 293–311.

Kotlyar, G., Zakharov, Y., Koczyrkevicz, B., Kropatcheva, G., Rostovcev, K., Chedija, I., Vuks, G., and Guseva, E. Pozdnepermskiy etap evolyutsii organicheskogo mira. Dzul'ficheskiy i dorashamskiy yarusy SSSR. In Gramm, M. and Rostovcev, K., editors, *Proekt No 106 ("Permo-Triasovaya stadiya geologicheskoy evolyutsii") mezhdunarodnoy programmy geologicheskoy skoy korrelatsii*, pages 1–70. 1983.

Kozur, H. 2007. Biostratigraphy and event stratigraphy in Iran around the Permian–Triassic Boundary (PTB): Implications for the causes of the PTB biotic crisis. *Global and Planetary Change*, 55(1-3): 155–176.

Kozur, H., Leven, E., Lozovskiy, V., and Pyatakova, M. 1980. Subdivision of Permian-Triasic beds in Transcaucasia on the basis of conodonts. *International Geology Review*, 22(3): 361–368.

Kozur, H. W. 2004. Pelagic uppermost Permian and the Permian– Triassic boundary conodonts of Iran, part I: taxonomy. *Hallesches Jahrbuech Geowissenschaften, Reihe B*, Beiheft 18: 36–68.

Kozur, H. 2005. Pelagic uppermost Permian and the Permian– Triassic boundary conodonts of Iran. Part II: investigated sections and evaluation of the conodont faunas. *Hallesches Jahrbuech Geowissenschaften, Reihe B*, Beiheft 19: 49–86.

Kryc, K. A., Murray, R. W., and Murray, D. W. 2003. Elemental fractionation of Si, Al, Ti, Fe, Ca, Mn, P, and Ba in five marine sedimentary reference materials: results from sequential extractions. *Analytica Chimica Acta*, 487: 117–128.

Kump, L. R., Pavlov, A., and Arthur, M. a. 2005. Massive release of hydrogen sulfide to the surface ocean and atmosphere during intervals of oceanic anoxia. *Geology*, 33(5): 397.

Lasaga, A. C., Berner, R. A., and Garrels, R. M. 1983. An improved geochemical model of atmospheric CO2 fluctuations over the past 100 million years. *Geophysical Monograph series*, 32: 397–411.

Lécuyer, C., Grandjean, P., O'Neil, J., Cappetta, H., and Martineau, F. 1993. Thermal excursions in the ocean at the Cretaceous—Tertiary boundary (northern Morocco): δ18O record of phosphatic fish debris. *Palaeogeography, Palaeoclimatology, Palaeoecology*, 105(3-4): 235–243.

Leda, L., Korn, D., Ghaderi, A., Hairapetian, V., Struck, U., and Reimold, W. U. 2014. Lithostratigraphy and carbonate microfacies across the Permian–Triassic boundary near Julfa (NW Iran) and in the Baghuk Mountains (Central Iran). *Facies*, 60(1): 295–325.

Looy, C. V., Brugman, W. a., Dilcher, D. L., and Visscher, H. 1999. The delayed resurgence of equatorial forests after the permian-triassic ecologic crisis. *Proceedings of the National Academy of Sciences of the United States of America*, 96(24): 13857–13862.

Lunt, D. J., Elderfield, H., Pancost, R., Ridgwell, A., Foster, G. L., Haywood, A., Kiehl, J., Sagoo, N., Shields, C., Stone, E. J., and Valdes, P. 2013. Warm climates of the past–a lesson for the future? *Philosophical transactions. Series A, Mathematical, physical, and engineering sciences*, 371(20130146): 1–13.

Meyer, K. M. and Kump, L. R. 2008. Oceanic Euxinia in Earth History: Causes and Consequences. *Annual Review of Earth and Planetary Sciences*, 36(1): 251–288.

Meyer, K., Kump, L., and Ridgwell, A. 2008. Biogeochemical controls on photic-zone euxinia during the end-Permian mass extinction. *Geology*, 36(9): 747.

Mohtat Aghai, P., Vachard, D., and Krainer, K. 2009. Transported foraminifera in Palaeozoic deep red nodular limestones exemplified by latest Permian Neoendothyra in the Zal section (Julfa area , NW Iran). *Revista Espanola de Micropaleontologia*, 41(1-2): 197–213.

Murienne, J., Daniels, S. R., Buckley, T. R., Mayer, G., and Giribet, G. 2014. A living fossil tale of Pangaean biogeography. *Proceedings of the Royal Society B: Biological sciences*, 281 (1775): 20132648.

Muttoni, G., Gaetani, M., Kent, D., Sciunnach, D., Angiolini, L., Berra, F., Garzanti, E., Mattei, M., and Zanchi, A. 2009a. Opening of the Neo-tethys ocean and the pangea B to pangea A transformation during the permian. *GeoArabia*, 14(4): 17–48.

Muttoni, G., Mattei, M., Balini, M., Zanchi, A., Gaetani, M., and Berra, F. The drift history of Iran from the Ordovician to the Triassic. In Brunet, M.-F., Wilmsen, M., and Granath, J., editors, *South Caspian to Central Iran Basins*, number April, pages 7–29. Geological Society of London Special Publication no. 312, London, 2009b.

Payne, J. L. and Clapham, M. E. 2012. End-Permian Mass Extinction in the Oceans: An Ancient Analog for the Twenty-First Century? *Annual Review of Earth and Planetary Sciences*, 40 (1): 89–111.

Payne, J. L., Lehrmann, D. J., Wei, J., Orchard, M. J., Schrag, D. P., and Knoll, A. H. 2004. Large perturbations of the carbon cycle during recovery from the end-permian extinction. *Science*, 305(5683): 506–509.

Pietzner, H., Vahl, J., Werner, H., and Ziegler, W. 1968. Zur chemischen Zusammensetzung und Mikromorphologie der Conodonten. *Palaeontographica Abteilung A*, pages 115–152.

Polyakov, I. V., Timokhov, L. a., Alexeev, V. a., Bacon, S., Dmitrenko, I. a., Fortier, L., Frolov, I. E., Gascard, J.-C., Hansen, E., Ivanov, V. V., Laxon, S., Mauritzen, C., Perovich, D., Shimada, K., Simmons, H. L., Sokolov, V. T., Steele, M., and Toole, J. 2010. Arctic Ocean Warming Contributes to Reduced Polar Ice Cap. *Journal of Physical Oceanography*, 40(12): 2743–2756.

Price, G. D., Twitchett, R. J., Wheeley, J. R., and Buono, G. 2013. Isotopic evidence for long term warmth in the Mesozoic. *Scientific reports*, 3: 1438.

Rampino, M. R. and Caldeira, K. 2005. Major perturbation of ocean chemistry and a 'Strangelove Ocean' after the end-Permian mass extinction. *Terra Nova*, 17(6): 554–559.

Raymo, M. E., Ruddiman, W. F., and Froelich, P. N. 1988. Influence of late Cenozoic mountain building on ocean geochemical cycles. *Geology*, 16(7): 649–653.

Reichow, M. K., Pringle, M., Al'Mukhamedov, A., Allen, M., Andreichev, V., Buslov, M., Davies, C., Fedoseev, G., Fitton, J., Inger, S., Medvedev, A., Mitchell, C., Puchkov, V., Safonova, I., Scott, R., and Saunders, A. 2009. The timing and extent of the eruption of the Siberian Traps large igneous province: Implications for the end-Permian environmental crisis. *Earth and Planetary Science Letters*, 277(1-2): 9–20.

Renne, P. R. and Basu, A. R. 1991. Siberian Traps Flood Basalts. *Science*, 253(11): 176–179.

Renne, P. R., Melosh, H. J., Farley, K. A., Reimold, W. U., Koeberl, C., Rampino, M. R., Kelly, S. P., and Ivanov, B. A. 2004. Is bedout an impact Crater? Take 2. *Science*, 306(5696): 611–612.

Renne, P. R., Deino, A. L., Hilgen, F. J., Kuiper, K. F., Mark, D. F., Mitchell, W. S., Morgan, L. E., Mundil, R., and Smit, J. 2013. Time scales of critical events around the Cretaceous-Paleogene boundary. *Science*, 339(6120): 684–7.

Retallack, G. J. 1995. Permian-triassic life crisis on land. *Science*, 267(5194): 77–80.

Retallack, G. J. and Jahren, a. H. 2008. Methane Release from Igneous Intrusion of Coal during Late Permian Extinction Events. *The Journal of Geology*, 116(1): 1–20.

Retallack, G. J. and Krull, E. S. 2006. Carbon isotopic evidence for terminal-Permian methane outbursts and their role in extinctions of animals, plants, coral reefs, and peat swamps. *Geological Society of America Special Papers*, 399: 249–268.

Richoz, S., Krystyn, L., Baud, A., Brandner, R., Horacek, M., and Mohtat-Aghai, P. 2010. Permian–Triassic boundary interval in the Middle East (Iran and N. Oman): Progressive environmental change from detailed carbonate carbon isotope marine curve and sedimentary evolution. *Journal of Asian Earth Sciences*, 39(4): 236–253.

Rostovtsev, K. O. and Azaryan, N. R. The Permian-Triassic Boundary in Transcaucasia. In *Permian Triassic Systems and Their Mutual Boundary*, pages 89–99. Canadian Society of Petroleum Geologists Special Memoir 2, 1973.

Rothman, D. H., Fournier, G. P., French, K. L., Alm, E. J., Boyle, E. A., Cao, C., and Summons, R. E. 2014. Methanogenic burst in the end-Permian carbon cycle. *Proceedings of the National Academy of Sciences of the United States of America*, 111(15): 5462–7.

Ruhl, M., Bonis, N. R., Reichart, G.-J., Sinninghe Damsté, J. S., and Kürschner, W. M. 2011. Atmospheric carbon injection linked to end-Triassic mass extinction. *Science*, 333(6041): 430–4.

Ruzhencev, V., Sarytcheva, T., and Shevyrev, A. Biostratigraficheskie vyvody. In Ruzhencev, V. and Sarytcheva, T., editors, *Razvitie i smena morskikh organizmov na Rubezhe Paleozoya i Mezozoya.*, pages 93–116. Trudy Paleontologicheskogo Instituta Akademiya Nauk SSSR, 108 edition, 1965.

Scheffer, M., Bascompte, J., Brock, W. A., Brovkin, V., Carpenter, S. R., Dakos, V., Held, H., van Nes, E. H., Rietkerk, M., and Sugihara, G. 2009. Early-warning signals for critical transitions. *Nature*, 461(7260): 53–9.

Schenck, H. G., Hedberg, H., Tomlinson, C., Eaton, J., and White, R. T. 1941. Stratigraphic Nomenclature:. *AAPG Bulletin*, 25(12): 2195–2211.

Schindewolf, O. 1954. Ueber die moeglichen Ursachen der grossen erdgeschichtlichen Faunenschnitte. *Neues Jahrbuch fuer Geologie und Palaeontologie Monatshefte*, 10: 457–465.

Schlanger, S. and Jenkyns, H. C. 1976. Cretaceous anoxic events: Causes and consequences. *Geologie en Mijnbouw*, 55: 179–184.

Schneebeli-Hermann, E., Kurschner, W. M., Hochuli, P. A., Ware, D., Weissert, H., Bernasconi, S. M., Roohi, G., Ur-Rehman, K., Goudemand, N., and Bucher, H. 2013. Evidence for atmospheric carbon injection during the end-Permian extinction. *Geology*, 41(5): 579–582.

Sengör, A. 1979. Mid-Mesozoic closure of Permo-Triassic Tethys and its implications. *Nature*, 279: 590–593.

Sephton, M. a., Looy, C. V., Brinkhuis, H., Wignall, P. B., de Leeuw, J. W., and Visscher, H. 2005. Catastrophic soil erosion during the end-Permian biotic crisis. *Geology*, 33(12): 941–944.

Sepkoski Jr., J. J. 1984. A Kinetic Model of Phanerozoic Taxonomic Diversity. III. Post-Paleozoic Families and Mass Extinctions. *Paleobiology*, 10(2): 246–267.

Shackleton, N. J. and Opdyke, N. D. 1973. Oxygen isotope and palaeomagnetic stratigraphy of Equatorial Pacific core V28-238: Oxygen isotope temperatures and ice volumes on a 105 year and 106 year scale. *Quaternary Research*, 3(1): 39–55.

Shen, J., Algeo, T. J., Zhou, L., Feng, Q., Yu, J., and Ellwood, B. 2012. Volcanic perturbations of the marine environment in South China preceding the latest Permian mass extinction and their biotic effects. *Geobiology*, 10(1): 82–103.

Shen, S.-z. and Mei, S.-l. 2010. Lopingian (Late Permian) high-resolution conodont biostratigraphy in Iran with comparison to South China zonation. *Geological Journal*, 45(2-3): 135–161.

Shen, S.-z., Crowley, J. L., Wang, Y., Bowring, S. a., Erwin, D. H., Sadler, P. M., Cao, C.-q., Rothman, D. H., Henderson, C. M., Ramezani, J., Zhang, H., Shen, Y., Wang, X.-d., Wang, W., Mu, L., Li, W.-z., Tang, Y.-g., Liu, X.-l., Liu, L.-j., Zeng, Y., Jiang, Y.-f., and Jin, Y.-g. 2011. Calibrating the end-Permian mass extinction. *Science*, 334(6061): 1367–72.

Sobolev, S. V., Sobolev, A. V., Kuzmin, D. V., Krivolutskaya, N. a., Petrunin, A. G., Arndt, N. T., Radko, V. a., and Vasiliev, Y. R. 2011. Linking mantle plumes, large igneous provinces and environmental catastrophes. *Nature*, 477(7364): 312–6.

Song, H., Tong, J., Algeo, T. J., Song, H., Qiu, H., Zhu, Y., Tian, L., Bates, S., Lyons, T. W., Luo, G., and Kump, L. R. 2014. Early Triassic seawater sulfate drawdown. *Geochimica et Cosmochimica Acta*, 128: 95–113.

Stampfli, G. M. and Borel, G. 2002. A plate tectonic model for the Paleozoic and Mesozoic constrained by dynamic plate boundaries and restored synthetic oceanic isochrons. *Earth and Planetary Science Letters*, 196(1): 17–33.

Stepanov, D., Golshani, F., and Stöcklin, J. 1969. Upper Permian and Permian-Triassic boundary in North Iran. *Geological Survey of Iran, Report*, 12: 1–73.

Stocker, T. F., Dahe Qin, Plattner, G.-K., Tignor, M. M., Allen, S. K., Boschung, J., Nauels, A., Bex, V., Xia, Y., and Midgley, P. M., editors. *Climate change: The Physical Science Basis. Working Group 1 Contribution to the fifth Assessment Report of the Intergovernment Panel on Climate Change.* Cambridge University Press, 2013.

Stoyanow, A. 1910. On the character of the boundary of Palaeozoic and Mesozoic near Djulfa. *Zap Imp Sankt-Peterburgskago Miner Obshch Nov Ser*, (47): 61–135.

Strauss, H. 1999. Geological evolution from isotope proxy signals — sulfur. *Chemical Geology*, 161(1-3): 89–101.

Sun, Y., Joachimski, M. M., Wignall, P. B., Yan, C., Chen, Y., Jiang, H., Wang, L., and Lai, X. 2012. Lethally Hot Temperatures During the Early Triassic Greenhouse. *Science*, 338(6105): 366–370.

Svensen, H., Planke, S., Polozov, A. G., Schmidbauer, N., Corfu, F., Podladchikov, Y. Y., and Jamtveit, B. r. 2009. Siberian gas venting and the end-Permian environmental crisis. *Earth and Planetary Science Letters*, 277(3-4): 490–500.

Sweet, W. and Mei, S. Conodont succesion of Permian Lopingian and basal Triassic in Northwest Iran. In *Proceedings of the international conference on Pangea and the Paleozoic-Mesozoic transition*, volume 33, pages 43–47. China University of Geosciences Press, Wuhan, 1999.

Taraz, H., Golshani, F., Nakazawa, K., Sgimuzu, D., Bando, Y., Ishi, K.-i., Murata, M., Okimura, Y., Sakagami, S., Nakamura, K., and Tokuoka, T. 1981. The Permian and the Lower Triassic Systems in Abadeh Region, Central Iran. *Memoirs of the Faculty of Science, Kyoto University, Series of Geology and Mineralogy*, 47(2): 61–133.

Teichert, C., Kummel, B., and Sweet, W. 1973. Permian-Triassic strata, Kuh-e-Ali Bashi, northwestern Iran. *Bulletin of The Museum of Comparative Zoology*, 145: 359–472.

Thomas, D. B., McGoverin, C. M., Fordyce, R. E., Frew, R. D., and Gordon, K. C. 2011. Raman spectroscopy of fossil bioapatite — A proxy for diagenetic alteration of the oxygen isotope composition. *Palaeogeography, Palaeoclimatology, Palaeoecology*, 310(1-2): 62–70.

Torsvik, T. H. and Cocks, L. R. M. 2004. Earth geography from 400 to 250 Ma: a palaeomagnetic, faunal and facies review. *Journal of the Geological Society*, 161(4): 555–572.

Ward, P. D., Botha, J., Buick, R., De Kock, M. O., Erwin, D. H., Garrison, G. H., Kirschvink, J. L., and Smith, R. 2005. Abrupt and gradual extinction among Late Permian land vertebrates in the Karoo basin, South Africa. *Science (New York, N.Y.)*, 307(5710): 709–714.

Wignall, P. B. 2007. The End-Permian mass extinction – how bad did it get? *Geobiology*, 5(4): 303–309.

Wignall, P. B. and Hallam, A. 1992. Anoxia as a cause of the Permian/Triassic mass extinction: facies evidence from northern Italy and the western United States. *Palaeogeography Palaeoclimatology Palaeoecology*, 93(1-2): 21–46.

Wignall, P. B. and Twitchett, R. J. 1996. Oceanic Anoxia and the End Permian Mass Extinction. *Science*, 272(5265): 1155–1158.

Winguth, A. M. and Winguth, C. 2013. Simulated Hothouse Climate at the P-Tr and implications for the mass extinction (Invited). *AGU Fall Meeting Abstracts*, 32C: 04.

Winguth, a. M. E., Heinze, C., Kutzbach, J. E., Maier-Reimer, E., Mikolajewicz, U., Rowley, D., Rees, A., and Ziegler, A. M. 2002. Simulated warm polar currents during the middle Permian. *Paleoceanography*, 17(4): 9–1.

Wotte, T., Shields-Zhou, G. a., and Strauss, H. 2012a. Carbonate-associated sulfate: Experimental comparisons of common extraction methods and recommendations toward a standard analytical protocol. *Chemical Geology*, 326-327: 132–144.

Wotte, T., Strauss, H., Fugmann, A., and Garbe-Schönberg, D. 2012b. Paired δ34S data from carbonate-associated sulfate and chromium-reducible sulfur across the traditional Lower–Middle Cambrian boundary of W-Gondwana. *Geochimica et Cosmochimica Acta*, 85: 228–253.

Yin, H., Zhang, K., Tong, J., Yang, Z., and Wu, S. 2001. The global stratotype section and point (GSSP) of the Permian-Triassic boundary. *Episodes*, 24(2): 102–114.

Yuan, D.-x., Shen, S.-z., Henderson, C. M., Chen, J., Zhang, H., and Feng, H.-z. 2014. Revised conodont-based integrated high-resolution timescale for the Changhsingian Stage and end-Permian extinction interval at the Meishan sections, South China. *Lithos*, 204: 220–245.

Zachos, J. C., Stott, L. D., and Lohmann, K. C. 1994. Evolution of early Cenozoic marine temperatures. *Paleoceanography*, 9(2): 353–387.

Zakharov, Y. The Permo–Triassic boundary in the southern and eastern USSR and its intercontinental correlation. In Sweet, W., Yang, Z., Dickins, J., and Yin, H., editors, *Permo–Triassic events in the eastern Tethys.*, pages 46–55. Cambridge University Press, Cambridge, 1992.

7 Papers

Paper 1

High-resolution stratigraphy of the Changhsingian (Late Permian) successions of NW Iran and the Transcaucasus based on lithological features, conodonts and ammonoids

Ghaderi, A. Leda, L., Schobben, M., Korn, D., Ashouri, A.R. (2014) High-resolution stratigraphy of the Changhsingian (Late Permian) successions of NW Iran and the Transcaucasus based on lithological features, conodonts and ammonoids Ghaderi, Fossil Record, 17, pp: 41-57, www.fossrec.net/17/41/2014/, doi:10.5194/fr-17-41-2014

cover shows the Zal section (NW Iran)

Foss. Rec., 17, 41–57, 2014
www.foss-rec.net/17/41/2014/
doi:10.5194/fr-17-41-2014

Fossil Record museum für naturkunde
Open Access berlin

High-resolution stratigraphy of the Changhsingian (Late Permian) successions of NW Iran and the Transcaucasus based on lithological features, conodonts and ammonoids

A. Ghaderi[1], **L. Leda**[2], **M. Schobben**[2], **D. Korn**[2], **and A. R. Ashouri**[1]

[1]Department of Geology, Faculty of Sciences, Ferdowsi University, Mashhad, Iran
[2]Museum für Naturkunde, Leibniz-Institut für Evolutions- und Biodiversitätsforschung,
Invalidenstraße 43, 10115 Berlin, Germany

Correspondence to: A. Ghaderi (abbas.ghaderi@gmail.com)

Received: 31 December 2013 – Revised: 8 February 2014 – Accepted: 10 February 2014 – Published: 7 March 2014

Abstract. The Permian–Triassic boundary sections in northwestern Iran belong to the most complete successions, in which the largest mass extinction event in the history of the Earth can be studied. We investigated the Changhsingian stage in six sections in the area of Julfa (Aras Valley) for their lithology, conodonts and ammonoids. Revision of the biostratigraphy led to the separation of 10 conodont zones (from bottom to top *Clarkina orientalis*–*C. subcarinata* interval zone, *C. subcarinata*, *C. changxingensis*, *C. bachmanni*, *C. nodosa*, *C. yini*, *C. abadehensis*, *C. hauschkei*, *Hindeodus praeparvus*–*H. changxingensis* and *Merrilina ultima*–*Stepanovites* ?*mostleri* zones) and 8 ammonoid zones (from bottom to top *Iranites transcaucasius*–*Phisonites triangulus*, *Dzhulfites nodosus*, *Shevyrevites shevyrevi*, *Paratirolites trapezoidalis*, *P. waageni*, *Stoyanowites dieneri*, *Abichites stoyanowi* and *Arasella minuta* zones). The new ammonoid genera *Stoyanowites* and *Arasella* are described.

1 Introduction

Permian–Triassic boundary sections in the vicinity of Julfa (East Azerbaijan Province, NW Iran) play a key role in the subdivision of the Late Permian sedimentary successions of the Palaeotethyan realm (Figs. 1, 2). The Changhsingian (latest Permian) deposits were accumulated on an outer shelf (Leda et al., 2014); they display a continuous succession and contain a considerably rich pelagic fauna consisting of conodonts and cephalopods, allowing for the separation of a number of biozones within this time unit.

While time-equivalent sedimentary successions in other regions such as South China have been studied in great detail (e.g. Sun et al., 2012; Romano et al., 2013, for more literature), the Transcaucasian and NW Iranian sections are known from fewer studies. Although sections in this region have attracted scientists for a long time (Abich, 1878; Frech and Arthaber, 1900; Bonnet and Bonnet, 1947), detailed lithostratigraphical and biostratigraphical studies of the Changhsingian sections in the Transcaucasus and NW Iran have only rarely been carried out. An exception is the conodont succession in these outcrops, which has been studied in greater detail by Kozur et al. (1980), Sweet and Mei (1999a, b), Partoazar (2002), Kozur (2004, 2005, 2007), Henderson et al. (2008) and Shen and Mei (2010). In addition, several investigations focused on the stable isotopes of the NW Iranian sections, such as δ^{13}C (Baud et al., 1989; Korte et al., 2004; Richoz, 2006; Korte and Kozur, 2010; Richoz et al., 2010), δ^{18}O (Schobben et al., 2013) and a Ce anomaly (Kakuwa and Matsumoto, 2006). These studies demonstrate the high potential for a subdivision of the Changhsingian stage of sections in the Palaeotethys, comparable or even finer than in the more intensely studied sections in South China.

In the following we present a correlation of lithostratigraphical data and the distribution of conodonts and ammonoids. It will be shown that the Changhsingian stage cannot only be subdivided into a number of zones by means of conodonts, but also of ammonoids. These two biostratigraphical subdivisions are supported by lithological characteristics.

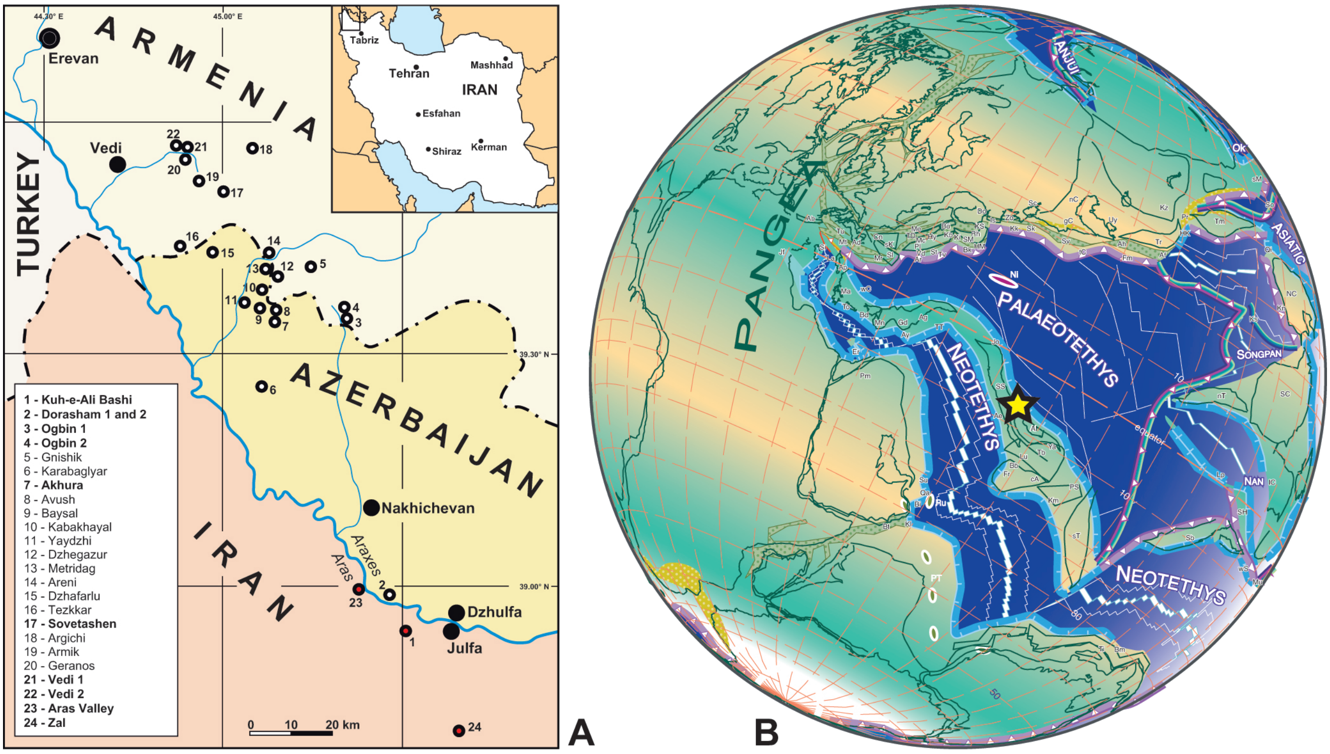

Figure 1. **(A)** Geographical position of Permian–Triassic boundary sections in the Transcaucasus and in NW Iran (after Arakelyan et al., 1965); sections investigated in this study are highlighted. **(B)** Palaeogeographic position of the Julfa area (after Stampfli and Borel, 2002).

Figure 2. The Permian–Triassic boundary sections in the Ali Bashi Mountains, NW Iran.

2 Localities

Sedimentary rocks representing the transition from the Palaeozoic into the Mesozoic in uninterrupted succession are very well exposed in the regions of Transcaucasia in Armenia, Azerbaijan and NW Iran (Fig. 1). The outcrops of Late Permian to Early Triassic successions studied by the authors are located south of the Aras (Araxes) River, which coincides with the political boundary between Iran and the province of Nakhichevan (Azerbaijan). The exposures are located west or south of the two neighbouring towns Dzhulfa (or Culfa, Nakhichevan province; Azerbaijan) and Julfa (or Jolfa, East Azerbaijan Province, Iran). We investigated and measured six fossil-rich pelagic Permian–Triassic (P–Tr) boundary sections in greater detail and recorded their petrography and carbonate microfacies as well as their conodont and ammonoid content:

(1) Aras Valley (39.0154° N, 45.4345° E): this section was described for the first time by Leda et al. (2014); it is situated about 19 km WNW of the towns of Dzhulfa and Julfa in a dry small side valley west of the Aras (Araxes) River. The new section has a position approximately 2 km northwest of the Dorasham I section of Ruzhencev et al. (1965). A nearly complete Wuchiapingian and Changhsingian succession is exposed at this locality with a considerably good outcrop of the lower, shale-dominated part of the Changhsingian, a perfect outcrop of the *Paratirolites* Limestone over an extension of 200 m and a rather good exposure of the “boundary clay” (renamed Aras Member here).

(2) P–Tr boundary beds crop out in several parallel sections over a range of about 1.5 km in the Ali Bashi Mountains (i.e. Kuh-e-Ali Bashi) 9 km west of Julfa (Fig. 1). The sedimentary and faunal succession and the thickness of the various rock units principally parallel the section in the Aras Valley. Four of the numerous sections were measured and sampled by us:

(a) Ali Bashi 1 section (38.9397° N, 45.5197° E) = Locality 1 of Teichert et al. (1973): it is the section described in detail by Teichert et al. (1973, p. 377). The section begins with red nodular marls and limestone beds of the upper part of the Wuchiapingian Julfa Formation (*Vedioceras* beds) and continues into the Early Triassic Elikah Formation. The entire Changhsingian succession is exposed in this section and allows for a detailed study.

(b) Ali Bashi 4 section (38.9416° N, 45.5158° E) = Locality 4 of Teichert et al. (1973): it is the section described in detail by Stepanov et al. (1969) and Ghaderi et al. (2013); Teichert et al. (1973, p. 380) gave a brief description of the lower part of the section (for a discussion of the correlation of the Ali Bashi 1 and Ali Bashi 4 sections, see Leda et al., 2014, and particularly Ghaderi et al., 2013). It is the most complete of all the sections in the Ali Bashi Mountains (Fig. 3), beginning with the early Wuchiapingian *Codonofusiella* beds and ranging into the Elikah Formation. Unfortunately, the lower shaly part of the Ali Bashi Formation is largely covered by scree and hence accessible only by trenching.

(c) Ali Bashi N section (38.9456° N, 45.5137° E): the newly discovered section begins with poor outcrops in the lower part of the Ali Bashi Formation and ends in the Elikah Formation. The *Paratirolites* Limestone is well-exposed over a distance of 200 m.

(d) Ali Bashi M section (38.9354° N, 45.5238° E) = Locality 1 with the sections I–IV of Kozur (2005): the outcrop in the main valley of the Ali Bashi Mountains shows rather poor outcrop conditions, but the complete Changhsingian interval can be measured.

(3) Zal: this section is situated 22 km SSW of Julfa and 2.2 km NNW of the village of Zal (38.7327° N, 45.5795° E). Columnar sections have been published by Korte et al. (2004), Kozur (2005, 2007) and Shen and Mei (2010). Lasemi et al. (2007) investigated the sedimentology of the Wuchiapingian succession. It is one of the best outcrops of the Permian–Triassic transitional beds in NW Iran and exposes the entire Late Permian and a large part of the Early Triassic succession.

3 Lithostratigraphy (Ghaderi, Leda, Schobben, Korn)

Three lithological units represent the Changhsingian stage in the Transcaucasus and NW Iran: from bottom to top, a so far unnamed shaly member (described as Zal Member here), the *Paratirolites* Limestone (both together composing the Ali Bashi Formation), and the “boundary clay” (described here as the Aras Member and is the base of the mainly Triassic Elikah Formation). This lithological succession has already been outlined by a number of previous studies; Arakelyan et al. (1965) as well as Rostovtsev and Azaryan (1973) described the sections in Armenia and the Nakhichevan province of Azerbaijan (including the Dorasham sections), and Stepanov et al. (1969) as well as Teichert et al. (1973) described the Ali Bashi section.

In the following, we discuss the three rock units in terms of their lithological features in ascending order (Fig. 3).

1. Ali Bashi Formation – two members compose this formation: a lower shale-dominated and a so far unnamed member described here as the Zal Member, and an upper carbonate-dominated member, for which the name *Paratirolites* Limestone has been coined.

(a) Zal Member (with the type locality in the Zal section 2.2 km NNW of the village of Zal) – the member has a thickness of 12.5 to 20 m in the vicinity of Julfa, i.e. 20 m in the Dorasham section according to Arakelyan et al. (1965), 13.5 m in the Aras Valley section, 18 m in the Ali Bashi 4 section according to Stepanov et al. (1969), 12.5 m in the Ali Bashi 1 section according Teichert et al. (1973) as well as

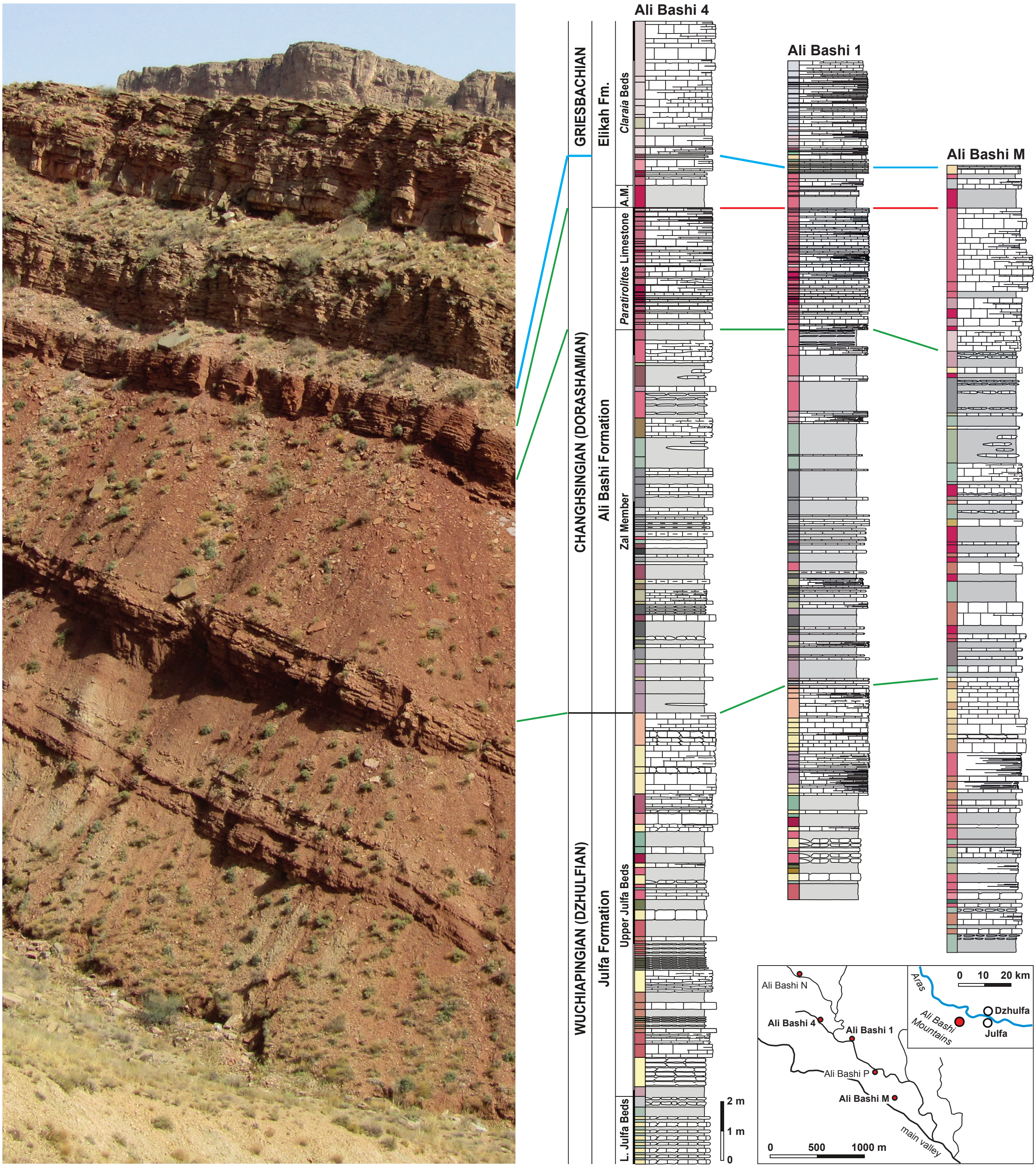

Figure 3. Ali Bashi 4 section and columnar sections of the entire Changhsingian in Ali Bashi 4, Ali Bashi 1 and Ali Bashi M sections with their conodont zonation.

new studies, and 16 m in the Zal section. All the mentioned sections show a very similar rock succession, which is dominated by dark-grey shales at the base turning violet-reddish towards the top. Marly and nodular limestone beds are intercalated and occur usually in packages; they are grey at the base of the member and red to pink at the top. The member is only occasionally rich in macrofossils, of which ammonoids, nautiloids and small brachiopods are the most common.

In the sections in Armenia and the northern part of Nakhichevan, the member is extremely reduced in thickness (Arakelyan et al., 1965). The shales are nearly absent there with the result that the entire member has a thickness of only 2–5 m in the Armenian sections of Vedi, Zangakatun (i.e. Khanakhchi or Sovetashen in the literature), and Ogbin (Rostovtsev and Azaryan, 1973).

(b) *Paratirolites* Limestone Member – the *Paratirolites* Limestone has a similar lithological appearance in all studied sections; usually it shows thicknesses ranging between about 4 and 5 m (Aras Valley: 4.60 m, Ali Bashi N: 4.50 m, Ali Bashi 4: 4.15 m, Ali Bashi 1: 4.15 m, Zal: 5.10 m). The unit is composed of 5 to 30 cm-thick, red nodular marly limestone beds with a $CaCO_3$ content ranging between 80 and 96 weight % (Fig. 4). It is typically developed in the Julfa area (Stepanov et al., 1969; Teichert et al., 1973), but similar sedimentary rocks occur in central Iran (e.g. Taraz, 1971; Taraz et al., 1981; Leda et al., 2014).

The carbonate microfacies of the *Paratirolites* Limestone has been intensely described by Leda et al. (2014); there it was shown that the unit is largely uniform but can be separated into two subunits because of microfacies characters:

(1) The base of the *Paratirolites* Limestone shows some rather compact limestone beds of 10–30 cm thickness; they are clearly separated by red shale and marl horizons ($CaCO_3$ down to 54 weight %). Distinct limestone beds can easily be correlated between neighbouring sections. The shale intercalations, which become much less prominent higher in the section, occasionally contain limestone nodules. In the middle of the *Paratirolites* Limestone (i.e. about 1.90 to 2.00 m below the top of the unit), a conspicuous limestone bed occurs in the Aras and Ali Bashi sections. This bed differs, in its much lighter colour and denser matrix, from the other beds of the *Paratirolites* Limestone. It works as a lithological index horizon in all studied sections around Julfa (Fig. 4). The clear separation between limestone beds and shale intercalations at the base of the *Paratirolites* Limestone diminishes towards the top of the member, but here an alternation of more compact limestone beds and horizons richer in clay can be recorded.

(2) The upper part (0.30 m thick in the Ali Bashi 1 section) of the *Paratirolites* Limestone shows evidence of stratigraphical condensation; it contains isolated nodules, which occasionally possess black ferruginous and manganese coatings and are preserved as hard-ground clasts (Leda et al., 2013).

A lithostratigraphical correlation of the sections of the *Paratirolites* Limestone in NW Iran can be performed by the use of limestone–clay alternations.

2. Elikah Formation – the majority of this formation belongs to the Triassic, and only the lowermost portion, described as “boundary clay” by Leda et al. (2014), is of Late Permian age. This will be described here as the Aras Member.

Aras Member (with the type locality in the Aras Valley section) – these beds represent the transition from the Permian into the Triassic; the shale-dominated member marks a drastic reduction of $CaCO_3$, down to 15–30 weight %. A detailed description of the occurrence in the Dorasham 2 section was provided by Zakharov (1992), and conodont faunas from the unit in the Ali Bashi Mountains were described by Kozur (2004, 2005, 2007). The carbonate microfacies and the fossil inventory were outlined by Leda et al. (2014).

The member has a variable thickness in the investigated sections and range from 0.50 m in the Zal section to 3.00 m in the Aras Valley section. It is largely composed of dark red to brownish shales with occasionally occurring greenish-grey intervals and thin marly limestone intercalations towards the top of the unit. A 10-centimetre-thick grey nodular limestone bed occurs as a lenticular intercalation in the Zal section.

The Aras Member is poor in macrofossils. Leda et al. (2014) showed that concentrations of sponge spicules and ostracods occur occasionally in thin carbonate-enriched horizons in the middle and upper part of the member; further macrofossils are rare gastropods and bivalves. Zakharov (1992) investigated the unit, which is well-exposed in the Dorasham section, in greater detail.

4 Conodont stratigraphy (Ghaderi, Ashouri)

The conodont biostratigraphy of the Changhsingian deposits of north-western Iran has been published in several pioneering papers (e.g. Sweet in Teichert et al., 1973; Kozur, 1975, 1978). A more precise resolution followed thereafter by Kozur (2004, 2005) and Shen and Mei (2010). Kozur (2005) subdivided the Changhsingian successions of north-west and central Iran into 10 conodont biozones, in ascending order: the *Clarkina hambastensis*, *C. subcarinata*, *C. bachmanni*, *C. nodosa*, *C. changxingensis*–*C. deflecta*, *C. zhangi*, *C. iranica*, *C. hauschkei*, *C. meishanensis*–*Hindeodus praeparvus* and *Merrillina ultima*–*Stepanovites* ?*mostleri*zones (Fig. 5).

According to Kozur (2005), the *C. hambastensis* and *C. subcarinata* biozones were recognized in the shaly unit (here described as Zal Member) of the Ali Bashi Formation. The *Paratirolites* Limestone includes the next six conodont biozones, and the upper two biozones (*C. meishanensis*–*H. praeparvus* and *Merrillina ultima*–*Stepanovites* ?*mostleri*) are situated within the boundary clay (here described as the Aras Member).

Later, Shen and Mei (2010) re-evaluated all collected and reported conodont materials by Teichert et al. (1973), ICRG

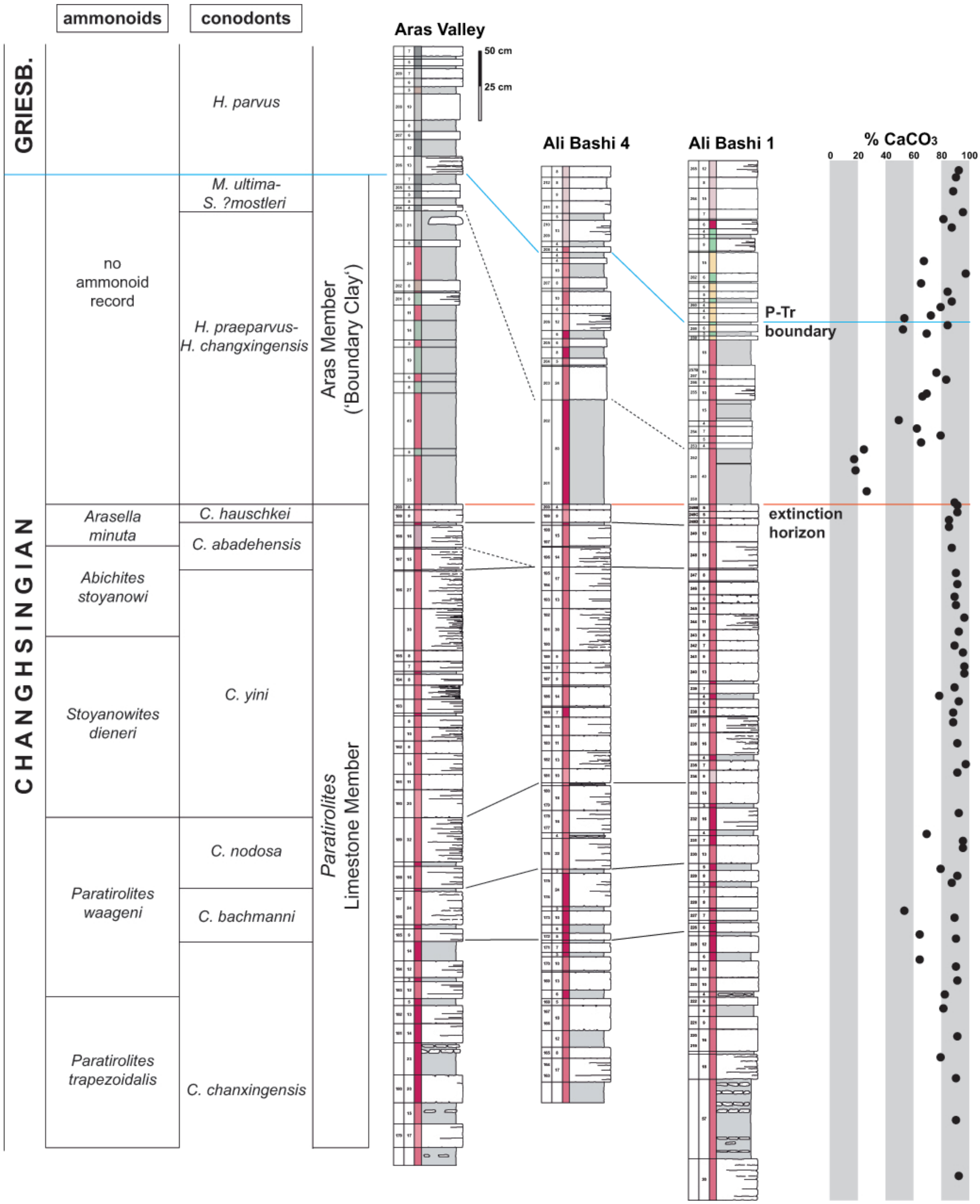

Figure 4. Columnar sections of the *Paratirolites* Limestone in the Aras Valley, Ali Bashi 4 and Ali Bashi 1 sections with their conodont and ammonoid zonation as well as the weight % of $CaCO_3$ (determined by the weight loss–acid digestion method) of the Ali Bashi 1 section.

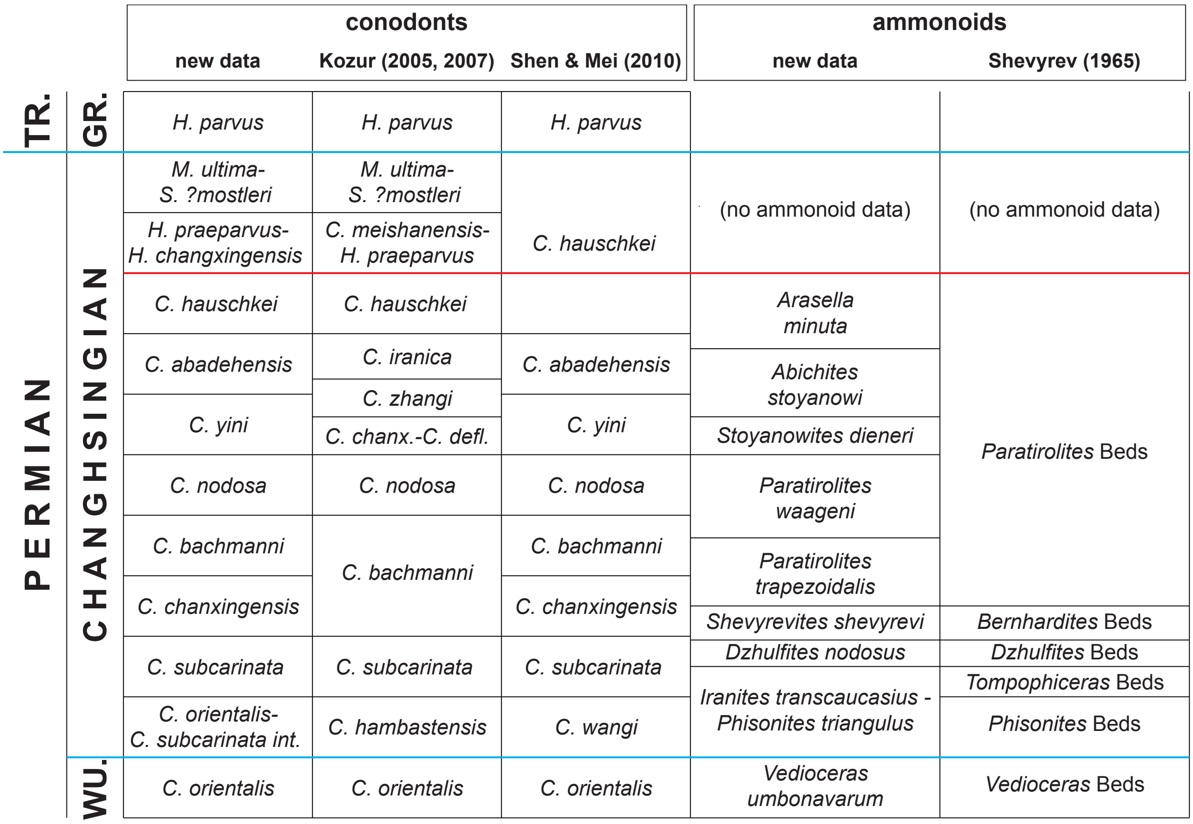

		conodonts			ammonoids	
		new data	Kozur (2005, 2007)	Shen & Mei (2010)	new data	Shevyrev (1965)
TR.	GR.	*H. parvus*	*H. parvus*	*H. parvus*		
PERMIAN	CHANGHSINGIAN	*M. ultima-* *S. ?mostleri*	*M. ultima-* *S. ?mostleri*	*C. hauschkei*	(no ammonoid data)	(no ammonoid data)
		H. praeparvus- *H. changxingensis*	*C. meishanensis-* *H. praeparvus*			
		C. hauschkei	*C. hauschkei*		*Arasella minuta*	*Paratirolites* Beds
		C. abadehensis	*C. iranica*	*C. abadehensis*	*Abichites stoyanowi*	
			C. zhangi			
		C. yini	*C. chanx.-C. defl.*	*C. yini*	*Stoyanowites dieneri*	
		C. nodosa	*C. nodosa*	*C. nodosa*	*Paratirolites waageni*	
		C. bachmanni	*C. bachmanni*	*C. bachmanni*	*Paratirolites trapezoidalis*	
		C. chanxingensis		*C. chanxingensis*	*Shevyrevites shevyrevi*	*Bernhardites* Beds
		C. subcarinata	*C. subcarinata*	*C. subcarinata*	*Dzhulfites nodosus*	*Dzhulfites* Beds
						Tompophiceras Beds
		C. orientalis- *C. subcarinata int.*	*C. hambastensis*	*C. wangi*	*Iranites transcaucasius - Phisonites triangulus*	*Phisonites* Beds
	WU.	*C. orientalis*	*C. orientalis*	*C. orientalis*	*Vedioceras umbonavarum*	*Vedioceras* Beds

Figure 5. The correlation of the conodont schemes by Kozur (2005, 2007), Shen and Mei (2010) and own results with the ammonoid stratigraphy by Shevyrev (1965) and own results.

(Iranian-Chinese Research Group) (1995), Yazdi and Shirani (2002) and Kozur (2004, 2005, 2007) based on the sample-population approach. They proposed eight biozones for the Changhsingian deposits of Iran, thus differing from Kozur's zonation. Their conodont biozones in ascending order are as follows: the *Clarkina wangi*, *C. subcarinata*, *C. changxingensis*, *C. bachmanni*, *C. nodosa*, *C. yini*, *C. abadehensis* and *C. hauschkei* zones (Fig. 5).

In their subdivision, the *C. wangi* and *C. subcarinata* zones are located in the Zal Member and the other biozones are distinguishable in the *Paratirolites* Limestone and the boundary clay (Aras Member).

We studied four sections by bed-by-bed sampling: the Aras Valley section as well as the Ali Bashi section 4, 1 and M. Our investigations, which apply the sample-population taxonomic approach (Mei et al., 2004), led to the separation of 10 conodont biozones for the Changhsingian sections of the Julfa area (Fig. 5, Table 1). Characteristic conodont specimens are illustrated in Fig. 6.

The zones are in ascending order:

1. *Clarkina orientalis–Clarkina subcarinata* interval zone (equivalent to the *C. wangi* Zone) – the new *C. orientalis–C. subcarinata* interval zone is defined in the sections near Julfa by the last occurrence of *C. orientalis* until the first occurrence of *C. subcarinata*.

The equivalent strata with this interval in the Meishan section (Zhejiang, South China) are regarded as *C. wangi* Zone by Mei et al. (2004) based on the first appearance of *C. wangi*, the base marker of Changhsingian stage. Jin et al. (2001) proposed the Global Boundary Stratotype Section and Point (GSSP) for the Wuchiapingian–Changhsingian stage boundary by the first appearance of *C. wangi* within the lineage from *C. longicuspidata* to *C. wangi* at Meishan section D above the flooding surface of the second parasequence in the Changxing Limestone.

This stage boundary was questioned by Kozur (2005), because he regarded *C. hambastensis* Kozur 2004 as the best index species for a definition of the Wuchiapingian–Changhsingian boundary. He therefore proposed the new *C. hambastensis* Zone based on the first appearance of *C. hambastensis* for the base of "Dorashamian" in the Hambast Mountains (Abadeh area, central Iran) instead of *C. wangi*, which was absent in his materials from Iran. However he reported the species *C. hambastensis* only from the Shahreza section and from sections V and VI of the Hambast Mountains, but not from the Julfa area.

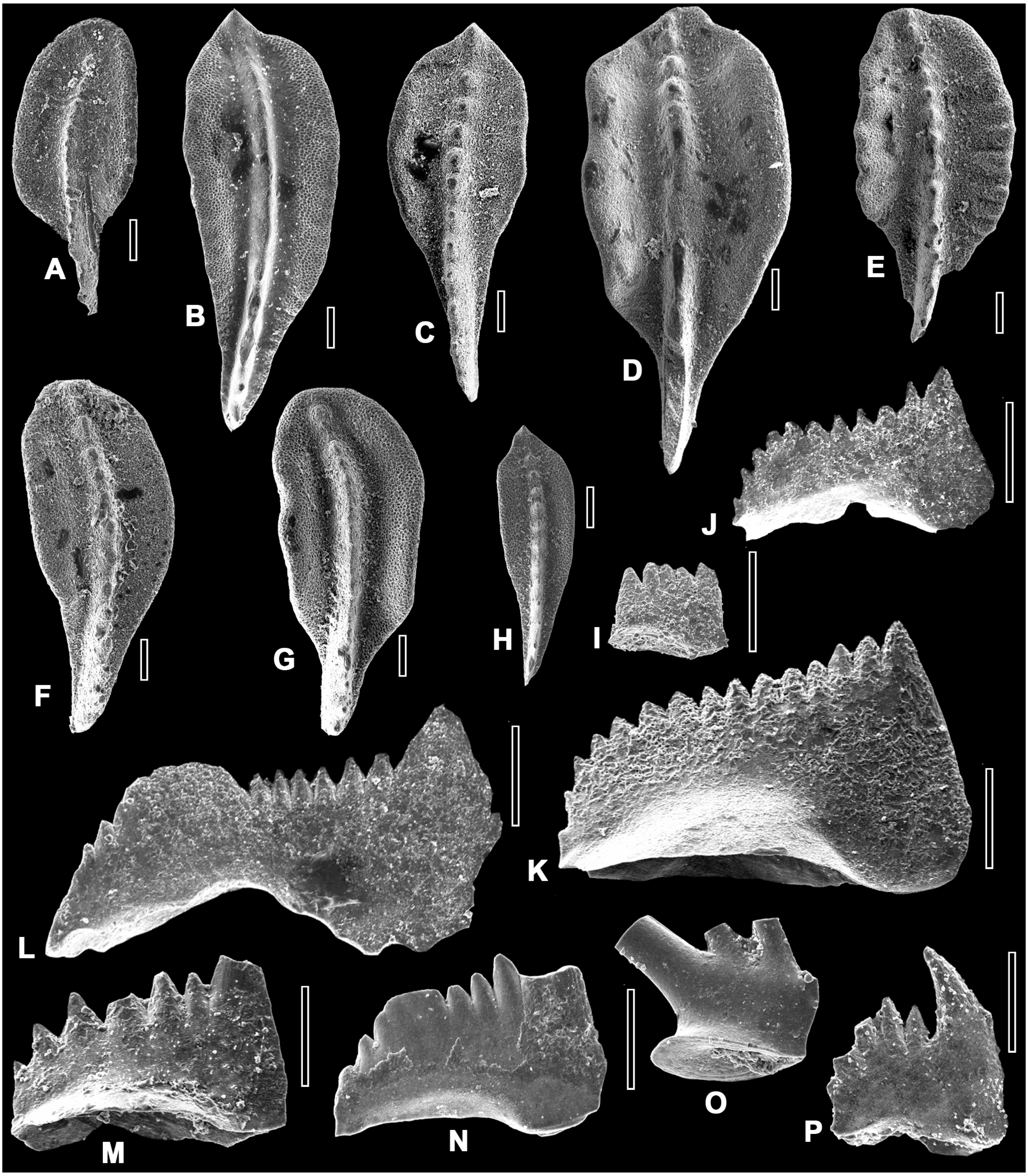

Figure 6.

Figure 6. Characteristic Changhsingian conodonts from the Julfa region (scale bars equal to 100 µm); all specimens stored in the collection of the Ferdowsi University, Mashhad. **(A)** *Clarkina orientalis* (Barskov and Koroleva, 1970); FUM#1J192.1; upper Julfa beds (*Vedioceras* beds), Ali Bashi 1 section. **(B)** *Clarkina subcarinata* Sweet, 1973; FUM#4J142.8; Zal Member (Ali Bashi Formation), Ali Bashi 4 section. **(C)** *Clarkina changxingensis* Wang and Wang, 1981; FUM#4J153.1; Zal Member (Ali Bashi Formation), Ali Bashi 4 section. **(D)** *Clarkina bachmanni* Kozur, 2004; FUM#AJ185.23; *Paratirolites* Limestone (Ali Bashi Formation), Aras Valley section. **(E)** *Clarkina nodosa* Kozur, 2004; FUM#G249.16; *Paratirolites* Limestone (Ali Bashi Formation), Ali Bashi M section. **(F)** *Clarkina yini* Mei, 1998; FUM#AJ192.4; *Paratirolites* Limestone (Ali Bashi Formation), Aras Valley section. **(G)** *Clarkina abadehensis* Kozur, 2004; FUM#1J248.9; *Paratirolites* Limestone (Ali Bashi Formation), Ali Bashi 1 section. **(H)** *Clarkina hauschkei* Kozur, 2004, FUM#1J249D.9; *Paratirolites* Limestone (Ali Bashi Formation), Ali Bashi 1 section. **(I)** *Hindeodus eurypyge* Nicoll, Metcalfe and Wang, 2002, FUM#1J255.7 (cusp broken); Zal Member (Ali Bashi Formation), Ali Bashi 1 section. **(J)** *Hindeodus typicalis* Sweet, 1970, FUM#G233.5; *Paratirolites* Limestone (Ali Bashi Formation), Ali Bashi M section. **(K)** *Hindeodus typicalis* Sweet, 1970, FUM#4J200.56; *Paratirolites* Limestone (Ali Bashi Formation), Ali Bashi 4 section. **(L)** *Hindeodus julfensis* Sweet, 1973, FUM#1J198.4; Zal Member (Ali Bashi Formation), Ali Bashi 4 section. **(M)** *Hindeodus praeparvus* Kozur, 1996, FUM#G274.6 (cusp broken); Aras Member (Elikah Formation), Ali Bashi M section. **(N)** *Hindeodus changxingensis* Wang, 1995, FUM#4J201.6 (cusp broken); Aras Member (Elikah Formation), Ali Bashi 4 section. **(O)** *Merrillina ultima* Kozur, 2004, FUM#AJ204.13; Aras Member (Elikah Formation), Aras Valley section. **(P)** *Hindeodus parvus* Kozur and Pjatakova, 1976, FUM#4J213.1; Elikah Formation; Ali Bashi 4 section.

Table 1. Thickness (in metres) of the conodont zones in sections in the area of Julfa.

Zone	Ali Bashi section 1	Ali Bashi section 4	Ali Bashi section M	Aras Valley
M. ultima–S. ?mostleri Zone	0.92	1.06	0.53	0.25
H. praeparvus–H. changxingensis Zone	0.40	0.80	0.65	2.30
C. hauschkei Zone	0.15	0.13	0.15	0.13
C. abadehensis Zone	0.31	0.30	0.35	0.18
C. yini Zone	1.51	1.55	1.50	1.95
C. nodosa Zone	0.58	0.62	0.45	1.25
C. bachmanni Zone	0.48	0.51	0.35	0.38
C. changxingensis Zone	6.70	6.72	6.95	4.30
C. subcarinata Zone	5.40	5.20	5.20	4.58
C. orientalis–C. subcarinata interval zone	0.85	1.10	0.90	1.65

Kozur (2005) suggested that a correlation of the Wuchiapingian–Changhsingian stage boundary of sections in Iran and South China is possible because *C. hambastensis* is also present in Changhsingian beds of the South Chinese intraplatform basins, where it was assigned to *C. wangi* by Jin et al. (2003). However, in the Iranian sections *C. hambastensis* appears somewhat earlier than true *C. wangi*, which is the marker for the base of the Changhsingian in China. Therefore, he proposed that this biozone is more complete in Iran, and the largest part of the *C. hambastensis* Zone is missing because of a gap in the Meishan section.

Henderson et al. (2008) confirmed the *C. wangi* Zone in the Zal section, but he did not provide any illustrations of the conodonts. The *C. wangi* Zone was also confirmed by Shen and Mei (2010) from sections in Iran, but again without any illustrations of the materials. In their paper (and in Nafi et al., 2006; Chen et al., 2008) *C. hambastensis* was regarded as a probable synonym of *C. wangi*. Shen and Mei (2010) indicated that *C. hambastensis* is less common in the population of *C. wangi* in South China. They wrote "if it can be established that *C. hambastensis* is more common in the sample-population of *C. wangi* in Iran than South China, *C. hambastensis* can be regarded as a subspecies or a geographical cline of *C. wangi*."

Our new investigations indicate there are no *C. hambastensis* or *C. wangi* specimens in the four investigated sections of the Julfa area. In the Ali Bashi sections 1 and 4 and Aras Valley, the *C. orientalis* Zone (equal to *Vedioceras* Zone according to the classical ammonoid stratigraphy) is overlain by 1–2 m of dark shale (base of the Ali Bashi Formation) with some intercalations of marly limestone. These are barren of clarkinids, but with many specimens of *H. typicalis*, *H. julfensis*, *Merrillina* sp. and some chondrichthyan teeth in all sections. The first carbonate rock unit above the mentioned shaly interval contains typical *C. subcarinata* specimens and a few other conodonts, but it is not possible to ascribe them to *C. wangi*.

We assume that there is no *C. wangi* or its probable synonym *C. hambastensis* in the sections of the Julfa area. At the same time, there are no traces of a sedimentary gap between the *C. orientalis* and *C. subcarinata* biozones. Hence, it would be possible to explain the lack of *C. wangi* with replacement by a hindeodid fauna due to changes in sedimentary facies and environmental conditions.

All sections in the Julfa area show that there are six short intervals within the Changhsingian, in which the clarkinid conodont fauna is replaced or strongly influenced by a hindeodid fauna or *Merrillina* sp. The first of these replacements is situated above the uppermost part of the Wuchiapingian succession, where the *C. orientalis* Zone is replaced by *H. typicalis*, *H. julfensis* and *Merrillina* sp. in the *C. orientalis*–*C. subcarinata* interval zone (equal to *C. wangi* Zone).

Comparison of the replacement horizons with the δ^{13}C curve of the Ali Bashi section 1 (Schobben et al., 2013) demonstrates minor to major accordance between the rise of hindeodid / clarkinid ratio (H/C ratio) and a negative excursion of the δ^{13}C curve. Faunal changes in these intervals were regarded as a replacement of a warm-water fauna by cool water forms (Kozur, 2005, 2007; Korte and Kozur, 2011). However, a correlation of H/C ratio and the δ^{18}O curve of the Ali Bashi section 1 (Schobben et al., 2013) cannot support this assumption.

According to Lai et al. (2001), the replacement of the *Clarkina* fauna by the *Hindeodus* fauna in P–Tr boundary deposits of the Meishan section is caused by the oxygen depletion in the basin, because clarkinids could not inhabit dysoxic–anoxic bottom waters. Lithology will support this idea, although at the moment we do not have enough measurements to state if anoxia or a change in the temperature from warm water to cool water in the *C. orientalis*–*C. subcarinata* interval zone caused the faunal replacement.

Lithological and palaeoenvironmental differences may explain the lack of *C. hambastensis* in the Julfa area and its appearance in the Shahreza and Hambast Mountain sections, which was reported by Kozur (2005). The lower shaly part of the Ali Bashi Formation in the Julfa area has carbonate equivalent intervals in the central Iran sections. Hence, there are no conspicuous changes in lithology and palaeoenvironmental conditions between the *Vedioceras* Zone and the *C. hambastensis* Zone in the Wuchiapingian–Changhsingian boundary interval in central Iran, and thus *C. hambastensis* could be present.

2. *Clarkina subcarinata* Zone – the base of this zone is defined by the first occurrence of the nominal species *C. subcarinata*, which was first recognized by Sweet in Teichert et al. (1973). In north-western Iran and Meishan, this zone is succeeded by the *C. changxingensis* Zone. However, Kozur (2005) placed the *C. bachmanni* Zone directly on top of the *C. subcarinata* Zone in Iran. *C. subcarinata* gradually evolves into *C. changxingensis* by reduction of posterior denticles and the gradual development of a gap between the cusp and posterior denticles (Mei et al., 1998a, and Shen and Mei, 2010).

The second and third replacement instances of clarkinids by hindeodids occur in the lower and upper parts of the *C. subcarinata* Zone. These replacements are supported by the dominance of *H. typicalis* and *H. julfensis* over *C. subcarinata* communities.

3. *Clarkina changxingensis* Zone – the first occurrence of *C. changxingensis* marks the base of this zone. Wang and Wang in Zhao et al. (1981) first defined the *C. changxingensis* Zone in the Meishan section. Elements of *C. changxingensis* are differentiated from those of its probable predecessor, *C. subcarinata*, by the relatively more strongly reduced posterior denticles of many individuals and, thus, by a more distinct depression between the cusp and posterior denticles in the carina profile (Shen and Mei, 2010).

The numbers of *H. typicalis* and *H. julfensis* increased in the fourth H/C replacement in the upper part of the *C. changxingensis* Zone. The *C. bachmanni* Zone begins directly above this major replacement.

4. *Clarkina bachmanni* Zone – in the Meishan section, the *C. changxingensis* Zone is succeeded by the *C. yini* Zone (Mei et al., 1998b). Kozur (2005) established the *C. bachmanni* Zone based on the full range of the nominate species *C. bachmanni* for the sections in central and north-western Iran. Because of the absence of *C. bachmanni* in the equivalent interval of the Meishan section, Kozur (2005) interpreted a gap in this section. Later, *C. bachmanni*, which has a short and broad platform with posterior pointed protrusion of the carina, was considered as a transitional morphotype between the round and narrow morphotypes of *C. yini* by Chen et al. (2008) and as a geographical variant of *C. yini* by Shen and Mei (2010). Individuals of *C. bachmanni* are very common in the sections of the Julfa area, especially in the Ali Bashi Mountains.

5. *Clarkina nodosa* Zone – the base of the *C. nodosa* Zone, which was first defined by Kozur (2005) from Iranian sections, is recognizable by the first occurrence of the nominate species. This full range zone above the *C. bachmanni* Zone yielded numerous specimens with wrinkled upper platform surfaces and with nodes and broad ridges. These wrinkled specimens were first illustrated by Sweet in Teichert et al. (1973) and were later named *C. nodosa* by Kozur (2004). He interpreted the absence of the *C. nodosa* as well as the *C. bachmanni* zones in the Meishan section as an indication of a gap. Later, Shen and Mei (2010) referred to this biozone as sample 22–14 (i.e. upper part of Bed 22) in the Meishan section, which contains individuals whose platforms are only slightly wrinkled compared to those from Iran (unpublished data).

6. *Clarkina yini* Zone – this biozone is defined by the first occurrence of *C. yini*, which in the Meishan section follows the *C. changxingensis* Zone and is itself overlain by the *C. meishanensis* Zone (Mei et al., 1998b). The stratigraphical scheme is somewhat different in the sections in north-western Iran, where the *C. bachmanni* and *C. nodosa* zones are very well preserved between the *C. changxingensis* and *C. yini* zones. Kozur (2005, 2007) regarded representatives of the *C. yini* Zone as belonging to either his *C. changxingensis*–*C. deflecta* Zone below or the *C. zhangi* Zone above,

which directly follow the *C. nodosa* Zone. Although the boundary between his *C. changxingensis–C. deflecta* and *C. zhangi* zones is not well defined, the mentioned species range into the higher biozones.

Mei et al. (1998b) assigned *C. zhangi* to narrow morphotypes of *C. yini* based on the sample-population approach. *C. changxingensis* was based originally on the round morphotypes, and *C. deflecta* was based on squared morphotypes. Using this diagnosis and the sample-population approach, Shen and Mei (2010) explained why *C. changxingensis* and *C. deflecta* of Kozur (2005) range into the *C. yini* Zone. We confirm here the view of Shen and Mei and suggest that the *C. changxingensis–C. deflecta* and *C. zhangi* zones of Kozur (2004, 2005), which are the lower and upper equivalents of the *C. yini* Zone, should be combined to a unique biozone.

The fifth replacement of clarkinid by hindeodid fauna occurs at about 0.50 m above the base of *C. yini* Zone in Ali Bashi Locality 1 and 4 sections and continues upwards till 0.90 m from the zonal base. This interval is characterized by a major invasion of small *H. typicalis* and intense reduction of clarkinids. The H/C ratio is associated with some fluctuations in *C. yini* Zone and allow us to consider two major amplifications in H/C ratio: first enrichment at about 0.50 m above the base of *C. yini* Zone and the second one at 1.15 m distance from the base in section 1 and 1.18 m distance from the base in section 4. Both horizons are equivalent with two unusual negative excursions of δ^{13}C in the *Paratirolites* Limestone.

7. *Clarkina abadehensis* Zone – the *C. yini* Zone is followed by the *C. meishanensis* Zone in the South Chinese sections. *C. meishanensis* has reduced posterior denticles and a wide gap between the usually reclined cusp and the first denticle in many individuals of the sample population in South China (Mei et al., 1998b). The morphological evolution of *C. yini* is different in the Iranian material where the cusp and posterior carina is reduced and sank into the platform through ontogeny. This different pattern has led Kozur (2004) to the definition of the two new species *C. abadehensis* and *C. iranica*. He used *C. abadehensis* for the wedge-like specimens with a deflected posterior carina and *C. iranica* for the slender to moderately wide specimens without deflected posterior end and with a symmetrical or slightly asymmetrical rounded or narrowly rounded posterior margin. The brim is always very wide in both species. Henderson et al. (2008) regarded *C. iranica* as a junior synonym of *C. abadehensis*, and because of the page priority of *C. abadehensis*, they accepted the name of *C. abadehensis* for this species. Later, Shen and Mei (2010) changed the name of the *C. iranica* Zone established by Kozur (2005) into the *C. abadehensis* Zone. *C. abadehensis*-like specimens are present in the lower part of the *C. meishanensis* Zone in the Xifanli section (Hubei, South China) (Lai and Zhang, 1999) but have not been confirmed subsequently.

8. *Clarkina hauschkei* Zone – the *C. hauschkei* Zone ends at the end-Permian mass extinction horizon. Kozur (2005) established the *C. hauschkei* Zone based on the nominate species *C. hauschkei*, which has a relatively flat platform, a narrowly rounded posterior end and a cusp that is separated from the widely spaced posterior denticles by a wider gap. These features are comparable with those of *C. meishanensis* elements, which occur in the upper part of the *C. meishanensis* Zone. Therefore, we suppose that the *C. hauschkei* Zone is equal to the upper part of the *C. meishanensis* Zone of Meishan. Shen and Mei (2010) stated that *C. hauschkei* probably represents a geographical variant of *C. meishanensis*. Both subspecies of *C. meishanensis*, *C. meishanensis zhangi* and *C. meishanensis meishanensis* are also present in the *C. hauschkei* Zone in our materials from north-western Iran. This co-occurrence may confirm the assumption by Shen and Mei (2010) that *C. hauschkei* is a geographical variant of *C. meishanensis*.

The sixth and final replacement of clarkinids by hindeodids in the Changhsingian begins in the upper *C. hauschkei* Zone and continues to the basal Triassic *H. parvus* Zone. *H. typicalis*, *H. latidentatus*, *H. changxingensis*, *H. praeparvus*, *H. eurypyge*, *H. inflatus*, *Merrillina ultima* and *Stepanovites* ?*mostleri* are the main hindeodid and ramiform elements and dominate the latest Permian clarkinid-based biozones.

9. *Hindeodus praeparvus–Hindeodus changxingensis* Zone – Kozur (2005) defined the *C. meishanensis–H. praeparvus* Zone in the boundary clay (lowermost Elikah Formation), with its lower boundary immediately at the mass extinction horizon. *C. meishanensis* is already present at the base of the *C. hauschkei* Zone, but rarely continues into the *C. meishanensis–H. praeparvus* Zone (Kozur, 2005). Only a few specimens of *C. meishanensis* were found at the top of the extinction horizon in the four sections during the present study. Instead, *H. praeparvus* and *H. changxingensis*, which appear in the lowest samples of the “boundary clay” for the first time, are very abundant. Thus, we name this interval the *H. praeparvus–H. changxingensis* Zone. The appearance of *H. changxingensis* as a characteristic marker index fossil immediately above the extinction horizon has been reported previously from South China (Wang and Wang in Zhao et al., 1981; Mei et al., 1998b), Italy (Wang, 1995; Nicoll et al., 2002), Iran (Kozur, 2004, 2005), Pakistan (Perri and Farabegoli, 2003) and Tibet (Shen et al., 2006). In the Abadeh region, *H. changxingensis* occurs in the upper part of the “boundary clay” – i.e. the upper part of *C. meishanensis–H. praeparvus* Zone according to the zonation of Kozur (2005). In the Zal section this species appears 30 cm above the extinction horizon (Kozur, 2005). In the Ali Bashi sections 1, 4 and M, *H. changxingensis* appears in the lower part of the “boundary clay”. We did not find specimens of *H. changxingensis* in the Aras Valley section, but *H. praeparvus* is abundant there. *H. praeparvus* has the

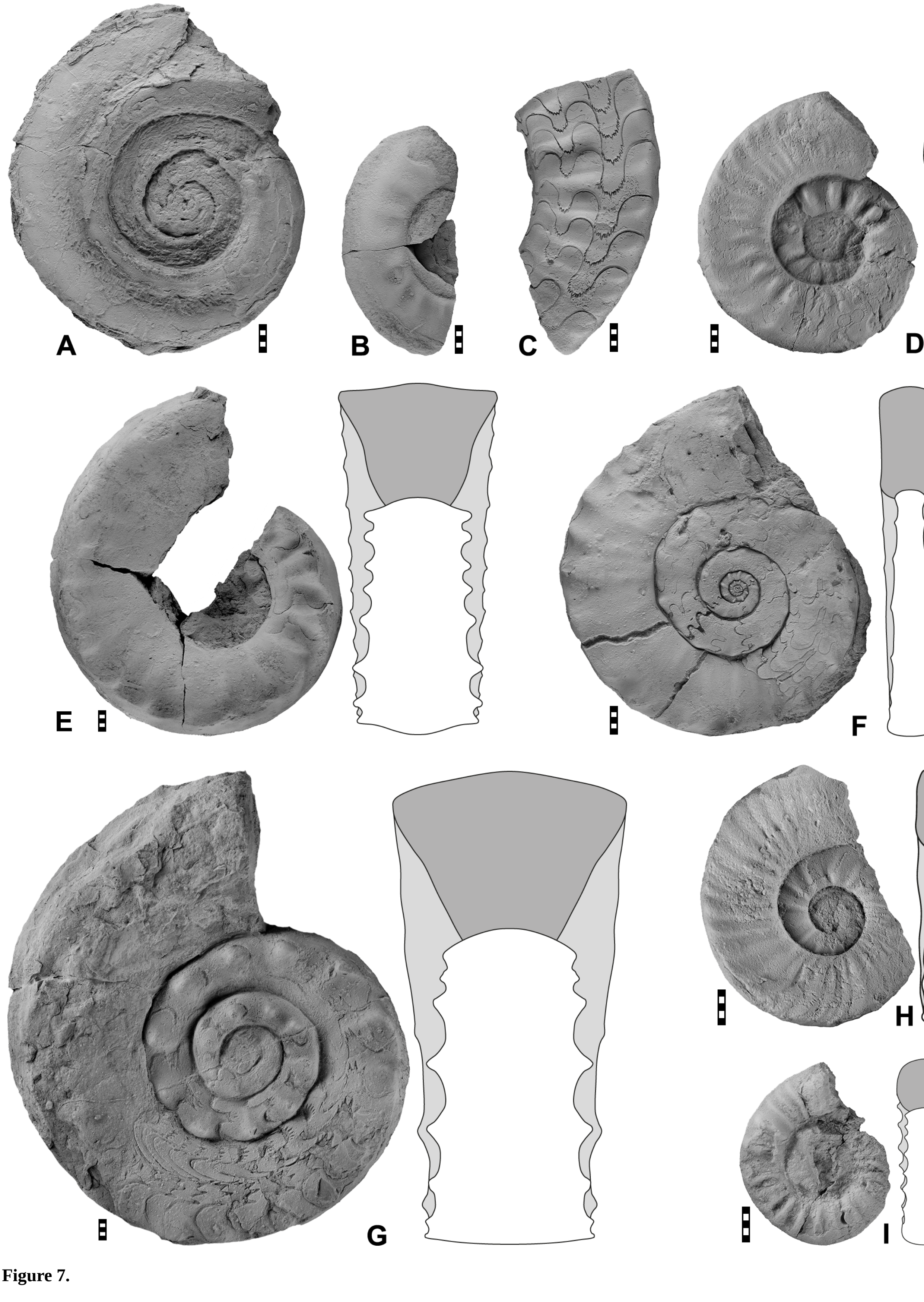

Figure 7.

Figure 7. Characteristic Changhsingian ammonoids from the Julfa region (scale bars equal to 5 mm); all specimens stored in the collection of the Museum für Naturkunde, Berlin. **(A)** *Phisonites triangulus* Shevyrev, 1965 from the Aras Valley section, specimen MB.C.22703; × 1.0. **(B)** *Iranites transcaucasius* (Shevyrev, 1965) from the Aras Valley section, specimen MB.C.22704; × 1.0. **(C)** *Dzhulfites nodosus* Shevyrev, 1965 from the Aras Valley section, specimen MB.C.22705; × 1.0. **(D)** *Shevyrevites nodosus* Shevyrev, 1965 from the Aras Valley section, specimen MB.C.22706; × 1.0. **(E)** *Paratirolites trapezoidalis* Shevyrev, 1965 from the Ali Bashi 4 section, specimen MB.C.22707; × 0.75. **(F)** *Stoyanowites dieneri* (Stoyanow, 1910) from the Aras Valley section, specimen MB.C.22708; × 1.0. **(G)** *Paratirolites vediensis* Shevyrev, 1965 from the Ali Bashi N section, specimen MB.C.22709; × 0.75. **(H)** *Abichites stoyanowi* (Kiparisova, 1947) from the Ali Bashi N section, specimen MB.C.22710; × 1.25. **(I)** *Arasella minuta* (Zakharov, 1983) from the Ali Bashi N section, specimen MB.C.22711; × 1.25.

identical first occurrence in all sections in north-western Iran; however its last occurrence appears to be heterochronous. *H. changxingensis* is limited to the “boundary clay” in the Julfa area sections, but *H. praeparvus* ranges higher into the *H. parvus* Zone.

10. *Merrilina ultima–Stepanovites ?mostleri* Zone – This biozone contains elements of *Merrilina ultima* in association with *H. preparvus* and rare *C. zhejiangensis* and was established by Kozur (2005). *M. ultima–S. ?mostleri* Zone is considered to be correlated with the *C. zhejiangensis* Zone of Mei et al. (1998a, b) in the Meishan section (Kozur, 2005). The presence of this biozone and the *C. meishanensis–H. praeparvus* Zone, which was defined by Kozur (2005), was questioned by Shen and Mei (2010). However, these authors did not have any samples with the elements of this biozone in their collections. Our sample populations of this interval yield and confirm the presence of the *M. ultima–S. ?mostleri* Zone in all sections of the Julfa area. As Kozur (2005) explained, this biozone includes cold water elements dominated by *M. ultima*, *S. ?mostleri*, *H. praeparvus* and very rare *C. zhejiangensis*, but without its Triassic component, which can be separated by the first appearance of *H. parvus*.

The upper limits of these intervals are characterized by the first appearance of *H. parvus*, which indicates the administrative Permian–Triassic boundary. The first appearance of *H. parvus* is situated at a distance 1.32 m in the Ali Bashi Locality 1, 1.86 m in the Ali Bashi Locality 4, 2.75 m in the Aras Valley section, 1.18 m in the main valley section.

5 Ammonoid stratigraphy (Korn)

The frame for the subdivision of the Changhsingian deposits in the area of Julfa was outlined by Ruzhencev and Shevyrev (1965); they separated five units now regarded as representing the Changhsingian (of which the upper four of these were at that time placed into the Triassic), in ascending order the *Phisonites* Zone, *Tompophiceras* Zone, *Dzhulfites* Zone, *Bernhardites* Zone and the *Paratirolites* Zone.

Stepanov et al. (1969) as well as Teichert et al. (1973) followed this scheme, and the latter authors replaced the genus names *Tompophiceras* and *Bernhardites*, which originally refer to Triassic ammonoids, by *Iranites* and *Shevyrevites*, respectively. Zakharov (1992) added another zone (“*Pleuronodoceras occidentale* Zone”) at the top of the succession, which represents the shaly interval (“boundary clay” of Leda et al., 2014) between the Late Permian and Early Triassic carbonates.

Up to now, a subdivision of the *Paratirolites* Limestone has not been achieved. Bed-by-bed collections of more than 250 ammonoids from this interval during four field campaigns between 2010 and 2013 offer the opportunity to subdivide this rock unit by means of ammonoid species and genera (Figs. 4, 5). Subdivision of this rock unit is particularly interesting because it has a very different composition (dominated by members of the family Dzhulfitidae) of ammonoids from the occurrences in South China (in which the Dzhulfitidae are either rare or totally missing) (Zhao et al., 1978).

A total of eight biozones (in ascending order) of the Changhsingian interval may be used for regional correlation, of which the lower three represent the lower shaly portion (Zal Member) of the Ali Bashi Formation and the upper five the *Paratirolites* Limestone (characteristic ammonoid specimens are illustrated in Fig. 7):

1. *Iranites transcaucasius–Phisonites triangulus* Zone – according to our collections, the zones separated by Shevyrev (1965) cannot be separated; *Iranites transcaucasius* (Shevyrev, 1965) was even collected below *Phisonites triangulus* Shevyrev, 1965. The unit is 7.00 m thick in the Dorasham 2 section after Arakelyan et al. (1965) and 6.50 m thick in the Ali Bashi 4 section after Stepanov et al. (1969).

The lowermost part of the Ali Bashi Formation contains ammonoid faunas in low diversity, and the specimens are usually poorly preserved. *Iranites transcaucasius* (Shevyrev, 1965) and *Phisonites triangulus* Shevyrev, 1965 occur, together with other smooth ceratitic ammonoids, at the base of the Ali Bashi Formation in the Aras Valley section. Arakelyan et al. (1965) listed frequent specimens of *Xenodiscus* and *Xenaspis* from this interval in the Dorasham 2 section. A newly collected fragment of *Vedioceras* sp. in the shales at the base of the Ali Bashi Formation in the Ali Bashi 1 section demonstrates the change from *Vedioceras*-dominated faunas of the Wuchiapingian to the xenodiscid-dominated faunas of the Changhsingian in this interval.

2. *Dzhulfites nodosus* Zone – it is 7.50 m thick in the Dorasham 2 section after Arakelyan et al. (1965) and 4.60 m thick in the Ali Bashi 4 section after Stepanovet al. (1969). Shevyrev (1965) described the two species *D. nodosus* and *D. spinosus*, which they exclusively attributed to the

Dzhulfites beds. In our field work we found that *D. spinosus* occurs also in the following zone.

3. *Shevyrevites shevyrevi* Zone – it is 5.50 m thick in the Dorasham 2 section after Arakelyan et al. (1965) and 6.10 m thick in the Ali Bashi 4 section after Stepanov et al. (1969). *Shevyrevites* has obviously only a very limited stratigraphical range and characterizes a thin interval of the Ali Bashi Formation below the *Paratirolites* Limestone. *Dzhulfites* occasionally occurs in this zone.

4. *Paratirolites trapezoidalis* Zone – this zone has a position at the base of the *Paratirolites* Limestone, where the taxonomic diversity of the ammonoid faunas is rather low. This interval contains paratirolitid ammonoids with unsubdivided or bifid prongs of the external lobe. *Paratirolites trapezoidalis* Shevyrev, 1965 best characterizes this interval, of which the base is difficult to recognize because of the scarcity of fossils at the base of the *Paratirolites* Limestone.

5. *Paratirolites waageni* Zone – this interval is characterized by the main occurrence of the genus *Paratirolites*, of which also *Paratirolites vediensis* Shevyrev, 1965 can be used as an index fossil besides the nominate species *Paratirolites waageni* (Stoyanow, 1910). Even without distinct species attribution, specimens of this zone are usually clearly assigned to this zone because of the strongly serrated external, adventive, and lateral lobes. This interval is, in the Aras Valley and Ali Bashi sections, often very fossiliferous and thus easily recognizable.

6. *Stoyanowites dieneri* Zone – the entry of paratirolitids with laterally compressed whorl sections, of which "*Paratirolites dieneri* Stoyanow, 1910" performs as the type species for the new genus *Stoyanowites*, characterizes the next biozone within the *Paratirolites* Limestone.

7. *Abichites stoyanowi* Zone – the upper portion of the *Paratirolites* Limestone is dominated by paratirolitid ammonoids with quadrate or slightly compressed whorl cross sections. Such forms usually belong to the genus *Abichites*, which possesses a suture line with unsubdivided or bifid prongs of the external lobe.

8. *Arasella minuta* Zone – at the top of the *Paratirolites* Limestone is a thin interval, about 30 cm thick, which is dominated by very small ammonoids with simple suture lines. *Arasella minuta* (Zakharov, 1983) is the most common of these and can be used for the definition of this zone.

(9). (*Pleuronodoceras occidentale* Zone) – Zakharov (1992) attributed the lower 2 m of the "boundary clay" of the Dorasham II section to the *Pleuronodoceras occidentale* Zone, based on a finding of the nominate species in the basal 9 cm of the interval. In our study, we did not find ammonoids in the Aras Member and thus cannot confirm this record.

Systematic descriptions, characterization of new taxa:

Order Ceratitida Hyatt, 1884

Suborder Paraceltitina Shevyrev, 1968

Superfamily Xenodiscaceae Frech, 1902

Family Dzhulfitidae Shevyrev, 1965

***Stoyanowites* n. gen.**

Derivation of name: after A.A Stoyanow, who gave the first description of paratirolitid ammonoids from the Aras Valley.

Type species: *Paratirolites Dieneri* Stoyanow, 1910.

Diagnosis: genus of the Dzhulfitidae with laterally compressed whorl cross section. Ornament with small ventrolateral nodes and often also dorsolateral nodes. Suture line with short external lobe, which reaches only 60 % of the depth of the adventive lobe.

Discussion: the specimens of the new genus are easily separable from the genera *Dzhulfites*, *Paratirolites* and *Abichites* by the laterally compressed whorl cross section with a ratio of whorl width / whorl height of less than 0.80 (usually more than 1.00 and reaching more than 2.00 in the other three genera).

***Arasella* n. gen.**

Derivation of name: after the Aras Valley, the locality of the type material.

Type species: *Sinoceltites minutus* Zakharov, 1983.

Diagnosis: genus of the Dzhulfitidae with small conch reaching 30 mm diameter. Conch widely umbilicate with circular whorl cross section. Ornament with sharp ribs. Suture line with short external lobe, which reaches only 50 % of the depth of the adventive lobe. Adventive lobe and lateral lobe rounded and unserrated.

Discussion: Zakharov (1983) described the species as belonging to *Sinoceltites*, a genus belonging to the family Tapashanitidae and known from occurrences in South China. The species has a particular position in two respects: (1) it is obviously the stratigraphically youngest ammonoid to appear before the end-Permian mass extinction event in the NW Iranian sections, and (2) it has a morphology characterized by reduction of morphological characters such as the suture line and thus is difficult to interpret in terms of phylogeny. Two possible phylogenetic origins may be discussed:

(1) A xenodiscid origin – this would imply a ghost lineage ranging through the higher part of the Changhsingian. Evidence of a xenodiscid origin is lacking.

(2) A paratirolitid origin – this would imply a simplification of conch and suture morphology. Indeed, obvious phylogenetic relationships occur between the stratigraphically older *Paratirolites* towards the younger *Abichites* in the reduction of size, the change from trapezoidal towards quadrate whorl cross sections, the disappearance of strong nodes in the sculpture and the reduction of sutural notching. *Arasella* has some similarities with the stratigraphically younger species of *Abichites* and may thus be an advanced but morphologically simplified descendent.

Acknowledgements. We thank the Aras Free Zone office for support during our field work. Financial support was provided by the Deutsche Forschungsgemeinschaft (project KO1829/12-1). We acknowledge the preparation of ammonoid specimens by E. Stenzel (Berlin) and check of the English text by S. A. Walton (Berlin). We kindly acknowledge the reviews by Vachik Hairapetian (Esfahan) and Shen Shu-Zhong (Nanjing).

Edited by: F. Witzmann
Reviewed by: S. Shen and V. Hairapetian

References

Abich, H.: Geologische Forschungen in den kaukasischen Ländern. Theil I. Eine Bergkalkfauna aus der Araxesenge bei Djoulfa in Armenien, 1878.

Arakelyan, R. A., Grunt, T. A., and Shevyrev, A. A.: Kratkiy stratigraficheskiy ocherk, Trudy Paleontologicheskogo Instituta Akademiya Nauk SSSR, 108, 20–25, 1965.

Baud, A., Magaritz, M., and Holser, W.: Permian-Triassic of the Tethys: Carbon isotope studies, Geol. Rundsch., 78, 649–677, 1989.

Bonnet, P. and Bonnet, N. M. T.: Description géologique de la Transcaucasie Méridionale (chaines de l'Araxe Moyen), Mémoires de la Société Géologique de France, Nouvelle Série, 25, 1–292, 1947.

Chen, J., Henderson, C. M., and Shen, S. Z.: Conodont succession around the Permian-Triassic boundary at the Huangzhishan Section, Zhejiang and its stratigraphic correlation, Acta Paleontogica Sinica, 47, 91–114, 2008.

Frech, F.: Lethaea geognostica oder Beschreibung und Abbildung der für die Gebirgs-Formationen bezeichnendsten Versteinerungen, I. Theil. Lethaea palaeozoica, 2. Band, 1897–1902.

Frech, F. and Arthaber, G. V.: Ueber das Palaozoicum in Hocharmenien und Persien, mit einem Anhang uber die Kreide von Sirab in Persien, Beitraege zur Palaeontologie Oesterreich-Ungarns, 12, 161–308, 1900.

Ghaderi, A., Ashouri, A. R., Korn, D., Mahmoudi Gharaie, M. H., and Leda, L.: New insight on stratigraphic correlation of the Permian-Triassic transitional beds in the Transcaucasus and northwest of Iran: Problems and guidelines, Sedimentary Facies, 5, 221–246, 2013.

Henderson, C. M., Mei, S., Shen, S., and Wardlaw, B. R.: Resolution of the reported Upper Permian conodont occurrences from northwestern Iran, Permophiles, 51, 2–9, 2008.

Hyatt, A.: Genera of fossil cephalopods, Proceedings of the Boston Society of Natural History, 253–338, 1883–1884.

ICRG (Iranian-Chinese Research Group): Field work on the Lopingian stratigraphy in Iran, Permophiles, 27, 5–8, 1995.

Jin, Y., Henderson, C. M., Wardlaw, B. R., Glenister, B. F., Mei, S., Shen, S., and Wang, X.: Proposal for the Global Stratotype Section and Point (GSSP) for the Guadalupian–Lopingian boundary, Permophiles, 39, 32–42, 2001.

Kakuwa, Y. and Matsumoto, R.: Cerium negative anomaly just before the Permian and Triassic boundary event – The upward expansion of anoxia in the water column, Palaeogeogr. Palaeocl., 229, 335–344, 2006.

Korte, C. and Kozur, H. W.: Carbon-isotope stratigraphy across the Permian-Triassic boundary: A review, J. Asian Earth Sci., 39, 215–235, 2010.

Korte, C. and Kozur, H. W.: Temperature changes across the Permian-Triassic boundary and observations pertaining to some geological/geochemical features around this level, Geol. Soc. Ind. Mem., 78, 100–139, 2011.

Korte, C., Kozur, H. W., and Partoazar, H.: Negative carbon isotope excursion at the Permian/Triassic boundary section at Zal, NW Iran, Hallesches Jahrbuch für Geowissenschaften, Reihe B, Beiheft, 18, 69–71, 2004.

Kozur, H. W.: Beiträge zur Conodontenfauna des Perm, Geologisch-Paläontologische Mitteilungen Innsbruck, 5, 1–44, 1975.

Kozur, H. W.: Beiträge zur Stratigraphie des Perms. Teil II, Die Conodontenchronologie des Perms, Freiberger Forschungshefte, Reihe C: Geowissenschaften, Mineralogie Geochemie, 334, 85–161, 1978.

Kozur, H. W.: The conodonts Hindeodus, Isarcicella and Sweetohindeodus in the uppermost Permian and lowermost Triassic, Geol. Croat., 49, 81–115, 1996.

Kozur, H. W.: Pelagic uppermost Permian and the Permian-Triassic boundary conodonts of Iran. Part 1: Taxonomy, Hallesches Jahrbuch für Geowissenschaften, Reihe B: Geologie Paläontologie Mineralogie, 18, 39–68, 2004.

Kozur, H. W.: Pelagic uppermost Permian and the Permian-Triassic boundary conodonts of Iran. Part II: Investigated sections and evaluation of the conodont faunas, Hallesches Jahrbuch für Geowissenschaften, Reihe B: Geologie Paläontologie Mineralogie Beiheft, 19, 49–86, 2005.

Kozur, H. W.: Biostratigraphy and event stratigraphy in Iran around the Permian-Triassic Boundary (PTB): Implications for the causes of the PTB biotic crisis, Global Planet. Change, 55, 155–176, 2007.

Kozur, H. W. and Pjatakova, M.: Die Conodontenart Anchignathodus parvus n. sp., eine wichtige Leitform der basalen Trias, Koninklijke Nederlandse Akademic van Wetenschappen, Proceedings, Series B, 79, 123–128, 1976.

Kozur, H., Leven, E. Y., Lozovskiy, V. R., and Pyatakova, M. V.: Subdivision of Permian-Triassic Boundary beds in Transcaucasia on the basis of conodonts, Int. Geol. Rev., 22, 361–368, 1980.

Lai, X. and Zhang, K.: A new paleoecological model of conodonts during the Permian-Triassic transitional period, Earth Science (Wuhan), 24, 33–38, 1999.

Lai, X. L., Wignall, P., and Zhang, K. X.: Palaeoecology of the conodonts Hindeodus and Clarkina during the Permian-Triassic transitional period, Palaeogeogr. Palaeocl., 171, 63–72, 2001.

Lasemi, Y., Bagheri, M., and Mahari, R.: Depositional environments and sequence stratigraphy of the Nesen Formation in Zal and Pir-Esagh area (south of Julfa), Journal of Sciences (Islamic Azad University), 17, 73–80, 2007.

Leda, L., Korn, D., Ghaderi, A., Hairapetian, V., Struck, U., and Reimold, W. U.: Lithostratigraphy and carbonate microfacies across the Permian-Triassic boundary near Julfa (NW Iran) and in the Baghuk Mountains (Central Iran), Facies, 60, 295–325, 2014.

Mei, S., Henderson, C. M., and Cao, C.: Conodont sample-population approach to defining the base of the Changhsingian Stage, Lopingian Series, Upper Permian, Geological Society, London, Special Publications, 230, 105–121, 2004.

Mei, S.-L., Jin, Y., and Wardlaw, B. R.: Conodont succession of the Guadalupian-Lopingian boundary strata in Laibin of Guangxi, China and West Texas, USA, Palaeoworld, 9, 53–57, 1998a.

Mei, S.-L., Zhang, K. X., and Wardlaw, B. R.: A refined succession of Changhsingian and Griesbachian neogondolellid conodonts from the Meishan section, candidate of the global stratotype section and point of the Permian-Triassic boundary, Palaeogeogr. Palaeocl., 143, 213–226, 1998b.

Nafi, M., Wenchen, X., and Ning, Z.: Late Permian (Changhsingian) conodont biozonation and the basal boundary, Ganxi section, western Hubei Province, south China, Can. J. Earth Sci., 43, 121–133, 2006.

Nicoll, R. S., Metcalfe, I., and Wang, C. Y.: New species of the conodont Genus Hindeodus and the conodont biostratigraphy of the Permian-Triassic boundary interval, J. Asian Earth Sci., 20, 609–631, 2002.

Partoazar, H.: Permian-Triassic boundary conodonts from Jolfa-Abadeh Belt along Northwest and Central Iran, Permophiles, 41, 34–40, 2002.

Perri, M. C. and Farabegoli, E.: Conodonts across the Permian – Triassic boundary in the southern Alps, Cour. For. Senckenbg., 245, 281–313, 2003.

Richoz, S.: Stratigraphie et variations isotopiques du carbone dans le Permien supérieur et le Trias inférieur de la Néotéthys (Turquie, Oman et Iran), Memoirs de Géologie (Lausanne), 46, 1–251, 2006.

Richoz, S., Krystyn, L., Baud, A., Brandner, R., Horacek, M., and Mohtat-Aghai, P.: Permian–Triassic boundary interval in the Middle East (Iran and N. Oman): Progressive environmental change from detailed carbonate carbon isotope marine curve and sedimentary evolution, J. Asian Earth Sci., 39, 236–253, 2010.

Romano, C., Goudemand, N., Vennemann, T. W., Ware, D., Schneebeli-Hermann, E., Hochuli, P. A., Brühwiler, T., Brinkmann, W., and Bucher, H.: Climatic and biotic upheavals following the end-Permian mass extinction, Nat. Geosci., 6, 57–60, 2013.

Rostovtsev, K. O. and Azaryan, N. R.: The Permian-Triassic Boundary in Transcaucasia, Canadian Society of Petroleum Geologists Memoir, 2, 89–99, 1973.

Ruzhencev, V. E. and Shevyrev, A. A.: Ammonoidei, in: Razvitie i smena morskikh organizmov na Rubezhe Paleozoya i Mezozoya, edited by: Ruzhencev, V. E. and Sarytcheva, T. G., Trudy Paleontologicheskogo Instituta Akademiya Nauk SSSR, 108, 47–57, 1965.

Ruzhencev, V. E., Sarytcheva, T. G., and Shevyrev, A. A.: Biostratigraficheskie vyvody, in: Razvitie i smena morskikh organizmov na Rubezhe Paleozoya i Mezozoya, edited by: Ruzhencev, V. E. and Sarytcheva, T. G., Trudy Paleontologicheskogo Instituta Akademiya Nauk SSSR, 108, 93–116, 1965.

Schobben, M., Joachimski, M. M., Korn, D., Leda, L., and Korte, C.: Palaeotethys seawater temperature rise and an intensified hydrological cycle following the end-Permian mass extinction, Gondwana Res., doi:10.1016/j.gr.2013.07.019, 2013.

Shen, S.-Z. and Mei, S.-L.: Lopingian (Late Permian) high-resolution conodont biostratigraphy in Iran with comparison to South China zonation, Geol. J., 45, 135–161, 2010.

Shen, S. Z., Cao, C.-Q., Henderson, C. M., Wang, X.-D., Shi, G. R., Wang, Y., and Wang, W.: End-Permian mass extinction pattern in the northern peri-Gondwanan region, Palaeoworld, 15, 3–30, 2006.

Shevyrev, A. A.: Nadortyad Ammonoidea, in: Razvitie i smena morskikh organizmov na Rubezhe Paleozoya i Mezozoya, edited by: Ruzhencev, V. E. and Sarytcheva, T. G., Trudy Paleontologicheskogo Instituta Akademiya Nauk SSSR, 108, 166–182, 1965.

Shevyrev, A. A.: Triasovye ammonoidei Yuga SSSR, Trudy Paleontologicheskogo Instituta Akademiya Nauk SSSR, 119, 1–272, 1968.

Stampfli, G. M. and Borel, G. D.: A plate tectonic model for the Paleozoic and Mesozoic constrained by dynamic plate boundaries and restored synthetic oceanic isochrons, Earth Planet. Sc. Lett., 196, 17–33, 2002.

Stepanov, D. L., Golshani, F., and Stöcklin, J.: Upper Permian and Permian–Triassic Boundary in North Iran, Geolological Survey of Iran, Report, 12, 1–72, 1969.

Sun, Y., Joachimski, M. M., Wignall, P. B., Yan, C., Chen, Y., Jiang, H., Wang, L., and Lai, X.: Lethally hot temperatures during the early Triassic greenhouse, Science, 338, 366–370, 2012.

Sweet, W. C.: Uppermost Permian and Lower Triassic conodonts of the Salt Range and Trans-Indus Ranges, West Pakistan, in: Stratigraphic boundary problems: Permian and Triassic of West Pakistan, edited by: Kummel, B. and Teichert, C., University of Kansas, Department of Geology, Special Publications, 4, 207–275, 1970.

Sweet, W. C. and Mei, S.-l.: The Permian Lopingian and basal Trassic Sequence in Northwest Iran, Permophiles, 33, 14–18, 1999a.

Sweet, W. C. and Mei, S.-l.: Conodont succession of Permian Lopingian and basal Triassic in northwest Iran, Paper read at Proceedings of the International Conference on Pangea and the Paleozoic-Mesozoic transition, China University of Geosciences Press, Wuhan, 1999b.

Taraz, H.: Uppermost Permian and Permian-Triassic Transition beds in Central Iran, Bulletin of the American Association of Petroleum Geologists, 55, 1280–1294, 1971.

Taraz, H., Golshani, F., Nakazawa, K., Sgimuzu, D., Bando, Y., Ishi, K.-i., Murata, M., Okimura, Y., Sakagami, S., Nakamura, K., and Tokuoka, T.: The Permian and the Lower Triassic Systems in Abadeh Region, Central Iran, Memoirs of the Faculty of Science, Kyoto University, Series of Geology and Mineralogy, 47, 61–133, 1981.

Teichert, C., Kummel, B., and Sweet, W. C.: Permian-Triassic strata, Kuh-e-Ali Bashi, Northwestern Iran, Bulletin of the Museum of Comparative Zoology, Harvard University, 145, 359–472, 1973.

Voinova, E. V., Kiparisova, L. D., and Robinson, V. H.: Klass Cephalopoda. Golovonogie, in: Atlas rukovodyashtchikh form iskopaemykh faun SSSR. VIII. Triasovaya sistema, Moskva-Leningrad, 1947.

Wang, C.-y.: Conodonts of Permian-Triassic boundary beds and biostratigraphic boundary, Acta Palaeontologica Sinica, 34, 129–151, 1995.

Yazdi, M. and Shirani, M.: First research on marine and nonmarine sedimentary sequences and micropaleontologic significance across Permian/Triassic boundary in Iran, (Isfahan and Abadeh), J. China Univ. Geosci., 13, 172–176, 2002.

Zakharov, Y. D.: Ammonoidea, in: Kotlyar, G. V., Zakharov, Yu. D., Koczyrkevich, B. V., Kropatcheva, G. S., Rostovtsev, K. O., Chedia, I. O., Vuks, G. P., and Guseva, E. A.: Dzhul'finskii i Dorashamskii yarusy SSSR, edited by: Gramm, M. N. and Rostovtsev, K. O., Pozdnepermiskii etap evoliutsii organicheskogo mira, 150–157, 1983.

Zakharov, Y. D.: The Permo-Triassic boundary in the southern and eastern USSR and its intercontinental correlation, edited by: Sweet, W. C., Zunyi, Y., Dickins, J. M., and Hongfu, Y., Cambridge, Cambridge University Press, 1992.

Zhao, J., Liang, X., and Zheng, Z.: Late Permian cephalopods from South China, Paleontologica Sinica, N.S. B, 12, 1–194, 1978.

Zhao, J.-K., Sheng, J.-Z., Yao, Z.-Q., Liang, X.-L., Chen, C.-Z., Rui, L., and Liao, Z.-T.: The Changhsingian and Permian-Triassic boundary of South China, Bulletin of the Nanjing Institute of Geology and Palaeontology, Academia Sinica, 2, 1–95, 1981.

Paper 2

Palaeotethys seawater temperature rise and an intensified hydrological cycle following the end-Permian mass extinction

Schobben, M., Joachimski, M.M., Korn, D., Leda, L., Korte, C. (2014) Palaeotethys seawater temperature rise and an intensified hydrological cycle following the end-Permian mass extinction, Gondwana Research 26, pp: 675–683, http://dx.doi.org/10.1016/j.gr.2013.07.019

cover shows the Kuh-e-Ali Bashi section 1 (NW Iran) in the foreground and section 4 in the background

The following paper can be found under: http://dx.doi.org/10.1016/j.gr.2013.07.019

Paper 3

Uncovering palaeoenvironmental information from bulk-carbonate δ^{13}C of Permian-Triassic 'Boundary Clay' sections

Schobben, M., Ullmann, C.V., Leda, L., Korn, D., Struck, U., Reimold, W.U., Algeo, T.J., Korte, C. (manuscript) Uncovering palaeoenvironmental information from bulk-carbonate δ^{13}C of Permian-Triassic ‘Boundary Clay’ sections

cover shows part of the Elikah formation at the Kuh-e-Ali Bashi locality North (NW Iran).

Uncovering palaeoenvironmental information from bulk-carbonate δ^{13}C of Permian-Triassic 'Boundary Clay' sections

Martin Schobben[a][1], Clemens V. Ullmann[b], Lucyna Leda[a], Dieter Korn[a], Ulrich Struck[a], Wolf Uwe Reimold[a,c], Abbas Ghaderi[d], Thomas J. Algeo[e f], Christoph Korte[b]

[a] Museum für Naturkunde, Leibniz Institut für Evolutions- und Biodiversitätsforschung, Invalidenstr 43, D-10115 Berlin, Germany
[b] Department of Geosciences and Natural Resource Management, University of Copenhagen, ØsterVoldgade 10, DK-1350, Copenhagen, Denmark
[c] Humboldt Universität zu Berlin, Unter den Linden 6, 10099 Berlin, Germany
[d] Department of Geology, Faculty of Sciences, Ferdowsi University of Mashhad, Azadi Square, 9177948974 Mashhad, Iran
[e] Department of Geology, University of Cincinnati, Cincinnati, OH 45221-0013, U.S.A.
[f] State Key Laboratories BGEG and GPMR, China University of Geosciences, Wuhan 430074, China

ARTICLE INFO

Keywords: Permian-Triassic boundary, carbon isotopes, carbon cycle, diagenesis, Iran

ABSTRACT

Sedimentary successions encompassing the end-Permian mass extinction are marked by a pronounced negative carbon isotopic excursion recorded in bulk-carbonates. It is found at many sites around the world and therefore generally considered to be related to a global carbon cycle perturbation. This negative carbon isotope excursion has been found for the two studied sections in northwestern Iran, with superimposed "second-order" δ^{13}C fluctuations, which vary in shape and magnitude. To improve our knowledge of how to interpret these latter excursions we evaluate here the carbonate genesis and post-depositional alteration by discussing the stable isotopes and elemental concentrations of bulk-rocks and fossils. The results show that the common use of Mn and Sr concentrations as well as paired δ^{13}C and δ^{18}O values are not sufficient to identify diagenetic alteration of carbonates and the resetting of the δ^{13}C; bed-by-bed geochemical analyses are necessary. This is important because secondarily induced δ^{13}C fluctuations are often regarded as being primary in origin, and this can mislead when using as stratigraphic markers. Our final evaluation suggests that palaeoenvironmental interpretations based on small-scale carbon isotope deviations must be regarded with caution, especially when a covariation with lithology or other geochemical signatures exists. The long-term δ^{13}C decline of P-Tr 'Boundary Clay' successions in NW Iran, however, can be related to palaeoenvironmental changes with relatively high confidence.

---

[1] Corresponding author: Phone: +49 (0) 3020938749, E-mail: martin.schobben@mfn-berlin.de, Postal address: Museum für Naturkunde, Leibniz Institut für Evolutions- und Biodiversitätsforschung, Invalidenstr 43, D-10115 Berlin, Germany

1 Introduction

The interval bracketing the Permian-Triassic (P-Tr) boundary (251.902 ± 0.024 Ma; Burgess et al., 2014) is associated with a large negative $\delta^{13}C$ excursion that has been attributed to a global carbon cycle perturbation (for a review, see Korte and Kozur, 2010). Carbon isotope records based on marine bulk-carbonate rock have been assumed to be a faithful proxy for the $\delta^{13}C$ of dissolved inorganic carbon (DIC) in palaeoseawater (Holser and Magaritz, 1987), and C-isotopic excursions are regarded as suitable stratigraphic correlation markers (Hermann et al., 2010; Korte and Kozur, 2010). However, different opinions exist regarding the reliability of bulk-carbonate $\delta^{13}C$ as a recorder of a primary palaeoseawater signal (for a discussion, see Brand et al., 2012a).

A long-term (~0.5-1.0 Myr) negative carbonate carbon isotope trend started in the latest Permian and continued into the earliest Triassic, a feature characteristic of many P-Tr successions around the globe (e.g., Baud et al 1989; Holser et al., 1989; Tong et al., 2007; Hermann et al., 2010; Korte and Kozur, 2010; Korte et al., 2010). This "first-order" $\delta^{13}C$ trend has been attributed to prolonged outgassing of isotopically depleted carbon by contemporaneous Siberian Traps volcanism (Sobolev et al., 2011), possibly in combination with related effects such as metamorphism of organic-rich sediments (Retallack and Krull, 2006; Svensen et al., 2009), erosion of organic matter from continents (Holser and Magaritz, 1987), and a reduction in marine primary productivity (Rampino and Caldeira, 2005). Superimposed fluctuations around the long-term carbon isotope trend have been reported (e.g., Algeo et al., 2007, 2008), and in the present study these short-term fluctuations are referred to as "second-order excursions". The latter have often been employed to recognize short stratigraphic intervals including individual lithological horizons (e.g., Richoz et al., 2010). For example, short-term (~2-20 kyr) negative $\delta^{13}C$ excursions coincident with the 'extinction horizon' at Meishan (South China) (Cao et al., 2009; Burgess et al., 2014) have been attributed to massive CH_4 release from methane clathrate dissociation (Berner, 2002; Benton and Twitchett, 2003) or rapid expansion of methanogens (Rothman et al., 2014).

Two P-Tr bounday sections (Kuh-e-Ali Bashi and Zal), located in NW Iran, were analysed in the present study. Both successions comprise the Late Permian 'Boundary Clay' that includes the main marine extinction event at its base (Stepanov et al., 1969; Teichert et al., 1973; Korte and Kozur, 2005; Kozur, 2007; Ghaderi et al., 2014; Leda et al., 2014). These 'Boundary Clay' sections differ from sites in Japan, China and Turkey, which all show erosional truncations within end-Permian strata possibly caused by submarine dissolution (Payne et al., 2007) or subaerial exposure (Collin et al., 2009). Local diagenetic alteration, implied by lithological and facies changes, has been put forward as an explanation for observed short-term $\delta^{13}C$ trends confined to the 'Boundary Clay' of some P-Tr sections found in Iran (Heydari et al., 2001, 2003; Korte et al., 2004a, 2004b; Korte and Kozur, 2005) and elsewhere. It has been suggested that calcareous clays, such as those found in the 'Boundary Clay' of these sections, are susceptible to post-depositional recrystallization that may alter the primary carbonate $\delta^{13}C$ composition (Knauth and Kennedy, 2009).

A better understanding of the genesis and diagenesis of carbonate rock is needed to isolate the primary versus secondary influences on bulk-rock $\delta^{13}C$ values. In attempts to evaluate potential diagenetic overprint on bulk-carbonate rock and its effect on $\delta^{13}C$, sedimentological, textural and chemical indices have been used (Brand and Veizer, 1980; Al-Aasm and Veizer, 1986; Melim et al., 2002). Evaluations based purely on textural changes, such as cementation and recrystallization features, give a general idea about the diagenetic history. However, they are often insufficient for a detailed reconstruction, as too little is known about the exact timing and the physical conditions under which these features developed (Munnecke et al., 1997; Melim et al., 2002). The utility of chemical tools for detecting diagenetic alteration, such as Sr and Mn ratios, has been demonstrated (Pingitore, 1978; Brand and Veizer, 1980; Middelburg et al., 1987; Pingitore Jr et al., 1988; Banner and Hanson, 1990). However, different diagenetic regimes and fluids with spatially and temporally variable chemical properties at different scales make a true quantification of these processes difficult.

We suggest that it is pertinent to better constrain the nature of the obtained δ^{13}C values; this is based on previous observations: (1) The high degree of secondary variation in δ^{13}C, superimposed on the general trend when comparing different sections. (2) The notion of secondary alteration of calcite, and possibly such overprint on δ^{13}C within the 'Boundary Clay' low in $CaCO_3$ and more generally in sections dominated by clastic sediments (e.g., Knauth and Kennedy, 2009). The implications of this study extend beyond our analysed samples, as doubt has been cast on the primary nature of "second-order" δ^{13}C fluctuations in other P-Tr sections (Jin et al., 2000; Korte and Kozur, 2010). Due to the inherent difficulties in constraining diagenetic alteration on δ^{13}C compilations, we discuss the possibility that environmental data are contained within these bulk-carbonate rock based geochemical proxies. We undertook an integrated and comparative fossil and bulk-rock geochemical investigation of P-Tr 'Boundary Clay' sections in NW Iran. The chemical analysis encompasses two whole-rock δ^{13}C records together with carbonate rock trace elements. Our investigation reveals a more accurate view on actual δ^{13}C changes in seawater DIC during one of the most critical intervals in Earth's history.

2 Localities investigated

The Kuh-e-Ali Bashi 1 (sensu Teichert et al., 1973) (38.940°N, 45.520°E) and Zal (38.733°N, 45.580°E) sections of the Julfa region (NW Iran, Fig. 1A) are located on the north-northeastern margin of the NW Iranian Terrane, which belonged during the latest Permian to the Cimmerian Microcontinents (Fig. 1B).

Carbonate rock successions in this area spanning the P-Tr boundary interval can be divided into three major lithological units (in stratigraphic order): the *Paratirolites* Limestone (which is the upper part of the Ali Bashi Formation), the 'Boundary Clay' (Aras Member sensu Ghaderi et al., 2014) and the '*Claraia*' Beds (which both compose the Elikah Formation).

The red nodular *Paratirolites* Limestone beds have $CaCO_3$ contents between 70 and 90 wt.% (Ghaderi et al., 2014), classifying them as argillaceous limestone. The limestone beds are separated by shale horizons, which become thinner towards the top of the *Paratirolites* Limestone. The individual limestone nodules have a partly rounded surface and show a micritic matrix of generally similar composition. The rare macrofossil assemblages are comprised of ammonites, nautiloids, rugose corals, fish remains and brachiopod shells. Microfossils are strikingly abundant, acid digestion reveals pectinoform and platform elements from conodonts and actinopterygian teeth from the insoluble residue. Calcareous green algae and radiolarians have been identified from thin sections (Leda et al., 2014). Other features of the *Paratirolites* Limestone are carbonate nodules coated with Fe-Mn crusts, and Fe-Mn coatings of discontinuity surfaces accompanied by biogenic encrustations (Mohtat Aghai et al., 2011; Leda et al., 2014). The matrix features, besides micrite, some minor sparry cement and in-situ recrystallization (neomorphic spar).

The 'Boundary Clay', common in most of the Iranian P-Tr sections (Taraz, 1971; Ezat Heydari et al., 2003; Kozur, 2007; Ghaderi et al., 2014; Leda et al., 2014), overlying the *Paratirolites* Limestone, reaching thicknesses of 1.2 m at Kuh-e-Ali Bashi and 0.6 m at Zal and contain 18 and 35 wt.% $CaCO_3$, respectively (Ghaderi et al., 2014). The lithology can be classified as red claystone and red/green argillaceous marl for both sections and skeletal components are less abundant. The base of the 'Boundary Clay' is marked by the extinction event, but ostracods, bellerophontids and sponge remains occur frequently throughout this unit. The matrix consists of microcrystalline spar and micrite intersected by abundant anastomosing stylolites.

From the overlying '*Claraia* Beds' the lower 5 to 10 m were studied here. The base of this unit is slightly below the conodont-defined P-Tr boundary (Kozur, 2007; Ghaderi et al., 2014). In contrast to the Zal section, the lower part of the '*Claraia* Beds' in Kuh-e-Ali Bashi has some similarities in the carbonate facies with the pre-extinction *Paratirolites* Limestone: argillaceous nodular limestone intercalates with abundant marl beds. Up section at Kuh-e-Ali Bashi, the

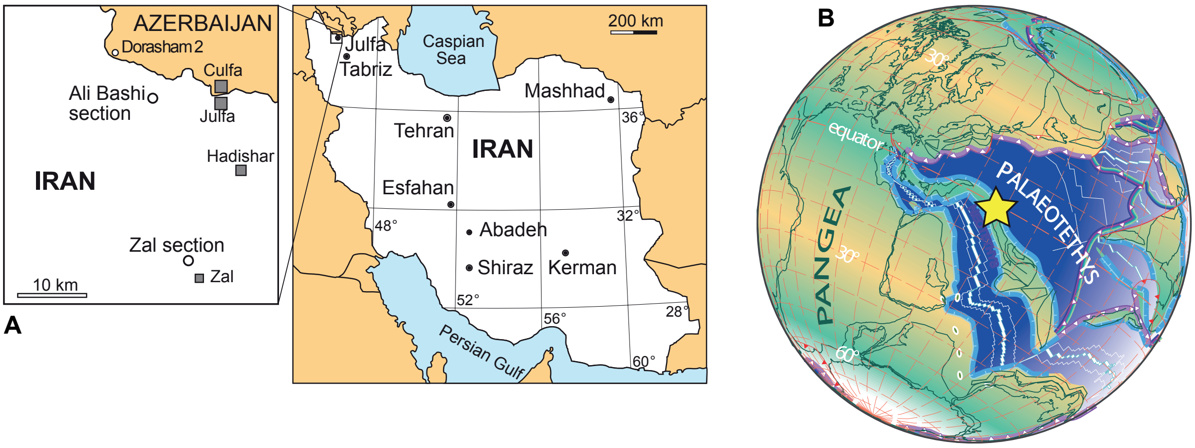

Figure 1 – (A) Geographical location and (B) palaeogeographic setting of the studied P-Tr boundary sections located in the Julfa region (NW Iran) (adapted from Stampfli and Borel (2002; also Stampfli, pers. com. 2011). Note that the colouring of the continents in the palaeogeographic map is not representative for climate zones and biomes.

lithology of the '*Claraia* Beds' is similar to that of the Zal consisting of grey, thick-bedded, platy limestone. Leda et al. (2014) recognised that these limestones exhibit a recrystallized texture, relating to microspar cementation and insitu recrystallization.

3 Methodology

Aliquots of the samples were taken from fresh surfaces of carbonate rocks, using a micro drill. Cracks, veins and stylolites were rejected to avoid contamination of the samples. Stable isotope measurements were carried out using a Thermo Finnigan Gasbench II linked online to a THERMO/Finnigan MAT V isotope ratio mass spectrometer in the stable isotope laboratory of the Museum für Naturkunde in Berlin. The accuracy of both, δ^{13}C and δ^{18}O was determined against laboratory standard material and the precision determined by repeated measurement was generally lower than ± 0.1 ‰ (1σ). Oxygen and carbon isotopes are reported relative to Vienna Pee Dee Belemnite (VPDB) in standard delta notation.

Bulk-rock samples, for elemental analysis, were optically inspected and any altered part, such as veins and weathering were cut off with a saw. The samples were subsequently crushed with the aid of a mechanical agate mill. Aliquots of one gram splits were used for elemental analysis of the acid soluble part; the remaining powder was used for bulk-rock element measurements. Acid digestion was carried out using 20 ml 0.33 M acetic acid and reacted over 48 hours, while constantly being agitated. The insoluble and soluble fractions were separated by filtration using a cellulose-nitrate membrane (0.45μm) and were then dried and weighed. A part of the soluble fraction was dissolved with a 0.2 M nitric acid in order to obtain a matrix matched solution for Inductively Coupled Plasma Optical Emission Spectrometer (ICP-OES) analysis carried out at the University of Copenhagen (Ullmann et al., 2013a). The Ca concentration of the solution was approximated; this allowed for a matrix match of the 0.2 M HNO_3 blank solution and multi-element reference solutions fabricated for a three-point calibration.

The precision was monitored by the international standards JDo-1 and JLs-1 yielding accuracies for Sr/Ca, Mn/Ca and Mg/Ca ratios with averages better than 5 % and reproducibility with averages better than 10% (2σ) (table 1) (Imai et al., 1996). Calcite ($CaCO_3$) concentrations of the samples were determined by the weight loss-acid digestion method by using a 2 M HCl solution (e.g., Siesser and Rogers, 1971). The program R and the packages; gridExtra, gTable and ggplot2, have been used for graphical plots and statistics (`http://cran.r-project.org/`).

Table 1 – Elemental ratios of the international certified standards JLs-1 and JDo-1 (published and measured; element ratios are taken from Imai et al., 1996).

	Sr/Ca	2σ	Mn/Ca	2σ	Mg/Ca	2σ
JDo-1 (n=3)						
measured	0.21	0.04	0.14	0.02	750.11	21.04
published	0.22		0.15		761.21	
JLs-1 (n=23)						
measured	0.34	0.01	0.03	0.00	14.09	0.24
published	0.34		0.03		15.02	

4 Results

4.1 *Carbon and oxygen isotopes*

Carbon and oxygen isotopes of carbonate bearing rocks from Kuh-e-Ali Bashi and Zal are -2.8 to 3.5 ‰ and -0.9 to 3.4 ‰ for δ^{13}C (VPDB), and -8.1 to -4.0 ‰ and -8.3 to -3.0 ‰ for δ^{18}O (VPDB), respectively (Figs. 2 and 3; Tables S2 and S3). We observed a general decline in whole-rock δ^{13}C upsection in both sections, starting within the *C. bachmanni* Zone. The pre-extinction brachiopod δ^{13}C values are slightly heavier but follow the general bulk-rock trend (Fig. 2; from Schobben et al., 2014). No articulated brachiopods are present in the post-extinction interval. The Kuh-e-Ali Bashi section is marked by two bulk-rock δ^{13}C minima of -1.4 and -0.7 ‰ at 1.70 and 0.71 m below the 'extinction horizon', respectively. An inflection to even lower bulk-rock values marks the transition towards the 'Boundary Clay'. However, this pattern is not observed at Zal, where bulk-rock δ^{13}C fluctuates around 1.5 ‰. Parallel bulk-rock δ^{13}C minima are observed at both sites within the *H. parvus* Zone. The carbon isotope values here are ~ -3.0 and -0.1 ‰ for Kuh-e-Ali Bashi and Zal, respectively, with a single sample in the latter section yielding a lower δ^{13}C value (-0.9 ‰ at +2.00 m). Post-extinction bulk-rock δ^{13}C of both sections remains more depleted than in pre-extinction strata, with values around -1 ‰. At Kuh-e-Ali Bashi, one additional negative δ^{13}C excursion (-1.4 ‰) occurs at 3.50 m above the 'extinction horizon'.

The bulk-rock oxygen isotope values from the lower *Paratirolites* Limestone of both sections are around -5.0 ‰ (Figs. 2 and 3; Tables S2 and S3). With the transition to the 'Boundary Clay' the values decline to -7.0 and -8.0 ‰, although slight fluctuations occur. The bulk-rock δ^{18}O remains more depleted (~ -7.0 ‰) upsection compared to pre-extinction strata. Calcite brachiopod shell δ^{18}O, taken from Schobben et al. (2014), are heavier than coeval bulk-rock data (-4.0 and -3.0 ‰ VPDB). A comparison of δ^{18}O of oxygen bound to phosphate- and carbonate-molecules from conodont apatite and bulk-rock carbonate, respectively, is not straightforward. This is due to different equilibrium fractionations between water and the respective solid phases caused by different temperature dependences constraining the fractionation factors (Wenzel et al., 2000). Corrections for conodont δ^{18}O (conodont δ^{18}O data are taken from Schobben et al., 2014), can be derived by two possibilities: (1) by comparing the offset between pristine brachiopod and conodont oxygen isotope data, and (2) by back-calculating conodont δ^{18}O derived palaeotemperatures (palaeotemperatures given in Schobben et al., 2014, with a carbonate-water fractionation equation, applying the equation of Kim and O'Neil, 1997).

Comparing the adjusted conodont δ^{18}O derived from these two methods reveal a discrepancy of up to 0.5 ‰ (cf. Wenzel et al., 2000 and Fig. S3). This uncertainty is given as error bars on the VPDB scale in Figures 2 and 3. Pre-extinction conodont δ^{18}O, with the applied correction, ranges between -4.0 and -3.0 ‰ VPDB (conodont δ^{18}O is often related to VSMOW, but we prefer here to present the data in the VPDB scale to simplify the carbonate/apatite comparison), with an uncertainty of about 0.5 ‰. Post-extinction conodont δ^{18}O values are more depleted and around -5.0 ‰ VPDB (uncertainty ~0.3 ‰).

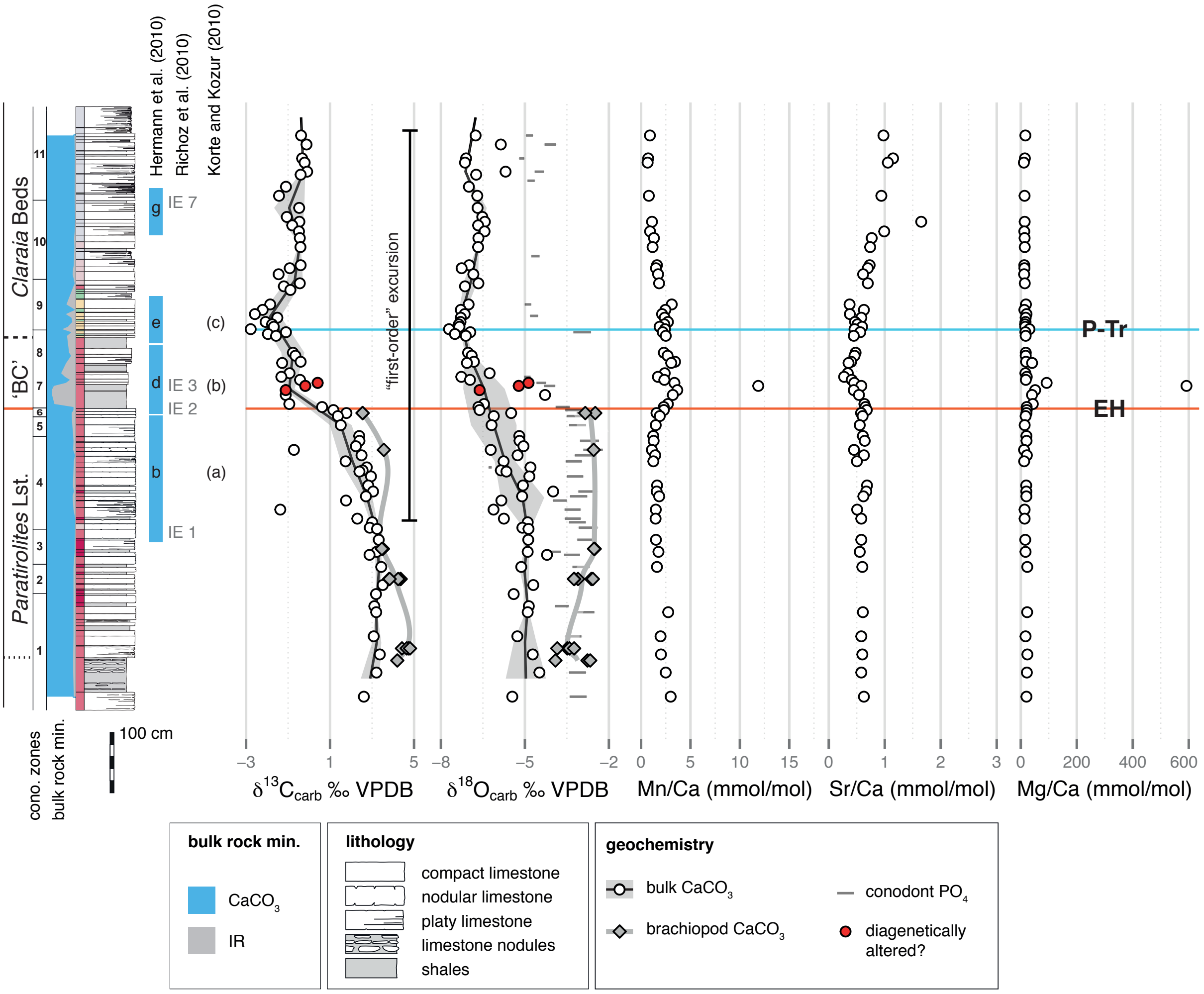

Figure 2 – (δ^{13}C, δ^{18}O, Mn/Ca, Sr/Ca and Mg/Ca of bulk-carbonate fraction and brachiopod calcite (Schobben et al., 2014) for the Kuh-e-Ali Bashi section. The conodont δ^{18}O taken from Schobben et al. (2014) are converted to the VPDB scale for a better comparison to the carbonate data. The widths of the bars of the conodont δ^{18}O data represent the carbonate/phosphate offset range constrained by the two different conversion methods (see section *4.1. Carbon and oxygen isotopes* and Fig. S3 for calculation). Bulk-rock mineralogy, respectively $CaCO_3$ and insoluble residue (IR), is depicted as percentage of total rock. A full explanation of the statistics for the trend lines of bulk-rock δ^{13}C and δ^{18}O is given in the supplementary discussion. First- and second-order carbon isotope trends are denoted next to the δ^{13}C values, according to the intervals of Hermann et al. (2010), isotope events (IE) of Richoz et al. (2010) and short-term trends of Korte and Kozur (2010). The brachiopod and bulk-rock δ^{13}C as well as the conodont and bulk-rock δ^{18}O show similar "first-order" stratigraphic trends toward lighter values in the post-extinction strata. The most outstanding features of bulk-rock element are the element enrichments within the 'Boundary Clay'. The red circles of the bulk-rock δ^{13}C and δ^{18}O are used to show elevated Mg/Ca (>mean + standard deviation; 1σ) Conodont zones are: (11) *I. staeschei*, (10) *H. lobota*, (9) *H. parvus*, (8) *M. ultima- S. ?mostleri*, (7) *H. praeparvus-H. changxingensis*, (6) *C. hauschkei*, (5) *C. abadehensis*, (4) *C. yini*, (3) *C. nodosa*, (2) *C. bachmanni*, (1) *C. changxingensis* (Kozur, 2007; Ghaderi et al., 2014).

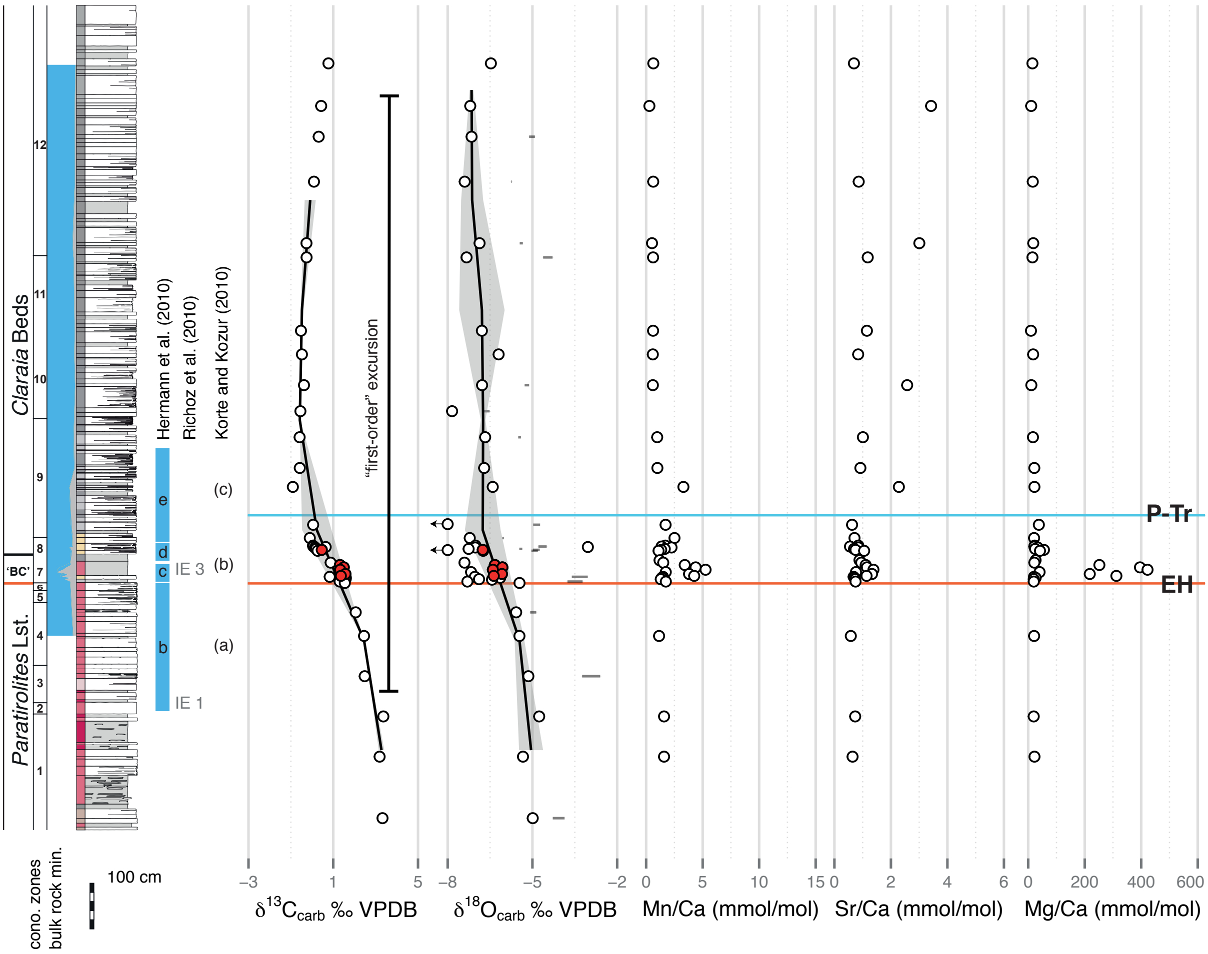

Figure 3 – δ^{13}C, δ^{18}O, Mn/ Ca, Sr/Ca and Mg/Ca of both bulk-carbonate fraction from the Zal section. Conodont δ^{18}O (taken from Schobben et al., 2014) are converted to the VPDB scale. The oxygen isotope trends from conodonts and bulk-rocks show similar trends to lighter values in the post-extinction strata. Element/Ca ratios are enriched in the 'Boundary Clay' unit with red circles of bulk-rock δ^{13}C and δ^{18}O representing elevated Mg/Ca ratios (>mean + standard deviation; 1σ). First- and "second-order" carbon isotope trends are denoted next to the δ^{13}C values, according to the intervals of Hermann et al. (2010), isotope events (IE) of Richoz et al. (2010) and short-term trends of Korte and Kozur (2010). Conodont zones are (12) *I. isarcica*, (11) *I. staeschei*, (10) *H. lobota*, (9) *H.parvus*, (8) *M. ultima- S. ?mostleri*, (7) *H. praeparvus-H. changxingensis*, (6) *C. hauschkei*, (5) *C. abadehensis*, (4) *C. yini*, (3) *C. nodosa*, (2) *C. bachmanni*, (1) *C. changxingensis* (reinterpreted from Kozur, 2007; Ghaderi et al., 2014).

4.2 *Element/Ca ratios*

Manganese – The *Paratirolites* Limestone of Kuh-e-Ali Bashi has relatively stable Mn/Ca ratios averaging about 1.8 mmol/mol (n = 25) for the calcite fraction (Fig. 2 and Table S2). A prominent peak of 11.9 mmol/mol occurs within the 'Boundary Clay' followed by a steady decrease, but remains higher than average pre-extinction values (mean of 2.4 mmol/mol; n = 24) up to a height of 2.35 m above the 'extinction horizon'. The lowest values at Kuh-e-Ali Bashi are recorded for the upper part of the '*Claraia* Beds', yielding an average of 0.9 mmol/mol (n = 9). The *Paratirolites* Limestone of Zal is marked by Mn/Ca ratios between 1.5 mmol/mol (n = 4) (Fig. 3 and Table S3). Similar to Kuh-e-Ali Bashi, the Zal section displays a marked positive excursion with a Mn/Ca maximum of 5.3 mmol/mol within the 'Boundary Clay'. Elevated Mn/Ca ratios between 1.1 and 3.3 mmol/mol occur within the interval up to 2.00 m above the 'extinction horizon'. The upper part of the '*Claraia* Beds' has Mn/Ca ratios of 0.6 to 0.7 mmol/mol (n = 10), and these are lowest ratios within the section.

Strontium – The Sr/Ca ratios are uniform throughout the *Paratirolites* Limestone of the Kuh-e-Ali Bashi section with an average 0.6 mmol/mol (n = 25) (Fig. 2 and Table S2). From the base of the 'Boundary Clay' to 2.00 m above, the Sr/Ca ratios are marked by some small fluctuations with a mean value of 0.5 mmol/mol (n = 23). The Sr/Ca ratios display an increase up to 0.9 mmol/mol in the '*Claraia* Beds' with a sharp positive excursion reaching 1.7 mmol/mol at 3.07 m above the 'extinction horizon'. The Sr/Ca ratios of the *Paratirolites* Limestone in the Zal section show an average of 0.7 mmol/mol (n = 4) (Fig. 3 and Table S3) with a peak of 1.4 mmol/mol within the 'Boundary Clay'. At 2.00 m above the 'extinction horizon', the Sr/Ca ratio displays large fluctuations with maxima of 2.32, 2.62, 3.05 and 3.48 mmol/mol.

Magnesium – The Mg/Ca values at Kuh-e-Ali Bashi and Zal are relatively stable for most of the successions with averages of 19.1 mmol/mol (sd = 6.3, n = 57) and 19.8 mmol/mol (sd = 6.7, n = 17), respectively. Distinctly higher Mg/Ca ratios occur in the 'Boundary Clay' of Kuh-e-Ali Bashi and Zal reaching 590 and 420 mmol/mol (Figs 2 and 3; Tables S2 and S3).

5 Discussion

5.1 *Comparison of P-Tr carbon isotope records*

The bulk-carbonate carbon isotope curves do not deviate substantially from earlier records (e.g., Korte et al., 2004c; Korte and Kozur, 2005; Richoz et al., 2010; Fig. 4). A long-term negative trend through the P-Tr boundary interval is clearly visible, resembling the results from coeval P-Tr 'Boundary Clay' sections (Abadeh and Meishan; Fig. 4) and shallow-water sections that lack a 'Boundary Clay' (Nhi Tao and Gartnerkofel; Fig. 4). The new isotope curves as well as published curves can be subdivided into intervals partly based on smaller-scale secondary δ^{13}C fluctuations superimposing the general long-term trend. This subdivision is implemented in coherence with previous interpretations of these curves, which will allow an evaluation of the validity of these views on stratigraphic importance as well as proposed causal relation to the end-Permian mass extinction (EPME) (e.g., Jin et al., 2000; Korte et al., 2004c; Korte and Kozur, 2005; Cao et al., 2009; Hermann et al., 2010; Richoz et al., 2010). In accordance with e.g., Hermann et al. (2010; cf. interval "b"), Richoz et al. (2010; cf. IE 1) and Korte and Kozur (2010; cf. short-term trend (a)) pre-extinction strata from the here considered 'Boundary Clay' and shallow-water sections are marked by a ~2 ‰ decrease in δ^{13}C (Figs. 2, 3 and 4). This excursion can be considered as the onset of the long-term negative carbon isotope trend which occurred before the EPME (Korte and Kozur, 2010; Fig. 4). A synchronous occurrence of this carbon isotope excursion among sites is likely but cannot be tested with the biostratigraphic framework as conodont specimens are lacking or difficulties exist when correlating different localities, for the South Chinese basin this is presumably due to endemism of conodont species (Kozur, 2007, but for a different opinion see Shen and Mei, 2010). In addition, pronounced secondary negative δ^{13}C spikes occur in the Paratirolites Limestone unit of the Kuh-e-Ali Bashi section (Figs. 3 and 4).

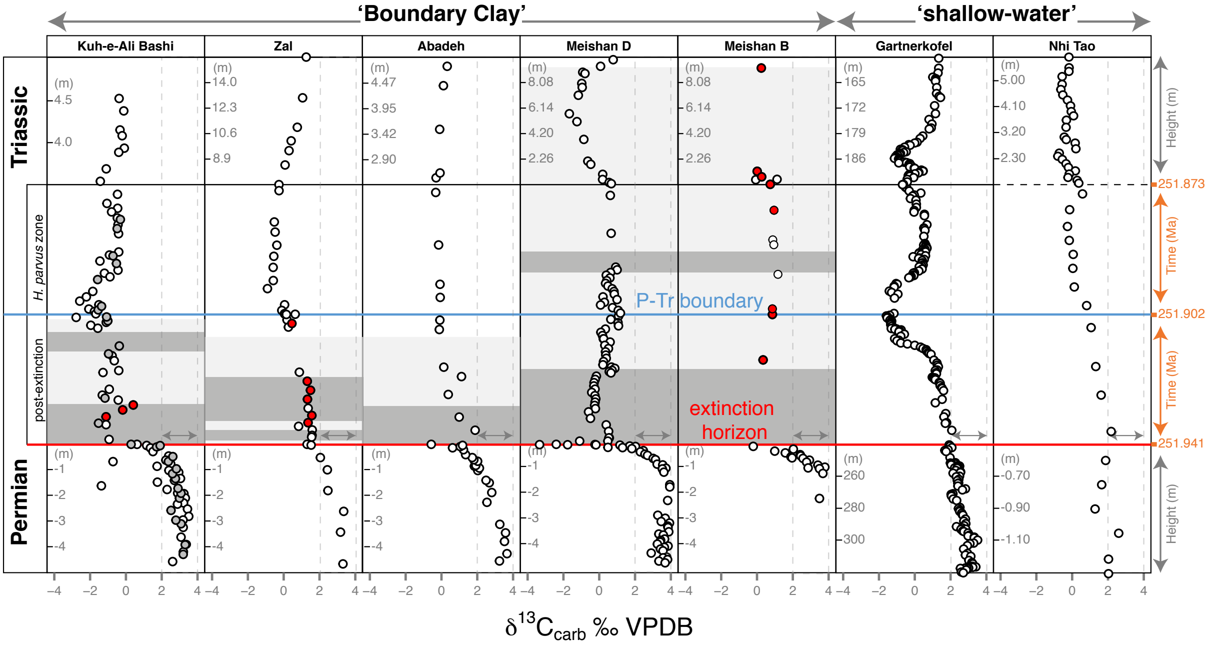

Figure 4 – δ^{13}C records from whole-rock, Kuh-e-Ali Bashi and Zal (this study—white dots; Korte and Kozur, 2005—grey dots), Abadeh (Korte et al., 2004a), Meishan D (Cao et al., 2009; Korte et al., 2005), Meishan B (Jin et al., 2000), Gartnerkofel (Holser et al., 1989) and Nhi Tao (Algeo et al., 2007, 2008). Note, that the y-axis partly represents stratigraphic heights and relative time. A relative timescale has been constructed for the interval between the 'extinction horizon' and the FAD *H. parvus* (post-extinction interval) and the *H. parvus* zone marked at the upper part by the FAD of *I. isarcica*. Biostratigraphy and 'extinction horizon' for Kuh-e-Ali Bashi and Zal (Kozur, 2007; Ghaderi et al., 2014), Meishan D and B (Jin et al., 2000; Yuan et al., 2014), and Gartnerkofel (Schönlaub, 1991; Korte and Kozur, 2010). Radiometric and interpolated ages are from Burgess et al. (2014). The FAD of *I. staeschei* zone is not recognized in the sites considered here but is likely analogous to the FAD of *I. isarcica*. A biostratigraphy for Nhi Tao is not available and correlation lines are therefore less certain. Red dots stand for δ^{13}C connected with significant Mg enrichment of the carbonate fraction (>mean + standard deviation; 1σ). The dark grey areas represent carbonate-bearing clay beds or volcanic ash layers (for Meishan). The light grey areas represent argillaceous limestone and limestone-clay alternations. Dotted vertical lines represent the pre-extinction baseline value for bulk-rock δ^{13}C.

However, these "second-order" δ^{13}C peaks are poorly supported by their surrounding values and are not observed at other sites, therefore they will not be further discussed.

The following interval, the 'extinction horizon', is marked by enhanced heterogeneity in stratigraphic whole-rock δ^{13}C patterns between the different sites due to small-scale secondary δ^{13}C fluctuations (Fig. 4). A shift to more negative carbon isotope values directly at the 'extinction horizon' is recorded at the Kuh-e-Ali Bashi, Abadeh and Meishan sections, possibly equivalent to IE 2 of Richoz et al. (2010) or interval "d" of Hermann et al. (2010). The most depleted values (-3.2 ‰) are reported by Cao et al. (2009) from a drillcore at Meishan D (Fig. 4). Many studies have placed an emphasis on large fluctuations in δ^{13}C, when searching for a causal relation with the EPME (for a discussion, see Korte and Kozur, 2010), recently, also the here considered δ^{13}C curve of Meishan D. The rapid secondary negative δ^{13}C fluctuation of ~7 ‰ of this record is possibly contained in an interval of ~2-20 kyr based on radiometric dates (Burgess et al., 2014) and has been explained by carbon isotope injection of isotopically depleted methane produced by newly evolved methanogens (Rothman et al., 2014). It is, however, possible that these clay-rich intervals have been affected by post-depositional alteration, thus the light δ^{13}C values might be the result of diagenetic alteration (for a discussion, see Korte and Kozur 2010 and Cao et al. 2009). These light, potentially secondary δ^{13}C values at the 'extinction horizon', have furthermore been related to local water-column conditions such as stratification and elevated organic matter remineralization (Cao et al., 2010). Similarly, the depleted δ^{13}C values at the 'extinction horizon' of the Kuh-e-Ali Bashi and Abadeh section compared to the Zal section (Fig. 4), is a feature that Korte and Kozur (2005, 2010) assigned to submodern weathering processes. In contrast, the δ^{13}C record of Zal, Nhi Tao, and Gartnerkofel show either a gradual depletion or even a stagnation (or plateau) across the 'extinction horizon' (Fig. 4). The latter feature, a δ^{13}C plateau, can be compared with interval "c" as described in Hermann et al. (2010), and according to Korte and Kozur (2010), these enriched δ^{13}C values are more likely to reflect primary seawater values (Figs. 2 and 3). Both Richoz et al. (2010) and Korte and Kozur (2010) suggested the existence of primary "second-order" positive δ^{13}C excursion in this interval, marked as respectively IE3 or short-term trend (b) for Kuh-e-Ali Bashi and Zal, in Figure 2 and 3.

A minimum in the "first-order" δ^{13}C trend at Kuh-e-Ali Bashi, Zal, Abadeh and Gartnerkofel (possibly also Nhi Tao) closely corresponds to the stratigraphic height of the FAD of *H. parvus* (Fig. 4) and is considered an important carbon isotope marker by Korte and Kozur (2010; cf. short-term trend (c)). However, clearly the FAD of *H. parvus* at the Meishan section is located at a "second-order" positive δ^{13}C excursion, and a minimum in the "first-order" δ^{13}C trend only follows up-section, which led Hermann et al. (2010) to suggest that *H. parvus* occurs diachronous at different sites. An Early Triassic "second-order" negative δ^{13}C excursion is often recognized at the height of the *I. isarcica* zone (cf. interval "g" of Hermann et al., 2010; Korte and Kozur, 2010) such as in the Gartnerkofel core (~ -2 ‰) and possibly the Kuh-e-Ali Bashi section (~ -1 ‰; Fig. 4). The intermediate stratigraphic δ^{13}C record (between the *H. parvus* and *I. isarcica* zone) represents a "second-order" positive δ^{13}C excursion at the Gartnerkofel and possibly Meishan and has been referred to as interval "f" by Hermann et al (2010) and is also reported by Korte and Kozur (2010). This has been postulated to represent a double peaked δ^{13}C curve (Xie et al., 2007). This double peaked carbon isotope excursion has been related two episodes of increased environmental disturbances and a second biodiversity crash (Jin et al., 2000; Xie et al., 2007; Yin et al., 2012). This feature, however, is difficult to extract from the new δ^{13}C record of Kuh-e-Ali Bashi and Zal. In addition, repeated Early Triassic "second-order" δ^{13}C excursions (<1 ‰) at the Nhi Tao section (Fig. 4) superimposed on the "first-order" δ^{13}C trend, have been related to episodic upwelling of sulphidic deep water on to the shelf (Algeo et al., 2007, 2008), such a mechanism might cause diachronous δ^{13}C fluctuations at different sites (Korte and Kozur, 2010).

This comparison reveals the different patterns and trends in bulk-rock δ^{13}C between Kuh-e-Ali Bashi, Zal and other sections. The origin of these δ^{13}C wiggles in our bulk-rock dataset will be discussed subsequently in relation to palaeoenvironmental parameters. To facilitate interpretation of their primary versus secondary origin, the “first-order” long-term and “second-order” short-term δ^{13}C trends will be discussed separately.

5.2 *”First-order”trend*

Micritic carbonate is mainly the product of biomineralization and carries geochemical signatures of the producing organism’s metabolism as well as the physical and chemical conditions in the ambient water. In addition, metastable biogenic carbonate, such as aragonite and high-Mg calcite, is generally transformed into secondary low-Mg calcite or dolomite during diagenesis, during which its chemical and physical properties can change (Veizer, 1983). Carbon as well as oxygen isotope chemistry of bulk-carbonate, however, can retain–at least to a certain degree–primary palaeoenvironmental information, but this depends on the extent of diagenesis, the burial temperature, and whether the diagenetic system was open or closed (Veizer, 1983; Marshall, 1992).

5.2.1 *Bulk-rock geochemical screening*

Bulk-rock δ^{13}C values are often screened by quantifying their correlation with δ^{18}O using Pearson’s r correlation coefficients (e.g., Heydari et al., 2001). Our data show a highly significant positive correlation between δ^{13}C and δ^{18}O (p-value <0.001; Table 2). This pattern is often ascribed to lithification of carbonate rocks under the influence of meteoric water or in phreatic lenses (Brand and Veizer, 1981). Such an interpretation may be too simplistic as a correlation can also represent a primary environmental signal (Marshall, 1992). The crossplots of the new as well as published isotope data (Fig. 5B) underscore the potential problem of using a correlation approach. The carbon and oxygen isotope pairs are positioned in a region of the plot that is not typical for carbonate rock lithified in contact with meteoric or phreatic water. In this representation mainly the bulk-rock δ^{18}O of Kuh-e-Ali Bashi, Zal and other P-Tr sections spread globally (southern Asia, southern Europe and Iran) are skewed to lower values, whereas bulk-rock carbon isotopes could constitute normal marine values (Fig. 5b). This is based upon a comparison with carbon and oxygen isotope values normally recorded in Cenozoic lithified carbonates not affected by late-stage diagenesis, reported by Knauth and Kennedy (2009). Cenozoic marine carbonate deposits lithified in coastal regions with exposure to meteoric water are often marked by isotopic depleted carbon and oxygen (Knauth and Kennedy, 2009). This covariant link between δ^{13}C and δ^{18}O has been related to post-depositional incorporation of isotopically light carbon from enzymatic decarboxylation of organic matter absorbed in the groundwater, which is recharged by low δ^{18}O of meteoric water. That lithification of our samples occurred in a marine environment without influence of meteoric water is in agreement with lithological results of the studied sections (Leda et al., 2014). In addition, the overlying >100 m of Triassic sediments contain no signs of subaerial exposure (see also Horacek et al., 2007; Richoz et al., 2010). Furthermore, brachiopod shell calcite δ^{13}C and δ^{18}O values represent normal marine values based on the screenings and on the crossplot in Figure 5B that is in agreement with interpretations of Schobben et al. (2014) of these samples from NW Iran.

Besides textural and lithological examination (e.g., Al-Aasm and Veizer, 1986), elemental data, especially Mn and Sr, are frequently utilized to identify diagenetic alteration in both bulk-rocks (Denison et al., 1994; Brand et al., 2012a, 2012b) and brachiopod shell calcite (Mii et al., 1999; Korte et al., 2005; Brand et al., 2012a). Manganese becomes normally enriched during post-depositional dissolution and recrystallization of carbonate (Pingitore, 1978; Brand and Veizer, 1980; Denison et al., 1994) while strontium, constrained by the initial primary concentration (Korte and Hesselbo, 2011), is lost due to dissolution of carbonate parts and recrystallization of diagenetic calcite phases (Veizer et al., 1971; Brand and Veizer, 1980). In addition, Mg/Ca ratios in calcite can help to distinguish between the different diagenetic end-members of low-Mg carbonate and dolomite (e.g., Brand and Veizer, 1980). Fixed elemental concentrations or ratios are often used to dis-

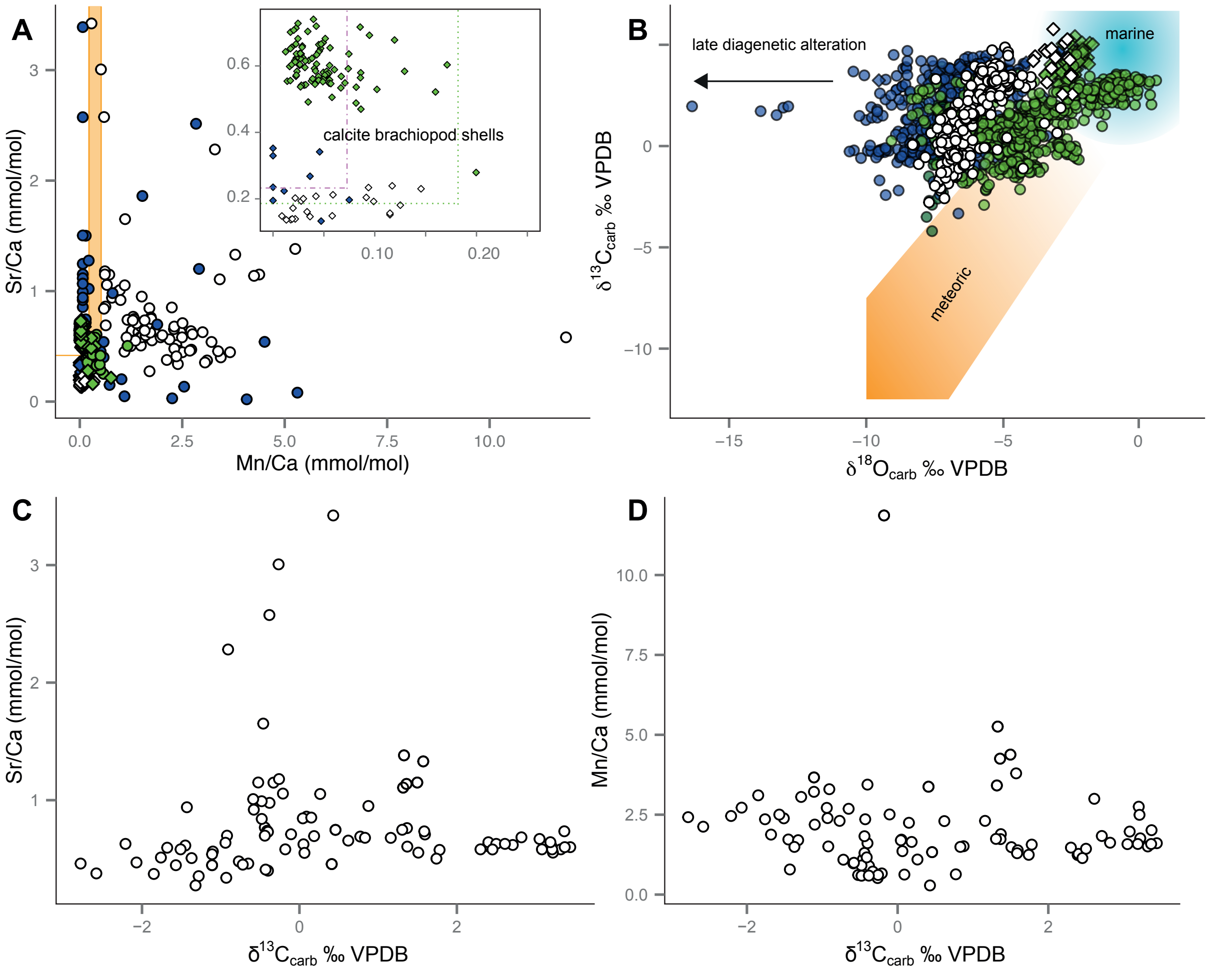

Figure 5 – Lumped stable isotope data and elemental concentrations. Diamonds represent brachiopods and open circles represent bulk-rock samples. (A) Boundaries for static limit based on calcite Mn and Sr concentrations as proposed for the selection of well-preserved bulk-rock samples (Denison et al., 1994) and brachiopods (Korte et al., 2003;2005; van Geldern et al., 2006). Elemental concentrations of brachiopod and whole-rock samples from Kuh-e-Ali Bashi, Zal (this study; Schobben et al., 2014), Val Brutta and Sas de Putia (Brand et al., 2012b) and Meishan (Korte et al., 2005; Riccardi et al., 2006). Note that most of the bulk-rock samples fall outside this range. (B) Plot of the paired stable isotope values from South China and Vietnam (blue), Meishan D (Cao et al., 2009; Korte et al., 2005), Meishan B (Jin et al., 2000), Nhi Tao (Algeo et al., 2007) and Cili (Luo et al., 2010); southern Alps and Bükk mountains (green), Val Brutta (Kearsey et al., 2009; Brand et al., 2012b), Sas de Putia (Korte and Kozur, 2005; Brand et al., 2012b), Tesero (Korte and Kozur, 2005), Gartnerkofel (Holser et al., 1989), Bulla (Korte and Kozur, 2005), Gerennavár (Korte and Kozur, 2005), Bálvány (Haas et al., 2006); Iran (white), Kuh-e-Ali Bashi, Zal (this study; Korte and Kozur, 2005; Schobben et al., 2014), Abadeh (Korte et al., 2004a). Included is the range of Cenozoic carbon and oxygen isotope values from rocks that lithified under influence of either marine or meteoric pore water from Knauth and Kennedy (2009). The arrows indicate the direction of the combined isotope signals normally followed during deep burial and metamorphic evolution. This representation shows that mainly the oxygen isotope values of bulk-rock are skewed to lighter values, which is normally not observed for calcite formed in a marine environment. In addition, the carbon isotope values are generally more enriched in ^{13}C than would be expected for lithification under the influence of meteoric or phreatic water. (C and D) $\delta^{13}C$ vs. Sr/Ca and Mn/Ca, respectively, from the Kuh-e-Ali Bashi and Zal sections.

Table 2 – Results for linear model fit between different chemical proxies. The correlation is calculated using Pearson's correlation coefficient (r^2), n = degrees of freedom, p = significance. High Pearson r^2 values indicate a high correlation; low p-values indicate a statistically significant correlation. IR = insoluble residue after acid digestion of a carbonate sample.

Section	x (response)	y (terms)	coefficient	Pearson r^2	*p*-value	n
Kuh-e-Ali Bashi	$\delta^{13}C$	$\delta^{18}O$	0.44	0.73	2.20E-16	78
Zal	$\delta^{13}C$	$\delta^{18}O$	0.51	0.34	5.64E-05	39
Kuh-e-Ali Bashi	Sr/Ca	Mn/Ca	-0.05	0.10	1.00E-02	58
Zal	Sr/Ca	Mn/Ca	-0.04	0.00	7.00E-01	33
Kuh-e-Ali Bashi	Sr/Ca	Mg/Ca	0.00	0.00	6.20E-01	58
Zal	Sr/Ca	Mg/Ca	0.00	0.00	7.80E-01	33
Kuh-e-Ali Bashi	Mn/Ca	$\delta^{13}C$	-0.18	0.02	2.93E-01	57
Zal	Mn/Ca	$\delta^{13}C$	0.27	0.08	9.95E-02	32
Kuh-e-Ali Bashi	Sr/Ca	$\delta^{13}C$	0.71	0.01	5.41E-01	57
Zal	Sr/Ca	$\delta^{13}C$	-0.55	0.11	5.77E-02	32
Kuh-e-Ali Bashi	Mn/Ca	IR	0.05	0.39	2.28E-07	55
Zal	Mn/Ca	IR	0.05	0.34	4.06E-04	31
Kuh-e-Ali Bashi	Sr/Ca	IR	-37.46	0.17	1.43E-03	55
Zal	Sr/Ca	IR	-2.87	0.02	4.59E-01	31

tinguish between altered and pristine carbonate (Fig. 5A). Applying these limits (whole-rock: Mn/Ca <0.22-0.51 mmol/mol and >Sr/Ca 0.42 mmol/mol, Denison et al., 1994; brachiopod shell: Mn/Ca <0.07 or 0.18 mmol/mol and Sr/Ca >0.18 or 0.23 mmol/mol, Korte et al., 2003; 2005; van Geldern et al., 2006), especially the high Mn/Ca ratios of the present dataset suggest clear post-depositional alteration of the bulk-rocks, but well preservation of the primary geochemical signal of the brachiopod shells (Schobben et al., 2014). Some Sr values of the brachiopods are relatively low but this is expected because this element can vary considerably through time, both within single specimens and in different fossil groups and were low in the latest Permian (for a discussion, see Steuber and Veizer, 2002; Korte and Hesselbo, 2011; Ullmann et al., 2013b). However, a number of arguments suggest, in this case, that elemental proxies do not unequivocally identify post-depositional alteration in bulk-rock samples:

(1) Correlations among the elemental proxies (Mn, Sr and Mg) are non-existent, suggesting that there is no common genetic link for these elements for indicating alteration (Table 2). (2) Partial retention of the primary Sr content in bulk-rocks is likely as the carbonate rock has comparatively higher Sr/Ca than brachiopod calcite (Fig. 5A) and measured calcite Sr/Ca is in the same range as that of modern carbonate deposits (Fig. 6B).

The observed elemental distribution might imply that the diagenetic history of the carbonate rock encompassed diagenetic fluids of variable chemical composition originating from differences in original mineralogy or sedimentation style. This suggests that fixed limits for elemental proxies can mislead in identifying altered carbonate $\delta^{13}C$ and $\delta^{18}O$. This is indicated by the absence of correlations between the elemental and isotopic data (Figs. 5C, D and Table 2)

5.2.2 *Comparative stable isotope geochemistry*

Calcite fossils, such as brachiopod shells, are relatively resistant to post-depositional alteration (Veizer et al., 1999; Korte et al., 2005). Hence, a comparison of geochemical data from whole-rock and fossils is potentially valuable as it can yield information about the extent of post-depositional alteration of the bulk-rock (e.g., Brand et al., 2012a, 2012b). Our carbon isotope data reveal an average offset of ~1.6 ‰ between brachiopods and bulk-rock samples (Fig. 2), which probably reflects pervasive weak alteration of bulk-rock $\delta^{13}C$ (cf.

Brand et al., 2012b) as there is no evidence for a general primary ^{13}C-enrichment in brachiopods compared to other carbonate fossils (Wefer and Berger, 1991). Calcite and aragonite components have typically different carbon isotope values, approximately 1.85 ‰ (Rubinson and Clayton, 1969), but a comparison of absolute values in the study units is hampered by the lack of knowledge about the original mineralogy of the bulk-rock carbonate. Primary marine carbonate in the study sections is likely to have been a mixture of different phases (Heydari et al., 2013) as is common with micritic carbonate rocks (Brand et al., 2012a, 2012b). A correction for whole-rock δ^{13}C of Late Permian carbonates was suggested by Brand et al. (2012b) assuming a possible original aragonite mineralogy.

This correction would result in a comparatively larger offset between δ^{13}C obtained from brachiopod shell and bulk-rock samples at the sites in NW Iran. In another approach, comparable relative changes in stratigraphic δ^{13}C trends for the Kuh-e-Ali Bashi and section suggest a common forcing and therefore an at least partial primary nature of bulk-rock carbon isotope values (Fig. 2). This suggests that at least parts of the primary signal are still retained in the bulk-carbonate rock (Ullmann et al., 2013a).

Recently, the application of oxygen isotopes measured on phosphate of conodont apatite has proven valuable for palaeoclimatic reconstructions of the latest Permian and Early Triassic (Joachimski et al., 2012; Sun et al., 2012; Romano et al., 2013; Schobben et al., 2014). Biogenic phosphate of conodont elements has been considered to be largely resistant to diagenesis, because of the highly impermeable nature of this biomineral matter (Wenzel et al., 2000; Pucéat et al., 2004; Joachimski et al., 2009).

In view of uncertainty in the conodont δ^{18}O correction factor (see section *4.1. Carbon and oxygen isotopes*), a 2 to 4 ‰ offset exists between the present conodont/brachiopod and bulk-carbonate δ^{18}O (Figs 2 and 3) suggesting strongly that the bulk-rock data are diagenetically altered. However, because the general decrease of the bulk-rock δ^{18}O matches across the extinction interval with that of conodont δ^{18}O (Joachimski et al., 2012; Schobben et al., 2014) diagenetically altered bulk-rocks can retain information about general palaeotemperature trends, despite loss of information regarding absolute palaeotemperatures (Figs 2 and 3). Oxygen isotopes of carbonate rocks of the investigated sites thus contain the burial temperature during recrystallization and/or the oxygen isotope composition of the diagenetic fluid. On the other hand, the retention of the palaeoenvironmental signal in the bulk-rock δ^{18}O would also suggest seawater warming across the EPME, verifying the interpretation of Holser et al. (1989), based on a bulk-rock δ^{18}O record from the southern Alps. Note, however, that the start of the bulk-rock oxygen isotope decrease is earlier than that of the conodonts (Fig. 2) and during a time when no trend is visible in the brachiopod data. This discrepancy in stratigraphic trends cannot be resolved at present.

Our observations imply a partial retention of primary carbon and oxygen isotope values in whole-rock samples - in both cases expressed as a preservation of stratigraphic trends in isotope composition. In contrast, comparisons of different components (calcite brachiopod shells, conodont elements and bulk-rock) from one horizon suggest an alteration of bulk-rock δ^{13}C and δ^{18}O. A relatively closed diagenetic environment with low water/rock ratios can explain the observed bulk-rock patterns (e.g., Banner and Hanson, 1990; Knauth and Kennedy, 2009). This further underscores that correlations of bulk-rock δ^{13}C and δ^{18}O can mislead when used to identify potential diagenetic alteration. In turn, the strong positive correlation between bulk-rock δ^{18}O and δ^{13}C at the P-Tr boundary is partly related to the palaeoenvironmental evolution (Figs. 2, 3, 5B; Table 2). It suggests that the often-ignored bulk-rock oxygen isotope data can be incorporated in evaluating diagenesis and palaeoenvironment.

5.3 *"Second-order" excursions*

An assessment of short-term carbon isotope excursions is complicated because of a lack of high-resolution biogenic collection and the difficulty in applying elemental concentrations as diagenetic tracers (see see section *5.2.1. Bulk-rock geochemical screening* and *5.2.2. Comparative stable isotope geochemistry*). The latter is mainly related to the spatial and temporal variation of both physical and chemical parameters during the diagenesis and/or in the marine environment. This is emphasized by the distribution patterns of Mn and Sr which is linked to lithological variation clearly visible at the unit boundaries (Figs. 5A and B) changing from nodular limestones (mainly *Paratirolites* Limestone unit) to clay ('Boundary Clay', or Aras Member) and platy limestones (mainly '*Claraia* Beds', see Supplementary Tables). The significance of this lithological subdivision in elemental data is further attested by a significant difference in Mn/Ca and Sr/Ca among lithological units, based on a Kruskal-Wallis rank sum test (p-value <0.001). This difference in elemental ratios is also expressed when comparing each of the lithological units, with each other, by a Mann-Whitney U test (p-value <0.001), except for Sr/Ca between the platy and clay unit of Zal.

The red-coloured nodular *Paratirolites* Limestone, which is the latest Permian pre-extinction lithology, is typified by hardground features such as microbial encrustation and ferromanganese crusts (Fig. 7A). The development of this sediment encompasses submarine carbonate dissolution, winnowing, and bio-erosion processes that are indicative of early seafloor lithification and diagenesis (Melim et al., 2002; Flügel, 2004). It is therefore tempting to relate the high Mn/Ca ratios from this unit (Fig. 6A) to a diagenetic fluid with high Mn concentrations due to reductive dissolution of abundant Mn-oxides and -hydroxides (Brand and Veizer, 1980; Banner and Hanson, 1990). A close correlation between Mn locked in calcite and in the clastic fraction (Table 2), especially in the 'Boundary Clay' (Fig. 2), may be attributable to diagenetic uptake of clay-derived Mn or, possibly, to the carbonate dissolution procedure that may have dissolved small quantities of Mn-oxides. In a study by Kuhn et al. (2005), calcite Mn was applied as a proxy to detect the continental detritus input; although their measured values and observed fluctuations are distinctly lower than those in the present study. Manganese enrichments by increased continental influx, however, fit also the interpretations explaining the nature of the 'Boundary Clay' which is related to a temporarily increased influx of weathered terrestrial material (Algeo and Twitchett, 2010; Algeo et al., 2011; Richoz et al., 2010; Leda et al., 2014). In addition, Mn is also a redox-sensitive element solubilized in oxygen-depleted water; it will be then incorporated in calcite during bio-mineralization (Freitas et al., 2006; Korte and Hesselbo, 2011). Mn enrichments can therefore be used as a tracer for dysoxic conditions, but oceanic anoxia are at odds with palaeoecological and facial interpretations of this interval at these sites (Kozur, 2007; Leda et al., 2014).

Strontium is highly enriched in the platy limestone unit of both sections (Fig. 6B). High Sr/Ca—almost equivalent to modern calcite deposits (Fig. 6B)—is a feature that has been related to an aragonite precursor rock (Veizer et al., 1971; Heydari et al., 2013). Cenozoic limestone units that do not undergo lithification under meteoric water influence are thought to preserve high-Sr aragonite constituents to some extent (Melim et al., 2002). Low Sr/Ca calcite observed in the nodular units could, in this view, relate to longer exposure to seawater that is undersaturated with respect to aragonite. The possible microbial origin of the platy limestone, possibly by authigenic aragonite precipitation, may also relate to higher carbonate Sr/Ca (Richoz et al., 2010; Leda et al., 2014). A higher degree of crystallization marks the platy limestone (Leda et al., 2014 and Fig. 7B) and is somewhat counter intuitive to the idea of a relative better Sr preservation. However, similar observations in Early Triassic rock have been explained by recrystallization of metastable high-Sr aragonite components (Heydari et al., 2013).

A conspicuous feature of element distribution patterns is the enrichment of Mg/Ca in calcite of the 'Boundary Clay' (Figs 2 and 3). Magnesium displays a disproportional increase when compared with increased clastic content of the 'Boundary Clay', Mg enrichment being ten times greater than the clastic content. In addition, some of these enriched Mg/Ca values are higher than normally observed in biological calcite suggesting diagenetic enrichment. This chemical signature is of importance, as it encompasses a critical interval within the studied section with respect to palaeoenvironmental studies dealing with the EPME. The high

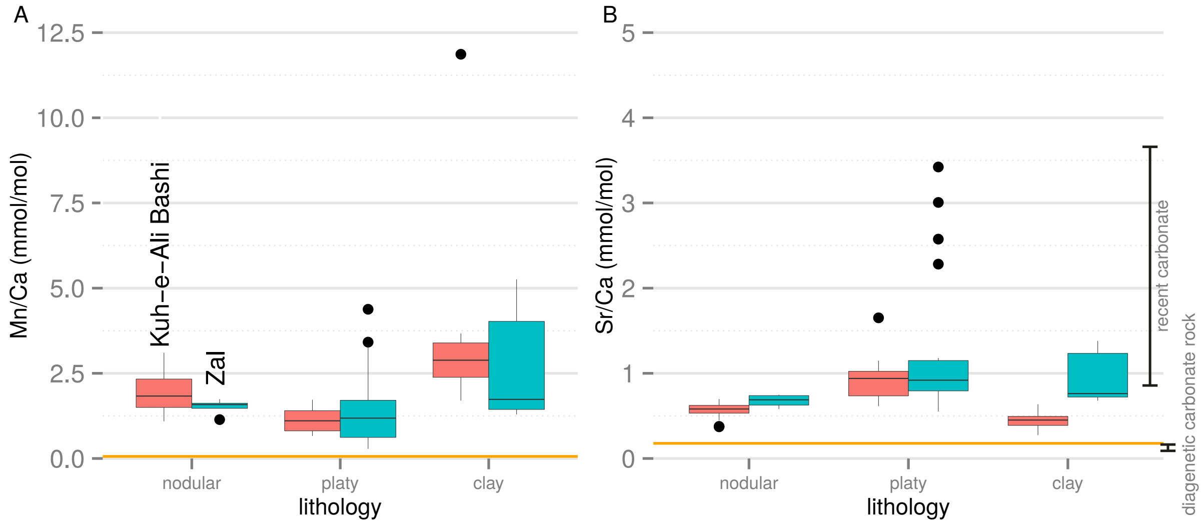

Figure 6 – Elemental data for the different lithological units (red: Kuh-e-Ali Bashi; blue: Zal), yellow lines representing the average value of the brachiopod calcite. (A) Mn/Ca, the lowest levels are seen in the platy limestone unit, the nodular limestone unit has slightly higher levels and the 'Boundary Clay' displays the highest and most variable Mn/Ca values. (B) Sr/Ca values differ substantially between the two limestone-dominated units (nodular and platy) for both sections, whereas the 'Boundary Clay' is marked by a higher variability within and between the sections. The range of Sr/Ca observed in modern carbonate deposits (Bathurst, 1976) is shown on the right hand side in the box plot; diagenetic cements (Banner, 1995) are added. Note that bulk-rock Sr/Ca falls in the range of values observed in modern carbonates.

Mg/Ca content, together with the occurrence of rhombic crystals of dolomite in this interval, suggests a localized process of dolomitization (Leda et al., 2014 and Fig. 5C). This late-stage dolomitization can occur due to the presence of Mg-enriched diagenetic fluids, with the transformation of smectite to illite as a source of Mg (Flügel, 2004, p. 330), and is a common type of late-stage dolomitization associated with argillaceous mudstones (McHargue and Price, 1982; Sternbach and Friedman, 1986). Furthermore, normal saline marine water and the below wave-base deposition of these rocks based on facies and faunal interpretations (Kozur, 2007; Leda et al., 2014), likely opposes the idea of an early-stage dolomite development.

We have demonstrated that ratios of Mn and Sr are inconclusive with regards to diagenetic alteration of carbonate rock in the investigated sections. Furthermore, the close correspondence of Mn and Sr with lithology might limit the common approach of using Mn/Sr ratios to detect carbonate diagenesis. The indication of dolomitization in the 'Boundary Clay' is a significant sign of post-depositional alteration of carbonate rock and is confined to a short stratigraphic interval in these P-Tr successions. We demonstrate with this observation that spatial heterogeneity in diagenesis exists, at a scale that is similar to the short-term secondary carbon isotope fluctuations (see section *5.1. Comparison of P-Tr carbon isotope records*). The significance of this is further expressed by the knowledge that dolomitization and clastic-dominated sections show a larger spread in both δ^{13}C and δ^{18}O (Knauth and Kennedy, 2009; Brand et al., 2012a). Note, however, that primary carbonate components should have existed based on calcite fossil (e.g., ostracods) occurrences detected in thin sections (Fig. 7D). In addition, a "second-order" δ^{13}C fluctuation is noted in the Early Triassic (*I. staeschei* conodont zone) of Kuh-e-Ali Bashi and cannot be assigned to a post-depositional overprint from the currently available geochemical and lithological data (Fig. 2).

5.4 *Relevance for the end-Permian carbon cycle perturbation*

The purpose of this section is to evaluate to what extent the δ^{13}C curves can be interpreted as genuine seawater chemistry changes with implications for commonly proposed causal rela-

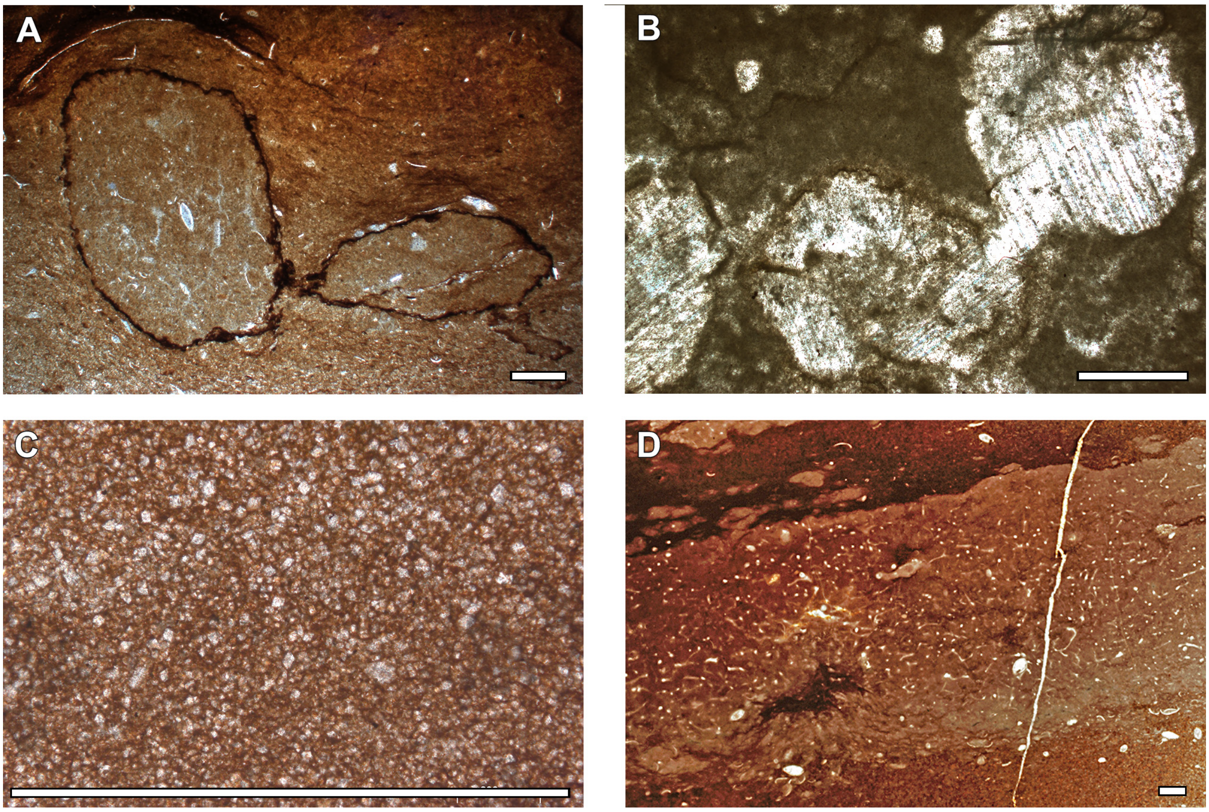

Figure 7 – Microphotographs of key lithological and textural observations (scale bars = 1 mm). (A) Carbonate rock from the *Paratirolites* Limestone (nodular limestone). Hardground intraclasts ('subsolutionclasts') with Fe–Mn crusts and biogenic encrustation around micrite clasts. Ali Bashi 1, 0.75 m below 'extinction horizon', adapted from Leda et al. (2014). (B) Sample from the base of the '*Claraia* Beds' (platy limestone) showing clear signs of recrystallization (e.g., sparry calcite spheres). Ali Bashi 1, 4.15 m above 'extinction horizon', adapted from Leda et al. (2014). (C) Example from the 'Boundary Clay' with abundant rhombic crystals floating in a clay matrix, Ali Bashi 1, 0.40 m above 'extinction horizon'. (D) Another example from the 'Boundary Clay' containing ostracods, sponge remains, and signs of bioturbation. Ali Bashi 1, 0.75 m above 'extinction horizon'.

tionships with the carbon cycle perturbation and EPME. The broad long-term depletion of carbon isotope ratios in marine carbonate successions bracketing the P-Tr boundary has been recognized in many sections worldwide (Korte and Kozur, 2010), including the sites studied here. This feature may be related with high confidence to a primary environmental signal based on comparative biogenic geochemistry. Preservation of this trend is possibly governed by marine lithification of the carbonate sediments, instead of lithification under the influence of meteoric water, as has been observed in recent and ancient subaerially exposed carbonates (Allan and Matthews, 1980; Algeo et al., 1992). This type of lithification and diagenetic pathway might be common for the preservation of an original geochemical signature, such as δ^{13}C and δ^{18}O in calcite, from the P-Tr time interval (Fig. 5B), and possibly other ancient time-intervals as well (e.g., Veizer et al., 1999). Contesting with Early P-Tr studies which commonly inferred a major sea-level fall owing to a perceived biostratigraphic gap at the boundary (references in Hallam and Wignall, 1999), and some recent studies (Yin et al., 2013). However, sedimentologic evidence for a sea-level fall remains weak: the karstic origin of bedding surfaces in South China carbonate sections (Payne et al., 2007) has been challenged (Wignall et al., 2009), and beds that were earlier interpreted as lowstand deposits at Guryul Ravine, India (Algeo et al., 2007) have more recently been re-interpreted as tsunamites (Brookfield et al., 2013).

Superimposed on this δ^{13}C trend are smaller-scale secondary fluctuations, which in some instances likely reflect original isotopic compositions of marine DIC. However, localized dolomitization in the 'Boundary Clay' may explain the somewhat deviating pattern of δ^{13}C between both sections (Figs. 2 and 3) and might suggest that the more enriched values at Zal (the plateau of δ^{13}C) are not as suggested by Korte and Kozur,(2010) a more reliable representation of original seawater chemistry. More so, it suggests that diagenetic alteration of calcite is possible in confined stratigraphic intervals, of perhaps 10 to 30 cm and is not easily identified when lumping all whole-rock δ^{13}C data together (Fig. 5B) and requires more detailed analysis. Thus, the isotope results should be interpreted with these observations in mind, at least for the P-Tr 'Boundary Clay' sections. The prevalence of 'Boundary Clay' type lithologies at other P-Tr sections, which has been argued to be the result of the selective extinction of calcite secreting organisms or increased terrigenous input (e.g., Knoll et al., 2007; Algeo and Twitchett, 2010; Algeo et al., 2011; Richoz et al., 2010; Leda et al., 2014), stands against palaeoenvironmental interpretations of the associated δ^{13}C signatures within these carbonate-bearing rocks. Besides the here studied sites elemental and isotope data from the Meishan B section (Figs. 4 and S4; Jin et al., 2000; Riccardi et al., 2006) might confirm a relation between dolomitization and more enriched δ^{13}C values at these sites as well. This makes the positive "second-order" δ^{13}C excursion confound to stratigraphic level of *H. parvus* at Meishan (B and D) as well as the spurious "second-order" negative carbon isotope excursion at the 'extinction horizon' (Cao et al., 2009; Korte and Kozur, 2010) a possible product of diagenetic alteration. In addition, a relation between dolomitization and more positive δ^{13}C values for these beds has already been pointed out by Xie and Wang (2011). This would suggest that interval "f" of Hermann et al, at least for bulk-carbonate rock δ^{13}C, is an artefact of diagenesis and that *H. parvus* occurs likely synchronous. Whereas, a "second-order" negative δ^{13}C excursion in the Early Triassic (interval "g"; Hermann et al., 2010 or IE 7; Richoz et al., 2010) is likely a primary signal and suggest that a second disturbance could relate to a second extinction peak an intensified environmental disturbances (Jin et al., 2000; Xie et al., 2007; Yin et al., 2012) or alternatively episodic upwelling of sulphidic deep water on to the shelf (Algeo et al., 2007, 2008). The high-variability in carbon isotope records from other P-Tr sections due to "second-order" δ^{13}C fluctuations of different shapes, stratigraphic positions, and magnitudes (for a comparison, see Korte and Kozur, 2010 and Fig. 4) require a pragmatic approach in interpretation. Conclusively, these P-Tr boundary "second-order" excursions are probably not useful as stratigraphic markers as seen when comparing the here discussed δ^{13}C records (Fig. 4). In addition the observed differences might be amplified by different sampling densities of the Kuh-e-Ali Bashi and Zal sections. Varying sampling strategies applied in different studies are probably a common factor to contend with. In addition, short-term differences in sedimentation rates between sections would result in a similar effect. This is, for instance, important when comparing the P-Tr localities in Iran and South China, as the latter are marked by higher sedimentation rates around the 'extinction horizon' (for a discussion, see Kozur, 2007).

We consider for the studied sections that the carbon isotope values connected with high Mg/Ca should be disregarded, to enable a direct comparison of the succession and in support of reliable palaeoenvironmental interpretations. Furthermore, a trend-line based on subsampling at the level of the minimum sampling density (see supplementary discussion) helps to best visualize general δ^{13}C changes (Figs. 2 and3). As such, the sedimentary record straddling the 'extinction horizon' from the *C. bachmanni* Zone up to the P-Tr boundary is distinct with decreasing δ^{13}C (Figs. 2 and 3) followed by a minimum of δ^{13}C close to the FAD of *H. parvus* , possibly followed by a "second-order" negative δ^{13}C spike at the height of the *I. staeschei* or *I. isarcica* zones. The studied sections show both the biotic decline as well as the lithological change: the 'Boundary Clay' associated with environmental changes precedes maximum depletion of whole-rock δ^{13}C (Figs. 2 and 3). This is the information that can be extracted from δ^{13}C of bulk-rock material of the studied sections with the highest likelihood of reflecting true ambient seawater DIC. We suspect that "second-order" negative as well as positive δ^{13}C excursions superimposed on the "first-order" δ^{13}C trend close to the 'extinction horizon' in 'Boundary Clay' P-Tr sections are influenced by diagenetic processes. We suggest, however, that the long-term "first-order" δ^{13}C trend may also directly be invoked in extinction scenarios. This long-term excursion could be interpreted as a prolonged carbon cycle perturbation (e.g., caused by accumulative volcanic outgassing and related effects), triggering at some level a cascading biological and environmental catastrophe or–in other words–crossing a tipping point in the Earth system, culminating in this rapid mass extinction interval (0.061 ± 0.048 Mya: Burgess et al., 2014). This would necessitate positive feedback loops or synergistic effects to initiate a rapid warming event as recorded by conodont oxygen isotope records (Joachimski et al., 2012; Schobben et al., 2014). Climate warming may trigger extinction mechanisms, such as water column euxinia or bio-calcification crises (Wignall, 2001; 2007; Kump et al., 2005; Knoll et al. 2007). These climate feedback mechanisms may constitute scenarios of dramatic carbon cycle perturbation—such as methane clathrate dissociation—which could have been recorded in the isotopic composition of time-equivalent marine DIC. However, this study highlights that small-scale secondary changes in carbonate δ^{13}C of bulk-rock cannot, on their own, be used as the basis for recognition of these types of carbon cycle perturbations. Consequently, we urge the use of multiple proxies, such as the application of carbon isotope analysis, on bulk or, even better, compound specific organic matter.

6 Conclusions

The application of geochemical screening to identify the extent of diagenetic alteration of calcite is difficult because Mn and Sr, which are often used as tracers for post-depositional alteration, also record palaeoenvironmental information. In addition, varying chemical and physical properties of diagenesis at different spatial and temporal scales complicate the matters. For example, diagenetic resetting in bulk-rock carbonate can overprint the palaeoclimatic signal, but, in turn, past climate information can be partially retained. The best evidence for post-depositional alteration is obtained by a bed-by-bed geochemical approach. Superimposed secondary δ^{13}C fluctuations that are confined to small stratigraphic intervals should be considered with caution when used for reconstructing palaeoenvironmental conditions, especially when occurring in clay-rich intervals such as the P-Tr 'Boundary Clay'. The general negative carbon isotope excursions across the P-Tr boundary, however, are a secular feature and caused by a strong and prolonged carbon cycle perturbation.

Acknowledgments

We acknowledge the Aras Free Zone office and particularly Adel Najafzadeh (Tabriz) for permission to sample the sites, Kuh-e-Ali Bashi and Zal. We sincerely thank Kathrin Krahn, Melanie Rühl and Carina Klein (Museum für Naturkunde) for technical assistance. We are grateful for assistance with statistical analysis by Melanie Tietje (Museum für Naturkunde) and a language check by Sonny A. Walton (Museum für Naturkunde). This investigation was funded by the Deutsche Forschungsgemeinschaft (DFG; projects KO1829/12-1, KO1829/12-2 and KO2011/8-1).

References

Al-Aasm, I.S., Veizer, J., 1986. Diagenetic stabilization of aragonite and low-Mg calcite; I, Trace elements in rudists. Journal of Sedimentary Research 56, 138-152.

Allan, J.R., and Matthews, R.K., 1982. Isotopic signatures associated with early meteoric diagenesis. Sedimentology 29, 797-817.

Algeo, T.J., Twitchett, R.J., 2010. Anomalous Early Triassic sediment fluxes due to elevated weathering rates and their biological consequences. Geology 38, 1023-1026.

Algeo, T.J., Shen, Y., Zhang, T., Lyons, T.W., Bates, S.M., Rowe, H., Nguyen, T.K.T., 2008. Association of ^{34}S-depleted pyrite layers with negative carbonate δ^{13}C excursions at the Permian/Triassic boundary: Evidence for upwelling of sulfidic deep-ocean watermasses. Geochemistry Geophysics Geosystems 9, Q04025, 10 pp.

Algeo, T.J., Ellwood, B.B., Nguyen, T.K.T., Rowe, H., Maynard, J.B., 2007. The Permian-Triassic boundary at Nhi Tao, Vietnam: Evidence for recurrent influx of sulfidic watermasses to a shallow-marine carbonate platform. Palaeogeography Palaeoclimatology Palaeoecology 252, 304-327.

Algeo, T.J., Chen, Z.Q., Fraiser, M.L., Twitchett, R.J., 2011. Terrestrial-marine teleconnections in the collapse and rebuilding of Early Triassic marine ecosystems. Palaeogeography Palaeoclimatology Palaeoecology 308, 1-11.

Algeo, T.J., Wilkinson, B.H., and Lohmann, K.C, 1992, Meteoric-burial diagenesis of Pennsylvanian carbonate: water/rock interactions and basin geothermics. Journal of Sedimentary Petrology 62, 652-670.

Algeo, T.J., Hannigan, R., Rowe, H., Brookfield, M., Baud, A., Krystyn, L., and Ellwood, B.B., 2007. Sequencing events across the Permian-Triassic boundary, Guryul Ravine (Kashmir, India). Palaeogeography Palaeoclimatology Palaeoecology 252, 328-346.

Auguie, B., 2012. gridExtra: functions in Grid graphics, R package version 0.9.1. ed.

Banner, J.L., 1995. Application of the trace element and isotope geochemistry of strontium to studies of carbonate diagenesis. Sedimentology 42, 805-824.

Banner, J.L., Hanson, G.N., 1990. Calculation of simultaneous isotopic and trace element variations during water-rock interaction with applications to carbonate diagenesis. Geochimica et Cosmochimica Acta 54, 3123-3137.

Bathurst, R.G.C., 1976. Carbonate sediments and their diagenesis. Elsevier, Amsterdam.

Benton, M.J., Twitchett, R.J., 2003. How to kill (almost) all life: the end-Permian extinction event. Trends in Ecology & Evolution 18, 358-365.

Berner, R.A., 2002. Examination of hypotheses for the Permo-Triassic boundary extinction by carbon cycle modeling. Proceedings of the National Academy of Sciences of the United States of America 99, 4172-4177.

Brand, U., Jiang, G., Azmy, K., Bishop, J., Montanez, I.P., 2012a. Diagenetic evaluation of a Pennsylvanian carbonate succession (Bird Spring Formation, Arrow Canyon, Nevada, USA)-1: Brachiopod and whole rock comparison. Chemical Geology 308, 26-39.

Brand, U., Posenato, R., Came, R., Affek, H., Angiolini, L., Azmy, K., Farabegoli, E., 2012b. The end-Permian mass extinction: A rapid volcanic CO_2 and CH_4-climatic catastrophe. Chemical Geology 322, 121-144.

Brand, U., Veizer, J., 1980. Chemical diagenesis of a multicomponent carbonate system-1: Trace elements. Journal of Sedimentary

Petrology 50, 1219-1236.

Brand, U., Veizer, J., 1981. Chemical diagenesis of a multicomponent carbonate system-2: stable isotopes. Journal of Sedimentary Research 51, 987-997.

Brookfield, M.E., Algeo, T.J., Hannigan, R., Williams, J., Bhat, G.M., 2013. Shaken and stirred: Seismites and tsunamites at the Permian-Triassic boundary, Guryul Ravine (Kashmir, India). Palaios 28, 568-582.

Burgess, S.D., Bowring, S., Shen, S.-z., 2014. High-precision timeline for Earth's most severe extinction. Proceedings of the National Academy of Sciences 111, 3316-3321.

Cao, C., Love, G.D., Hays, L.E., Wang, W., Shen, S., Summons, R.E., 2009. Biogeochemical evidence for euxinic oceans and ecological disturbance presaging the end-Permian mass extinction event. Earth and Planetary Science Letters 281, 188-201.

Cao, C.Q., Yang, Y.C., Shen, S.Z., Wang, W., Zheng, Q.F., Summons, R.E., 2010. Pattern of $\delta^{13}C_{carb}$ and implications for geological events during the Permian-Triassic transition in South China. Geological Journal 45, 186-194.

Collin, P.-Y., Kershaw, S., Crasquin-Soleau, S., Feng, Q., 2009. Facies changes and diagenetic processes across the Permian-Triassic boundary event horizon, Great Bank of Guizhou, South China: a controversy of erosion and dissolution. Sedimentology 56, 677-693.

Denison, R.E., Koepnick, R.B., Fletcher, A., Howell, M.W., Callaway, W.S., 1994. Criteria for the retention of original seawater ^{87}Sr/^{86} in ancient shelf limestones. Chemical Geology 112, 131-143.

Erwin, D.H., Bowring, S.A., Jin, Y.-g., 2002. End-Permian mass extinctions: A review., in: Koeberl, C., MacLeod, K.G. (Eds.), Catastrophic events and mass extinctions: Impacts and beyond. Geological Society of America Special Paper pp. 363–383.

Flügel, E., 2004. Microfacies of carbonate rock. Springer, Berlin, Germany.

Freitas, P.S., Clarke, L.J., Kennedy, H., Richardson, C.A., Abrantes, F., 2006. Environmental and biological controls on elemental (Mg/Ca, Sr/Ca and Mn/Ca) ratios in shells of the king scallop Pecten maximus. Geochimica et cosmochimica acta 70, 5119-5133.

Ghaderi, A., Leda, L., Schobben, M., Korn, D., Ashouri, A.R., 2014. High-resolution stratigraphy of the Changhsingian (Late Permian) successions of NW Iran and the Transcaucasus based on lithological features, conodonts and ammonoids.Fossil Record 17, 41-57.

Haas, J., Demény, A., Hips, K., Vennemann, T.W., 2006. Carbon isotope excursions and microfacies changes in marine Permian–Triassic boundary sections in Hungary. Palaeogeography, Palaeoclimatology, Palaeoecology 237, 160-181.

Hallam, A., and Wignall, P.B., 1999. Mass extinctions and sea-level changes. Earth-Science Reviews 48, 217-250.

Heydari, E., Arzani, N., Safaei, M., Hassanzadeh, J., 2013. Ocean's response to a changing climate: Clues from variations in carbonate mineralogy across the Permian–Triassic boundary of the Shareza Section, Iran. Global and Planetary Change 105, 79-90.

Heydari, E., Hassanzadeh, J., Wade, W.J., Ghazi, A.M., 2003. Permian-Triassic boundary interval in the Abadeh section of Iran with implications for mass extinction: Part 1-Sedimentology. Palaeogeography Palaeoclimatology Palaeoecology 193, 405-423.

Heydari, E., Wade, W.J., Hassanzadeh, J., 2001. Diagenetic origin of carbon and oxygen isotope compositions of Permian-Triassic boundary strata. Sedimentary Geology 143, 191-197.

Hermann, E., Hochuli, P.A., Bucher, H., Vigran, J.O., Weissert, H., Bernasconi, S.M., 2010. A close-up view of the Permian–Triassic boundary based on expanded organic carbon isotope records from Norway (Trøndelag and Finnmark Platform). Global and Planetary Change 74, 156-167.

Holser, W.T., Magaritz, M., 1987. Events near the Permian–Triassic boundary. Modern Geology 11, 155–180.

Holser, W.T., Schönlaub, H.-P., Attrep, M., Boeckelmann, K., Klein, P., Magaritz, M., Orth, C.J., Fenninger, A., Jenny, C., Kralik, M., 1989. A unique geochemical record at the Permian/Triassic boundary. Nature 337, 39-44.

Horacek, M., Richoz, S., Brandner, R., Krystyn, L., Spötl, C., 2007. Evidence for recurrent changes in Lower Triassic oceanic circulation of the Tethys: The δ^{13}C record from marine sections in Iran. Palaeogeography, Palaeoclimatology, Palaeoecology 252, 355-369.

Imai, N., Terashima, S., Itoh, S., Ando, A., 1996. Compilation Of Analytical Data On Nine Gsj Geochemical Reference Samples, “sedimentary Rock Series”. Geostandards Newsletter 20, 165-216.

Jin, Y.G., Wang, Y., Wang, W., Shang, Q.H., Cao, C.Q., Erwin, D.H., 2000. Pattern of marine mass extinction near the Permian-Triassic boundary in South China. Science 289, 432-436.

Joachimski, M.M., Breisig, S., Buggisch, W., Talent, J.A., Mawson, R., Gereke, M., Morrow, J.R., Day, J., Weddige, K., 2009. Devonian climate and reef evolution: Insights from oxygen isotopes in apatite. Earth and Planetary Science Letters 284, 599-609.

Joachimski, M.M., Lai, X., Shen, S., Jiang, H., Luo, G., Chen, B., Chen, J., Sun, Y., 2012. Climate warming in the latest Permian and the Permian-Triassic mass extinction. Geology 40, 195-198.

Kearsey, T., Twitchett, R.J., Price, G.D., Grimes, S.T., 2009. Isotope excursions and palaeo-temperature estimates from the Permian/
Triassic boundary in the Southern Alps (Italy). Palaeogeography, Palaeoclimatology, Palaeoecology 279, 29-40.

Kim, S.T., O’Neil, J.R., 1997. Equilibrium and nonequilibrium oxygen isotope effects in synthetic carbonates. Geochimica Et Cosmochimica Acta 61, 3461-3475.

Knauth, L.P., Kennedy, M.J., 2009. The late Precambrian greening of the Earth. Nature 460, 728-732.

Knoll, A.H., Barnbach, R.K., Payne, J.L., Pruss, S., Fischer, W.W., 2007. Paleophysiology and end-Permian mass extinction. Earth and Planetary Science Letters 256, 295-313.

Korte, C., Hesselbo, S.P., 2011. Shallow marine carbon and oxygen isotope and elemental records indicate icehouse-greenhouse cycles during the Early Jurassic. Paleoceanography 26, PA4219.

Korte, C., Jasper, T., Kozur, H.W., Veizer, J., 2005. δ^{18}O and δ^{13}C of Permian brachiopods: a record of seawater evolution and continental glaciation. Palaeogeography, Palaeoclimatology, Palaeoecology 224, 333-351.

Korte, C., Kozur, H.W., 2005. Carbon isotope stratigraphy across the Permian/Triassic boundary at Jolfa (NW-Iran), Peitlerkofel (Sass de Pütia, Sass de Putia), Pufels (Bula, Bulla), Tesero (all three Southern Alps, Italy) and Gerennavár (Bükk Mts., Hungary). Journal of Alpine Geology 47, 119-135.

Korte, C., Kozur, H.W., 2010. Carbon-isotope stratigraphy across the Permian-Triassic boundary: A review. Journal of Asian Earth Sciences 39, 215-235.

Korte, C., Kozur, H.W., Bruckschen, P., Veizer, J., 2003. Strontium isotope evolution of Late Permian and Triassic seawater. Geochimica Et Cosmochimica Acta 67, 47-62.

Korte, C., Kozur, H.W., Joachimski, M.M., Strauss, H., Veizer, J., Schwark, L., 2004a. Carbon, sulfur, oxygen and strontium isotope records, organic geochemistry and biostratigraphy across the Permian/Triassic boundary in Abadeh, Iran. International Journal of Earth Sciences 93, 565-581.

Korte, C., Kozur, H.W., Mohtat-Aghai, P., 2004b. Dzhulfian to lowermost Triassic δ^{13}C record at the Permian/Triassic boundary section at Shahreza, Central Iran. Hallesches Jahrbuch für Geowissenschaften, Reihe B, Beiheft 18, 73-78.

Korte, C., Kozur, H.W., Partoazar, H., 2004c. Negative carbon isotope excursion at the Permian/Triassic boundary section at Zal, NW Iran. Hallesches Jahrbuch für Geowissenschaften, Reihe B, Beiheft 18, 69-71.

Korte, C., Pande, P., Kalia, P., Kozur, H.W., Joachimski, M.M., Oberhänsli, H., 2010. Massive volcanism at the Permian-Triassic boundary and its impact on the isotopic composition of the ocean and atmosphere. Journal of Asian Earth Sciences 37, 293-311.

Kozur, H.W., 2007. Biostratigraphy and event stratigraphy in Iran around the Permian-Triassic Boundary (PTB): Implications for the causes of the PTB biotic crisis. Global and Planetary Change 55, 155-176.

Kuhn, O., Weissert, H., Föllmi, K., Hennig, S., 2005. Altered carbon cycling and trace-metal enrichment during the late Valanginian and early Hauterivian. Eclogae Geologicae Helvetiae 98, 333-344.

Kump, L.R., Pavlov, A., Arthur, M.A., 2005. Massive release of hydrogen sulfide to the surface ocean and atmosphere during intervals of oceanic anoxia. Geology 33, 397-400.

Leda, L., Korn, D., Ghaderi, A., Hairapetian, V., Struck, U., Reimold, W., 2014. Lithostratigraphy and carbonate microfacies across the Permian–Triassic boundary near Julfa (NW Iran) and in the Baghuk Mountains (Central Iran). Facies 59, 1-31.

Luo, G., Kump, L.R., Wang, Y., Tong, J., Arthur, M.A., Yang, H., Huang, J., Yin, H., Xie, S., 2010. Isotopic evidence for an anomalously low oceanic sulfate concentration following end-Permian mass extinction. Earth and Planetary Science Letters 300, 101-111.

Marshall, J.D., 1992. Climatic and oceanographic isotopic signals from the carbonate rock record and their preservation. Geological Magazine 129, 143-160.

McHargue, T.R., Price, R.C., 1982. Dolomite from clay in argillaceous or shale-associated marine carbonates. Journal of Sedimentary Research 52.

Melim, L.A., Westphal, H., Swart, P.K., Eberli, G.P., Munnecke, A., 2002. Questioning carbonate diagenetic paradigms: evidence from the Neogene of the Bahamas. Marine Geology 185, 27-53.

Middelburg, J.J., De Lange, G.J., van Der Weijden, C.H., 1987. Manganese solubility control in marine pore waters. Geochimica et Cosmochimica Acta 51, 759-763.

Mii, H.-s., Grossman, E.L., Yancey, T.E., 1999. Carboniferous isotope stratigraphies of North America: Implications for Carboniferous paleoceanography and Mississippian glaciation. Geological Society of America Bulletin 111, 960-973.

Mohtat Aghai, P., Vachard, D., Krainer, K., 2011. Transported foraminifera in Palaeozoic deep red nodular limestones exemplified by latest Permian Neoendothyra in the Zal section (Julfa area, NW Iran). Revista española de micropaleontología 41, 197-213.

Munnecke, A., Westphal, H., Reijmer, J.J.G., Samtleben, C., 1997. Microspar development during early marine burial diagenesis: a comparison of Pliocene carbonates from the Bahamas with Silurian limestones from Gotland (Sweden). Sedimentology 44, 977-990.

Payne, J.L., Lehrmann, D.J., Follett, D., Seibel, M., Kump, L.R., Riccardi, A., Altiner, D., Sano, H., Wei, J.Y., 2007. Erosional truncation of uppermost Permian shallow-marine carbonates and implications for Permian-Triassic boundary events. Geological Society of America Bulletin 119, 771-784.

Pingitore Jr, N.E., Eastman, M.P., Sandidge, M., Oden, K., Freiha, B., 1988. The coprecipitation of manganese(II) with calcite: an experimental study. Marine Chemistry 25, 107-120.

Pingitore, N., 1978. The behavior of Zn^{2+} and Mn^{2+} during carbonate diagenesis; theory and applications. Journal of Sedimentary Research 48, 799-814.

Pucéat, E., Reynard, B., Lécuyer, C., 2004. Can crystallinity be used to determine the degree of chemical alteration of biogenic apatites? Chemical Geology 205, 83-97.

Rampino, M.R., Caldeira, K., 2005. Major perturbation of ocean chemistry and a 'Strangelove Ocean' after the end-Permian mass extinction. Terra Nova 17, 554-559.

RCoreTeam, 2014. A language and environment for statistical computing. . R Foundation for Statistical Computing, Vienna, Austria.

Retallack, G.J., Krull, E.S., 2006. Carbon isotopic evidence for terminal-Permian methane outbursts and their role in extinctions of animals, plants, coral reefs, and peat swamps. Geological Society of America Special Papers 399, 249-268.

Riccardi, A.L., Arthur, M.A., Kump, L.R., 2006 Sulfur isotopic evidence for chemocline upward excursions during the end-Permian mass extinction. Geochimica et Cosmochimica Acta 70, 5740-5752.

Richoz, S., Krystyn, L., Baud, A., Brandner, R., Horacek, M., Mohtat-Aghai, P., 2010. Permian–Triassic boundary interval in the

Middle East (Iran and N. Oman): Progressive environmental change from detailed carbonate carbon isotope marine curve and sedimentary evolution. Journal of Asian Earth Sciences 39, 236-253.

Romano, C., Goudemand, N., Vennemann, T.W., Ware, D., Schneebeli- Hermann, E., Hochuli, P.A., Bruhwiler, T., Brinkmann, W., Bucher, H., 2013. Climatic and biotic upheavals following the end-Permian mass extinction. Nature Geosciences 6, 57-60.

Rothman, D.H., Fournier, G.P., French, K.L., Alm, E.J., Boyle, E.A., Cao, C., Summons, R.E., 2014. Methanogenic burst in the end-Permian carbon cycle. Proceedings of the National Academy of Sciences 111, 5462-5467.

Rubinson, M., Clayton, R.N., 1969. Carbon-13 fractionation between aragonite and calcite. Geochimica et Cosmochimica Acta 33, 997-1002.

Schobben, M., Joachimski, M.M., Korn, D., Leda, L., Korte, C., 2014. Palaeotethys seawater temperature rise and an intensified hydrological cycle following the end-Permian mass extinction. Gondwana Research 26, 675-683.

Schönlaub, H.P., 1991. The Permian–Triassic of the Gartnerkofel-1 core (Carnic Alps, Austria): conodont biostratigraphy. Abhandlungen der Geologischen Bundesanstalt Wien 45, 79-98.

Shen, S.-Z., Mei, S.-L., 2010. Lopingian (Late Permian) high-resolution conodont biostratigraphy in Iran with comparison to South China zonation. Geological Journal 45, 135-161.

Siesser, W.G., Rogers, J., 1971. An investigation of the suitability of four methods used in routine carbonate analysis of marine sediments. Deep Sea Research and Oceanographic Abstracts 18, 135-139.

Sobolev, S.V., Sobolev, A.V., Kuzmin, D.V., Krivolutskaya, N.A., Petrunin, A.G., Arndt, N.T., Radko, V.A., Vasiliev, Y.R., 2011. Linking mantle plumes, large igneous provinces and environmental catastrophes. Nature 477, 312-316.

Stampfli, G.M., Borel, G.D., 2002. A plate tectonic model for the Paleozoic and Mesozoic constrained by dynamic plate boundaries and restored synthetic oceanic isochrons. Earth and Planetary Science Letters 196, 17-33.

Stepanov, D.L., Golshani, F., Stocklin, J., 1969. Upper Permian and Permian-Triassic boundary in North Iran. Report Geological Survey of Iran 12, 1-72.

Sternbach, C., Friedman, G., 1986. Dolomites formed under conditions of deep burial: Hunton Group carbonate rocks (Upper Ordovician to Lower Devonian) in the deep Anadarko Basin of Oklahoma and Texas. Carbonates Evaporites 1, 61-73.

Steuber, T., Veizer, J., 2002. Phanerozoic record of plate tectonic control of seawater chemistry and carbonate sedimentation. Geology 30, 1123-1126.

Sun, Y., Joachimski, M.M., Wignall, P.B., Yan, C., Chen, Y., Jiang, H., Wang, L., Lai, X., 2012. Lethally hot temperatures during the early Triassic greenhouse. Science 338, 366-370.

Svensen, H., Planke, S., Polozov, A.G., Schmidbauer, N., Corfu, F., Podladchikov, Y.Y., Jamtveit, B., 2009. Siberian gas venting and the end-Permian environmental crisis. Earth and Planetary Science Letters 277, 490-500.

Taraz, H., 1971. Uppermost Permian and Permian-Triassic Transition beds in Central Iran. Bulletin of the American Association of Petroleum Geologists 55, 1280-1294.

Teichert, C., Kummel, B., Sweet, W.C., 1973. Permian-Triassic strata, Kuh-e-Ali Bashi, Northwestern Iran. Bulletin of the Museum of Comparative Zoology, Harvard University 145(8), 359-472.

Tong, J.N., Zuo, J.X., Chen, Z.Q., 2007. Early Triassic isotope excursions from South China: proxies for devastation and restoration of marine ecosystems following the end-Permian mass extinction. Geological Journal 42, 371-389.

Ullmann, C.V., Campbell, H.J., Frei, R., Hesselbo, S.P., Pogge von Strandmann, P.A., Korte, C., 2013a. Partial diagenetic overprint of Late Jurassic belemnites from New Zealand: Implications for the preservation potential of δ^7Li values in calcite fossils. Geochimica et Cosmochimica Acta 120, 80-96.

Ullmann, C.V., Hesselbo, S.P., Korte, C., 2013b. Tectonic forcing of Early to Middle Jurassic seawater Sr/Ca. Geology 41, 1211-1214.

van Geldern, R., Joachimski, M.M., Day, J., Jansen, U., Alvarez, F., Yolkin, E.A., Ma, X.P., 2006. Carbon, oxygen and strontium isotope records of Devonian brachiopod shell calcite. Palaeogeography, Palaeoclimatology, Palaeoecology 240, 47-67.

Veizer, J., 1983. Chemical diagenesis of carbonates: theory and application of trace element technique, in: Arthur, M.A., et al. (Ed.), Stable Isotopes in Sedimentary Geology. Society of Economic Palaeontologists and Mineralogists, Tulsa, pp. 3.1-3.100.

Veizer, J., Ala, D., Azmy, K., Bruckschen, P., Buhl, D., Bruhn, F., Carden, G.A.F., Diener, A., Ebneth, S., Godderis, Y., Jasper, T., Korte, C., Pawellek, F., Podlaha, O.G., Strauss, H., 1999. ^{87}Sr/^{86}, δ^{13}C and δ^{18}O evolution of Phanerozoic seawater. Chemical Geology 161, 59-88. Veizer, J., Demovic, R., Turan, J., 1971. Possible use of strontium in sedimentary carbonate rocks as a paleoenvironmental indicator. Sedimentary Geology 5, 5-22.

Wefer, G., Berger, W.H., 1991. Isotope paleontology: growth and composition of extant calcareous species. Marine Geology 100, 207-248.

Wenzel, B., Lécuyer, C., Joachimski, M.M., 2000. Comparing oxygen isotope records of silurian calcite and phosphate—δ^{18}O compositions of brachiopods and conodonts. Geochimica et Cosmochimica Acta 64, 1859-1872.

Wickham, H., 2012. gtable: Arrange grobs in tables, R package version 0.1.2. ed.

Wickham, H., 2009. ggplot2: elegant graphics for data analysis. Springer, New York.

Wignall, P.B., 2001. Large igneous provinces and mass extinctions. Earth Sci. Rev. 53, 1–33.

Wignall, P.B., 2007. The end-Permian mass extinction—how bad did it get? Geobiology 5, 303-309.

Wignall, P.B., Kershaw, S., Collin, P.-Y., and Crasquin-Soleau, S., 2009. Erosional truncation of uppermost Permian shallow-marine carbonates and implications for Permian-Triassic boundary events: Comment. Geological Society of America Bulletin 121, 954-956.

Xie, S., Pancost, R.D., Huang, J., Wignall, P.B., Yu, J., Tang, X., Chen, L., Huang, X., Lai, X., 2007. Changes in the global carbon cycle occurred as two episodes during the Permian-Triassic crisis. Geology 35, 1083-1086.

Xie, S., Wang, Y., 2011. Geomicrobiological perspective on the pattern and causes of the 5-million-year Permo/Triassic biotic crisis. Frontiers in Earth Science 5, 23-36.

Yin, H., Xie, S., Luo, G., Algeo, T.J., Zhang, K., 2012. Two episodes of environmental change at the Permian–Triassic boundary of the GSSP section Meishan. Earth-Science Reviews 115, 163-172.

Yin, H.F., Jiang, H.S., Xia, W.C., Feng, Q.L., Zhang, N., and Shen, J., 2013. The end-Permian regression in South China and its implication on mass extinction. Earth-Science Reviews, in press.

Yuan, D.-x., Shen, S.-z., Henderson, C.M., Chen, J., Zhang, H., Feng, H.-z., 2014. Revised conodont-based integrated high-resolution timescale for the Changhsingian Stage and end-Permian extinction interval at the Meishan sections, South China. Lithos 204, 220-245.

Paper 4

A flourishing ocean caused the marine Late Permian mass extinction

Schobben, M., Stebbins, A., Ghaderi, A., Strauss, H., Korn, D., Hannigan, R., Korte, C. (manuscript) A flourishing ocean caused the marine Late Permian mass extinction

cover shows the Aras Valley section (NW Iran) on the foreground, the river Aras (or Araxes) which is the border between Azerbaijan and Iran. In the background the Dorasham 2 section on Azerbaijan territory can be seen.

A flourishing ocean caused the marine Late Permian mass extinction

Martin Schobben[1], Alan Stebbins[2], Abbas Ghaderi[3], Harald Strauss[4], Dieter Korn[1], Robyn Hannigan[2], Christoph Korte[5]

The end-Permian mass extinction, the most severe biotic crisis in the Phanerozoic, is accompanied by climate change and expansion of oceanic anoxic zones[1,2]. Climate feedback mechanisms might have played an important role in this biodiversity crisis[3]. The partitioning of sulphur among different exogenic reservoirs by biological and physical processes has been suggested to be of importance for this biodiversity crisis[4,5]. However, the exact role of bio-essential sulphur in the mass extinction is still unclear. Here we show that globally increased production of organic matter affected the seawater sulphate sulphur isotope signature near the Permian-Triassic boundary. Furthermore, the increase anaerobic organic matter degradation with the use of sulphate as an electron acceptor was not a consequence of adverse oceanic conditions, as postulated in earlier studies[4–6]. The new data demonstrate that the expansion of euxinic and anoxic zones are symptoms of increased biological carbon recycling in the marine realm, initiated by global warming and consequential fertilization of the oceans by large influxes of weathered material from the continents[1,2,7,8]. The results provide evidence that punctuate biodiversity crises in Earth's history do not necessarily implicate a death world[9], rather the demise of certain multicellular life forms. It also emphasizes that, besides the property of organisms to construct a habitable planet[10], they might as well govern as a catalyst of destruction.

Sulphur isotopes in marine sediments provide important information about biologically induced S transmissions among different reservoirs, the biogeochemical S cycle. A new high-resolution carbonate associated sulphate (CAS) and chromium-reducible sulphide (CRS) dataset for the Kuh-e-Ali Bashi and Zal sections (NW Iran) presented here (Fig. 1) allows for a better understanding of the S cycle across the end-Permian mass extinction (EPME) enabling the assessment of its potential impact on biodiversity.

We identified samples likely to contain a primary seawater chemistry signal, as sources of contamination, such as leachable non-CAS and sulphide minerals and their respective isotope chemistry, have been quantified and culle out (Supplementary Information). This enables the construction of the primary stratigraphic CAS oxygen and sulphur isotopic record. The carbonate successions accumulated on a carbonate platform in the Palaeotethys ocean; they establish a good stratigraphic correlation and age assignment (Supplementary Information) and bear the largest potential for obtaining secular changes of past ocean chemistry across the EPME (Extended data Figure 1). In contrast to previous CAS studies of this time-interval[4,5] the pre-extinction CAS isotope record ($\sim$2 Myr) is remarkably stable and $\delta^{34}S_{CAS}$ and $\delta^{18}O_{CAS}$ values are in a range of $\sim$1 and 2–3 ‰, respectively (Fig. 1). A $\sim$ 3 ‰ negative $\delta^{34}S_{CAS}$ excursion and a 5-7 ‰ positive shift in $\delta^{18}O_{CAS}$ can be traced for both sites during a $\sim$ 40 kyr period following the marine 'extinction horizon'. The $\delta^{34}S_{CAS}$ excursion reaches slightly above the conodont-defined P-Tr boundary $\sim$ 2 ‰ heavier values compared to pre-extinction strata.

A depleted sulphate reservoir, in comparison to modern values of 28 mM, has been implied for allowing rapid changes of seawater $\delta^{34}S_{SO_4}$ [10], such as observed here for the EPME (7.5 ‰ kyr^{-1})[4]. The constant 15-16 ‰ offset in δ^{34}S between CAS and CRS can be related to equally reduced sulphate levels within sedimentary pore water, resulting in a small fractionation during microbial sulphate reduction (MSR) (cf. ref. 11). Anaerobic oxidation of organic matter within modern shelf sediments is mainly related to MSR[12]; this serves as a connection to the biogeochemical carbon cycle[11,13]. The reduction of sulphate by microbe metabolism is an important aspect in the S cycle and is associated with a large isotopic fractionation leading to ^{34}S and ^{18}O enrichments in the residual sulphate pool[4,13]. Most of the MSR-produced H_2S will be re-oxidized and only a small fraction is buried as sedimentary sulphide serving as a sink for ^{32}S[14]. The latter sulphide burial and continental oxidative weathering, evaporite burial as well as mantle derived S determine the isotopic composition of seawater sulphate[4,11,13]. In contrast, $\delta^{18}O_{SO_4}$ is mainly affected by microbial S cycling by MSR and sulphide oxidation and might lead to a dissimilar temporal evolution of marine sulphate S and O isotope compostion[4,15], such as the deviating sulphate δ^{34}S and δ^{18}O at the 'extinction horizon' in the present dataset (Fig. 1).

We applied a box-model calculation to delineate the fluxes that determine the isotopic composition of the marine sulphate across the P-Tr transition. Palaeontological and sedimentological evidence from the Iranian sections show no indications of pervasive water column anoxia (Supplementary Information); this is in contrast to the inferred late Permian marine anoxia at sites in South China

---

[1] Museum für Naturkunde, Leibniz Institut für Evolutions- und Biodiversitätsforschung, Invalidenstr 43, D-10115 Berlin, Germany [2] School for the Environment, University of Massachusetts at Boston, 100 Morrissey Blvd, Boston, MA 02125, US [3] Department of Geology, Faculty of Sciences, Ferdowsi University of Mashhad, Azadi Square, 9177948974 Mashhad, Iran [4] Institut für Geologie und Paläontologie, Westfälische Wilhelms, Universität Münster, Corrensstraße 24, 48149 Münster, Germany, Department of Geosciences and Natural Resource Management, University of Copenhagen, Øster-Voldgade 10, DK-1350, Copenhagen, Denmark

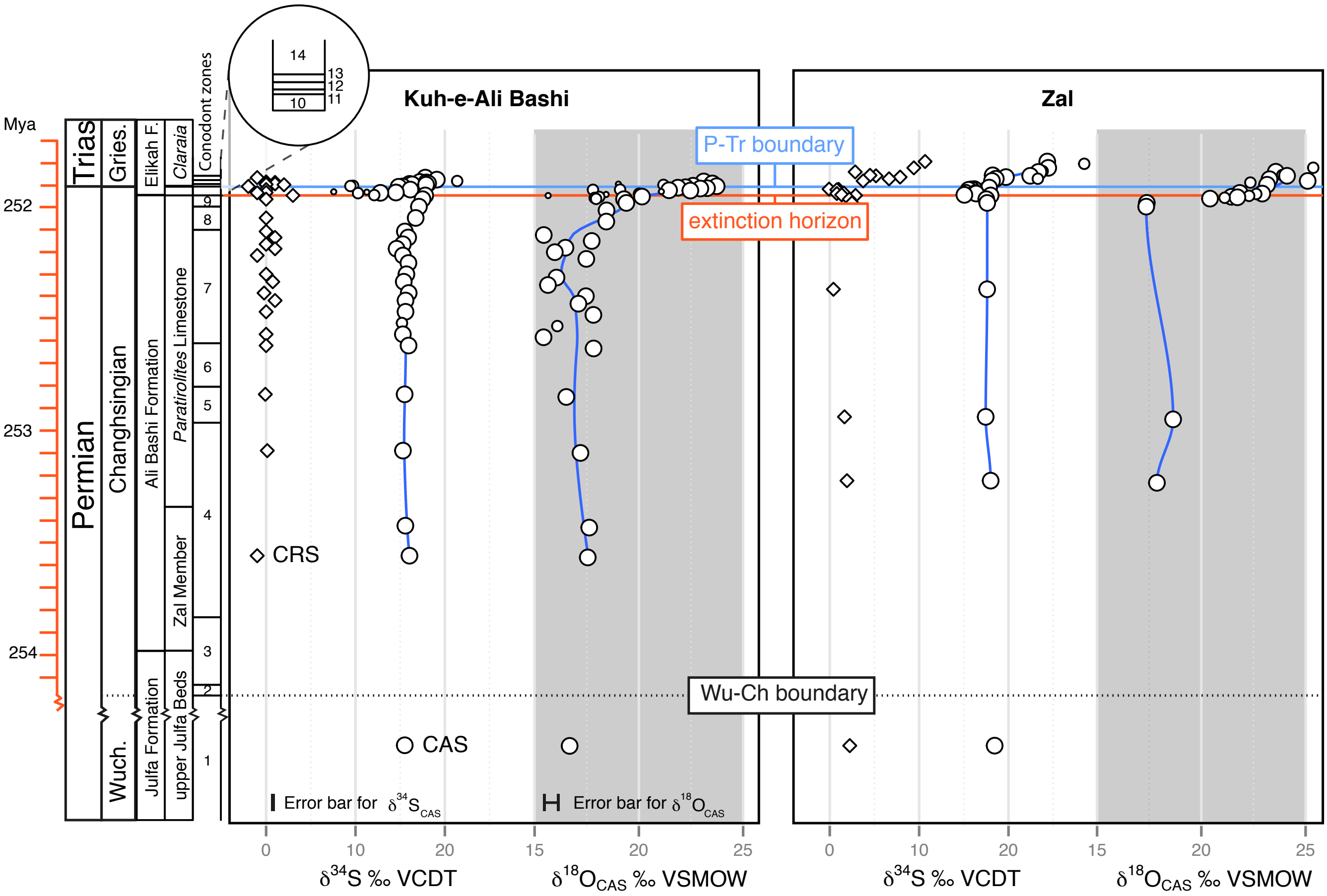

Figure 1 – Isotopic composition of CAS and CRS of carbonates from NW Iran. Significant changes in $\delta^{34}S_{CAS}$ and $\delta^{18}O_{CAS}$ mark the 'extinction horizon' and suggest substantial perturbation of the S cycle. $\delta^{34}S_{CRS}$ and $\delta^{34}S_{CAS}$ have a constant offset of 15-16‰. The temporal framework is constructed by interpolated ages for conodont biozones (Supplementary Information). The error bars stand for external reproducibility of the isotope measurement (2σ) (Supplementary Information). The size of individual CAS data points stand for the assigned confidence of representing true seawater chemistry, large stands for high-confidence, low non-CAS/CAS and low CRS/CAS, medium stands for intermediate-confidence, either high non-CAS/CAS or CRS/CAS and small stands for low-confidence, both high non-CAS/CAS and CRS/CAS (Supplementary Information).

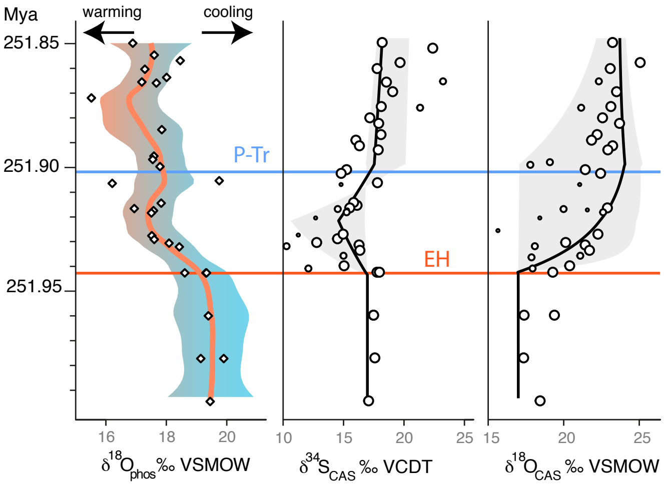

Figure 2 – Numerical model and CAS isotope comparison. The solid line in $\delta^{34}S_{CAS}$ and $\delta^{18}O_{CAS}$ represents the numerical solution when perturbing the system with a 16 times increase in the global weathering flux and the grey area represents a minimum (1*x*) and maximum (64*x*) perturbation. A good agreement exists with the geochemical data. This would suggest that a 1.3 times larger OC pool stimulates a 17 times increased MSR flux. A concomitant decrease in pyrite burial would be the result of a globally increased extent of iron limited euxinic regions and allows a negative $\delta^{34}S_{CAS}$ excursion. Time-equivalent seawater temperature rise, seen in $\delta^{18}O_{phos}$ taken from ref. 7, can enforce an enhanced hydrological cycle and would, among other processes, stimulate larger terrestrial fluxes.

and Australia[16,17]. This spatial heterogeneous pattern can be best explained by increased nutrient influx only into parts of the Tethys. This influx caused regional eutrophication associated with the increasing extents of oxygen minimum zones[18] and euxinic conditions[19] rather than deep bottom water anoxia by a stagnant water column[18]. Widespread ocean fertilisation and drawdown of water column O_2 levels have been related to increased fluxes of terrigenously derived material[18,19] from soil erosion[8] and enhanced chemical weathering[20] initiated by acid precipitation and destabilization of vegetation and soils, global warming and an associated intensified hydrological cycle at that time[1,7]. The climax of this biogeochemical cascade correlates with the greenhouse warming often associated with coeval Siberian Trap volcanism[2]. The importance of organic substrates for MSR justifies the incorporation of the organic carbon (OC) pool with the link to continental weathering in our box-model, particularly, as oxygenation of seawater has likely a subordinate effect on the amount of OC reaching the sediment[14]

A best model fit, based on sensitivity experiments (Supplementary Information), suggests a 16 times increased weathering rate starting at the 'extinction horizon' and lasting for a period of 40 kyr (Fig. 2). This simulates large MSR activity but also sulphur disproportionation, although it has been suggested that the latter could not explain an O isotope fractionation > 18 ‰ between water and sulphate[15]. An average $\delta^{18}O_{seawater}$ of $\sim$ -1 ‰[1] and $\delta^{18}O_{CAS}$ excursion to values of over 20 ‰ make sulphur disproportionation an unlikely candidate (Supplementary Information). Increased OC degradation by MSR is a strong and robust argument for the reconstructed scenario and explains the observed $\delta^{18}O_{CAS}$ excursion. Independent numerical exercises with higher complexity models suggest that $>$ 4 times enhanced continental weathering increases considerably the primary productivity in shelf settings[19,21], followed by anoxic and sulphidic conditions as a consequence of increased (an)aerobic OC remineralization.

The negative $\delta^{34}S_{SO_4}$ excursion also suggests that pyrite burial did not increase, according to the increased MSR, as often assumed[4,13], The main controlling factors for pyrite formation are labile OC, sulphide formation, oxygenation and reactive iron availability of the sediment and water column[14]. In sulphidic water column conditions, such as in the modern Black Sea representing only a fraction of the total modern ocean volume[13], pyrite formation is a syngenetic process rather than a diagenetic process[22,23]. This pyrite sedimentation style depletes reactive iron already in the water column and inhibits largely the pyrite formation within the sediment[22]. In such euxinic settings pyrite formation becomes iron-limited and pyrite burial becomes sensitive to the supply of reactive iron to the ocean[24]. Mechanisms for reactive iron supply are hydrothermal input, windblown dust, riverine input and diagenetic Fe cycling on the shelf[25,26]. Although the iron flux from the continent is potentially large, 70-90 % of the dissolved iron is already lost as particles in estuaries[26]. The iron, reaching the ocean, is especially sensitive to water turbulence and grain concentrations delivered by rivers[26]. Relating all this to the end-Permian scenario, a situation under a high sea level[2] and with a sudden influx of soils[8] accompanied by high physical erosion rates[20] due to an intensified hydrological cycle in a warmer ocean[7] would create an environment that already depletes reactive iron before entering the ocean (Fig. 3).

We do not provide an estimation of the pyrite flux change. However, under the Late Permian oceanic conditions it was not necessary that pyrite burial increased concomitantly with increasing MSR. The diverging CAS-sulphur and oxygen isotope pattern can be best explained by increased MSR, but decreased pyrite burial, compatible with an enlarged global extend of iron-limited euxinic seawater (Figs. 2 and 3). The presence of green sulphur bacteria—which thrive in H_2S rich surface water—during the time interval of the S cycle perturbation, evidenced by biomarker analyses[16] suggests widespread euxinia. Moreover, ocean fertilization is in concert with an independent model for the Late Permian ocean, suggesting 10 times higher nutrient levels to induce globally pervasive water column H_2S[19]. The new CAS isotope data and the related environmental conditions suggest that the euxinic zones expanded suddenly at the 'extinction horizon' (Figs. 1 and 2), implying that the sulphidic toxicity caused the EPME[6].

This scenario to explain the EPME enhances the notion that life can influence seawater chemistry[14] and the relationship to OC remineralization[17]. CAS isotopes provide a more direct view on biological productivity in past oceans, suggesting a flourishing of life. It contrasts the concept of decreased organic production, or 'Strangelove Ocean', often implied in extinction scenarios[9]. However, marine life might have been very different with mainly prokaryotes dominating over eukaryotes[27]. A return to nearly pre-extinction $\delta^{34}S_{CAS}$, within 40 kyr, suggests recommencing pyrite burial; the disturbance was therefore a rather transient event, which agrees with the postulated short duration of soil erosion and local euxinic seawater conditions[8,16]. It argues either for enhanced supply of iron, possibly under reduced detrital loading of river discharge, or waning of the global extent of euxinic conditions and consequential increase of diagenetic pyrite accumulation, or both.

The subsequent Early Triassic positive $\delta^{34}S_{CAS}$ is apparently not directly related to the biodiversity crisis (Fig. 1). Rather it records increased sequestration of S by authigenic pyrite caused by the lack of organisms that normally irrigated sediments with O_2 by burrowing[14] (Fig. 3). The relative stable high $\delta^{18}O_{CAS}$ in this period indicates that MSR remained important during the Early Triassic. The former suggests a prevailing large OC pool, together with a long-lasting (~800 kyr) increase in continental weathering[20], a perturbed C cycle and high global temperatures the latter two returning in intervals throughout a period of almost 4 Myr[28,29]. These Earth surface processes are regarded as an important negative feedback loop of the carbon cycle, where enhanced production and sequestration of OC is stimulated by global warming and subsequent chemical weathering rates[21]. The prolonged disturbance after the EPME contradicts a fast return to pre-disturbance climate and C cycle, enforced by C sequestration, as suggested for other events marked by greenhouse warming and widespread anoxia, such as the Cenozoic hyperthermals[30] (<100 kyr) and Mesozoic ocean anoxic events[31]. Enhanced MSR, and its role in C cycling, potentially had a crucial effect on the Early Triassic C-cycle and would affect marine redox conditions (see ref. 21) and climate with an adverse effect on the biotic recovery.

Methods

Isotope analysis

CAS and CRS were extracted according to standard protocols. Note, that for CAS extraction, sediments were pre-treated with a NaCl solution to clean the sediment of SO_4 not bound to the calcite lattice. Sulphur isotope ratios are reported in the standard ($\delta^{34}S$) notation relative to Vienna Cañon Diablo Troilite (VCDT) in ‰. Oxygen isotope

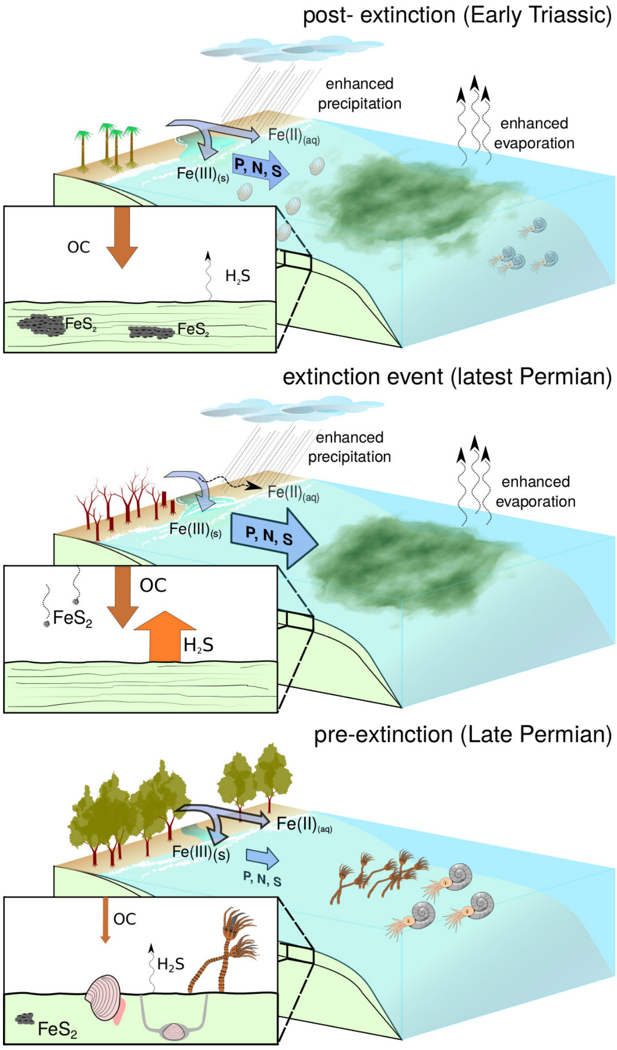

Figure 3 – Conceptual model for environmental changes around the P-Tr boundary. This cartoon depicts the shelf settings that are prone to be affected by a scenario of intensified continental influx. Pre-extinction time shows late Permian marine communities consisting of multiple trophic levels. Authigenic pyrite formation is restricted by oxygenation of sediments by burrowers. The extinction event marks increased terrigenous influx causing local eutrophication, aided by an active hydrological cycle with increasing precipitation and evaporation rates due to global warming. Increased sediment load and turbulence of river discharge flocculates $Fe(III)_{(S)}$ in estuaries, reducing the ocean $Fe(II)_{(aq)}$ inventory. Consequential OC remineralization by MSR and Fe limitation raises seawater H_2S. Sulphide toxicity alongside marine anoxia sustains a low diversity and primitive marine community. Pyrite sedimentation is limited to small amounts of syngenetic pyrite precipitation. Relaxation of continental weathering reduces ocean input of nutrients and raises $Fe(II)_{(aq)}$ delivery to the post-extinction ocean, thereby reducing sulphidic water column conditions and relocating pyrite sedimentation towards the sediments, where decreased O_2 irrigation due to a less active benthic community stimulates authigenic pyrite formation. The enlarged OC pool is sustained due to C recycling by an active microbial community.

ratios are reported in the standard (δ^{18}O) notation relative to Vienna Standard Mean Ocean Water (VSMOW) in ‰. A more detailed report of the protocols and the analytical error margins of isotope values are given in the Supplementary Information.

Box-model

A box-model was constructed, in order to delineate which fluxes could be responsible for isotopic changes in marine sulphate and thus could explain the stratigraphic CAS isotope record. Sulphate mass (M_{SO_4}) and isotopic composition (δ_{SO_4}) are estimated with the following equations, adapted from ref. 11:

$$\frac{dM_{SO_4}}{dt} = Q_w + Q_v + Q_m - (F_p + F_e) \tag{1}$$

$$\frac{d\delta_{SO_4}}{dt} = \frac{Q_w\delta_w + Q_v\delta_v + Q_m\delta_m - \delta_{SO_4}(Q_w + Q_v + Q_m) - F_p\Delta_{MSR}}{M_{SO_4}} \tag{2}$$

Where, Q_w represents the weathering input flux, δ_w is the isotopic composition of weathering input, Q_v is the volcanic input flux, δ_v is the isotopic composition of volcanic input, Q_m is the hydrothermal input flux, δ_m is the isotopic composition of the hydrothermal input flux, F_e is the evaporite burial flux, F_p is the pyrite burial flux and Δ_{MSR} is the average isotopic fractionation associated with MSR. The O and S isotopic compositions of marine sulphate are affected by different processes. Two aspects are mainly responsible for this difference, microbial S cycling and the exchange and cycling through the oceanic crust. Microbial S cycling results in the loss of O during MSR (F_{MSR}), whereas the product sulphide is oxidized and mainly via microbial sulphur disproportionation[15] transformed back to sulphate (Q_{ox}), both with an effect on the isotopic composition. The surplus of these bacterial processes will be buried as sedimentary sulphide, mainly pyrite and can be envisioned as:

$$F_p = F_{MSR} - Q_{ox} \tag{3}$$

Whereas marine sulphate-δ^{34}S is only affected by hydrothermal S input in one direction, sulphate-δ^{18}O is modified by oxidation of sulphides at these hydrothermal vents (Q_h) and acquire a δ^{18}O similar to ocean water[15]. On the other hand, anhydrite formation in the oceanic crust is an effective sink for sulphate oxygen (F_s), without fractionation[15] and can be described by:

$$Q_m = Q_h - F_s \tag{4}$$

To adjust for these differences imposed upon the marine sulphate δ^{18}O, equations (3) and (4), are substituted in equation (2), yielding:

$$\frac{d\delta_{SO_4}}{dt} = \frac{Q_w\delta_w + Q_v\delta_v + Q_h\delta_m + Q_{ox}\delta_{ox}}{M_{SO_4}} \frac{-\delta_{SO_4}(Q_w + Q_v + Q_h + Q_{ox}) - F_{MSR}\Delta_{MSR}}{M_{SO_4}} \tag{5}$$

Where δ_{ox} stands for the isotopic composition of sulphate originating from sulphur disproportionation. Steady state was achieved by modifying Holocene reservoir and flux size and isotopic composition, to approximate the S cycle of the P-Tr interval (Supplementary Information). To exploit the important impact of MSR on OC remineralization[12], an OC pool (M_{OC}) was introduced to the model, by linking Q_w linearly to ocean primary productivity (Q_{po}). OC burial (F_{bo}) and OC remineralization (F_{OC}) are determined by the size of the OC pool as first-order rate constants (k values). K values are determined by assuming that 99% of OC is remineralized of which part by MSR (F_{MSR}: Supplementary Information),and according to stoichiometry of the two biochemical reactions:

$$CH_2O + O_2 \Longleftrightarrow CO_2 + H_2O \tag{6}$$

$$2CH_2O2 + SO_4^{2-} \Longleftrightarrow 2HCO_3^- + H_2S \tag{7}$$

The size of the marine OC pool is described by:

$$M_{OC(t)} = \left(\left(\frac{Q_{po(i)}}{k_1 + k_2} \right) - \left(\left(\frac{Q_{po(i)}}{k_1 + k_2} \right) + M_{OC(i)} \right) e^{(-(k_1+k_2)t)} \right) + 2F_{MSR} \tag{8}$$

where (i) stands for the initial pool and (t) for the pool changing with time. First-order removal constants (k) are calculated by using initial Holocene values for the OC pool (Supplementary Information).The relation between the OC pool and MSR is described in the following equation, taken from ref. 14:

$$F_{MSR} = \alpha M_{OC}[SO_4^{2-}]^y \tag{9}$$

which considers that the size of the OC pool has a direct impact on the availability of OC for sulphate reduction. Factor α is calculated by solving the equation with the initial values and y has been taken as 0.3, in accordance with ref. 14. The model was perturbed by varying the weathering flux concomitant with the 'extinction horizon' for a duration of 40 kyr. Various simulations were performed with the weathering flux changing from 2 to 64 times larger than the background value. The Triassic weathering flux is taken to be 7 times higher than the Permian as suggested in ref. 20. To simulate the effect of a largely iron limited euxinic ocean the fraction of pyrite buried was set to 10 times reduced for 20 kyr following the 'extinction horizon', followed by a 2 times increase for another 20 kyr when compared to the pre-perturbed value.

1. Joachimski MM, Lai X, Shen S, Jiang H, Luo G, Chen B, et al. Climate warming in the latest Permian and the Permian–Triassic mass extinction. Geology 2012, 40(3): 195-198.
2. Wignall PB, Twitchett RJ. Oceanic Anoxia and the End Permian Mass Extinction. Science 1996, 272(5265): 1155-1158.
3. Erwin DH. The Permo-Triassic extinction. Nature 1994, 367 (6460): 231-236.
4. Newton RJ, Pevitt EL, Wignall PB, Bottrell SH. Large shifts in the isotopic composition of seawater sulphate across the Permo–Triassic boundary in northern Italy. Earth and Planetary Science Letters 2004, 218(3–4): 331-345.
5. Riccardi AL, Arthur MA, Kump LR. Sulfur isotopic evidence for chemocline upward excursions during the end-Permian mass extinction. Geochimica et Cosmochimica Acta 2006, 70(23): 5740-5752.
6. Kump LR, Pavlov A, Arthur MA. Massive release of hydrogen sulfide to the surface ocean and atmosphere during intervals of oceanic anoxia. Geology 2005, 33(5): 397-400.
7. Schobben M, Joachimski MM, Korn D, Leda L, Korte C. Palaeotethys seawater temperature rise and an intensified hydrological cycle following the end-Permian mass extinction. Gondwana Research 2014, 26(2): 675-683.
8. Sephton MA, Looy CV, Brinkhuis H, Wignall PB, de Leeuw JW, Visscher H. Catastrophic soil erosion during the end-Permian biotic crisis. Geology 2005, 33(12): 941-941.
9. Rampino MR, Caldeira K. Major perturbation of ocean chemistry and a 'Strangelove Ocean' after the end-Permian mass extinction. Terra Nova 2005, 17(6): 554-559.
10. Kah LC, Lyons TW, Frank TD. Low marine sulphate and protracted oxygenation of the Proterozoic biosphere. Nature 2004, 431(7010): 834-838.
11. Adams DD, Hurtgen MT, Sageman BB. Volcanic triggering of a biogeochemical cascade during Oceanic Anoxic Event 2. Nature Geosci 2010, 3(3): 201-204.
12. Jørgensen BB. Mineralization of organic matter in the sea bed-the role of sulphate reduction. Nature 1982, 296 (5858): 643-645.
13. Owens JD, Gill BC, Jenkyns HC, Bates SM, Severmann S, Kuypers MMM, et al. Sulfur isotopes track the global extent and

dynamics of euxinia during Cretaceous Oceanic Anoxic Event 2. Proceedings of the National Academy of Sciences 2013, 110(46): 18407-18412.

14. Canfield DE, Farquhar J. Animal evolution, bioturbation, and the sulfate concentration of the oceans. Proceedings of the National Academy of Sciences 2009, 106(20): 8123-8127.
15. Turchyn AV, Schrag DP. Oxygen Isotope Constraints on the Sulfur Cycle over the Past 10 Million Years. Science 2004, 303(5666): 2004-2007.
16. Grice K, Cao C, Love GD, Böttcher ME, Twitchett RJ, Grosjean E, et al. Photic Zone Euxinia During the Permian-Triassic Superanoxic Event. Science 2005, 307(5710): 706-709.
17. Brennecka GA, Herrmann AD, Algeo TJ, Anbar AD. Rapid expansion of oceanic anoxia immediately before the end-Permian mass extinction. Proceedings of the National Academy of Sciences 2011, 108(43): 17631-17634.
18. Winguth C, Winguth AME. Simulating Permian–Triassic oceanic anoxia distribution: Implications for species extinction and recovery. Geology 2012, 40(2): 127-130.
19. Meyer KM, Kump LR, Ridgwell A. Biogeochemical controls on photic-zone euxinia during the end-Permian mass extinction. Geology 2008, 36(9): 747-750.
20. Algeo TJ, Twitchett RJ. Anomalous Early Triassic sediment fluxes due to elevated weathering rates and their biological consequences. Geology 2010, 38(11): 1023-1026.
21. Ozaki K, Tajima S, Tajika E. Conditions required for oceanic anoxia/euxinia: Constraints from a one-dimensional ocean biogeochemical cycle model. Earth and Planetary Science Letters 2011, 304(1–2): 270-279.
22. Wilkin RT, Arthur MA. Variations in pyrite texture, sulfur isotope composition, and iron systematics in the Black Sea: evidence for Late Pleistocene to Holocene excursions of the o_2-h_2s redox transition. Geochimica et Cosmochimica Acta 2001, 65(9): 1399-1416.
23. Lyons TW, Berner RA. Carbon-sulfur-iron systematics of the uppermost deep-water sediments of the Black Sea. Chemical Geology 1992, 99(1–3): 1-27.
24. Poulton SW, Canfield DE. Ferruginous Conditions: A Dominant Feature of the Ocean through Earth's History. Elements 2011, 7(2): 107-112.
25. Lyons TW, Severmann S. A critical look at iron paleoredox proxies: New insights from modern euxinic marine basins. Geochimica et Cosmochimica Acta 2006, 70(23): 5698-5722.
26. Raiswell R. Iron Transport from the Continents to the Open Ocean: The Aging–Rejuvenation Cycle. Elements 2011, 7(2): 101-106.
27. Algeo TJ, Henderson CM, Tong J, Feng Q, Yin H, Tyson RV. Plankton and productivity during the Permian–Triassic boundary crisis: An analysis of organic carbon fluxes. Global and Planetary Change 2013, 105(0): 52-67.
28. Sun Y, Joachimski MM, Wignall PB, Yan C, Chen Y, Jiang H, et al. Lethally Hot Temperatures During the Early Triassic Greenhouse. Science 2012, 338(6105): 366-370.
29. Payne JL, Lehrmann DJ, Wei J, Orchard MJ, Schrag DP, Knoll AH. Large Perturbations of the Carbon Cycle During Recovery from the End-Permian Extinction. Science 2004, 305(5683): 506-509.
30. Bains S, Norris RD, Corfield RM, Faul KL. Termination of global warmth at the Palaeocene/Eocene boundary through productivity feedback. Nature 2000, 407(6801): 171-174.
31. Arthur MA, Dean WE, Pratt LM. Geochemical and climatic effects of increased marine organic carbon burial at the Cenomanian/Turonian boundary. Nature 1988, 335(6192): 714-717.

Acknowledgements This project was funded by the DFG (project KO2011/8-1 and KO1829/12-2) and the National Science Foundation Graduate Research Fellowship Program (Grant No. DGE-1356104). Any opinions, findings, and conclusions or recommendations expressed in this material are those of the author(s) and do not necessarily reflect the views of the National Science Foundation. Acknowledgements are also due to the Environmental Analytical Facility at the University of Massachusetts Boston (NSF Award Number No. 09-42371 DBI, Hannigan and Christian). The Aras Free Zone office and Adel Najafzadeh are thanked for permission to sample the locations in the Julfa region.

8 Supplementary material

Supplementary material: Paper 2

Palaeotethys seawater temperature rise and an intensified hydrological cycle following the end-Permian mass extinction

SUPPLEMENTARY MATERIAL

Palaeotethys seawater temperature rise and an intensified hydrological cycle following the end-Permian mass extinction

Martin Schobben, Michael M. Joachimski, Dieter Korn, Lucyna Leda, Christoph Korte

EVALUATION OF SAMPLE PRESERVATION

Conodonts

Conodonts with a conodont alteration index (CAI) of up to 5 and even with some surface recrystallization can record the primary seawater δ^{18}O signature at the time of growth (Barham et al., 2012; Joachimski et al., 2009). The conodonts from the Iranian sections, Kuh-e-Ali Bashi and Zal have a CAI between 1 and 1.5, indicating only low thermal maturation. Additional analyzes were performed to evaluate the potential degree of alteration. Conodonts investigated using the Scanning Electron Microscope (SEM) show no coarse surface structures, which indicates minimum recrystallization. In addition, Raman spectroscopy was performed to obtain the peak position of v1-PO_4 (phosphate symmetric-stretching bound) and its respective full width at half maximum (FWHM) of conodont apatite. This is presumed to be a measure of ions substituting into (Sr^2, F^-) or out of the lattice (CO_3^{2-}) and has been suggested as a proxy for the diagenetic alteration of the oxygen isotopic composition of fossil apatite (Thomas et al., 2011). This approach, however, can be used only as a qualitative check, because many more ions can be incorporated post-depositionally (Katvala and Henderson, 2012; Trotter and Eggins, 2006) and influence the peak position and FWHM of v1-PO_4. We used a modern fish tooth and magmatic apatite standards as chemical end-members for biologically unaltered and most severely diagenetically altered apatite, respectively. The peak of our conodonts and actinopterygian teeth, v1-PO_4, and its FWHM plot around the values obtained for the modern fish tooth (Fig. S1), which suggests no or minor alteration only.

Brachiopods

The secondary layers of the brachiopod shells show smooth fibrous and lamellar surfaces under the binocular microscope and SEM. This is indicative of pristine calcite and therefore data from these layers represent reliable δ^{18}O values reflecting past seawater composition and temperatures. Mn and Sr concentrations are <250 and >400 ppm, respectively, and were used in earlier studies to identify and exclude altered brachiopod shells (Korte et al., 2003; 2005a; 2005b; 2008; see also Popp et al., 1986). It is, however, very difficult to set strict limits for the identification of pristine samples by trace element concentrations. Manganese, for example, can vary considerably in seawater because it depends on local redox conditions; higher concentrations occur under more reducing environments and are subsequently incorporated into the calcite shells (Freitas et al., 2006; Korte and Hesselbo, 2011). The Mn concentrations of our brachiopods, however, are all below 250 ppm and hence match the limits used for pristine specimens in earlier Permian and Triassic studies (Korte et al., 2003; 2005a; 2005b; 2008). Strontium on the other hand decreases in calcite with progressive diagenesis (Brand and Veizer, 1980) and may vary considerably in single specimens and in different fossil groups (discussion in Korte and Hesselbo, 2011). Moreover, seawater Sr concentrations have varied throughout Earth's history with minimum values at the Permian-Triassic boundary (Steuber and Veizer, 2002). The present study dataset (Table S3) shows a clear trend to lower values towards the PTB (see also datasheet in Korte et al., 2005b). Due to this clear trend, and because no additional indication for diagenetic alteration is indicated by the other methods (Mn, SEM, binocular microscope), we did not exclude isotope data measured on brachiopods with less than 400 ppm Sr. We consider these strontium-depleted shells as pristine.

δ^{18}O OF LATE PERMIAN SEAWATER

The establishment of regional δ^{18}O variations for ancient seawater is important to determine reliable palaeotemperatures from apatite and calcite δ^{18}O. This is particularly challenging since the recorded δ^{18}O is a reflection of surface seawater as most of the Permian and Triassic deposits comprise palaeosettings of continental shelf or inter-continental oceans with only shallow water depths and with different palaeolatitudes. Surface ocean water is affected by evaporation and precipitation, influencing the$\delta^{18}O_{sw}$ to various degree in different regions (Zachos et al., 1994) and evaporation-precipitation ratios depending on latitude lead to varying sea-surface δ^{18}O values at specific latitudes. The relation between Sea Surface Salinity (SSS) and$\delta^{18}O_{sw}$ appears to be roughly linear in at a global scale, based on modern ocean observations and modeling experiments (Schmidt, 1999). Hence, we use SSS from the modeling study of Kiehl and Shields (2005; also Shields, pers. com. 2013) to estimate the palaeo-$\delta^{18}O_{sw}$ of the discussed sections. The southern Chinese sections were deposited in an epicontinental location at about 23-25 °N (Liu, 1999) and on the margins of the Palaeotethys and the Panthalassa Oceans. The corresponding salinity on the SSS world map (Fig. S2) is 35 ‰. The Iranian sections are located near the equator (Muttoni et al., 2009a; 2009b) in the western part of the Palaeotethys, suggesting, salinities of 33 ‰using the SSS map from Kiehl and Shields (2005; also Shields, pers. com. 2013) (Fig. S2). According to Schmidt (1999), a regional δ^{18}O-SSS line is more appropriate for the tropics since the global linear δ^{18}O-SSS line breaks down more at lower latitudes than at the mid-latitudes. Hence, we consider that for the studied sections, equation 1 of Watanabe et al. (2001) would best represent the palaeooceanic conditions, since this equation resembles a δ^{18}O-SSS relationship for the tropical latitudes and semi-enclosed basins (Craig and Gordon, 1965; Rostek et al., 1993; Schmidt, 1999).

$$\delta^{18}O_{sw} = 2.04(\pm0.03)SSS - 6.54(\pm0.68) \tag{1}$$

Applying equation 1 for the SSS values obtained from the model experiment of Kiehl and Shields (2005) results in a $\delta^{18}O_{sw}$ of -0.81‰(±0.31) for NW Iran and -0.4‰(±0.37) for South China when corrected additionally with a value of -1 for the seawater of an ice-free world as expected for the investigated time span (Lhomme et al., 2005).

References

Barham, M., Joachimski, M.M., Murray, J., Williams, D.M., 2012. Diagenetic alteration of the structure and δ^{18}O signature of Palaeozoic fish and conodont apatite: Potential use for corrected isotope signatures in palaeoenvironmental interpretation. Chemical Geology 298–299, 11-19.

Brand, U., Veizer, J., 1980. Chemical diagenesis of a multicomponent carbonate system -1: Trace elements. Journal of Sedimentary Petrology 50, 1219-1236.

Craig, H., Gordon, L.I., 1965. Deuterium and oxygen 18 variations in the ocean and the marine atmosphere In: Tongiorgi (Ed.), Stable Isotopes in Oceanographic Studies and Paleotemperatures. Consiglio Nazionale di Richerche, Spoleto, Italy, pp. 9–131.

Freitas, P.S., Clarke, L.J., Kennedy, H., Richardson, C.A., Abrantes, F., 2006. Environmental and biological controls on elemental (Mg/Ca, Sr/Ca and Mn/Ca) ratios in shells of the king scallop Pecten maximus. Geochimica et Cosmochimica Acta 70, 5119-5133.

Joachimski, M.M., Breisig, S., Buggisch, W., Talent, J.A., Mawson, R., Gereke, M., Morrow, J.R., Day, J., Weddige, K., 2009. Devonian climate and reef evolution: Insights from oxygen isotopes in apatite. Earth and Planetary Science Letters 284, 599-609.

Katvala, E.C., Henderson, C.M., 2012. Chemical element distributions within conodont elements and their functional implications. Paleobiology 38, 447-458.

Kiehl, J.T., Shields, C.A., 2005. Climate simulation of the latest Permian: Implications for mass extinction. Geology 33, 757-760.

Korte, C., Hesselbo, S.P., 2011. Shallow marine carbon and oxygen isotope and elemental records indicate icehouse-greenhouse cycles during the Early Jurassic. Paleoceanography 26, pp. 18.

Korte, C., Jasper, T., Kozur, H.W., Veizer, J., 2005a. δ^{18}O and δ^{13}C of Permian brachiopods: a record of seawater evolution and continental glaciation. Palaeogeography, Palaeoclimatology, Palaeoecology 224, 333-351.

Korte, C., Jones, P.J., Brand, U., Mertmann, D., Veizer, J., 2008. Oxygen isotope values from high-latitudes: Clues for Permian sea-surface temperature gradients and Late Palaeozoic deglaciation. Palaeogeography, Palaeoclimatology, Palaeoecology 269, 1-16.

Korte, C., Kozur, H.W., Bruckschen, P., Veizer, J., 2003. Strontium isotope evolution of Late Permian and Triassic seawater. Geochimica et Cosmochimica Acta 67, 47-62.

Korte, C., Kozur, H.W., Veizer, J., 2005b. δ^{13}C and δ^{18}O values of Triassic brachiopods and carbonate rocks as proxies for coeval seawater and palaeotemperature. Palaeogeography Palaeoclimatology Palaeoecology 226, 287-306.

Lhomme, N., Clarke, G.K.C., Ritz, C., 2005. Global budget of water isotopes inferred from polar ice sheets. Geophysical Research Letters 32, L20502.

Liu, Y.Y.Z., Y.M. Tian, W.H., 1999. New magnetostratigraphic results from Meishan section, Changxing County, Zhejiang province. Earth Science Journal of China University of Geosciences Wuhan 24, 151-154.

Muttoni, G., Gaetani, M., Kent, D.V., Sciunnach, D., Angiolini, L., Berra, F., Garzanti, E., Mattei, M., Zanchi, A., 2009a. Opening of the Neo-Tethys Ocean and the Pangea B to Pangea A transformation during the Permian. GeoArabia 14, 17-48.

Muttoni, G., Mattei, M., Balini, M., Zanchi, A., Gaetani, M., Berra, F., 2009b. The drift history of Iran from the Ordovician to the Triassic. Geological Society, London, Special Publications 312, 7-29.

Popp, B.N., Anderson, T.F., Sandberg, P.A., 1986. Brachiopods as indicators of original isotopic compositions in some Paleozoic limestones. Geological Society of America Bulletin 97, 1262-1269.

Rostek, F., Ruhland, G., Bassinot, F., Müller, P., Labeyrie, L., Lancelot, Y., Bard, E., 1993. Reconstructing sea surface temperature and salinity using δ^{18}O and alkenone records. Nature 364, 319-321.

Schmidt, G.A., 1999. Error analysis of paleosalinity calculations. Paleoceanography 14, 422-429.

Steuber, T., Veizer, J., 2002. Phanerozoic record of plate tectonic control of seawater chemistry and carbonate sedimentation. Geology 30, 1123-1126.

Thomas, D.B., McGoverin, C.M., Fordyce, R.E., Frew, R.D., Gordon, K.C., 2011. Raman spectroscopy of fossil bioapatite—A proxy for diagenetic alteration of the oxygen isotope composition.

Palaeogeography, Palaeoclimatology, Palaeoecology 310, 62-70. Trotter, J.A., Eggins, S.M., 2006. Chemical systematics of conodont apatite determined by laser ablation ICPMS. Chemical Geology 233, 196-216.

Watanabe, T., Winter, A., Oba, T., 2001. Seasonal changes in sea surface temperature and salinity during the Little Ice Age in the Caribbean Sea deduced from Mg/Ca and 18O/16O ratios in corals. Marine Geology 173, 21-35.

Zachos, J.C., Stott, L.D., Lohmann, K.C., 1994. Evolution of early Cenozoic marine temperatures. Paleoceanography 9, 353-387.

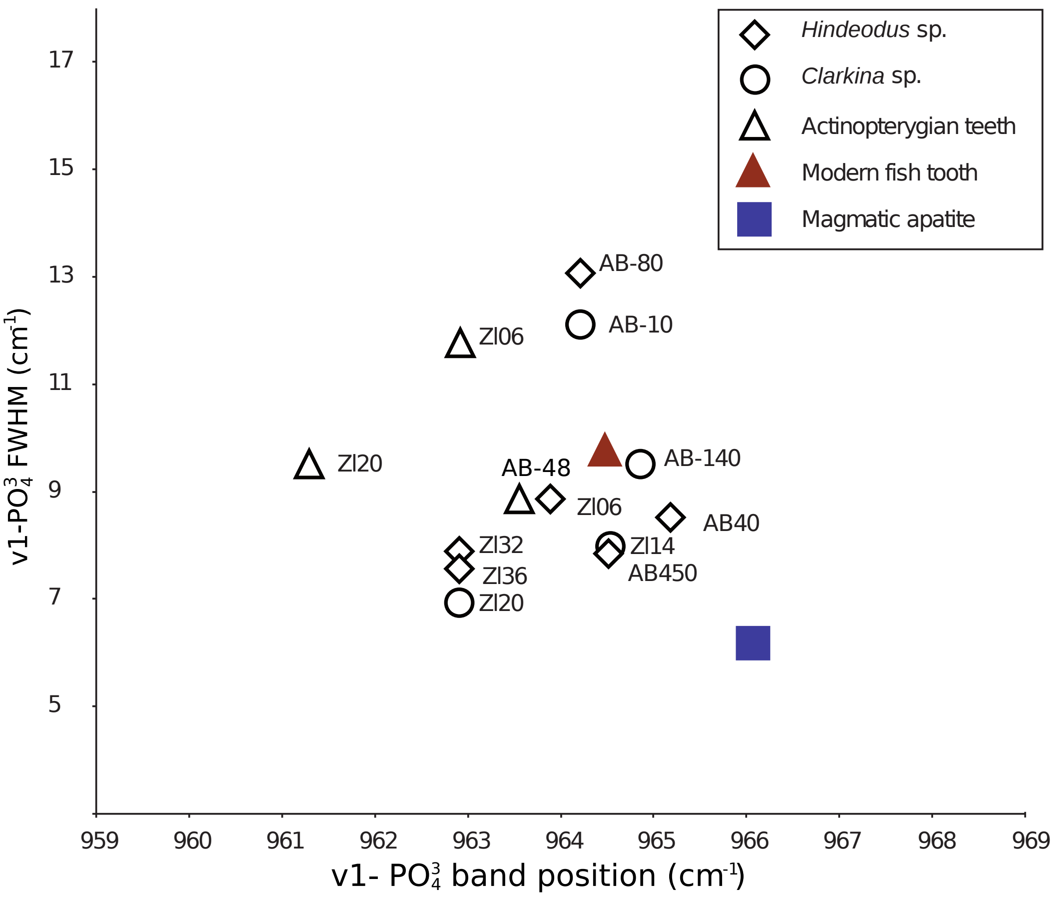

Figure S 1 – Raman spectroscopy of conodont and actinopterygian teeth from Kuh-e-Ali Bashi and Zal. FWHM is plotted against the peak position of the v1-PO4 symmetric stretching bound with chemical endmembers for unaltered (modern fish tooth) and most diagenetically altered apatite (magmatic apatite).

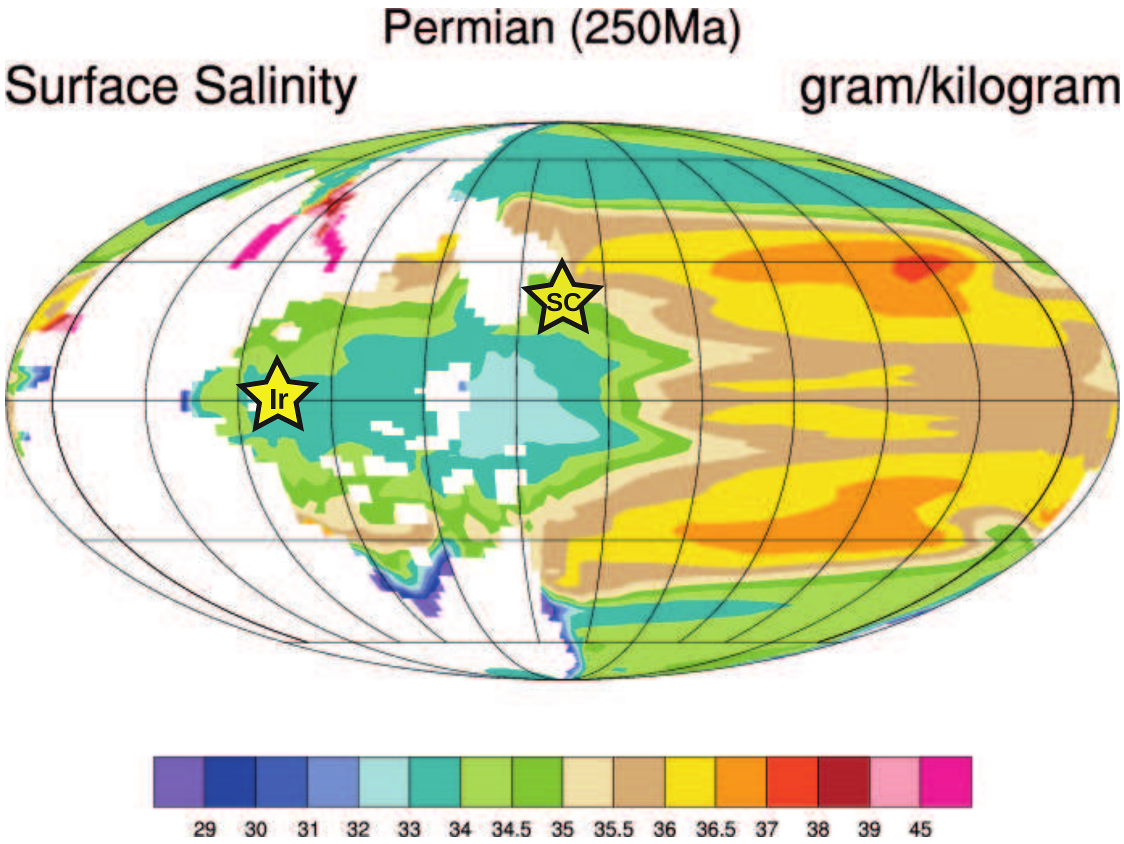

Figure S 2 – SSS world map for the late Permian modified from Kiehl and Shields (2005 and Shields pers. com. 2013) with the locations of the Southern Chinese and NW Iranian sections marked by stars.

Table S 1 – Oxygen isotopes of conodonts from Kuh-e-Ali Bashi.

Sample	Position (m) from base	$\delta^{13}C_{carb}$ (VPDB)	Conodont taxa	$\delta^{18}O_{phos}$ (VSMOW)	Internal reproducibility (1σ)	n
Elikah Formation						
AB +450	24.50	-0.33	*Hindeodus* sp. (P1) + indet. (ramiform)	17.60	0.21	3
AB +435	24.35	-0.12	*Hindeodus* sp. (P1) + indet. (ramiform)	18.46	0.42	2
AB +412	24.12	-0.33	*Hindeodus* sp. (P1) + indet. (ramiform)	17.29	0.38	3
AB +390	23.90	-0.09	*Hindeodus* sp. (P1) + indet. (ramiform)	18.01	0.11	2
AB +285	22.85		*Hindeodus* sp. (P1) + indet. (ramiform)	17.67	-	1
AB +250	22.50		*Hindeodus* sp. (P1) + indet. (ramiform)	17.85	0.11	2
AB +170	21.70	-1.85	*Hindeodus* sp. (P1) + indet. (ramiform)	17.55	-	1
AB +151	21.51		*Hindeodus* sp. (P1) + indet. (ramiform)	17.79	-	1
AB +124	21.24	-1.10	*Hindeodus* sp. (P1) + indet. (ramiform)	19.75	-	1
'Boundary Clay'						
AB+50	20.50	-1.32	*Hindeodus* sp. (P1) + indet. (ramiform)	17.52	-	1
AB+45	20.45	-0.43	*Hindeodus* sp. (P1) + indet. (ramiform)	17.6	-	1
AB+40	20.40	0.41	*Hindeodus* sp. (P1) + indet. (ramiform)	18.09	0.60	2
*Paratirolites*Limestone						
AB-0	20.00	0.62	*Clarkina* sp. (P1)	19.31	0.19	3
AB-0	20.00	0.62	*Hindeodus* sp. (P1)	18.61	-	1
AB-5	19.95	1.25	*Clarkina* sp. (P1)	19.39	0.01	2
AB-10	19.90	1.78	*Clarkina* sp. (P1)	19.90	0.28	3
AB-15	19.85	1.37	*Clarkina* sp. (P1)	19.45	0.14	3
AB-30	19.70	1.51	*Clarkina* sp. (P1)	19.56	0.09	3
AB-56	19.44	2.40	*Hindeodus* sp. (P1)	20.04	-	1
AB-71	19.29	-0.72	*Hindeodus* sp. (P1)	20.18	-	1
AB-80	19.20	2.34	*Clarkina* sp. (P1)	19.81	0.05	3
AB-90	19.10	2.00	*Clarkina* sp. (P1)	19.41	0.32	2
AB-100	19.00	2.75	*Hindeodus* sp. (P1)	15.97	-	1
AB-115	18.85	2.95	*Clarkina* sp. (P1)	19.46	0.27	2
AB-140	18.60	3.05	*Clarkina* sp. (P1)	19.97	0.24	3
AB-148	18.52	2.71	*Clarkina* sp. (P1)	19.61	0.13	3
AB-155	18.45	1.76	*Clarkina* sp. (P1)	18.85	0.26	3
AB-170	18.30	-1.37	*Clarkina* sp. (P1)	19.36	0.06	3
AB-185	18.15	2.08	*Clarkina* sp. (P1)	19.37	0.18	3

Table S 1 – Oxygen isotopes of conodonts from Kuh-e-Ali Bashi.

Sample	Position (m) from base	$\delta^{13}C_{carb}$ (VPDB)	Conodont taxa	$\delta^{18}O_{phos}$ (VSMOW)	Internal reproducibility (1σ)	n
AB-191	18.09	3.01	*Clarkina* sp. (P1)	19.56	0.01	2
AB-200	17.98	3.24	*Clarkina* sp. (P1)	19.98	0.03	2
AB-220	17.8	3.32	*Clarkina* sp. (P1)	19.92	0.09	3
AB-240	17.6	3.22	*Clarkina* sp. (P1)	18.63	0.21	2
AB-245	17.55	2.88	*Clarkina* sp. (P1)	19.34	0.25	3
AB-265	17.35	3.46	*Clarkina* sp. (P1)	19.71	0.16	3
AB-330	16.70	3.11	*Clarkina* sp. (P1)	18.94	0.12	3
AB-340	16.60	3.20	*Clarkina* sp. (P1)	19.87	0.09	3
AB-380	16.20	3.08	*Clarkina* sp. (P1)	19.39	0.04	3
Ali Bashi Formation						
AB-440	15.60	3.21	*Clarkina* sp. (P1)	19.56	0.15	3
AB-480	15.20	3.10	*Clarkina* sp. (P1)	19.58	0.10	3
AB-570	14.30	3.15	*Clarkina* sp. (P1)	19.25	0.21	3
AB-690	13.10	2.84	*Clarkina* sp. (P1)	18.79	0.54	3
AB-895	11.05	3.8	*Clarkina* sp. (P1)	19.74	0.06	3
AB-1240	7.60	3.92	*Clarkina* sp. (P1)	20.04	0.18	3
AB-1290	7.10	3.89	*Clarkina* sp. (P1)	19.33	0.19	3
AB-1480	5.20	3.67	*Clarkina* sp. (P1)	18.82	0.04	2
AB-1605	3.95	3.27	*Clarkina* sp. (P1)	19.80	0.02	3
Julfa Beds						
AB-1740	2.60	3.69	*Clarkina* sp. (P1)	19.07	0.21	3
AB-1815	1.85	3.33	*Clarkina* sp. (P1)	19.05	0.21	3
AB-1830	1.70	3.56	*Clarkina* sp. (P1)	19.01	0.35	3
AB-1905	0.95	3.52	*Clarkina* sp. (P1)	19.25	0.09	3
AB-1995	0.05	3.57	*Clarkina* sp. (P1)	18.70	0.14	2

Table S 2 – Oxygen isotopes of conodonts from Zal.

Sample	Position (m) from base	$\delta^{13}C_{carb}$ (VPDB)	Conodont taxa	$\delta^{18}O_{phos}$ (VSMOW)	Internal reproducibility (1σ)	n
Elikah Formation						
Zl +940	29.40	0.31	*Hindeodus* sp. (P1) + indet. (ramiform)	17.40	-	1
Zl +845	28.45	0.09	*Hindeodus* sp. (P1) + indet. (ramiform)	16.55	-	1
Zl +715	27.15	-0.23	*Hindeodus* sp. (P1) + indet. (ramiform)	16.96	-	1
Zl +685	26.85	-0.26	*Hindeodus* sp. (P1)	18.05	0.06	2
Zl +480	24.80	-0.53	*Hindeodus* sp. (P1)	17.19	-	1
Zl +415	24.15	-0.43	*Hindeodus* sp. (P1) + indet. (ramiform)	15.52	-	1
ZL +360	23.60	-0.55	*Hindeodus* sp. (P1)	16.89	-	1
Zl +200	22.00	-0.94	*Hindeodus* sp. (P1)	17.59	0.51	2
Zl +70	20.70	-0.11	*Hindeodus* sp. (P1) + indet. (ramiform)	16.21	-	1
ZL+52	20.52	0.01	*Hindeodus* sp. (P1) + indet. (ramiform)	17.83	0.13	3
'Boundary Clay'						
Zl +47	20.47	0.26	*Hindeodus* sp. (P1) + indet. (ramiform)	16.94	-	1
Zl +45	20.45	0.51	*Hindeodus* sp. (P1) + indet. (ramiform)	17.58	0.21	3
Zl +43	20.43	0.32	*Hindeodus* sp. (P1) + indet. (ramiform)	17.51	0.26	3
ZL +10	20.10	0.79	*Clarkina* sp. (P1)	19.33	0.17	3
*Paratirolites*Limestone						
ZL 0	20.00	1.17	*Clarkina* sp. (P1)	19.14	0.16	3
Zl -65	19.35	2.10	*Hindeodus* sp. (P1)	17.45	-	1
Zl -200	18.00	2.62	*Clarkina* sp. (P1)	19.78	0.18	3
Ali Bashi Formation						
ZL -500	15.00	3.32	*Clarkina* sp. (P1)	18.73	0.06	2
ZL -500	15.00	3.32	*Hindeodus* sp. (P1)	18.24	0.17	3
ZL -630	13.70	3.03	*Clarkina* sp. (P1)	18.85	0.27	3
ZL -825	11.75	3.45	*Clarkina* sp. (P1)	19.63	0.07	3
ZL -1070	9.30	3.70	*Clarkina* sp. (P1)	19.12	0.17	3
ZL -1370	6.30	3.41	*Clarkina* sp. (P1)	19.15	0.11	3
ZL -1370	6.30	3.41	*Hindeodus* sp. (P1)	19.74	0.31	3
Julfa Beds						
ZL -1680	3.20		*Clarkina* sp. (P1)	19.00	0.24	3

Table S 2 – Oxygen isotopes of conodonts from Zal.

Sample	Position (m) from base	$\delta^{13}C_{carb}$ (VPDB)	Conodont taxa	$\delta^{18}O_{phos}$ (VSMOW)	Internal reproducibility (1σ)	n
ZL -1775	2.25	3.48	*Clarkina* sp. (P1)	19.74	0.20	3
ZL -1815	1.85	3.25	*Clarkina* sp. (P1)	19.65	0.01	2

Table S 3 – Oxygen and carbon isotope values and trace element concentrations of brachiopod shells.

Sample	$\delta^{13}C_{carb}$ (VPDB)	$\delta^{18}O_{carb}$ (VPDB)	Locality	Sr(ppm)	Mn(ppm)
Paratirolites Limestone					
AB-10	2.55	-2.49	Ali Bashi 1	303	31
AB-10	2.55	-2.84	Ali Bashi 1	323	84
AB-70	3.56	-2.54	Ali Bashi N	315	49
AB-235	3.52	-2.51	Ali Bashi N	295	24
AB-235	3.47	-2.53	Ali Bashi N	337	158
AB-285	4.36	-3.1	Ali Bashi N	327	160
AB-285	4.35	-2.63	Ali Bashi N	294	18
AB-285	4.24	-2.57	Ali Bashi N	300	26
AB-285	3.81	-3.23	Ali Bashi N	413	136
AB-285	3.84	-3.25	Ali Bashi N	389	172
AB-400	4.73	-3.49	Ali Bashi B	416	38
AB-400	4.43	-3.84	Ali Bashi B	447	58
AB-400	4.65	-3.41	Ali Bashi B	431	41
AB-400	4.81	-3.24	Ali Bashi B	370	27
Ali Bashi Formation					
AB-420	5.09	-2.76	Ali Bashi B	346	46
AB-420	4.2	-3.91	Ali Bashi B	456	81
AB-420	5.27	-2.67	Ali Bashi B	319	12
Zl-1060	4.23	-3.19	Zal	609	113
Zl-1060	4.36	-2.66	Zal	505	73
AB-1345	4.28	-3.11	Ali Bashi 1	495	200
AB-1345	4.6	-3.05	Ali Bashi 1	439	126
AB-1345	4.44	-3.17	Ali Bashi 1	514	161
AB-1345	4.26	-3.32	Ali Bashi 1	503	129

Supplementary material: Paper 3

Uncovering palaeoenvironmental information from bulk-carbonate δ^{13}C of Permian-Triassic 'Boundary Clay' sections

SUPPLEMENTARY MATERIAL

Uncovering palaeoenvironmental information from bulk-carbonate δ^{13}C of Permian-Triassic 'Boundary Clay' sections

Martin Schobben[a1], Clemens V. Ullmann[b], Lucyna Leda[a], Dieter Korn[a], Ulrich Struck[a], Wolf Uwe Reimold[a,c], Abbas Ghaderi[d], Thomas J. Algeo[e f], Christoph Korte[b]

[a] Museum für Naturkunde, Leibniz Institut für Evolutions- und Biodiversitätsforschung, Invalidenstr 43, D-10115 Berlin, Germany
[b] Department of Geosciences and Natural Resource Management, University of Copenhagen, ØsterVoldgade 10, DK-1350, Copenhagen, Denmark
[c] Humboldt Universität zu Berlin, Unter den Linden 6, 10099 Berlin, Germany
[d] Department of Geology, Faculty of Sciences, Ferdowsi University of Mashhad, Azadi Square, 9177948974 Mashhad, Iran
[e] Department of Geology, University of Cincinnati, Cincinnati, OH 45221-0013, U.S.A.
[f] State Key Laboratories BGEG and GPMR, China University of Geosciences, Wuhan 430074, China

Sequential extraction

(Weak) acid digestion has been a widely applied method to liberate trace elements from $CaCO_3$, in soil chemistry studies (Gleyzes et al., 2002) and studies of pelagic sediments (Chester and Hughes, 1967; Kryc et al., 2003; Martin et al., 1987), but also for carbonate rock (Barber, 1974; Brand and Veizer, 1980; Kryc et al., 2003; Neaman et al., 2004; Préat et al., 2006). To evaluate the effectiveness of trace element partitioning between carbonate minerals and non-carbonate detrital minerals, we measured the Al/Ca and Fe/Ca ratios in a subset of our samples. Aluminum and Fe of the soluble fraction were proposed first by Brand and Veizer (1980) as a tracer for contamination during the leaching procedure, because the acid could potentially etch parts of the aluminosilicate lattice, although the use of acetic acid would largely prevent this (Barber, 1974; Chester and Hughes, 1967). When comparing the $CaCO_3$ content with Al/Ca and Fe/Ca ratios (Tables S2 and 3), an obvious enrichment in samples with a high non-carbonate detrital component (clay and marl) becomes apparent (Fig. S1). A high Fe content can, however, exist in $CaCO_3$ with a possible hydrogenous (e.g., limonite or Fe-oolites; Kuhn et al., 2005) or diagenetic incorporation of Fe (e.g., dolomite; Barber, 1974). As both Al/Ca and Fe/Ca show a similar pattern of enrichment in low $CaCO_3$ rock, a clastic origin of high Al and Fe in the soluble fraction becomes a plausible explanation.

When comparing Al/Ca and Fe/Ca derived from two consecutive leaching stages on the same sample, the results suggest that contribution from the clastic fraction to the first leach is, on average, smaller than that of the second leach. Additionally, elevated Fe/Ca of the second leach is paired with higher Al/Ca and is characterized by a linear relationship, suggesting increased potential for contamination with the second leaching procedure (Fig. S1 and Table S1). Reduced buffering capacity against acetic acid of initial low $CaCO_3$ rock or by consecutive acid digestion, together with a high clastic content, results in leaching of the non-carbonate compounds. Comparing Mn/Ca, Sr/Ca and Mg/Ca with Al/Ca of both leaching procedures does not result in any linear relationship suggesting that etching of the non-carbonate detrital fraction did not contribute to these elements (Table S1). In summary, lowered $CaCO_3$ content

---

[1] Corresponding author: Phone: +49 (0) 3020938749, E-mail: martin.schobben@mfn-berlin.de, Postal address: Museum für Naturkunde, Leibniz Institut für Evolutions- und Biodiversitätsforschung, Invalidenstr 43, D-10115 Berlin. Germany

increases the risk of contamination by the leaching procedure through dissolution of clastic minerals; however, digestion with weak acetic acid has likely prevented alteration of Mn/Ca, Sr/Ca and Mg/Ca by the dissolution of the clastic detrital fraction. Besides clastic minerals, other bulk-rock constituents like Fe-oxides and Mn-oxides are dissolvable in acidic solutions (Chester and Hughes, 1967; Martin et al., 1987; Neaman et al., 2004). The acetic acid solution used in this study has an approximate pH of 2 and has particular implications for Mn/Ca, as lignand promoted and reductive dissolution of Mn-oxide by organic acids enhances solubility of Mn-oxides (Li and Schwartz, 2004). Fe-oxides, on the other hand, have a lower solubility in dilute acetic acid (Chester and Hughes, 1967).

Stratigraphic fixed median and appropriate bandwidth selection

To obtain a coherent δ^{13}C record throughout a specific interval sampling should be carried out in a consistent way, with a fixed sampling density. This is often not possible, for practical reasons such as absence of suitable limestone horizons. In addition, in the study of catastrophic events such as the P-Tr boundary interval, sampling tends to be concentrated around the horizon of interest (e.g., this study; Cao et al., 2009). This approach often results in a biased dataset from a statistical point of view. Added to this is the possibility of local diagenetic overprinting, such as in the here presented study, and the fact that bulk-rock carbonate samples are a mixture of different compounds of possibly different δ^{13}C. Subsampling and smoothing of these datasets possibly enables meaningful inferences upon these δ^{13}C records in terms of palaeoenvironmental changes as well as creating a possibility to use δ^{13}C as a stratigraphic tool. This procedure inevitability reduces the amount of information that can be obtained from the data but it also highlights the more significant changes within the studied interval that could possibly be obscured by the aforementioned inferences upon the data.

The method subdivides the studied interval into fixed stratigraphic intervals or bandwidths. The median is taken from the available δ^{13}C data of this interval and is subsequently taken as a representative value for the selected interval. The effect of bandwidth selection becomes visible when plotting a derivative of the produced trend line for consecutive bandwidths (Fig. S2). With this approach it becomes apparent that with increasing bandwidth less variability is emphasized within the smoothed curve. For the studied sections, a bandwidth comparative to one and half times the maximum distance between data points has been chosen, which logically resulted in stratigraphic bins of at least one data point. This also ensures that a fair amount of information can be extracted from the data at hand and the respective sampling distribution. In this way potential local variation in δ^{13}C, which lies below the minimum sampling density, caused by mechanisms as mentioned before and within the text, can be excluded. This method does not take into account differences caused by varying sedimentation rates, which might also have potential to create discrepancy between δ^{13}C curves of different sites.

The R source code is provided as a supplement (appendix).

References

Barber, C., 1974. Major and trace element associations in limestones and dolomites. Chemical Geology 14, 273-280.

Brand, U., Veizer, J., 1980. Chemical diagenesis of a multicomponent carbonate system-1: Trace elements. Journal of Sedimentary Petrology 50, 1219-1236.

Cao, C., Love, G.D., Hays, L.E., Wang, W., Shen, S., Summons, R.E., 2009. Biogeochemical evidence for euxinic oceans and ecological disturbance presaging the end-Permian mass extinction event. Earth and Planetary Science Letters 281, 188-201.

Chester, R., Hughes, M.J., 1967. A chemical technique for the separation of ferro-manganese minerals, carbonate minerals and adsorbed trace elements from pelagic sediments. Chemical

Geology 2, 249-262.

Gleyzes, C., Tellier, S., Astruc, M., 2002. Fractionation studies of trace elements in contaminated soils and sediments: a review of sequential extraction procedures. TrAC Trends in Analytical Chemistry 21, 451-467.

Jin, Y.G., Wang, Y., Wang, W., Shang, Q.H., Cao, C.Q., Erwin, D.H., 2000. Pattern of marine mass extinction near the Permian-Triassic boundary in South China. Science 289, 432 -436.

Kim, S.T., O'Neil, J.R., 1997. Equilibrium and nonequilibrium oxygen isotope effects in synthetic carbonates. Geochimica Et Cosmochimica Acta 61, 3461-3475.

Kryc, K.A., Murray, R.W., Murray, D.W., 2003. Elemental fractionation of Si, Al, Ti, Fe, Ca, Mn, P, and Ba in five marine sedimentary reference materials: results from sequential extractions. Analytica Chimica Acta 487, 117-128.

Kuhn, O., Weissert, H., Föllmi, K., Hennig, S., 2005. Altered carbon cycling and trace-metal enrichment during the late Valanginian and early Hauterivian. Eclogae Geologicae Helvetiae 98, 333-344.

Li, X.D., Schwartz, F.W., 2004. DNAPL remediation with in situ chemical oxidation using potassium permanganate: Part I. Mineralogy of Mn oxide and its dissolution in organic acids. Journal of Contaminant Hydrology 68, 39-53.

Martin, J.M., Nirel, P., Thomas, A.J., 1987. Sequential extraction techniques: Promises and problems. Marine Chemistry 22, 313-341.

Neaman, A., Mouélé, F., Trolard, F., Bourrié, G., 2004. Improved methods for selective dissolution of Mn oxides: applications for studying trace element associations. Applied Geochemistry 19, 973-979.

Préat, A., Morano, S., Loreau, J.-P., Durlet, C., Mamet, B., 2006. Petrography and biosedimentology of the Rosso Ammonitico Veronese (middle-upper Jurassic, north -eastern Italy). Facies 52, 265-278.

Pucéat, E., Joachimski, M.M., Bouilloux, A., Monna, F., Bonin, A., Motreuil, S., Moriniere, P., Henard, S., Mourin, J., Dera, G., Quesne, D., 2010. Revised phosphate-water fractionation equation reassessing paleotemperatures derived from biogenic apatite. Earth and Planetary Science Letters 298, 135-142.

Riccardi, A.L., Arthur, M.A., Kump, L.R., 2006. Sulfur isotopic evidence for chemocline upward excursions during the end-Permian mass extinction. Geochimica et Cosmochimica Acta 70, 5740-5752.

Yuan, D.-x., Shen, S.-z., Henderson, C.M., Chen, J., Zhang, H., Feng, H.-z., 2014. Revised conodont-based integrated high-resolution timescale for the Changhsingian Stage and end-Permian extinction interval at the Meishan sections, South China. Lithos 204, 220 -245.

Appendix

The R source code for the function of the stratigraphic fixed median (or *stratmedian*):

```
stratmedian <- function(height, proxy, t){

fixi <- c(seq(range(height)[1], range(height)[2], t), head(height,1))

fixed_carb <- c()

er<-c()

for(i in 1:(length(fixi)-1))

if(i==1)
r <- which(height <= fixi[i+1])
fixed_carb <- c(fixed_carb, median(proxy[r], na.rm=TRUE))
er<-c(er, mad(proxy[r], na.rm=TRUE))
}

if(i>1){
r <- which(height <= fixi[i+1] & fixi[i] <height)
fixed_carb <- c(fixed_carb, median(proxy[r], na.rm=TRUE))
er<-c(er, mad(proxy[r], na.rm=TRUE))
}

}
f2 <- fixi+((1/2)*t)
height <- f2[-(length(fixi)-1)]
proxy <- fixed_carb
sdmar<-er
res <- data.frame(height, proxy, sdmar)
Good<-complete.cases(res$height,res$proxy)
res<-res[Good,]
res <- res[order(-res[,1]), ]
}
```

The function *stratmedian* relies on three input parameters; *height* defines a variable which stands for stratigraphic heights (alternatively time of a time-series). *proxy* defines a variable which stands for the proxy (i.e. δ^{13}C) which will be sub-sampled for the selected bandwidth and smoothed by application of a median. *t* stands for the bandwidth (the stratigraphic interval) used to smooth the data. The smoothed proxy data will be printed as a data frame, containing a column of new stratigraphic height, smoothed proxy data and the respective standard deviation.

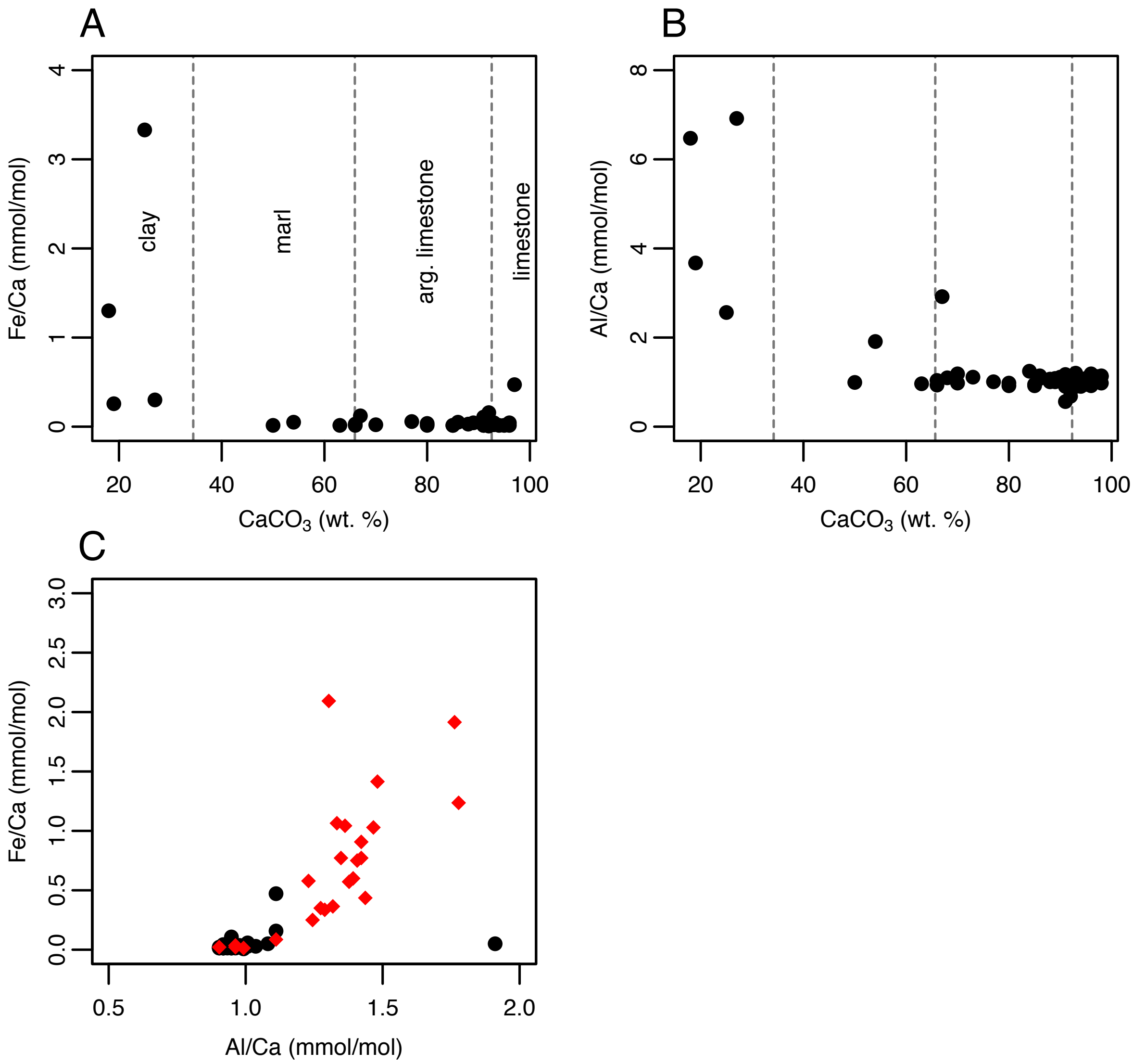

Figure S 1 – (A) Control experiment to evaluate the effect of $CaCO_3$ (wt. %) content on contamination by Fe from leaching of the aluminosilicate lattice. (B) Control experiment for the effect of $CaCO_3$ (wt. %) content on contamination by Al from leaching of the aluminosilicate lattice. (C) The effect of artificially lowering $CaCO_3$ content by two consecutive leaches on the leaching potential of Al and Fe from the aluminosilicate lattice. The black dots and red diamonds represent the first and second leach, respectively, and the linear regression line of the second leach is shown in black (see Table S1).

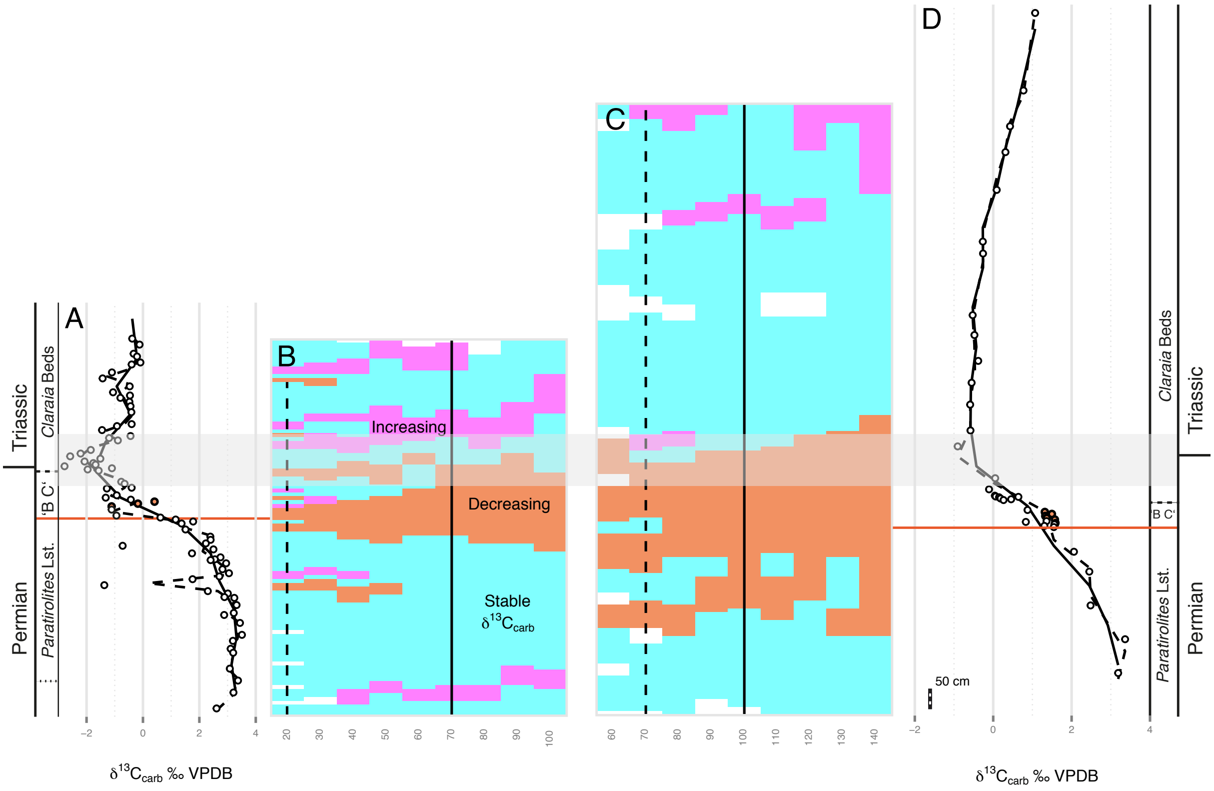

Figure S 2 – (A and D) δ^{13}C curves for Kuh-e-Ali Bashi and Zal, respectively. (B and C) These plots represent the respective derivative calculated from the trend-line of δ^{13}C between each consecutive interval (stratigraphic height) relating to the chosen bandwidth (x-axis) for Kuh-e-Ali Bashi and Zal data, respectively. The colors illustrate whether the derivative shows a significant change in comparison with the derivatives throughout the studied interval of each consecutive bandwidth. The red areas represent a significant decrease in δ^{13}C as such that the respective derivative is smaller than 68 % (1 σ) of all derivatives for each specific bandwidth. The purple area represents a significant increase in δ^{13}C such that the respective derivative is larger than 68 % (1 σ) of all derivatives for each specific bandwidth. Light blue areas suggest no change and the derivative of this δ^{13}C lies within the standard deviation (1 σ). The solid or dotted lines of the δ^{13}C curve and derivative plots represent the generalized trend for different bandwidths (stratigraphic fixed intervals).

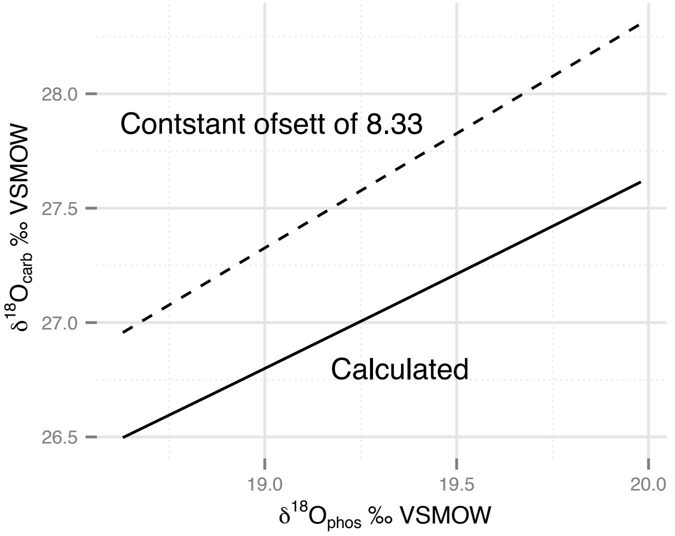

Figure S 3 – The conversion factor for conodont oxygen isotopes measured on phosphate. Comparison between conodont and brachiopod oxygen isotope compositions yields a conversion factor of 8.33 ‰ to be added to the conodont values relative to VSMOW, resulting in the stippled line. The second approach constitutes a back-calculation from palaeotemperatures based on conodont oxygen isotope composition by using the temperature equilibration of Kim and O'Neil (1997), resulting in the solid line. The palaeotemperature from conodont isotope signatures were initially calculated by the function of Pucéat et al. (2010). Note, the offset between the two different approaches, which converge towards lower values.

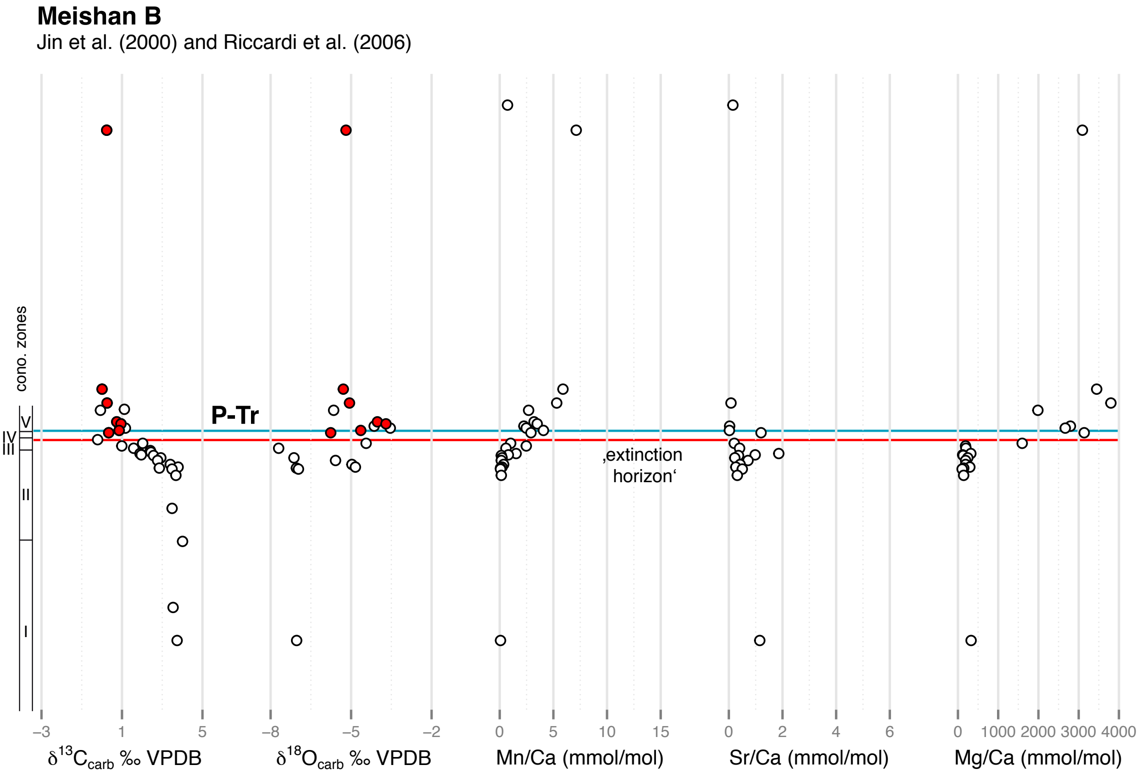

Figure S 4 – δ^{13}C, δ^{18}O, Mn/ Ca, Sr/Ca and Mg/Ca of both bulk-carbonate fraction from the Meishan B section (Jin et al., 2000; Riccardi et al., 2006). The red circles of the bulk-rock δ^{13}C and δ^{18}O are used to show elevated Mg/Ca (>mean + standard deviation; 1σ). Note that elevated Mg are linked to increased whole-rock δ^{18}O, which is typical for dolomite. In addition, similar to the Kuh-e-Ali Bashi 1 and Zal section enriched Mg are linked to higher Mn/Ca values. Conodont zones; (I) *C. changxingensis*, (II) *C. yini*, (III) *C. meishanensis*, (IV) *C. zhejiangensis – H. changxingensis*, (V) *H. parvus* (Yuan et al., 2014).

Table S 1 – Results for a linear model fit of different chemical parameters and consecutive leaching procedure, with Al/Ca indicating the degree of contamination by leaching from the aluminosilicate lattice. Goodness of correlation is shown by Pearson r^2, significance as the p-value, and the degrees of freedom by n. High Pearson r^2 suggests a good correlation, whereas low *p*-values stand for a significant correlation.

	x (response)	y (terms)	Peasron r^2	*p*-value	n
1st leach	Al/Ca	Fe/Ca	0.16	2.00E-02	33
2nd leach			0.54	4.10E-05	22
1st leach	Al/Ca	Mn/Ca	0.10	1.00E-02	58
2nd leach			0.29	1.00E-02	22
1st leach	Al/Ca	Sr/Ca	0.01	3.70E-01	58
2nd leach			0.07	2.30E-01	22
1st leach	Al/Ca	Mg/Ca	0.05	9.00E-02	58
2nd leach			0.10	1.40E-01	22

Table S 2 – Geochemical results for Kuh-e-Ali Bashi. $CaCO_3$ (wt. %) partly given in Ghaderi et al. (2014). 2^{nd} stands for the order of consecutive elemental analysis on the same sample.

Height	Lithology	$\delta^{13}C_{carb}$	$\delta^{18}O_{carb}$	$CaCO_3$*	Sr/Ca_{sol}	Mg/Ca_{sol}	Mn/Ca_{sol}	Al/Ca_{sol}	Fe/Ca_{sol}	Sr/Ca_{sol}	2ndMg/Ca_{sol}	2ndMn/Ca_{sol}	2ndAl/Ca_{sol}	2ndFe/Ca_{sol}	2nd
4.50	platy limestone	-0.4	-6.8	95	1.0	16.4	0.9	1.1	NA		NA	NA	NA	NA	NA
4.35	platy limestone	-0.1	-5.9	93	NA	NA	NA	NA	NA		NA	NA	NA	NA	NA
4.12	platy limestone	-0.3	-7.1	97	1.1	14.6	0.7	1.1	0.5		NA	NA	NA	NA	NA
4.05	platy limestone	-0.2	-7.1	97	1.1	11.0	0.7	1.1	NA		1.1	14.7	0.7	1.3	2.1
3.90	platy limestone	-0.1	-5.7	93	NA	NA	NA	NA	NA		NA	NA	NA	NA	NA
3.85	platy limestone	-0.4	-6.7	NA	NA	NA	NA	NA	NA		NA	NA	NA	NA	NA
3.65	platy limestone	-1.1	-7.0	96	NA	NA	NA	NA	NA		NA	NA	NA	NA	NA
3.50	platy limestone	-1.4	-6.7	96	0.9	13.6	0.8	0.9	0.0		NA	NA	NA	NA	NA
3.30	platy limestone	-0.5	-6.7	NA	NA	NA	NA	NA	NA		NA	NA	NA	NA	NA
3.15	platy limestone	-1.1	-6.5	95	NA	NA	NA	NA	NA		NA	NA	NA	NA	NA
3.07	platy limestone	-0.5	-6.4	98	1.6	13.9	1.1	1.1	NA		1.4	11.3	0.8	1.2	0.6
3.01	platy limestone	-0.8	-6.7	97	NA	NA	NA	NA	NA		NA	NA	NA	NA	NA
2.91	platy limestone	-0.5	-6.4	96	1.0	12.6	0.9	0.9	0.0		NA	NA	NA	NA	NA
2.80	platy limestone	-0.4	-6.7	94	0.8	13.6	1.3	0.9	0.0		NA	NA	NA	NA	NA
2.65	platy limestone	-0.4	-6.7	95	0.7	14.2	1.2	0.9	0.0		NA	NA	NA	NA	NA
2.35	platy limestone	-0.4	-7.0	93	0.7	12.5	1.6	0.9	0.0		NA	NA	NA	NA	NA
2.30	platy limestone	-0.9	-7.3	91	0.7	13.1	1.5	0.9	0.0		NA	NA	NA	NA	NA
2.20	platy limestone	-1.4	-6.8	89	0.6	11.9	1.7	1.1	NA		0.6	10.7	1.7	1.3	1.1
2.05	nodular limestone	-0.4	-6.7	96	0.7	14.3	1.8	1.2	NA		0.7	13.3	1.8	0.9	0.0
2.00	nodular limestone	-1.2	-7.1	82	NA	NA	NA	NA	NA		NA	NA	NA	NA	NA
1.94	nodular limestone	-0.9	-8.1	88	NA	NA	NA	NA	NA		NA	NA	NA	NA	NA
1.70	nodular limestone	-1.9	-7.0	68	0.4	18.4	3.1	1.1	NA		0.3	30.3	3.6	1.8	1.2
1.61	nodular limestone	-2.2	-7.3	56	0.6	12.8	2.5	1.0	NA		0.4	25.8	3.1	1.8	1.9
1.54	nodular limestone	-2.6	-7.1	66	0.4	20.4	2.1	0.9	0.0		NA	NA	NA	NA	NA
1.48	nodular limestone	-1.5	-7.3	85	0.6	17.4	2.4	0.9	0.0		NA	NA	NA	NA	NA
1.41	nodular limestone	-2.1	-7.3	79	0.5	17.0	2.7	1.1	NA		0.7	12.6	2.8	1.4	1.1
1.37	nodular limestone	-1.8	-7.4	88	0.5	15.4	2.4	0.9	0.0		NA	NA	NA	NA	NA
1.33	nodular limestone	-1.7	-7.3	80	0.6	15.9	1.9	1.1	NA		0.6	13.6	2.0	1.3	0.4
1.29	nodular limestone	-2.8	-7.7	73	0.5	30.8	2.4	1.9	0.0		NA	NA	NA	NA	NA
1.24	nodular limestone	-1.1	-6.9	54	0.6	16.5	2.2	0.9	0.0		NA	NA	NA	NA	NA
1.21	nodular limestone	-2.0	-7.5	53	NA	NA	NA	NA	NA		NA	NA	NA	NA	NA
1.18	nodular limestone	-1.6	-7.1	70	0.4	17.5	2.5	1.2	NA		0.4	13.3	3.0	1.4	0.4
0.90	clay	-0.8	-7.0	77	0.5	17.8	2.3	1.0	0.1		NA	NA	NA	NA	NA

Table S 2 – Geochemical results for Kuh-e-Ali Bashi. $CaCO_3$ (wt. %) partly given in Ghaderi et al. (2014). 2^{nd} stands for the order of consecutive elemental analysis on the same sample.

Height	Lithology	$\delta^{13}C_{carb}$	$\delta^{18}O_{carb}$	$CaCO_3$*	Sr/Ca_{sol}	Mg/Ca_{sol}	Mn/Ca_{sol}	Al/Ca_{sol}	Fe/Ca_{sol}	Sr/Ca_{sol}	2ndMg/Ca_{sol}	2ndMn/Ca_{sol}	2ndAl/Ca_{sol}	2ndFe/Ca_{sol}	2nd
0.85	clay	-0.6	-6.9	84	0.5	17.7	2.7	1.2	NA		0.5	18.1	3.1	1.4	0.8
0.75	clay	-0.4	-6.8	70	0.4	18.8	3.4	1.0	0.0		NA	NA	NA	NA	NA
0.73	clay	-1.3	-7.1	67	0.4	40.4	3.1	2.9	0.1		NA	NA	NA	NA	NA
0.56	clay	-0.9	-6.3	50	0.3	16.5	2.4	1.0	0.0		NA	NA	NA	NA	NA
0.50	clay	-1.3	-7.3	63	0.3	21.4	1.7	1.0	0.0		NA	NA	NA	NA	NA
0.45	clay	-0.4	-7.0	80	0.4	18.0	2.4	1.0	0.0		NA	NA	NA	NA	NA
0.40	clay	0.4	-4.9	66	0.5	92.4	3.4	1.0	0.0		NA	NA	NA	NA	NA
0.35	clay	-0.2	-5.2	25	0.6	592.1	11.9	2.6	3.3		NA	NA	NA	NA	NA
0.28	clay	-1.1	-6.6	18	0.4	51.3	3.7	6.5	1.3		NA	NA	NA	NA	NA
0.20	clay	-1.1	-4.3	19	0.5	40.1	3.2	3.7	0.3		NA	NA	NA	NA	NA
0.05	clay	-0.9	-6.5	27	0.6	43.0	2.7	6.9	0.3		NA	NA	NA	NA	NA
0.00	clay	0.6	-6.7	92	0.7	21.1	2.3	1.0	0.0		NA	NA	NA	NA	NA
-0.05	nodular limestone	1.2	-6.6	92	0.7	21.3	2.3	1.1	0.2		NA	NA	NA	NA	NA
-0.10	nodular limestone	1.8	-5.5	86	0.6	20.4	1.6	1.1	NA		0.5	23.4	1.6	1.0	0.0
-0.15	nodular limestone	1.4	-6.1	86	0.6	17.4	1.9	1.1	0.1		NA	NA	NA	NA	NA
-0.30	nodular limestone	1.5	-6.2	88	0.6	13.9	1.5	1.0	0.0		NA	NA	NA	NA	NA
-0.48	nodular limestone	2.4	-5.2	91	0.6	20.2	1.2	1.2	NA		0.6	21.0	1.4	1.5	1.0
-0.56	nodular limestone	2.4	-5.2	92	0.6	20.6	1.3	1.0	NA		0.5	23.0	1.3	1.5	1.4
-0.65	nodular limestone	2.2	-5.1	90	NA	NA	NA	NA	NA		NA	NA	NA	NA	NA
-0.71	nodular limestone	-0.7	-6.2	91	0.5	11.7	1.1	0.9	0.0		NA	NA	NA	NA	NA
-0.80	nodular limestone	2.5	-5.3	97	0.6	21.7	1.4	1.1	NA		0.5	25.1	1.1	1.0	0.0
-0.90	nodular limestone	1.7	-5.8	93	0.5	12.1	1.2	1.2	NA		0.6	18.8	1.5	1.0	0.0
-1.00	nodular limestone	2.8	-4.8	90	NA	NA	NA	NA	NA		NA	NA	NA	NA	NA
-1.05	nodular limestone	2.5	-5.9	NA	NA	NA	NA	NA	NA		NA	NA	NA	NA	NA
-1.07	nodular limestone	2.4	-5.7	96	0.6	16.7	1.4	1.2	NA		0.6	19.8	1.5	1.1	0.1
-1.15	nodular limestone	2.9	-4.8	97	NA	NA	NA	NA	NA		NA	NA	NA	NA	NA
-1.30	nodular limestone	2.8	-5.1	90	0.7	19.4	1.6	1.1	NA		0.5	21.9	1.3	1.4	0.9
-1.40	nodular limestone	3.1	-4.0	93	0.7	19.7	1.6	1.1	NA		0.6	20.1	1.4	1.4	0.6
-1.48	nodular limestone	2.7	-5.1	89	0.6	20.0	1.8	1.0	0.0		NA	NA	NA	NA	NA
-1.55	nodular limestone	1.8	-5.8	89	NA	NA	NA	NA	NA		NA	NA	NA	NA	NA
-1.70	nodular limestone	-1.4	-6.1	92	0.5	13.7	1.5	1.1	NA		0.4	14.1	1.3	1.3	0.3
-1.85	nodular limestone	2.3	-5.8	98	0.6	13.7	1.5	1.1	NA		0.4	12.8	1.2	1.3	0.4
-2.00	nodular limestone	2.9	-5.1	NA	NA	NA	NA	NA	NA		NA	NA	NA	NA	NA

Table S 2 – Geochemical results for Kuh-e-Ali Bashi. CaCO$_3$ (wt. %) partly given in Ghaderi et al. (2014). 2nd stands for the order of consecutive elemental analysis on the same sample.

Height	Lithology	$\delta^{13}C_{carb}$	$\delta^{18}O_{carb}$	CaCO$_3$*	Sr/Ca$_{sol}$	Mg/Ca$_{sol}$	Mn/Ca$_{sol}$	Al/Ca$_{sol}$	Fe/Ca$_{sol}$	Sr/Ca$_{sol}$	2ndMg/Ca$_{sol}$	2ndMn/Ca$_{sol}$	2ndAl/Ca$_{sol}$	2ndFe/Ca$_{sol}$	2nd
-2.02	nodular limestone	3.2	-4.9	90	0.6	20.3	1.7	1.0	0.0		NA	NA	NA	NA	NA
-2.20	nodular limestone	3.3	-4.9	93	0.6	16.0	1.5	1.1	NA		0.6	20.6	1.7	1.3	0.8
-2.40	nodular limestone	3.2	-4.9	96	0.6	17.0	1.8	1.1	NA		0.6	19.3	1.8	1.4	0.8
-2.45	nodular limestone	2.9	-4.2	96	NA	NA	NA	NA	NA		NA	NA	NA	NA	NA
-2.65	nodular limestone	3.4	-5.1	92	0.6	23.2	1.6	1.0	0.0		NA	NA	NA	NA	NA
-2.95	nodular limestone	3.5	-4.7	90	NA	NA	NA	NA	NA		NA	NA	NA	NA	NA
-3.10	nodular limestone	3.2	-5.4	91	NA	NA	NA	NA	NA		NA	NA	NA	NA	NA
-3.30	nodular limestone	3.1	-4.9	91	NA	NA	NA	NA	NA		NA	NA	NA	NA	NA
-3.40	nodular limestone	3.2	-4.9	92	0.6	22.7	2.8	0.7	NA		0.5	20.9	1.9	1.4	0.6
-3.80	nodular limestone	3.1	-5.3	92	0.6	17.1	2.0	1.0	0.0		NA	NA	NA	NA	NA
-4.10	nodular limestone	3.4	-4.7	91	0.6	23.6	2.0	0.6	NA		0.5	22.4	1.9	1.2	0.3
-4.40	nodular limestone	3.2	-4.5	91	0.6	21.7	2.5	1.0	0.1		NA	NA	NA	NA	NA
-4.80	nodular limestone	2.6	-5.5	93	0.6	20.3	3.0	0.9	0.0		NA	NA	NA	NA	NA

Table S 3 – Geochemical results for Zal. 2^{nd} stands for the order of consecutive elemental analysis on the same sample.

Height	Lithology	$\delta^{13}C_{carb}$	$\delta^{18}O_{carb}$	$CaCO_3$ (wt. %)	Sr/Ca_{sol}	Mg/Ca_{sol}	Mn/Ca_{sol}	Al/Ca_{sol}	Sr/Ca_{sol} 2nd	Mg/Ca_{sol} 2nd	Mn/Ca_{sol} 2nd	Al/Ca_{sol} 2nd
10.95	platy limestone	0.8	-6.5	98	0.69	14.99	0.63	0.63	0.67	16.16	0.68	1.32
10.05	platy limestone	0.4	-7.2	95	3.42	10.58	0.29	NA	NA	NA	NA	NA
9.40	platy limestone	0.3	-7.2	NA	NA	NA	NA	NA	NA	NA	NA	NA
8.45	platy limestone	0.1	-7.4	95	0.86	16.18	0.63	NA	NA	NA	NA	NA
7.15	platy limestone	-0.3	-6.9	88	3.00	17.95	0.52	NA	NA	NA	NA	NA
6.85	platy limestone	-0.3	-7.3	91	1.18	15.05	0.61	NA	NA	NA	NA	NA
5.30	platy limestone	-0.5	-6.8	95	1.15	9.76	0.61	0.77	1.26	10.17	0.49	0.95
4.80	platy limestone	-0.5	-6.2	94	0.84	17.48	0.59	NA	NA	NA	NA	NA
4.15	platy limestone	-0.4	-6.8	96	2.57	11.10	0.59	NA	NA	NA	NA	NA
3.60	platy limestone	-0.6	-7.8	NA	NA	NA	NA	NA	NA	NA	NA	NA
3.05	platy limestone	-0.6	-6.7	91	1.01	16.83	0.98	NA	NA	NA	NA	NA
2.40	platy limestone	-0.6	-6.7	94	0.92	21.64	0.99	NA	NA	NA	NA	NA
2.00	platy limestone	-0.9	-6.4	77	2.28	22.01	3.29	NA	NA	NA	NA	NA
1.20	platy limestone	0.1	-8.3	84	0.62	37.78	1.72	NA	NA	NA	NA	NA
0.92	platy limestone	-0.1	-7.2	88	0.71	20.83	2.50	0.63	0.53	34.72	3.08	1.61
0.76	platy limestone	0.0	-7.0	87	0.84	22.82	1.70	NA	NA	NA	NA	NA
0.74	platy limestone	0.1	-8.3	88	0.55	21.54	1.36	0.65	0.40	25.99	1.64	1.43
0.73	platy limestone	0.6	-3.0	NA	NA	NA	NA	NA	NA	NA	NA	NA
0.72	platy limestone	0.2	-7.0	79	0.85	33.59	2.24	NA	NA	NA	NA	NA
0.69	platy limestone	0.2	-7.3	84	0.69	24.50	1.65	NA	NA	NA	NA	NA
0.67	platy limestone	0.5	-6.8	87	0.75	55.77	1.33	NA	NA	NA	NA	NA
0.65	platy limestone	0.3	-6.7	85	1.05	41.78	1.10	NA	NA	NA	NA	NA
0.40	clay	0.9	-7.4	80	0.95	21.68	1.51	NA	NA	NA	NA	NA
0.35	clay	1.3	-6.3	81	1.10	252.38	3.41	NA	NA	NA	NA	NA
0.30	clay	1.5	-6.1	66	1.15	396.41	4.38	NA	NA	NA	NA	NA
0.25	clay	1.3	-6.4	55	1.38	423.19	5.25	NA	NA	NA	NA	NA
0.20	clay	1.4	-7.2	35	0.76	40.36	1.73	NA	NA	NA	NA	NA
0.16	clay	1.6	-6.1	70	1.33	218.38	3.79	NA	NA	NA	NA	NA
0.12	clay	1.4	-6.4	61	1.14	312.71	4.25	NA	NA	NA	NA	NA
0.10	clay	0.8	-7.0	49	0.68	20.47	1.49	0.80	0.52	23.06	2.02	0.96
0.08	clay	1.6	-6.1	87	0.71	26.38	1.38	NA	NA	NA	NA	NA
0.05	clay	1.6	-6.9	62	0.73	19.92	1.29	NA	NA	NA	NA	NA
0.04	clay	1.6	-6.4	84	NA	NA	NA	NA	NA	NA	NA	NA
0.00	nodular limestone	1.3	-7.3	80	0.75	19.79	1.74	NA	NA	NA	NA	NA

Table S 3 – Geochemical results for Zal. 2^{nd} stands for the order of consecutive elemental analysis on the same sample.

Height	Lithology	$\delta^{13}C_{carb}$	$\delta^{18}O_{carb}$	$CaCO_3$ (wt. %)	Sr/Ca_{sol}	Mg/Ca_{sol}	Mn/Ca_{sol}	Al/Ca_{sol}	Sr/Ca_{sol} 2nd	Mg/Ca_{sol} 2nd	Mn/Ca_{sol} 2nd	Al/Ca_{sol} 2nd
-0.03	nodular limestone	1.5	-5.5	72	NA	NA	NA	NA	NA	NA	NA	NA
-0.65	nodular limestone	2.1	-5.6	72	NA	NA	NA	NA	NA	NA	NA	NA
-1.15	nodular limestone	2.5	-5.5	89	0.58	20.92	1.14	0.71	0.43	20.57	1.12	0.97
-2.00	nodular limestone	2.5	-5.1	89	NA	NA	NA	NA	NA	NA	NA	NA
-2.85	nodular limestone	3.4	-4.8	90	0.73	19.54	1.58	0.64	0.45	22.56	1.26	1.40
-3.70	nodular limestone	3.2	-5.3	93	0.64	22.24	1.58	NA	NA	NA	NA	NA
-5.00	nodular limestone	3.3	-5.0	NA	NA	NA	NA	NA	NA	NA	NA	NA

Supplementary material: Paper 4

A flourishing ocean caused the marine Late Permian mass extinction

SUPPLEMENTARY INFORMATION

1 Supplementary methods and materials

1.1 Localities

The Kuh-e-Ali Bashi 1, sensu ref.1, (38.940 °N, 45.520 °E) and Zal (38.733 °N, 45.580 °E) sections of the Julfa region (NW Iran, Extended Data Fig. 1) are situated on the north-northeastern margin of the NW Iranian Terrane, belonging to the Cimmerian Microcontinents during the latest Permian (Extended Data Fig. 1). Carbonate rock successions in this area spanning the Permian-Triassic (P-Tr) boundary interval can be divided into two major lithological units: the Ali Bashi Formation of which the Paratirolites Limestone Member marks the upper part and the Zal Member the lower part. The Aras Member sensu ref. 2 (or 'Boundary Clay') and the following limestone unit, belonging to the Elikah Formation (Extended Data Figs. 2 and 3). The Zal Member consists, dominantly, of shales with some intercalations of limestone and marls. $CaCO_3$ contents of the red nodular Paratirolites Limestone beds ranges between 70 and 90 wt. % (ref. 2), and rocks are classified as argillaceous limestone. The latter unit contains abundant hardground features, such as ferromanganese crusts, microbial encrustations and hardground intraclasts. Macrofossil assemblages consist of rare ammonites, nautiloids, rugose corals and brachiopod shells. Microfossil assemblages consist of abundant conodont elements and actinopterygian teeth. This unit is conformably overlain by the Aras Member which records a marked reduction of $CaCO_3$ to about 18 wt. %[2]. Fossil remains become rare in this unit but ostracods, sponge remains, bellerophontids and conodont elements can still be found. The Elikah Formation with predominant limestone beds follows the clay-rich Aras Member. A slight difference between the two sections exists, where the lower part of the latter unit at the Kuh-e-Ali Bashi section resembles the Paratirolites Limestone, the Zal section is marked from the base onward with a platy limestone lithology.

1.2 Carbonate-associated sulphate (CAS) extraction and isotope analysis

The applied CAS extraction method minimizes the potential alteration of the CAS-sulphur or oxygen isotope signal during the analytical procedure by the use of subsequent NaCl leaches[3]. The NaCl leaches are precipitated with a $BaCl_2$ solution and, subsequently, the concentration of the sulphate fraction not structurally substituted within the $CaCO_3$ lattice (leachable non-CAS) is determined gravimetrically. These steps are repeated until no leachable non-CAS is observed. In follow up, acid digestion of the sample is performed with 25 % HCl under restricted atmospheric exchange and in a time window in generally not more than 3 hours to prevent oxidation of sulphide species[4]. The sulphate of the digested carbonate rock (i.e. the CAS fraction) is also precipitated as barium sulphate and CAS concentrations are gravimetrically determined. The sulphur isotopic composition of the leachable non-CAS and CAS was obtained by an Elemental Analyzer connected to a ThermoFinnigan Delta Plus mass spectrometer. Precision was confirmed by repeated measurements on the international standards (IAEA-S-1, IAEAS-2, IAEA-S-3, NBS127) and internal lab standards (CdS, Ag2S). This yielded an accuracy of 0.09 ‰ and a reproducibility on average better than 0.40 ‰ (Supplementary Table 1). The oxygen isotopic composition of the leachable non-CAS and CAS was measured with a TC/EA interfaced to a ThermoFinnigan Delta Plus XL mass spectrometer. International standards (IAEA-SO-5, IAEA-SO-6, NBS127) and an in-house standard ($BaSO_4$) were used to determine the precision of the procedure. This resulted in an accuracy of 0.40 ‰ and a reproducibility of ± 0.80 ‰ (Supplementary Table 2).

1.3 Chromium reducible sulphur (CRS) extraction and isotope analysis

The CRS content was extracted from the remaining residue after the CAS extraction by the chromium reduction method[5]. Under continuous N_2 flow, samples were reacted with HCl and chromium powder to produce acidic chromium chloride and were heated to a gentle boil for 1.5 hours. Sulphur was trapped as zinc sulphide in a zinc acetate solution and converted to silver sulphide for filtrating and drying. The

CRS concentrations were determined gravimetrically. For sulphur isotopic analyses ($\delta^{34}S_{CRS}$), extracted silver sulphide was weighed into tin capsules with added V_2O_5 to aid in combustion. Isotope measurements were performed on a Costech Elemental Analyzer ECS 4010 connected to a Thermo Delta V+ Isotope Ratio Mass Spectrometer. Precision was confirmed by repeated measurements on the international standards (IAEA-S-1, IAEAS-2, IAEA-S-3, NBS127) and resulted in an accuracy of 0.24 ‰ and a reproducibility better than 0.40 ‰.

2 Supplementary discussion

2.1 Facies description

The successive lithological change from dominantly clastic to nodular Paratirolites limestone has been related to drowning of the carbonate platform[6,7]. This notion is enforced by lithological features, such as frequent hardgrounds as well as the distinctive iron colour of the latter unit—plausibly related to authigenic iron accumulation, and suggest a low rate of carbonate accumulation[8,9], and see ref. 10. The Zal Member in contrast to the *Paratirolites* Limestone Member probably had a higher siliciclastic input and, hence, higher sedimentation rates. Deposition of these units occurred at a depth below the storm wave base in a well oxygenated environment by a productive skeletal carbonate factory[6,7,11]. The Aras Member has been assigned to increased terrigenous input, based on the thickness of this unit[6], expressing, possibly, high sediment accumulation rates[11]. Although concomitant reduced carbonate production could have been equally important, e.g. see ref. 6,10. However, depth of deposition was likely still below storm wave base in an oxic environment, based on ostracod assemblages[11,12]. Somewhat higher CRS values in this unit might relate to a higher local production of sulphide by MSR (Supplementary Tables 3 and 4). Increased pyrite content, or other iron sulphides, in the sediment can be a function of lower oxygenation or higher OC availability, but the two parameters are likely linked, e.g. see ref. 13. The sulphide-oxygen front, at these sites, was most likely located within the sediments as a high resolution microfacies analysis, by ref. 10, did not reveal framboidal pyrite, a sign of water column sulphide, see ref. 14. A continuation of deep-water conditions, especially for the nodular lithology, which resembles the pre-extinction strata—deep water facies, has been implied for the first few meters above the Aras Member at the Kuh-e-Ali Bashi site. The platy limestone beds of the Elikah Formation might, however, indicate a somewhat shallower depth[10] but no high amplitude sea level changes[6,10]. Lithological indices for pervasive anoxia and euxinia, such as framboidal pyrite or high OC accumulation, are absent. Assemblages of ostracods together with abundant bivalve specimens, *Claraia*, might, however, indicate slight or episodic dysoxic bottom water conditions[6,11].

2.2 Timescale

U-Pb geochronology has provided absolute dates for the chemo- and biostratigraphically well-resolved P-Tr GSSP of Meishan[15–17]. Recent advances in U-Pb dating with ID TIMS and especially the use of a more precisely calibrated tracer solution (EARTHTIME) resulted in dates with an analytical uncertainty less than 100 kyr[18]. We used the radiometric datums of ref. 18 to make linear interpolations for conodont zones of the Meishan section, taken from ref. 19. Notably the top of *H. hindeodus* zone is 251.873 ± 0.004 Mya and the first occurrence datum (FAD) of *C. yini* is 252.046 Mya. In addition, the FAD of *H. hindeodus* is 251.902 ± 0.024 Mya, the 'extinction horizon' (base bed 25 Meishan) is 251.941± 0.037 Mya from ref. 18 FAD of *C. wangi*: 254.150 Mya from ref. 17, are used in the age model. The linear interpolations have some inherent uncertainties, which can be potentially large as used sediment accumulation rates may not account for hiatuses in the Meishan section. However, these datums present, in our opinion, the best possibility to construct a timeframe for the studies sites in NW Iran. Recently developed Late Permian high-resolution conodont zonation constructed by the sample-population taxonomic approach for the Kuh-e-Ali Bashi sections as well as for Meishan, together with some new data for the Early Triassic in Iran (Extended Data Fig. 4), tentatively enables to correlate these sections[19,20]. However, inconsistencies arise when correlating the base of the *C. bachmanni* zone of the P-Tr section in NW Iran with the base of the *C. yini* zone of the Meishan section as proposed by ref. 21. The resulting sedimentation rates for the *Paratirolites* Limestone Member and the Zal Member seem to contradict with the facies interpretation of these units (Extended Data Fig. 5 and section *Facies*). The inconsistency relating to conodont biozones correlation, could possibly relate to endemism in the south Chinese basin from the base of the *H. changhxingensis* zone up to the 'extinction horizon'[11]. The 'extinction horizon' and the marker species for the Triassic can be traced to the south Chinese sections with relative great confidence[11]. We consider a sedimentation rate of 0.3 cm kyr^{-1} for the *Paratirolites* Limestone Member. This is similar to sedimentation rates obtained, by using the same conodont dates, for the uniform nodular limestone unit that spans the complete Changhsingian of the Abadeh section (central Iran, Extended Data Fig. 5). In addition, a sedimentation rate of about 0.3 cm kyr^{-1}, is typical for these kind of lithlogies[22,23] and agrees with inferences from ref. 6. The pre-extinction samples, belonging to the *Paratirolites* Limestone Member, together with, the post-extinction samples, can in this way be placed into a temporal framework for the sites in NW Iran with relative confidence.

2.3 Reliability of the CAS proxy

Sulphate is incorporated into the calcite lattice as an anion substitution with no apparent fractionation of the sulphur isotopes and would therefore record the $\delta^{34}S$ composition of the ambient seawater sulphate[24,25]. The reliability of CAS oxygen isotopes in recording certain aspects of the global sulphur cycle has been acknowledged in a recent study of ref. 26. However, they pointed out that questions remain about the influence of possible vital fractionation effects and specific microhabitats upon $\delta^{18}O_{CAS}$. In contrast, other studies[4,27], have shown that ancient CAS oxygen isotopes agree well with time equivalent $\delta^{18}O$ from sulphate locked in evaporites, suggesting that $\delta^{18}O_{CAS}$ can be a proxy for seawater chemistry. Multiple high amplitude variations in the isotopic composition of CAS - thought to represents original seawater chemistry - has been used to explain scenarios describing the end-Permian mass extinction[27,28]. This large $\delta^{34}S_{CAS}$ variability, however, may also reflect post-depositional alteration[28].

CRS, leachable non-CAS and CAS are marked with distinct isotopic values (Extended Data Fig. 6). Based on this observation we imply that leachable non-CAS and CRS could be potential sources to alter the original isotopic composition of CAS. Hence, to identify possible alteration of the CAS isotope signature, the relative abundance of CRS, leachable non-CAS and CAS for each sample is helpful in this respect. More so, considering the evidence that initial large CAS concentrations buffer against diagenetic overprinting of the isotope signal[29,30]. To approximate the likelihood that our obtained isotope values reflect ambient seawater sulphate-$\delta^{34}S$ and $\delta^{18}O$, concentrations of CRS and non-CAS sulphate relative to CAS are compared with $\delta^{34}S_{CAS}$ of each sample (Extended Data Fig. 7).

Samples with comparatively high CRS seem to be prepositioned towards lower $\delta^{34}S_{CAS}$, whereas both depleted and enriched values dominate the sample population marked by a relatively high amount of leachable non-CAS (Extended Data Fig. 7). Noteworthy, is that depleted values of $\delta^{34}S_{CAS}$, accompanied by high CRS/CAS or leachable non-CAS/CAS, are mainly found at a low $CaCO_3$ % interval around the 'extinction horizon', especially for the Kuh-e Ali Bashi (Extended Data Figs. 2, 3 and 7). It is therefore perceivable that these depleted $\delta^{34}S_{CAS}$ from low carbonate samples and consequentially low CAS concentrations are in part an effect of the oxidation of sulphide species, such as H_2S, or sulphide minerals, such as pyrite or greigite, during the rock diagenesis[4,31]. These likely altered $\delta^{34}S_{CAS}$ lie in the same range as the low $\delta^{34}S$ values of the CRS and leachable non-CAS fractions (Extended Data Fig. 6). In addition, these low-carbonate rocks are also marked by some depleted $\delta^{18}O_{CAS}$ relative to values bracketing those (Extended Data Fig. 2 and 3). The concomitant low $\delta^{34}S_{CAS}$ and $\delta^{18}O_{CAS}$ of this interval in the Kuh-e-Ali Bashi section results in a positive correlation with $\delta^{34}SCAS$ (de-trended r^2 =0.71). This observation suggests a common mechanism for these paired low $\delta^{34}S_{CAS}$ and $\delta^{18}O_{CAS}$ for which oxidation of sulphide is the most likely one. This chemical reaction mainly uses H_2O as an oxygen source with a value close to VSMOW[4,32].

On the other hand, some of the samples, mainly from the Triassic part of the Zal section, with relative high leachable non-CAS concentrations are marked by enriched $\delta^{34}S_{CAS}$. These enriched values could be suggestive of an isotopic evolution reflecting progressing MSR in an evolving sulphate pool approaching closed system conditions[4]. This would also agree with the often enriched $\delta^{18}O_{CAS}$ and $\delta^{34}S$ from leachable non-CAS and CRS, respectively (e.g., Zl 4.15 and 10.05 m, see Supplementary Tables 3 and 4). Enriched sulphate-$\delta^{34}S$ produced by the isotope fractionation associated with MSR might be incorporated during authigenic carbonate formation. More so, as post-depositional carbonate precipitation could be a direct result of increased pore water alkalinity due to sulphate reduction[33]. As such, we argue that the ratios of CRS and leachable non-CAS with CAS provide a good impression of the likelihood that an actual seawater sulphate isotope signal is recorded in CAS. Based on the density distribution (Extended Data Fig. 7), CRS/CAS of 0.1 and non-CAS/CAS of 0.4 are used as static cut-off boundaries for the here-presented CAS isotope values. The resulting time series for $\delta^{34}S_{CAS}$ and $\delta^{18}O_{CAS}$, with the highest probability of capturing seawater sulphate, show close to identical isotope patterns (Fig. 1).

2.4 Steady state P-Tr S cycle model

The observed lower background value for Late Permian marine sulphate is 17‰, considering the measured pre-extinction $\delta^{34}S_{CAS}$ (Fig. 1). Low S isotope marine sulphate can be considered to reflect either a change in S input, specifically the input of S with a lower isotopic composition or reduced global pyrite burial, e.g. see ref. 34. We hypothesize that exposed Carboniferous and Permian strata on the continents were rich in isotopically depleted pyrite sulphur[34]. Hence, to achieve steady state, we solved the following equation for δ_w, assuming that Δ_{MSR} is 35 ‰, e.g. ref. 36, 37, and taking Holocene values for the other parameters (Supplementary Table 5.)

$$\delta_w = \frac{F_p(\delta_{SO_4} + \Delta_{MSR}) + F_e\delta_{SO_4} - Q_v\delta_v + Q_m\delta_m}{Q_w} \tag{S1}$$

This calculation yielded a value of 1.9 ‰ for δ_w, which is in the lower range of presently observed values[38,39]. Low oxygen isotopic values for the weathering flux, normally assumed e.g. ref. 40 cannot, however, equate for the Permian background $\delta^{18}O_{SO_4}$ values of 17 ‰, as observed in $\delta^{18}O_{CAS}$ (Fig. 1). A different mechanism is required to explain this feature. The fluxes associated with anhydrite formation (F_s) and subsequent sulphide oxidation (Q_h) by cycling of seawater through oceanic crust at hydrothermal systems, which only have a net effect on the S isotope part of S cycle by (Q_m)[36], present a good candidate. We postulate that F_s and Q_h could have been more important during this time interval. We estimated the difference in F_s to Holocene values by solving the following equation:

$$F_s = \frac{(Q_w\delta_w + Q_v\delta_v + Q_h\delta_m + Q_{ox}\delta_{ox}) - F_{MSR}(\delta_{SO_4} + \Delta_{MSR}) + F_e\delta_{SO_4}}{\delta_{SO_4}} \tag{S2}$$

Keeping Q_m constant, required for the S isotope part of the S cycle, necessitates a concomitant change in Q_h, seen in equation (5). The cycling of seawater to oceanic crust would be 5.2 times larger than e.g. proposed by ref. 37 to sustain steady state with P-Tr background values. Initial steady state between the OC (M_{oc}) and sulphate (M_{SO_4}) reservoirs was reached by drawing a linear relation between primary productivity (Q_{po}) and sulphate weathering flux (Q_w) and using initial values to calculate this linear relation.

2.5 Sensitivity experiments

By conducting sensitivity experiments we determined if the solutions with a best fit to the data are unique or can be explained in alternative scenarios. A critical aspect of the Permian and Triassic is the necessity of lowered marine sulphate levels with respect to modern levels. A low oceanic sulphate reservoir can explain sulphate isotope excursions constrained to short time intervals—shorter than the residence time of marine sulphate (sub-million year)—without unrealistically large changes in fluxes[41]. This would be most appropriate for the excursions in the records of sulphate-sulphur and oxygen isotope presented here which occur within an interval smaller than 40 kyr. This would require that estimates for P-Tr sulphate levels ranging from 18 mM[42] , based on fluid inclusion in marine late Permian halite, to

<4 mM, based on rate variation of 100 ‰ Myr^{-1} in sulphur isotopes in the Early Triassic, and suggested to be a consequence of, e.g., evaporite deposition during the Permian[41] are valid. We test the influence of the initial seawater sulphate concentration by performing each experiment with a spectrum of sulphate concentrations between 2-18 mM (Extended Data Figs. 8 and 9).

A scenario to explain the observed S cycle perturbation is volcanism[27], besides scenarios associated with the fluxes of MSR[28]. Total volume of S released by volcanism outgassing of basalts produced by the Siberian trap is estimated as 6300-7800 Gt[42], with S isotope values close to values for background volcanism. Although crustal contamination of evaporite derived S has been suggested to enrich evolved sulphate with ^{34}S, this mechanism does in general not drive S isotope values higher than 5 ‰[43]. The main eruption phase of the Siberian Trap basalts has been constrained to a short magmatic event <2 Ma, with the main phase correlated with bed 24 in Meishan[45]. Based on conodont correlation, this is close to the 'extinction horizon' found at the studied sites in NW Iran. Volcanic pulses of less than 10^4 years may have contributed to concentrated fluxes of volatiles into the atmosphere, in maybe as much as 25 pulses[43,46]. This would constitute a $\sim$ 30 times bigger S flux then background volcanism, based on the accumulative volatile release during these pulses. The sulphate oxygen isotope composition of this flux could near 34 ‰ when considering that equilibrium between water and sulphate is faster in an acidic medium[32]. Acidic meteoric water associated with Siberian trap volcanism could be realistic as concomitant land-plant deconstruction has been related to acid rain[47]. When constructing a model scenario with these boundary conditions, however, an excursion as observed in the geochemical data requires unrealistic large sulphate contributions from volcanism over an extended period of time (Extended Data Fig. 8). Based on a set of analysis with our S-Cycle coupled to an OC pool, we consider an increased weathering flux as most probable for producing a deviating pattern of sulphate-$\delta^{34}S$ and δ^{18}O. This scenario does not necessitate unrealistic changes in in the isotopic composition or sizes of fluxes. The simultaneous reduction of S burial as pyrite, and S input via weathering can explain the negative sulphate S isotope excursion as observed in CAS, without temporary sequestration of microbially produced H_2S as proposed by ref. 27, 28, which is unlikely as pre-extinction large-scale bottom water anoxia in a stagnant ocean has been largely dismissed[48,49]. A low marine sulphate level (2 mM) for the later Permian to Early Triassic ocean, as proposed by ref. 41, 50, is, however necessary to allow fluctuations in $\delta^{34}S_{SO_4}$.

1. Teichert C, Kummel B, Sweet WC. Permian-Triassic strata, Kuh-e-Ali Bashi, Northwestern Iran. Bulletin of the Museum of Comparative Zoology, Harvard University 1973, 145(8): 359-472.
2. Ghaderi A, Leda L, Schobben M, Korn D, Ashouri AR. High-resolution stratigraphy of the Changhsi gian (Late Permian) successions of NW Iran and the Transcaucasus based on lithological features, conodonts and ammonoids. Fossil Record 2014, 17(1): 41-57.
3. Wotte T, Shields-Zhou GA, Strauss H. Carbonate-associated sulfate: Experimental comparisons of common extraction methods and recommendations toward a standard analytical protocol. Chemical Geology 2012, 326–327(0): 132-144.
4. Goldberg T, Poulton SW, Strauss H. Sulphur and oxygen isotope signatures of late Neoproterozoic to early Cambrian sulphate, Yangtze Platform, China: Diagenetic constraints and seawater evolution. Precambrian Research 2005, 137(3–4): 223-241.
5. Canfield DE, Raiswell R, Westrich JT, Reaves CM, Berner AE. The use of chromium reduction in the analysis of reduced inorganic sulfur in sediments and shales. Chemical Geology 1986, 54(1–2): 149-155.
6. Richoz S, Krystyn L, Baud A, Brandner R, Horacek M, Mohtat-Aghai P. Permian–Triassic boundary interval in the Middle East (Iran and N. Oman): Progressive environmental change from detailed carbonate carbon isotope marine curve and sedimentary evolution. Journal of Asian Earth Sciences 2010, 39(4): 236-253.
7. Aghai PM, Vachard D, Krainer K. Transported foraminifera in Palaeozoic deep red nodular limestones exemplified by latest Permian Neoendothyra in the Zal section (Julfa area , NW Iran). Revista Espanola de Micropaleontologia 2009, 41(1-2): 197-213.
8. Flügel E. Microfacies of carbonate rock. Springer: Berlin, Germany, 2004.
9. White WM. The Oceans as a Chemical System. 1998, pp 645-699.

10. Leda L, Korn D, Ghaderi A, Hairapetian V, Struck U, Reimold W. Lithostratigraphy and carbonate microfacies across the Permian–Triassic boundary near Julfa (NW Iran) and in the Baghuk Mountains (Central Iran). Facies 2014, 59(2): 1-31.
11. Kozur HW. Biostratigraphy and event stratigraphy in Iran around the Permian-Triassic Boundary (PTB): Implications for the causes of the PTB biotic crisis. Global and Planetary Change 2007, 55(1-3): 155-176.
12. Korte C, Kozur HW. Carbon isotope stratigraphy across the Permian/Triassic boundary at Jolfa (NW-Iran), Peitlerkofel (Sass de Pütia, Sass de Putia), Pufels (Bula, Bulla), Tesero (all three Southern Alps, Italy) and Gerennavár (Bükk Mts., Hungary). Journal of Alpine Geology 2005, 47: 119-135.
13. Canfield DE. Sulfate reduction and oxic respiration in marine sediments: implications for organic carbon preservation in euxinic environments. Deep Sea Research Part A Oceanographic Research Papers 1989, 36(1): 121-138.
14. Wilkin RT, Arthur MA. Variations in pyrite texture, sulfur isotope composition, and iron systematics in the Black Sea: evidence for Late Pleistocene to Holocene excursions of the o2-h2s redox transition. Geochimica et Cosmochimica Acta 2001, 65(9): 1399-1416.
15. Bowring SA, Erwin DH, Jin YG, Martin MW, Davidek K, Wang W. U/Pb zircon geochronology and tempo of the end-Permian mass extinction. Science 1998, 280(5366): 1039-1045.
16. Mundil R, Ludwig KR, Metcalfe I, Renne PR. Age and timing of the Permian mass extinctions: U/Pb dating of closed-system zircons. Science 2004, 305(5691): 1760-1763.
17. Shen S-z, Crowley JL, Wang Y, Bowring SA, Erwin DH, Sadler PM, et al. Calibrating the End-Permian Mass Extinction. Science 2011, 334(6061): 1367-1372.
18. Burgess SD, Bowring S, Shen S-z. High-precision timeline for Earth's most severe extinction. Proceedings of the National Academy of Sciences 2014, 111(9): 3316-3321.
19. Yuan D-x, Shen S-z, Henderson CM, Chen J, Zhang H, Feng H-z. Revised conodont-based integrated high-resolution timescale for the Changhsingian Stage and end-Permian extinction interval at the Meishan sections, South China. Lithos (0).
20. Ghaderi A, Leda L, Schobben M, Korn D, Ashouri AR. High-resolution stratigraphy of the Changhsir gian (Late Permian) successions of NW Iran and the Transcaucasus based on lithological features, conodonts and ammonoids. Foss Rec 2014, 17(1): 41-57.
21. Shen S-Z, Mei S-L. Lopingian (Late Permian) high-resolution conodont biostratigraphy in Iran with comparison to South China zonation. Geological Journal 2010, 45(2-3): 135-161.
22. Wendt J, Aigner T, Neugebauer J. Cephalopod limestone deposition on a shallow pelagic ridge: the Tafilalt Platform (upper Devonian, eastern Anti-Atlas, Morocco). Sedimentology 1984, 31(5): 601-625.
23. Martire L. Stratigraphy, facies and synsedimentary tectonics in the Jurassic Rosso Ammonitico Veronese (Altopiano di Asiago, NE Italy). Facies 1996, 35(1): 209-236.
24. Strauss H. Geological evolution from isotope proxy signals — sulfur. Chemical Geology 1999, 161(1–3): 89-101.
25. Kampschulte A, Strauss H. The sulfur isotopic evolution of Phanerozoic seawater based on the analysis of structurally substituted sulfate in carbonates. Chemical Geology 2004, 204(3–4): 255-286.
26. Rennie VCF, Turchyn AV. The preservation of and in carbonate-associated sulfate during marine diagenesis: A 25 Myr test case using marine sediments. Earth and Planetary Science Letters 2014, 395(0): 13-23.
27. Newton RJ, Pevitt EL, Wignall PB, Bottrell SH. Large shifts in the isotopic composition of seawater sulphate across the Permo–Triassic boundary in northern Italy. Earth and Planetary Science Letters 2004, 218(3–4): 331-345.
28. Riccardi AL, Arthur MA, Kump LR. Sulfur isotopic evidence for chemocline upward excursions during the end-Permian mass extinction. Geochimica et Cosmochimica Acta 2006, 70(23): 5740-5752.
29. Gill BC, Lyons TW, Frank TD. Behavior of carbonate-associated sulfate during meteoric diagenesis

and implications for the sulfur isotope paleoproxy. Geochimica et Cosmochimica Acta 2008, 72(19): 4699-4711.

30. Lyons TW, Walter LM, Gellatly AM, Martini AM, Blake RE. Sites of anomalous organic remineralization in the carbonate sediments of South Florida, USA: The sulfur cycle and carbonate-associated sulfate. Geological Society of America Special Papers 2004, 379: 161-176.
31. Marenco PJ, Corsetti FA, Hammond DE, Kaufman AJ, Bottjer DJ. Oxidation of pyrite during extraction of carbonate associated sulfate. Chemical Geology 2008, 247(1–2): 124-132.
32. Llyod RM. Oxygen-18 Composition of Oceanic Sulfate. Science 1967, 156(3779): 1228-1231.
33. Schrag DP, Higgins JA, Macdonald FA, Johnston DT. Authigenic Carbonate and the History of the Global Carbon Cycle. Science 2013, 339(6119): 540-543.
34. Paytan A, Kastner M, Campbell D, Thiemens MH. Seawater Sulfur Isotope Fluctuations in the Cretaceous. Science 2004, 304(5677): 1663-1665.
35. Berner RA, Canfield DE. A new model for atmospheric oxygen over Phanerozoic time. American Journal of Science 1989, 289(4): 333-361.
36. Adams DD, Hurtgen MT, Sageman BB. Volcanic triggering of a biogeochemical cascade during Oceanic Anoxic Event 2. Nature Geosci 2010, 3(3): 201-204.
37. Arthur MA. Volcanic contributions to the carbon and sulfur geochemical cycle and global change. In: Sigurdsson H, Houghton B, McNutt SR, Rymer H, Stix J (eds). Encyclopedia of volcanoes. Academic Press: California, 2000, pp 1045-1056.
38. Krouse H. Sulphur isotopes in our environment. Handbook of environmental isotope geochemistry 1980, 1: 435-471.
39. Hurtgen MT, Arthur MA, Suits NS, Kaufman AJ. The sulfur isotopic composition of Neoproterozoic seawater sulfate: implications for a snowball Earth? Earth and Planetary Science Letters 2002, 203(1): 413-429.
40. Turchyn AV, Schrag DP. Oxygen Isotope Constraints on the Sulfur Cycle over the Past 10 Million Years. Science 2004, 303(5666): 2004-2007.
41. Song H, Tong J, Algeo TJ, Song H, Qiu H, Zhu Y, et al. Early Triassic seawater sulfate drawdown. Geochimica et Cosmochimica Acta 2014, 128(0): 95-113.
42. Horita J, Zimmermann H, Holland HD. Chemical evolution of seawater during the Phanerozoic: Implications from the record of marine evaporites. Geochimica et Cosmochimica Acta 2002, 66(21): 3733-3756.
43. Black BA, Elkins-Tanton LT, Rowe MC, Peate IU. Magnitude and consequences of volatile release from the Siberian Traps. Earth and Planetary Science Letters 2012, 317–318(0): 363-373.
44. Ripley EM, Lightfoot PC, Li C, Elswick ER. Sulfur isotopic studies of continental flood basalts in the Noril'sk region: implications for the association between lavas and ore-bearing intrusions. Geochimica et Cosmochimica Acta 2003, 67(15): 2805-2817.
45. Reichow MK, Pringle MS, Al'Mukhamedov AI, Allen MB, Andreichev VL, Buslov MM, et al. The timing and extent of the eruption of the Siberian Traps large igneous province: Implications for the end-Permian environmental crisis. Earth and Planetary Science Letters 2009, 277(1–2): 9-20.
46. Pavlov VE, Fluteau F, Veselovskiy RV, Fetisova AM, Latyshev AV. Secular geomagnetic variations and volcanic pulses in the Permian-Triassic traps of the Norilsk and Maimecha-Kotui provinces. Izv, Phys Solid Earth 2011, 47(5): 402-417.
47. Visscher H, Looy CV, Collinson ME, Brinkhuis H, Cittert J, Kürschner WM, et al. Environmental mutagenesis during the end-Permian ecological crisis. Proceedings of the National Academy of Sciences of the United States of America 2004, 101(35): 12952-12956.
48. Winguth AME, Maier-Reimer E. Causes of the marine productivity and oxygen changes associated with the Permian–Triassic boundary: A reevaluation with ocean general circulation models. Marine Geology 2005, 217(3–4): 283-304.
49. Brennecka GA, Herrmann AD, Algeo TJ, Anbar AD. Rapid expansion of oceanic anoxia immediately before the end-Permian mass extinction. Proceedings of the National Academy of Sciences 2011, 108(43): 17631-17634.

50. Luo G, Kump LR, Wang Y, Tong J, Arthur MA, Yang H, et al. Isotopic evidence for an anomalously low oceanic sulfate concentration following end-Permian mass extinction. Earth and Planetary Science Letters 2010, 300(1–2): 101-111.
51. Brand W, A., Coplen T, B., Vogl J, Rosner M, Prohaska T. Assessment of international reference materials for isotope-ratio analysis (IUPAC Technical Report). Pure and Applied Chemistry; 2014. p. 425.
52. Canfield DE, Farquhar J. Animal evolution, bioturbation, and the sulfate concentration of the oceans. Proceedings of the National Academy of Sciences 2009, 106(20): 8123-8127.
53. Holt BD, Kumar R. Oygen isotope fractionation for understanding the sulfur cycle. In: Krouse H, Grinenko VA (eds). Stable isotopes Natural and anthropogenic sulphur in the environment SCOPE 43. Wiley and sons: New York, 1991, pp 27-44.
54. Böttcher ME, Thamdrup B, Vennemann TW. Oxygen and sulfur isotope fractionation during anaerobic bacterial disproportionation of elemental sulfur. Geochimica et Cosmochimica Acta 2001, 65(10): 1601-1609.
55. Joachimski MM, Lai X, Shen S, Jiang H, Luo G, Chen B, et al. Climate warming in the latest Permian and the Permian–Triassic mass extinction. Geology 2012, 40(3): 195-198.
56. Stampfli, GM and Borel, GD. A plate tectonic model for the Paleozoic and Mesozoic constrained by dynamic plate boundaries and restored synthetic oceanic isochrons. Earth and Planetary Science Letters 2002, 196: 17-33.

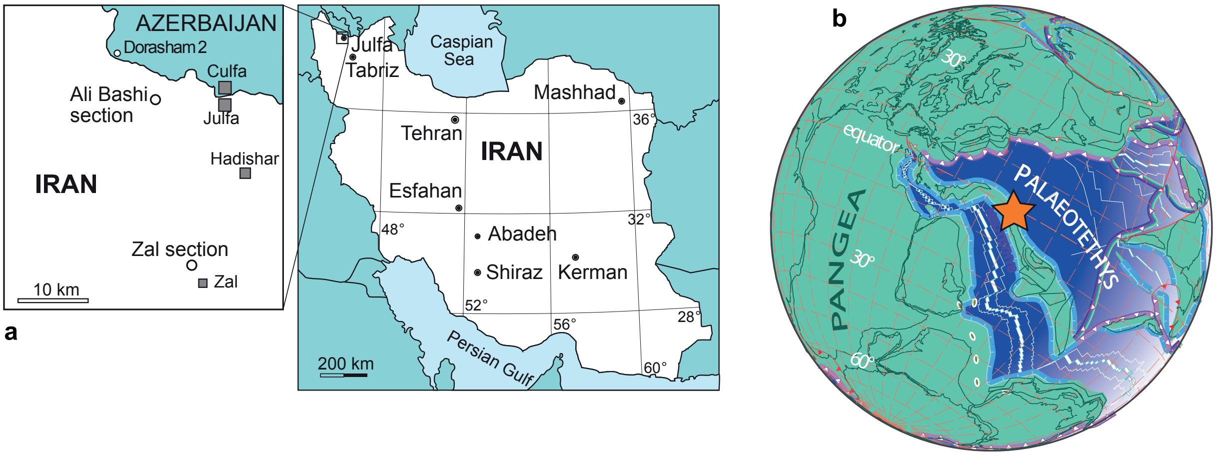

Extended data Figure 1 – Geographic and palaeogeographic setting. (a) Geographic setting of the Zal and Kuh-e-Ali Bashi 1 sections in NW Iran (b) Geographic location of the studied sections during the P-Tr interval[56].

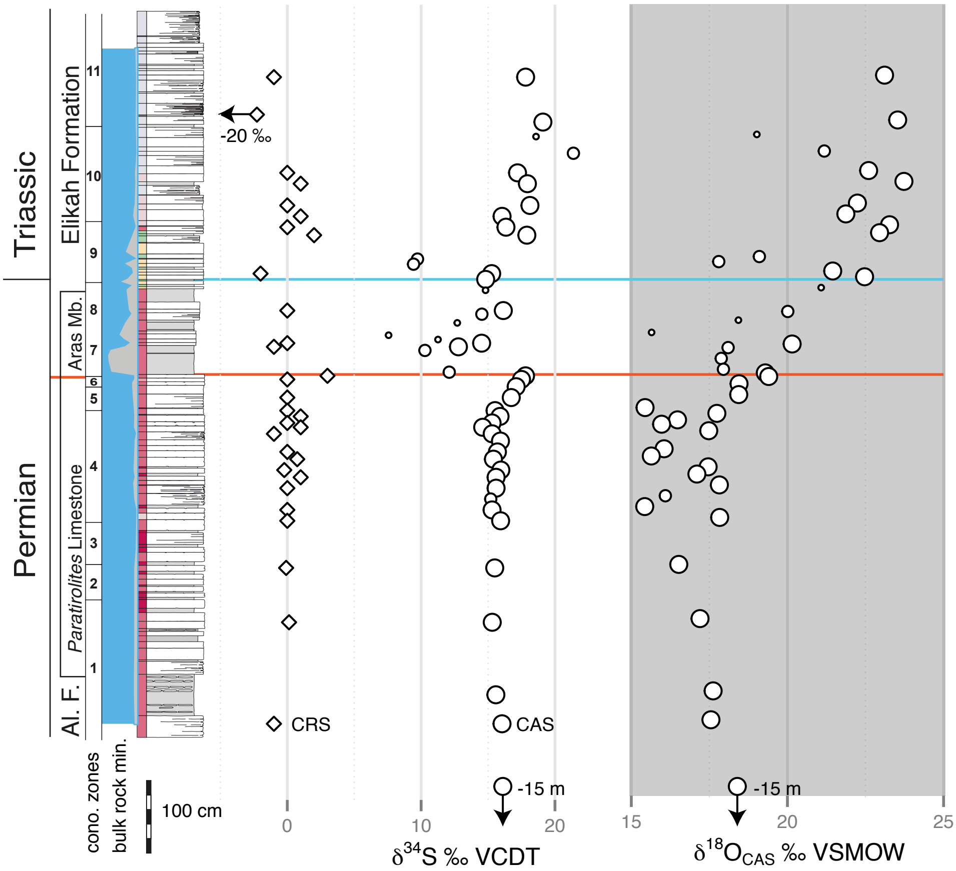

Extended data Figure 2 – Stratigraphic column of the Kuh-e-Ali Bashi 1 section. Lithological column and stratigraphic position of $\delta^{34}S_{CRS}$, $\delta^{34}S_{CAS}$ and $\delta^{18}O_{CAS}$. Conodont zones: (11) *I. staeschei*, (10) *H. lobota*, (9) *H.parvus*, (8) *M. ultima - S. ?mostleri*, (7) *H. praeparvus-H. changxingensis*, (6) *C. hauschkei*, (5) *C. abadehensis*, (4) *C. yini*, (3) *C. nodosa*, (2) *C. bachmanni*, (1) *C. changxingensis*.

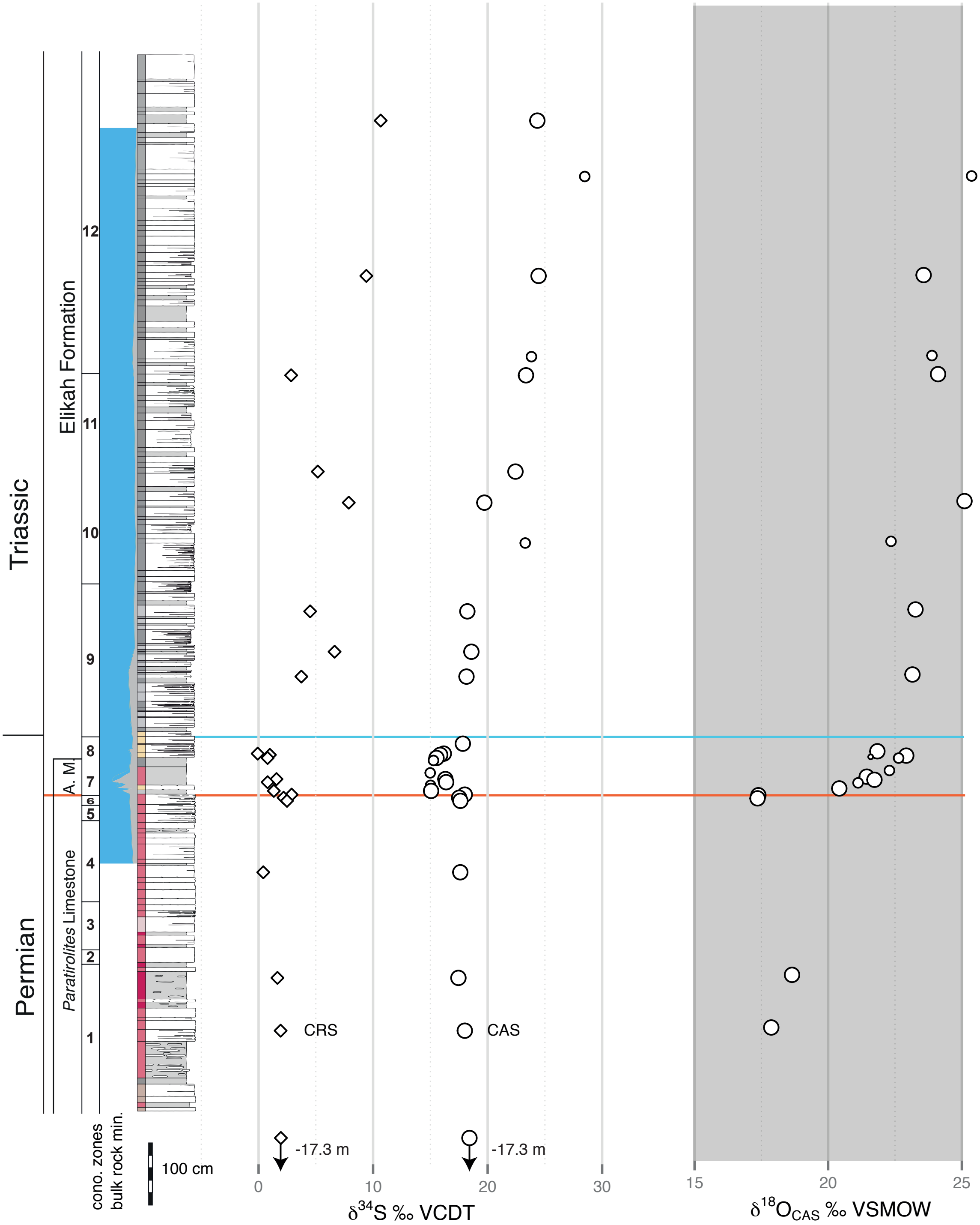

Extended data Figure 3 – Stratigraphic column of the Kuh-e-Ali Bashi 1 section. Lithological column and stratigraphic position of $\delta^{34}S_{CRS}$, $\delta^{34}S_{CAS}$ and $\delta^{18}O_{CAS}$. Conodont zones: (11) *I. staeschei*, (10) *H. lobota*, (9) *H.parvus*, (8) *M. ultima - S. ?mostleri*, (7) *H. praeparvus-H. changxingensis*, (6) *C. hauschkei*, (5) *C. abadehensis*, (4) *C. yini*, (3) *C. nodosa*, (2) *C. bachmanni*, (1) *C. changxingensis*.

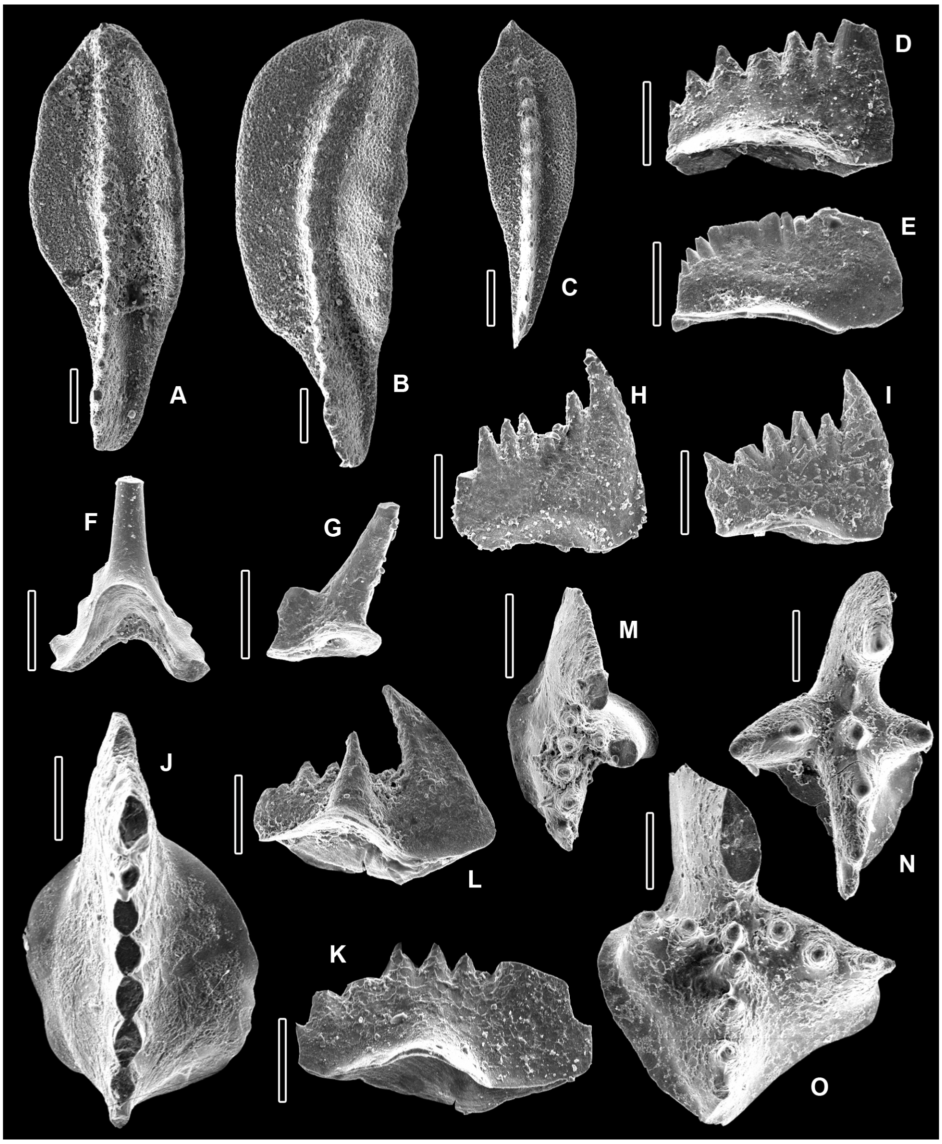

Extended data Figure 4 – Characteristic Late Changhsingian – Early Griesbachian conodonts from the Julfa region (scale bars equal to 100 μm). All specimens stored in the collection of the Ferdowsi University of Mashhad. (A) *Clarkina yini* (Mei et al., 1998); FUM# G258-6, Ali Bashi Formation, Main Valley Section, upper view. (B) *Clarkina abadehensis abadehensis* (Ghaderi et al., 2014); FUM# 1J248-6, Ali Bashi Formation, Ali Bashi 1 Section, upper view. (C) *Clarkina hauschkei* (Kozur, 2004); FUM# 1J249D-9, Ali Bashi Formation, Ali Bashi 1 Section, upper view. (D) *Hindeodus praeparvus* (Kozur, 1996); FUM# G274-6, Elikah Formation, Main Valley Section, lateral view. (E) *Hindeodus changxingensis* (Wang, 1995); FUM# 1J252-11, Elikah Formation, Ali Bashi 1 Section, lateral view. (F) *Stepanovites ?mostleri* (Kozur, 2004); M element, FUM# 1J253-16, Elikah Formation, Ali Bashi 1 Section, lateral view. (G) *Merrillina ultima* (Kozur, 2004); Pa element, FUM# 4J203-7, Elikah Formation, Ali Bashi 4 Section, lateral view. (H) *Hindeodus parvus* (Kozur and Pjatakova, 1976); FUM# G278-17, Elikah Formation, Main Valley Section, lateral view. (I) *Hindeodus parvus* (Kozur and Pjatakova, 1976); FUM# AJ206-2, Elikah Formation, Aras Valley Section, lateral view. (J) *Hindeodus lobata* (Ghaderi et al., 2014); FUM# 4J217-5, Elikah Formation, Ali Bashi 4 Section, upper view. (K) *Hindeodus lobata* (Ghaderi et al., 2014); FUM# 1J265-4, Elikah Formation, Ali Bashi 1 Section, lateral view. (L) *Isarcicella staeschei* (Dai and Zhang, 1989); FUM# 1J270-4, Elikah Formation, Ali Bashi 1 Section, lateral view. (M) *Isarcicella staeschei* (Dai and Zhang, 1989); FUM# 4J222-7, Elikah Formation, Ali Bashi 4 Section, upper view. (N) *Isarcicella isarcica* (Huckriede, 1958); FUM# 1J281-1, Elikah Formation, Ali Bashi 1 Section, upper view. (O) *Isarcicella isarcica* (Huckriede, 1958); FUM# 4J225-4, Elikah Formation, Ali Bashi 4 Section, upper view.

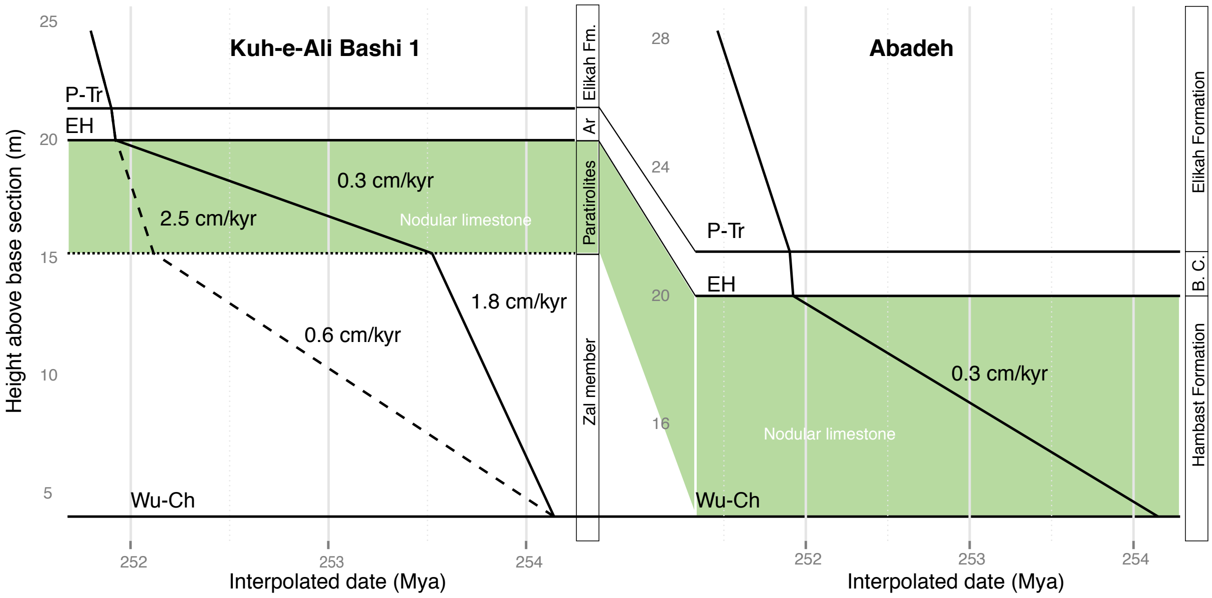

Extended data Figure 5 – Age model for the Kuh-e-Ali Bashi 1 and the Abadeh P-Tr sections. Note the high sedimentation rates for the *Paratirolites* Limestone unit when relying on age constrained conodont zones of the latest Permian (dotted line). An alternative age model for the latest Permian represents the sedimentation rate calculated for nodular limestones of the Abadeh section (solid line). This latter sedimentation rate has been calculated by dates of the 'extinction horizon' (EH) and the base of the Changhsingian system (*C. wangi*) (Supplementary Information).

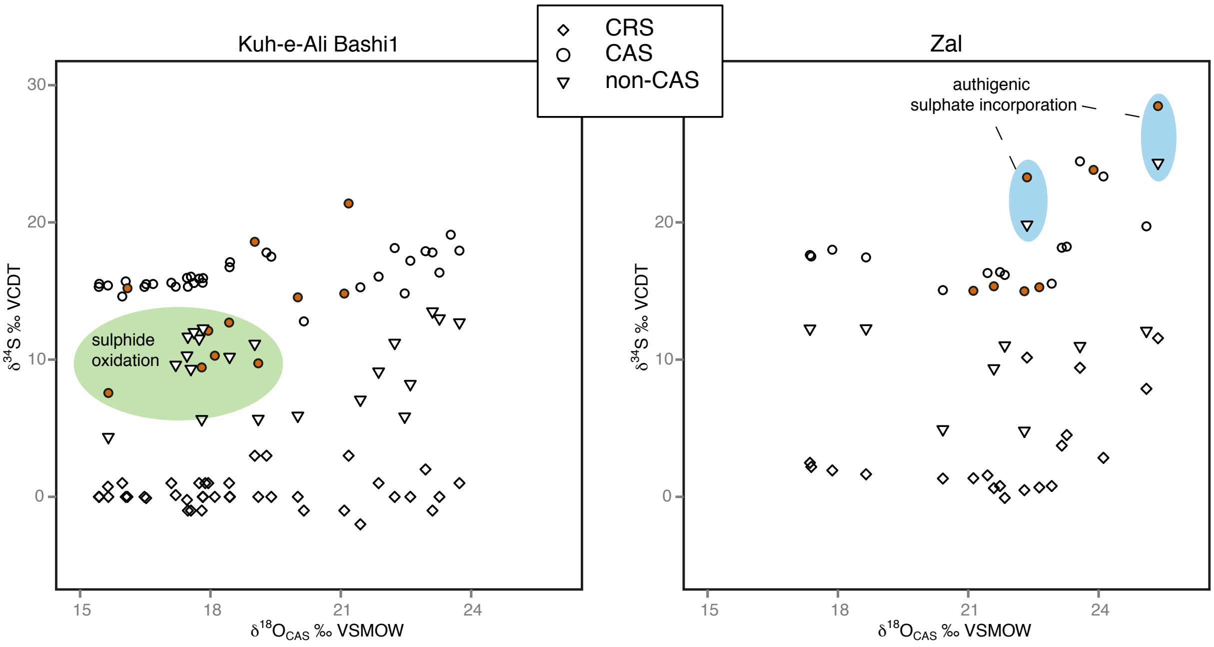

Extended data Figure 6 – Sulphur isotope composition of the extracted sulphur species. CRS, leachable non-CAS and CAS plotted against CAS-oxygen isotope values of both sections. Most δ^{34}S from CRS, non-CAS and CAS have distinctive values. However, some CAS are marked by δ^{34}S that fall in the region of non-CAS δ^{34}S values, and are often linked to comparatively high CRS/CAS or non-CAS/CAS ratios (red dots). These anomalous values accompanied by lower $\delta^{18}O_{CAS}$ might represent oxidation of sulphide during diagenesis. On the other hand some $\delta^{34}S_{CAS}$, mainly the Zal section, are enriched as well as paired with high CRS/CAS or non-CAS/CAS ratios and high $\delta^{34}S_{CRS}$, $\delta^{34}S_{non-CAS}$ and $\delta^{18}O_{CAS}$ and could therefore constitute post-depositional incorporation of CAS, from an evolved sulphate pool in a closed system (Supplementary Information).

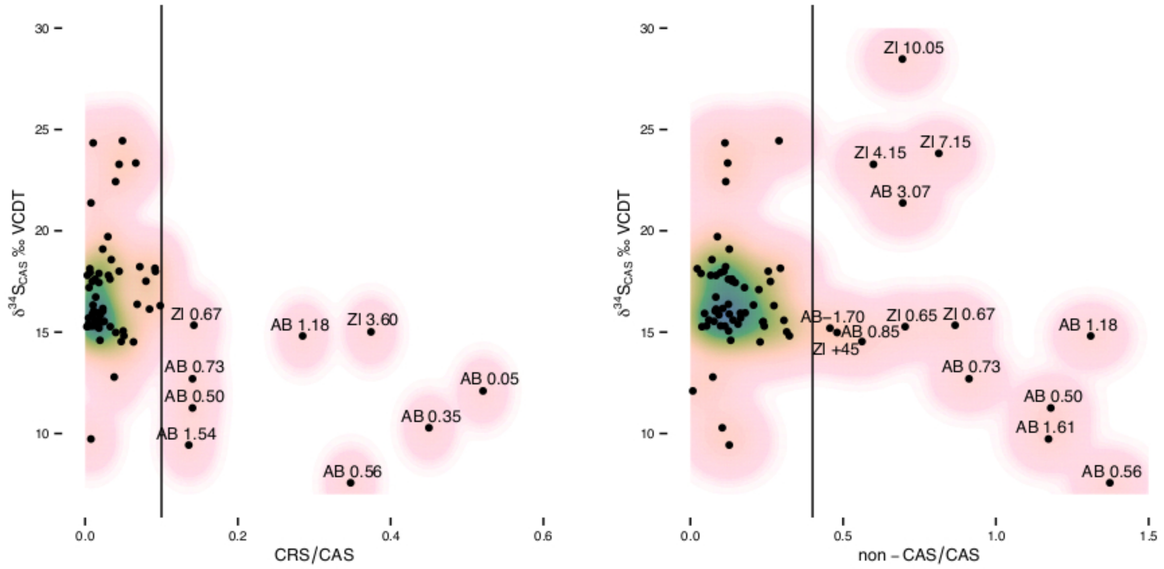

Extended data Figure 7 – Relative concentrations of CRS and leachable non-CAS in respect to CAS. CRS/CAS or non-CAS/CAS ratios plotted against CAS sulphur isotopes. The lines represent static cut-off boundary values; samples to the right are presumed vulnerable to post-depositional alteration because relative high concentrations of CRS or non-CAS could cause mixing of isotope signals (Supplementary Information).

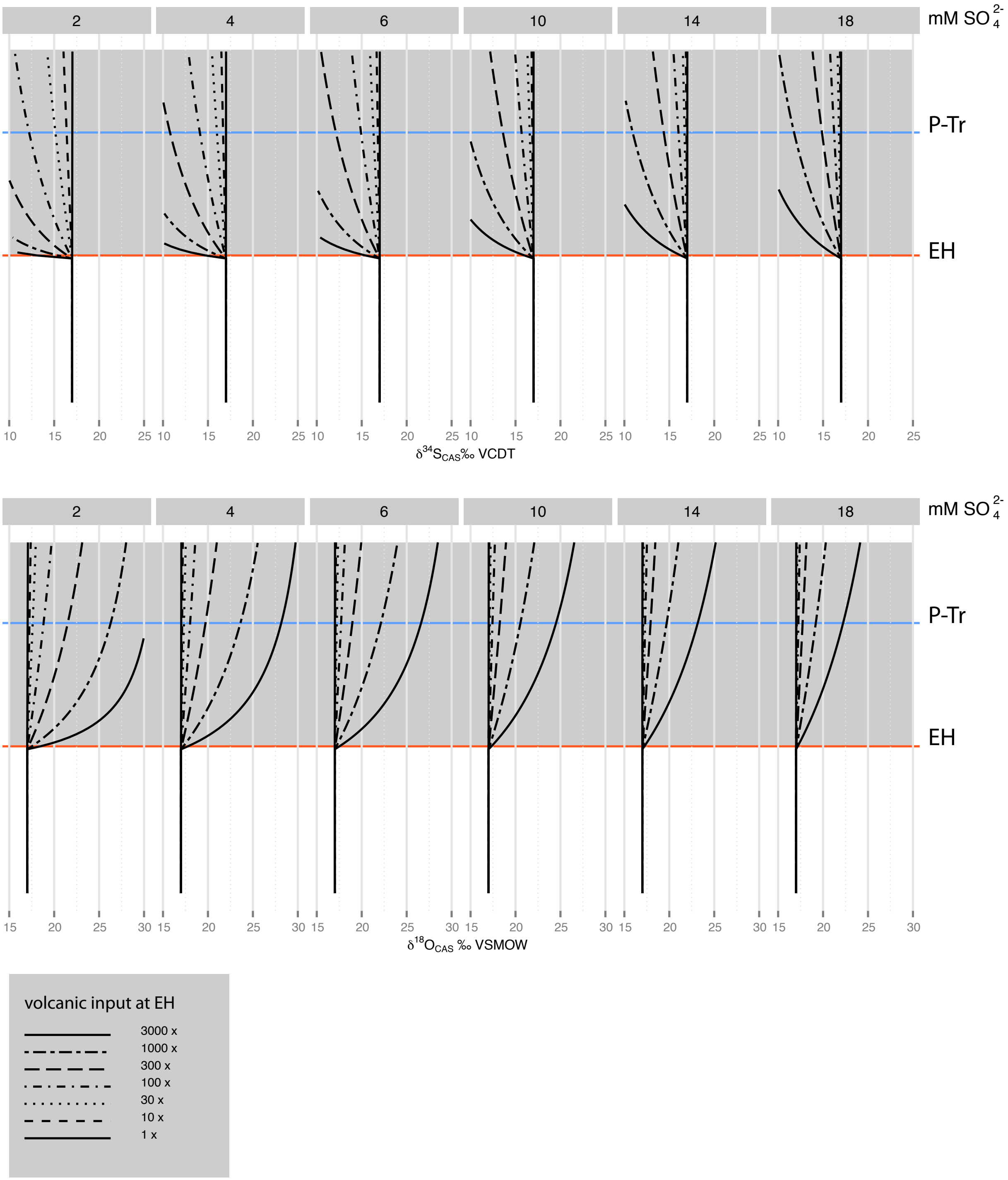

Extended data Figure 8 – Sensitivity experiment for a volcanic induced S-cycle perturbation. This scenario encompasses an influx of simultaneous isotopically depleted sulphur ($\delta^{34}S_{SO_4}$ = 3 ‰) and isotopically enriched oxygen flux ($\delta^{18}O_{SO_4}$ = 34 ‰) from a volcanic source. Coloured time interval stands for the perturbation (Supplementary Information)

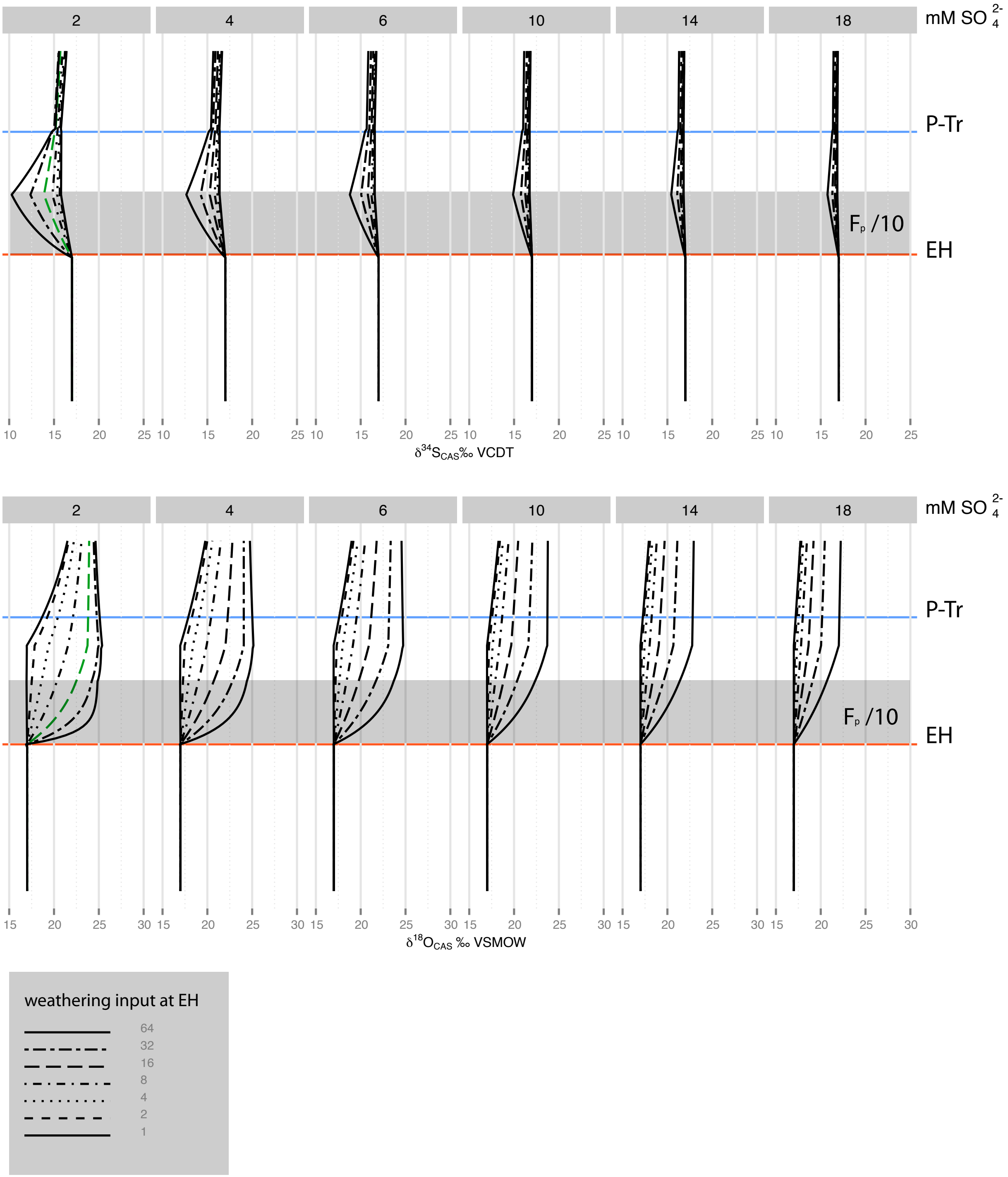

Extended data Figure 9 – Sensitivity experiment for a scenario of increased continental weathering fluxes into the ocean basin. The fraction of sulphide buried as pyrite is lowered 10 times for an interval of 20 kyr after the ‘extinction horizon’, where after the fraction of pyrite burial is increased 2 times for an equivalent time period. Coloured time interval stands for the perturbation. Continental weathering is maintained to 7 times the pre-extinction value from the P-Tr boundary till the end of the model run.

Supplementary Table 1 – Sulphur isotope composition of international and in-house standards

	δ^{34}S (‰)	2σ
IAEA -S-1		
measured	-0.35	0.20
published	-0.30	
IAEA -S-2		
measured	21.52	0.16
published	21.55	
IAEA -S-3		
measured	-31.31	0.44
published	-31.40	
NBS 127		
measured	20.38	0.17
published	20.30	
Ag2S (Lab.)		
measured	2.47	0.39
CdS (Lab.)		
measured	10.76	0.32

Isotope values obtained by replicate analyses of standard material and published values for certified reference material as given by ref. 50

Supplementary Table 2 – Oxygen isotope composition of international and in-house standards

	δ^{18}O (‰)	2σ
NBS 127		
measured	8.94	0.85
published	9.30	
IAEA-SO-5		
measured	11.97	0.70
published	12.00	
IAEA-SO-6		
measured	-11.36	0.50
published	-11.34	
BaSO4 (Lab.)		
measured	12.59	1.05

Isotope values obtained by replicate analyses of standard material and published values for certified reference material as given by ref. 50

Supplementary Table 3 – Data Kuh-e-Ali Bashi

Identifier	Height (m)*	Time (Mya)	$\delta^{34}S_{CRS}$ ‰VCDT	$\delta^{34}S_{CAS}$ ‰VCDT	$\delta^{34}S_{non-CAS1}$ ‰VCDT†	$\delta^{34}S_{non-CAS2}$ ‰VCDT†	$\delta^{18}O_{CAS}$ ‰VSMOW	$\delta^{18}O_{non-CAS1}$ ‰VSMOW†	CAS (μg/g)	non-CAS (μg/g)	CRS (μg/g)
AB	4.12	251.860	-0.90	17.81	13.51	NA	23.11	16.29	1320	88	4
AB	3.50	251.870	-20.01	19.10	NA	NA	23.53	NA	567	72	13
AB	3.30	251.870	2.98	18.59	11.15	NA	19.02	13.26	1	153	7
AB	3.07	251.880	3.07	21.38	NA	NA	21.18	NA	439	305	3
AB	2.80	251.880	0.38	17.20	8.22	NA	22.60	11.47	775	137	4
AB	2.65	251.880	0.80	17.94	12.71	12.84	23.73	15.51	745	74	5
AB	2.35	251.890	0.47	18.13	11.22	NA	22.24	13.08	1128	25	7
AB	2.20	251.890	0.61	16.05	9.13	NA	21.87	13.92	565	46	6
AB	2.05	251.890	-0.09	16.34	13.00	NA	23.27	17.32	384	79	4
AB	1.94	251.890	2.18	17.90	NA	NA	22.95	NA	327	11	6
AB	1.61	251.900	0.07	9.73	5.68	NA	19.10	6.61	168	197	1
AB	1.54	251.900	-0.64	9.43	5.66	NA	17.80	8.20	196	25	27
AB	1.41	251.900	-1.67	15.27	7.08	NA	21.45	10.40	1826	69	4
AB	1.33	251.900	-5.43	14.82	5.85	NA	22.47	7.61	284	92	14
AB	1.18	251.900	-0.66	14.81	NA	NA	21.08	NA	156	205	44
AB	0.90	251.910	0.30	16.14	7.28	NA	NA	NA	292	25	25
AB	0.85	251.910	0.09	14.54	5.91	NA	20.01	6.80	246	138	12
AB	0.73	251.910	0.65	12.70	NA	NA	18.43	NA	226	206	32
AB	0.56	251.910	-0.43	7.57	4.36	NA	15.65	4.94	111	152	39
AB	0.50	251.920	0.03	11.26	4.81	NA	NA	NA	108	128	15
AB	0.45	251.920	0.28	14.52	NA	NA	NA	NA	224	51	14
AB	0.40	251.920	-0.63	12.79	NA	NA	20.15	NA	524	39	20
AB	0.35	251.920	-0.49	10.28	NA	NA	18.10	NA	111	12	50
AB	0.28	251.920	-0.14	NA	NA	NA	NA	NA	26	3	44
AB	0.20	251.920	1.23	NA	NA	NA	17.88	NA	89	1	87
AB	0.05	251.920	1.32	12.10	NA	NA	17.95	NA	96	1	50
AB	0.00	251.940	3.22	17.80	NA	NA	19.29	NA	557	47	17
AB	-0.05	251.960	-0.18	17.50	NA	NA	19.40	NA	555	145	5
AB	-0.15	251.990	0.18	17.10	NA	NA	18.45	NA	370	83	NA
AB	-0.30	252.040	-0.02	16.73	10.20	NA	18.44	13.07	648	54	9
AB	-0.48	252.100	-0.02	15.52	NA	NA	15.44	NA	534	127	8
AB	-0.56	252.130	0.96	15.90	11.53	NA	17.74	14.66	533	68	5
AB	-0.65	252.160	0.07	15.30	NA	NA	16.48	NA	444	50	7

Supplementary Table 3 – Data Kuh-e-Ali Bashi

Identifier	Height (m)*	Time (Mya)	$\delta^{34}S_{CRS}$ ‰VCDT	$\delta^{34}S_{CAS}$ ‰VCDT	$\delta^{34}S_{non-CAS1}$ ‰VCDT†	$\delta^{34}S_{non-CAS2}$ ‰VCDT†	$\delta^{18}O_{CAS}$ ‰VSMOW	$\delta^{18}O_{non-CAS1}$ ‰VSMOW†	CAS (μg/g)	non-CAS (μg/g)	CRS (μg/g)
AB	-0.71	252.180	0.70	14.60	NA	NA	15.97	NA	310	41	6
AB	-0.80	252.210	-1.01	15.31	11.67	NA	17.48	13.29	537	29	5
AB	-0.90	252.240	NA	15.93	10.86	NA	NA	NA	439	20	NA
AB	-1.05	252.290	0.21	15.70	NA	NA	16.05	NA	391	64	2
AB	-1.15	252.320	0.74	15.40	NA	NA	15.64	NA	571	89	2
AB	-1.30	252.370	-0.23	15.96	10.30	NA	17.46	14.15	465	83	8
AB	-1.40	252.410	0.62	15.60	NA	NA	17.10	NA	476	67	8
AB	-1.55	252.460	-0.40	15.60	NA	NA	17.82	NA	418	25	5
AB	-1.70	252.510	0.31	15.20	NA	NA	16.09	NA	266	122	5
AB	-1.85	252.560	0.10	15.30	NA	NA	15.43	NA	342	83	1
AB	-2.00	252.610	0.19	15.94	12.27	NA	17.83	15.21	430	70	5
AB	-2.65	252.820	-0.09	15.50	NA	NA	16.52	NA	415	98	9
AB	-3.40	253.070	0.13	15.31	9.62	NA	17.20	14.53	628	62	5
AB	-4.40	253.410	NA	15.58	12.00	NA	17.62	16.18	500	153	NA
AB	-4.80	253.540	-1.01	16.04	9.32	NA	17.55	13.31	826	71	19
AB	-19.95	NA	NA	15.51	NA	NA					

Sample labels are composed of identifier and height (m). *Height is relative to the ‘extinction horizon’. †Numbering for non-CAS isotope values stand for the respective leaching procedure.

Supplementary Table 4 – Data Zal

Identifier	Height (m)*	Time (Mya)	$\delta^{34}\mathrm{S}_{CRS}$ ‰VCDT	$\delta^{34}\mathrm{S}_{CAS}$ ‰VCDT	$\delta^{34}\mathrm{S}_{non-CAS1}$ ‰VCDT†	$\delta^{18}\mathrm{O}_{CAS}$ ‰VSMOW	$\delta^{18}\mathrm{O}_{non-CAS1}$ ‰VSMOW†	CAS (μg/g)	non-CAS (μg/g)	CRS (μg/g)
Zl	10.95	251.790	10.66	24.34	17.18	NA	NA	372	42	4
Zl	10.05	251.800	11.56	28.48	24.34	25.37	19.91	458	318	NA
Zl	8.45	251.820	9.41	24.45	10.99	23.57	11.75	358	104	18
Zl	6.85	251.840	2.84	23.35	NA	24.11	NA	515	63	34
Zl	5.30	251.850	5.17	22.43	8.81	NA	NA	425	49	17
Zl	4.80	251.860	7.87	19.71	12.10	25.10	15.45	880	78	26
Zl	4.15	251.870	10.15	23.28	19.84	22.35	15.11	493	295	22
Zl	3.05	251.880	4.50	18.23	NA	23.27	NA	761	88	55
Zl	2.40	251.890	6.64	18.58	NA	NA	NA	867	61	30
Zl	2.00	251.890	3.74	18.15	-9.35	23.15	10.60	755	222	69
Zl	0.92	251.910	2.45	17.83	7.43	NA	NA	NA	261	31
Zl	0.76	251.910	-0.08	16.17	11.03	21.84	14.50	467	50	11
Zl	0.74	251.910	0.99	15.86	11.60	NA	NA	483	45	10
Zl	0.69	251.920	0.79	15.53	NA	22.92	NA	467	36	12
Zl	0.67	251.920	0.64	15.34	9.36	21.59	13.23	75	65	11
Zl	0.65	251.920	0.69	15.27	NA	22.63	NA	416	293	14
Zl	0.45	251.930	0.49	14.98	4.82	22.29	12.92	435	209	17
Zl	0.35	251.930	1.56	16.31	NA	21.44	NA	453	124	45
Zl	0.30	251.930	0.79	16.38	NA	21.73	NA	410	51	28
Zl	0.25	251.930	1.36	15.02	NA	21.12	NA	195	61	73
Zl	0.16	251.940	1.33	15.06	4.92	20.42	4.04	775	97	39
Zl	0.10	251.940	2.89	18.00	11.82	NA	NA	666	73	61
Zl	0.05	251.960	2.18	17.52	NA	17.39	NA	712	98	57
Zl	0.00	251.970	2.48	17.62	12.26	17.36	15.76	551	75	18
Zl	-1.15	252.360	0.41	17.61	10.59	NA	NA	578	72	8
Zl	-2.85	252.920	1.65	17.45	12.27	18.65	NA	479	70	9
Zl	-3.70	253.210	1.93	18.01	NA	17.87	NA	391	100	17
Zl	-21.00	NA	2.24	18.45	13.08	NA	NA	540	40	8

Sample labels are composed of identifier and height (m). *Height is relative to the ‘extinction horizon’. †Numbering for non-CAS isotope values stand for the respective leaching procedure.

Supplementary Table 5 – Boundary conditions for reservoirs and fluxes used in the box-model.

Reservoir/flux	Description	Value	Reference
M_{SO_4}	Initial size of sulphate reservoir	Var.	*Sensitivity experiments*
$M_{OC(i)}$	Initial size of OC reservoir	$1.10e^{17}$ mol kyr^{-1}	Ref. 49
Q_w	Flux of SO_4^{2-} weathering	$1.47e^{15}$ mol kyr^{-1}	Ref. 36
Q_v	Flux of SO_4^{2-} volcanism	$0.33e^{15}$ mol kyr^{-1}	Ref. 36
Q_m	Flux of SO_4^{2-} hydrothermal/mantle	$0.20e^{15}$ mol kyr^{-1}	Ref. 36
Q_{ox}	Flux of microbial sulphide oxidation	Calc.	*Methods*
Q_h	Flux of hydrothermal sulphide oxidation	Calc.	*Steady state P-Tr S cycle model*
Q_{po}	Flux of OC primary production	6 mol m^{-2} yr^{-1}	Ref. 49
F_p	Flux of pyrite burial	$0.90e^{15}$ mol kyr^{-1}	Ref. 49
F_e	Flux of SO_4^{2-} evaporite burial	$1.10e^{15}$ mol kyr^{-1}	Ref. 36
F_{MSR}	Flux of microbial SO_4^{2-} reduction	$40.00e^{15}$ mol kyr^{-1}	Ref. 51
F_s	Flux of mantle SO_4^{2-} anhydrite formation	$17.00e^{15}$ mol kyr^{-1}	*Steady state P-Tr S cycle model*
$F_{oc(i)}$	Flux of OC remineralization	$0.99Q_{po}$ - $2F_{MSR}$	*Methods*
$F_{bo(i)}$	Flux of OC burial	Q_{po} - $F_{oc(i)}$	*Methods*
δ_{SO_4}	Initial isotopic value of SO_4^{2-} reservoir	δ^{34}S = 17‰, δ^{18}O = 17‰	*Steady state P-Tr S cycle model*
δ_w	Isotopic value of SO_4^{2-} weathering flux	δ^{34}S = Calc., δ^{18}O = 4‰	*Steady state P-Tr S cycle model* and ref. 39
δ_v	Isotopic value of SO_4^{2-} volcanic flux	δ^{34}S = 3‰, δ^{18}O = 11‰	Ref. 26, 36, 52
δ_m	Isotopic value of SO_4^{2-} mantle flux	δ^{34}S = 3.5‰, δ^{18}O = -1‰	Ref. 26, 36, 52
δ_{ox}	Isotopic value of sulphide oxidation	δ^{18}O = Δ^{18}O(18‰) + $\delta^{18}O_{seawater}$	Ref. 39, 53 and Permian $\delta^{18}O_{seawater}$ -1‰[54]
Δ_{MSR}	Fractionation of MSR between SO_4^{2-} and sulphide	Δ^{34}S =- 35‰, δ^{18}O =Δ^{34}S/4	Ref. 36, 49
k_1	First order removal constant OC remineralization	$(M_{OC(i)}/F_{oc(i)})^{-1}$	-
k_2	First order removal constant OC remineralization	$(M_{OC(i)}/F_{bo(i)})^{-1}$	-

Fluxes signified by Q are flowing into the reservoir and F out of the reservoir. Var. stands for varied as initial value. Calc. stands for calculated value.